Nanostructured Semiconductor Oxides and Oxynitrides for Photocatalysis

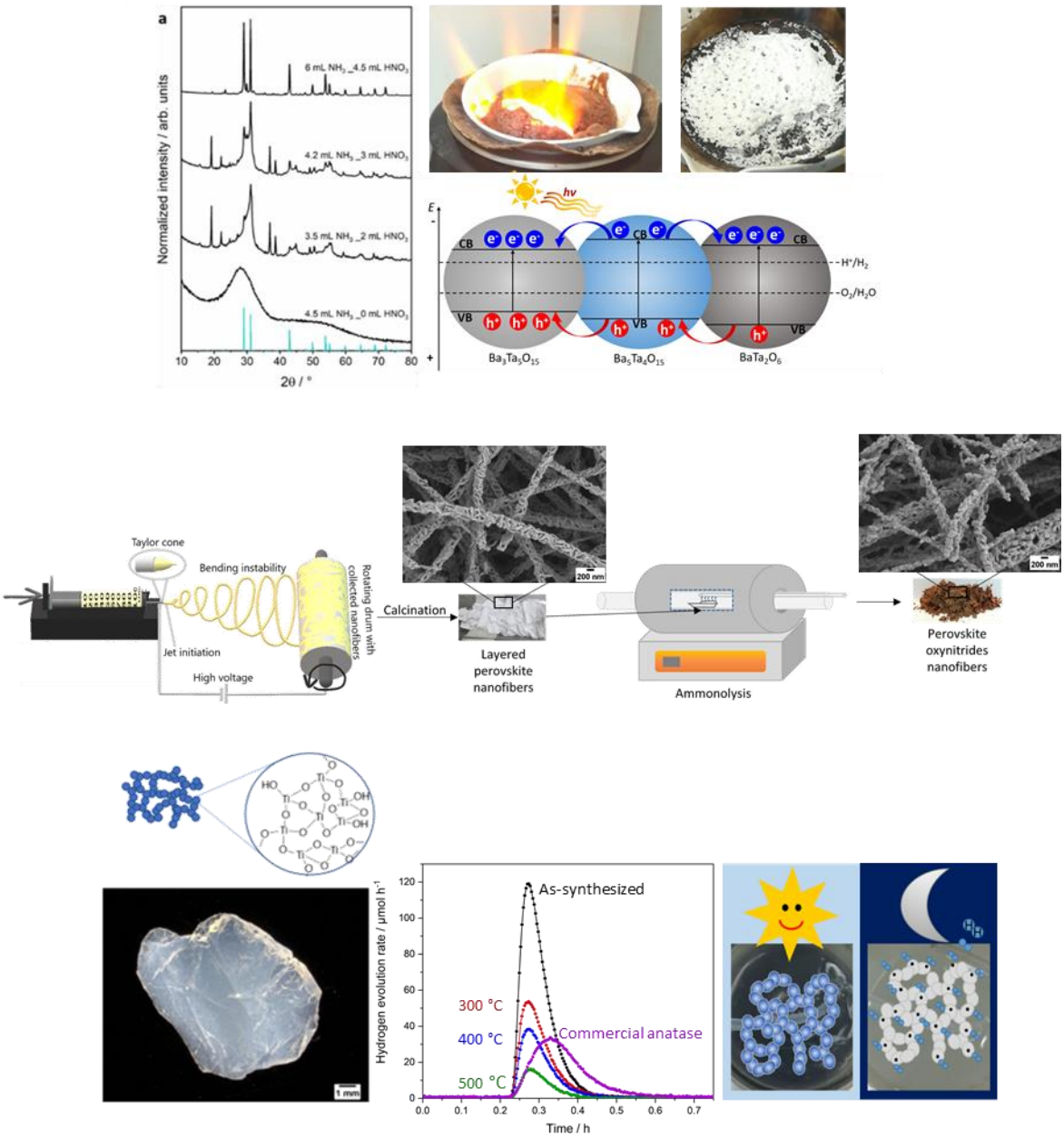

Anja Hofmann

Nanostructured Semiconductor Oxides and Oxynitrides for Photocatalysis

Dissertation

zur Erlangung des akademischen Grades

„doctor rerum naturalium“

(Dr. rer. nat.)

in der Bayreuther Graduiertenschule für Mathematik und Naturwissenschaften (BayNAT)

der Universität Bayreuth

vorgelegt von

Anja Hofmann, M. Sc.

geboren in Zittau

Bayreuth, 2022

Die vorliegende Arbeit wurde in der Zeit von Februar 2019 bis September 2022 am Lehrstuhl Physikalische Chemie III der Universität Bayreuth unter Betreuung von Herrn Prof. Dr. Roland Marschall angefertigt.

Vollständiger Abdruck der von der Bayreuther Graduiertenschule für Mathematik und Naturwissenschaften (BayNAT) der Universität Bayreuth genehmigten Dissertation zur Erlangung des akademischen Grades einer Doktorin der Naturwissenschaften (Dr. rer. nat.).

Dissertation eingereicht am: 26.09.2022

Zulassung durch das Leitungsgremium: 18.10.2022

Wissenschaftliches Kolloquium: 27.03.2023

Amtierender Direktor: Prof. Dr. Hans Keppler

Prüfungsausschuss:

Prof. Dr. Roland Marschall (Gutachter)

Prof. Dr. Andreas Greiner (Gutachter)

Prof. Dr. Matthias Breuning (Vorsitz)

Prof. Dr. Rhett Kempe

Table of Contents

List of Symbols and Abbreviations

A	– acceptor	***α***	– absorption coefficient
arb. u.	– arbitary units	**as-syn**	– as-synthesized
at%	– atomic percent	**B**	– donor
BET	– Brunauer-Emmett-Teller	**BJH**	– Barrett-Joyner-Halenda
BPI	– Bavarian polymer institute	**CB**	– conduction band
COD	– Crystallography Open Database	**DLR**	– German Aerospace Center
DOS	– density of states	**DRIFT**	– diffuse reflectance infrared Fourier transform spectroscopy
E	– energy	E_{CB}	– energy of the conduction band minimum
E_F	– Fermi level	E_g	– band gap energy
E_{vac}	– vacuum energy	E_{VB}	– energy of the valence band maximum
e^-	– electron	**EA**	– elemental analysis
EDTA	– ethylenediaminetetraacetic acid	**EDX**	– energy dispersive X-ray (spectroscopy)
e.g.	– *exempli gratia* (for example)	***et al.***	– *et alii* (and others)
EPR	– Electron paramagnetic resonance	**EtOH**	– ethanol
F(*R*)	– Kubelka-Munk function	Φ_m	– metal work function
Φ_S	– semiconductor work function	Φ_{SB}	– Schottky barrier
FTIR	– Fourier-transform infrared	**FTO**	– fluorine doped tin oxide
ΔG	– Gibbs energy	**GC**	– gas chromatography/gas chromatograph
hv	– photon energy	h^+	– hole
HER	– hydrogen evolution reaction	**ICSD**	– Inorganic Crystal Structure Database
i.e.	– *id est* (that is)	**IR**	– infrared
IPA	– isopropanol	**IUPAC**	– International Union of Pure and Applied chemistry

ITO	– indium tin oxide	**JCPDS**	– Joint Committee on Powder Diffraction Standards, now International Centre for Diffraction Data (ICDD)
λ	– wavelength	L_D	– minority carrier diffusion length
M	– molar concentration	**MEK**	– methyl ethyl ketone
MeOH	– methanol	**MFC**	– mass flow controller
MS	– mass spectrometry/mass spectrometer	M_W	– molecular weight
$Nb(OEt)_5$	– niobium (V) ethoxide	**NF**	– nanofiber/s
NHE	– normal hydrogen electrode	**NIR**	– near infrared
NIST	– National Institute of Standards and Technologies	**OER**	– oxygen evolution reaction
p	– pressure	p_0	– saturation pressure
PEG	– polyethylene glycol	**pH**	– potential of hydrogen
PVP	– polyvinylpyrrolidone	R	– gas constant
R	– reflectance	R_{exp}	– expected profile R-factor
R_{wp}	– weighted profile R-factor	**RHE**	– reversible hydrogen electrode
SAED	– selected area electron diffraction	**SCR**	– space charge region
SEM	– scanning electron microscopy	**SHE**	– standard hydrogen electrode
SI	– supporting information	**SSR**	– solid-state reaction
t	– tolerance factor	T	– temperature
$Ta(OEt)_5$	– tantalum (V) ethoxide	**TCD**	– thermal conductivity detector
TEM	– transmission electron microscopy	**TG-MS**	– thermogravimetric analysis coupled with online mass spectrometry
ϑ	– Bragg angle	**THF**	– tetrahydrofuran
TOC	– total organic carbon	**TTIP**	– titanium (IV) isopropoxide
UV	– ultraviolet	**VB**	– valence band
vis	– visible	**vs**	– versus
wt. %	– weight percent	**XPS**	– X-ray photoelectron spectroscopy
XRD	– X-ray diffraction	χ^2	– “goodness of fit”

1 Summary / Zusammenfassung

1.1 Summary

With respect to the ever-growing energy demand, the finiteness of carbon-based fossil fuels, and the rise of CO_2 emissions, solar-light induced photocatalytic water splitting for the generation of clean and renewable hydrogen as an alternative energy carrier becomes increasingly important. In this regard, energy efficient syntheses for the reduction of energy consumption are as important as the syntheses of highly efficient and stable photocatalysts. The present thesis deals with both aspects, first presenting an energy efficient way for the synthesis of layered perovskite heterojunctions,[1] and second a research dealing with the synthesis of visible-light absorbing nanostructured perovskite oxynitrides.[2] Nanostructuring is a promising and important approach to enhance the activity of photocatalysts and was therefore also studied in the third research project of this thesis dealing with TiO_2 aerogels.[3]

Layered perovskite composites such as $Ba_5Ta_4O_{15}$-$Ba_3Ta_5O_{15}$ and $Ba_5Ta_4O_{15}$-$Ba_3Ta_5O_{15}$-$BaTa_2O_6$ are known to be much more active in photocatalysis than phase-pure $Ba_5Ta_4O_{15}$.[4–6] An energy efficient synthesis of such composites is presented in the first study of this thesis. The presented synthesis allows for the preparation of $Ba_5Ta_4O_{15}$-$Ba_3Ta_5O_{15}$-$BaTa_2O_6$ at ambient pressure and at comparatively low temperatures. An additional energy intensive calcination step is not required anymore. For this, a citrate synthesis route[4] was optimized by a systematic adjustment of the combustion reaction. Thereby, the composition of the composite could be tailored with $Ba_5Ta_4O_{15}$ occuring as the main phase for all samples. The synthesis directly yielding a crystalline product resulted in the highest amount of by-phases with around 12 % of $Ba_3Ta_5O_{15}$ and 12 % of $BaTa_2O_6$ as revealed by Rietveld refinement. Photocatalytic activity tests in hydrogen evolution and overall water splitting showed the highest activity for the non-calcined sample. This can be explained by an improved charge carrier separation due to an optimized composition of this layered perovskite heterojunction. This synthesis route could be used for the preparation of many other semiconductor materials, as it combines energy efficiency and time saving without diminishing the photocatalytic activity.

Although the activity of the layered perovskites could be enhanced by the formation of a heterojunction, the photocatalytic activity is still limited to the UV light range. Visible-light absorption can be obtained by ammonolysis of layered perovskite oxides leading to cubic perovskite oxynitrides.[7,8] The second work reported herein focused on the nanostructuring of $BaNbO_2N$ perovskite oxynitrides since ammonolysis often leads to micrometer-sized particles.[9,10] For this, a sol-gel derived electrospinning approach was established. Layered perovskite $Ba_5Nb_4O_{15}$ nanofibers with adjusted diameter were prepared *via* electrospinning and converted by ammonolysis to perovskite oxynitride nanofibers. It was possible to retain the nanofiber morphology during ammonolysis and to tailor the nanofiber diameter in a range of 135 to 213 nm. Thorough characterization revealed the formation of the novel perovskite oxynitride composite $BaNbO_2N$-Ba_2NbO_3N. These $BaNbO_2N$-Ba_2NbO_3N nanofibers showed diameter-dependent photocatalytic hydrogen and oxygen evolution after decoration with Pt or $CoNbO_4$ with an optimum nanofiber diameter of 213 nm. The herein presented synthesis strategy could be used to synthesize other nanostructured perovskite oxynitrides and could pave the way to other nanostructuring strategies for perovskite oxynitrides.

The generation of mesoporosity, *i.e.* in aerogels, as one other nanostructuring strategy besides the electrospinning can be similarly or even more effective for the enhancement of the activity of photocatalysts. Aerogels are a group of nanostructured materials for photocatalysis, offering the possibility of tailoring the surface area and crystallinity in a wide range.[11,12] Mesoporous TiO_2 aerogels were investigated for their electron storage abilities and hydrogen evolution activities in the third study. These aerogels were prepared *via* a novel modified acid catalyzed sol-gel synthesis with subsequent supercritical drying. By varying the heat treatment conditions, the surface area could be adjusted in a range of 92 $m^2\ g^{-1}$ up to 600 $m^2\ g^{-1}$. The electron storage ability increased with increasing surface area, *i.e.* lower calcination temperature, and depended on the hole scavenger concentration, *i.e.* methanol concentration. Quantification of the stored photoelectrons was performed by measuring the evolved hydrogen amount in the dark after reductive Pt deposition in the dark, which revealed increased hydrogen amounts with increasing surface area. Moreover, the direct photocatalytic sacrificial hydrogen evolution increased with decreasing surface area and electron storage ability, which can be

explained by better crystallinity of the calcined TiO_2 aerogels. A nitrogen reduction reaction to ammonia in the dark, using the stored photoelectrons in the TiO_2 aerogels could be finally performed, representing a promising on-demand application for these TiO_2 aerogels.

1.2 Zusammenfassung

Aufgrund des ständig wachsenden Energiebedarfs, der Endlichkeit fossiler Energieträger und des Anstiegs von CO_2-Emissionen, erlangt die Erzeugung von sauberem und erneuerbarem Wasserstoff als alternativem Energieträger durch photokatalytische Wasserspaltung mittels Sonnenlicht immer mehr an Bedeutung. Diesbezüglich sind energie-effiziente Synthesen zur Reduzierung des Energieverbrauchs genauso wichtig wie Synthesen von hocheffizienten und stabilen Photokatalysatoren. In der vorliegenden Dissertation wird eine energie-effiziente Synthese von Schichtperowskit-Heterostrukturen vorgestellt,[1] sowie eine Synthese von nanostrukturierten Perowskit-Oxynitriden, die sichtbares Licht absorbieren,[2] und damit auf beide Aspekte eingegangen. Nanostrukturierung ist ein interessanter und wichtiger Ansatz zur Aktivitätssteigerung von Photokatalysatoren und wurde daher auch in der dritten präsentierten Arbeit über TiO_2 Aerogele untersucht.[3]

Schichtperowskit-Komposite wie $Ba_5Ta_4O_{15}$-$Ba_3Ta_5O_{15}$ und $Ba_5Ta_4O_{15}$-$Ba_3Ta_5O_{15}$-$BaTa_2O_6$ sind dafür bekannt, deutlich aktiver in der Photokatalyse zu sein als das phasen-reine $Ba_5Ta_4O_{15}$.[4–6] Eine energie-effiziente Synthese solcher Kompositmaterialien wird in der ersten Arbeit dieser Dissertation vorgestellt. Die gezeigte Synthese ermöglicht die Herstellung von $Ba_5Ta_4O_{15}$-$Ba_3Ta_5O_{15}$-$BaTa_2O_6$ bei Umgebungsdruck und vergleichsweise geringen Temperaturen. Ein zusätzlicher energieintensiver Kalzinierungsschritt ist nicht mehr notwendig. Dafür wurde eine Citratsynthese[4] durch systematisches Anpassen der Verbrennungsreaktion optimiert. Damit konnte die Zusammensetzung des Komposits angepasst werden, wobei $Ba_5Ta_4O_{15}$ in allen Proben die Hauptphase darstellte. Die Synthese, die direkt zu einem kristallinen Produkt führte, wies den größten Anteil an Nebenphasen mit etwa 12 % $Ba_3Ta_5O_{15}$ und 12 % $BaTa_2O_6$ auf, was durch Rietveld-Verfeinerung gezeigt werden konnte. Untersuchungen der photokatalytischen Aktivität in der Wasserstoffentwicklung und Wasserspaltung zeigten die höchste Aktivität für die nicht-kalzinierte Probe. Dies kann

durch eine verbesserte Ladungsträgertrennung durch die optimierte Zusammensetzung dieser Schichtperowskit-Heterostruktur erklärt werden. Dieser Syntheseweg könnte für die Herstellung vieler anderer Halbleitermaterialien genutzt werden, da Energieeffizienz und Zeitersparnis kombiniert wurden, ohne die photokatalytische Aktivität zu verringern.

Obwohl die Aktivität der Schichtperowskite durch die Bildung der Heterostrukturen verbessert werden konnte, ist die photokatalytische Aktivität auf den UV-Bereich beschränkt. Absorption von sichtbarem Licht kann durch Ammonolyse von Schichtperowskiten erreicht werden, wodurch die Perowskit-Oxynitride erhalten werden.[7,8] Die zweite Arbeit, die in dieser Dissertation vorgestellt wird, war auf die Nanostrukturierung von $BaNbO_2N$ Perowskit-Oxynitriden ausgerichtet, da die Ammonolyse oft zu Mikrometer-großen Partikeln führt.[9,10] Dafür wurde ein Sol-Gel-Elektrospinn-Ansatz etabliert. $Ba_5Nb_4O_{15}$ Schichtperowskit-Nanofasern mit eingestellten Durchmessern wurden durch Elektrospinnen hergestellt und anschließend durch Ammonolyse zu Perowskit-Oxynitrid-Nanofasern umgewandelt. Es war möglich, die Nanofasermorphologie beizubehalten und den Nanofaserdurchmesser in einem Bereich von 135 bis 213 nm einzustellen. Die detaillierte Charakterisierung zeigte die Bildung eines neuen $BaNbO_2N$-Ba_2NbO_3N Perowskit-Oxynitrid-Komposits. Diese $BaNbO_2N$-Ba_2NbO_3N Nanofasern zeigten eine durchmesserabhängige photokatalytische Wasserstoff- und Sauerstoffentwicklung nach Dekoration mit Pt oder $CoNbO_4$ mit einem optimalen Nanofaserdurchmesser von 213 nm. Die hier gezeigte Synthesestrategie könnte für die Synthese anderer nanostrukturierter Perowskit-Oxynitride genutzt werden, und den Weg zu anderen Nanostrukturierungsstrategien für Perowskit-Oxynitride bereiten.

Die Erzeugung von Mesoporosität, d.h. in Aerogelen, als eine weitere Strategie zur Nanostrukturierung neben dem Elektrospinnen, kann vergleichbar oder sogar effektiver für die Aktivitätssteigerung von Photokatalysatoren sein. Aerogele sind eine Gruppe von nanostrukturierten Materialien für die Photokatalyse, die die Möglichkeit bieten, die Oberfläche und die Kristallinität in einem weiten Bereich maßzuschneidern.[11,12] In der dritten Arbeit wurden mesoporöse TiO_2 Aerogele hinsichtlich ihrer Fähigkeit zur Elektronenspeicherung und ihrer Aktivität in der Wasserstoffentwicklung mit Opferreagenzien untersucht. Diese Aerogele wurden mittels einer neuen angepassten Säure-katalysierten Sol-Gel-Synthese mit anschließender superkritischer Trocknung

hergestellt. Durch Variation in der thermischen Behandlung konnte die Oberfläche in einem Bereich von 92 $m^2 g^{-1}$ bis zu 600 $m^2 g^{-1}$ angepasst werden. Die Fähigkeit Elektronen zu speichern stieg dabei mit ansteigender Oberfläche und geringerer Kalzinierungstemperatur an und war zudem abhängig von der Konzentration des Lochfängers Methanol. Die gespeicherten Photoelektronen wurden durch Nachweis des im Dunklen entstehenden Wasserstoffs nach reduktiver Pt Abscheidung im Dunklen quantfiziert, was ansteigende Wasserstoffmengen mit steigender Oberfläche nachwies. Weiterhin stieg die sakrifizielle Wasserstoffentwicklung mit sinkender Oberfläche und damit geringerer Elektronenspeicherung, was durch eine bessere Kristallinität der kalzinierten TiO_2 Aerogele erklärt werden kann. Eine Stickstoffreduktion zu Ammoniak im Dunkeln, die die gespeicherten Photoelektronen in den TiO_2 Aerogelen nutzt, konnte am Ende der Studie erfolgreich durchgeführt werden, und stellt eine zukunftsträchtige Bei-Bedarf-Anwendung für solche TiO_2 Aerogele dar.

2 Introduction and Theory

2.1 Challenges in Future Energy Supply and Demand

Climate change is one of the major challenges of our time and humanity is already facing the consequences. The global temperature increased by 1.01 °C since 1880, the artic sea ice is declining at a rate of 13 % per decade, earth's polar ice sheets are loosing mass – 427 tons per year since 2002 – and the global average sea level has risen by 178 mm in the past 100 years caused by the increase of the water's internal heat (all for 2021).[13] Most climate scientists agree that global warming is human-made.[14–18] It is caused by the emission of greenhouse gases, including major contributing gases CO_2, CH_4, N_2O, and SO_2. The major sources for these gases are fossil fuel combustion and deforestation, biomass combustion and agricultural wastes, fertilizer use, and combustion of coal, oil, and diesel.[18] Emissions of CO_2, which is the most important greenhouse gas forcing the greenhouse effect, increased from 277 ppm in 1750 to 412 ppm in 2020.[19] 30 % of the anthropogenic CO_2 emissions in the period from 1850-2020 can be accounted to land-use change and 70 % to fossil fuel emission.[19] In this period, the proportion of CO_2 emissions from fossil fuels increased significantly since 1960 as can be also seen in the global primary energy consumption by fossil fuels shown in **Figure 1**.[19,20]

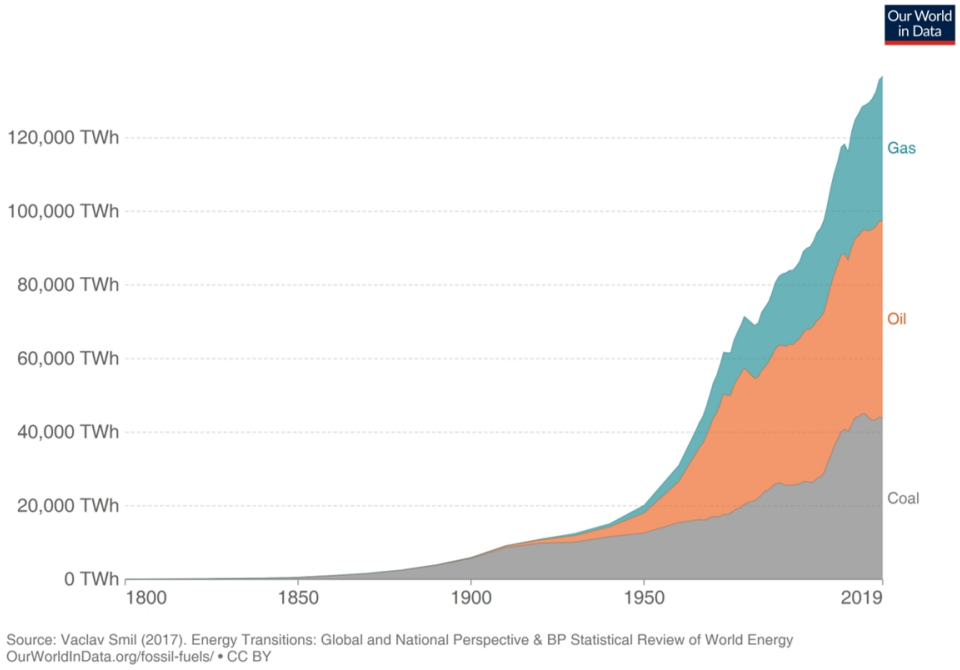

***Figure 1**: Global primary energy consumption by fossil fuels from 1800 to 2019. Reprinted with permission from Ritchie et al. (Our World in Data)[20], licensed under CC BY 4.0.*

In 2021, still 82 % of the primary energy consumption was based on fossil fuels, which is a decrease of only 5 % in the last five years.[21] Furthermore, 2021 was the second year in a row with a record in methane emissions, which is the second most important greenhouse gas after CO_2.[22,23] The annual increase was 17 ppb, reaching an atmospheric methane level around 162 % above the pre-industrial level.[23] It is more important than ever to reduce the global greenhouse gas emissions; therefore the Paris agreement was negotiated in 2015 with the ambition to limit global warming well below 2 °C with efforts to limit warming below 1.5 °C compared to the pre-industrial level.[24] **Figure 2** presents different scenarios for changes in global greenhouse gas emissions and the global temperature increase following from these emissions in 2100.[25] If countries do not implement climate reduction policies, and all humans proceed as they did for the last decades, the global warming will further proceed to 4.1 up to 4.8 °C in 2100 compared to pre-industrial temperature level inducing dramatic changes in the world's climate.

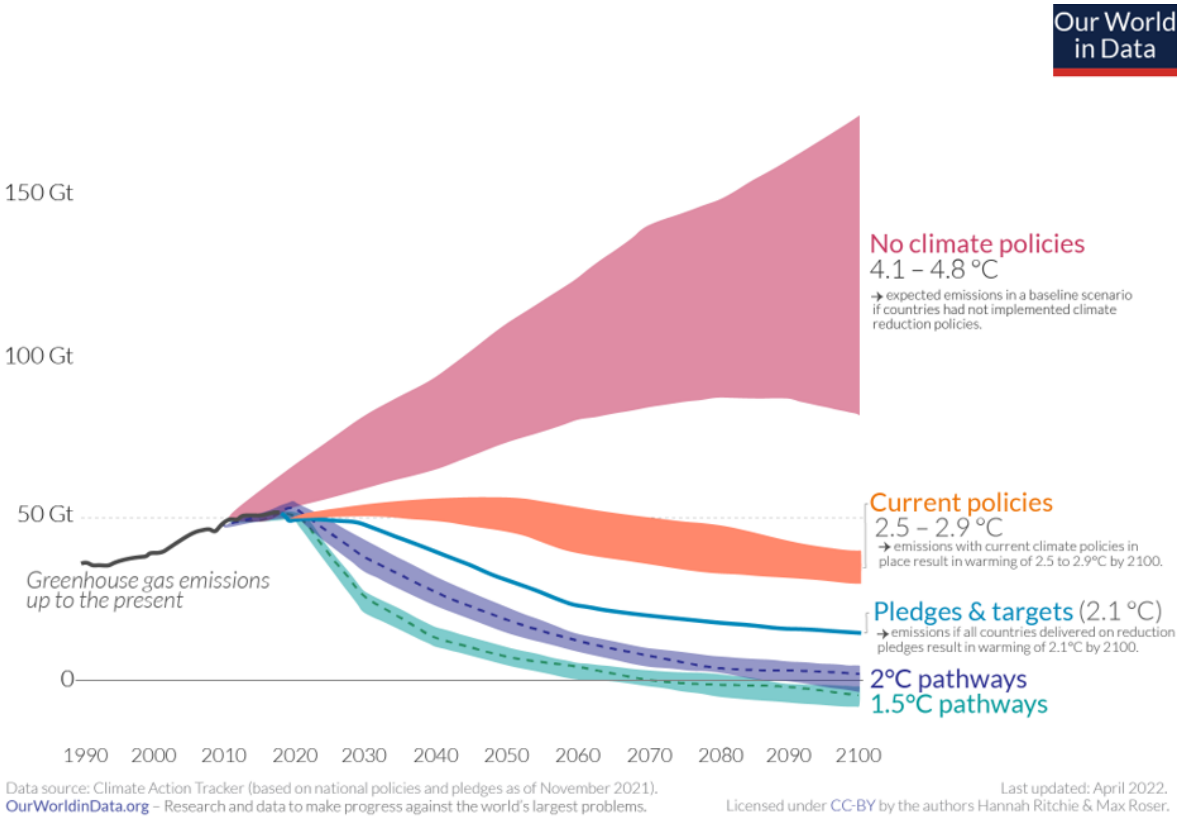

***Figure 2**: Global greenhouse gas emissions and warming scenarios. Annual global greenhouse gas emissions are given in giga-tons of CO_2-equivalents. Shading from low to high emissions for each scenario marks the uncertainty of each pathway. The given temperature increase for each scenario is relative to the pre-industrial temperatures and refers to the expected global temperature rise by 2100. Reprinted with permission from Ritchie et al. (Our World in Data)[25], licensed under CC BY 4.0.*

To reach the goal of the Paris agreement, decarbonisation of the global energy sector is one of the key responsibilities in the next years, also facing the finiteness of fossil fuels, which will cause a dramatic price increase. Prices for oil, coal, and natural gas already increased strongly in 2021.[21] In 2021 a global energy consumption of 18.53 TWy y^{-1} up to 20.13 TWy y^{-1} and a recoverable reserve of 220 TWy of natural gas and 1010 TWy of coal were estimated.[26] Furthermore it is estimated, that the global energy consumption will further increase up to 27 TWy y^{-1} in 2050.[27] Following from this, renewable energy sources have to play a major role in the future global energy supply. **Figure 3** shows the progress of global energy generation from renewable energies (biomass not included) since 1965, showing a rapid increase in wind and solar power since 2000.[20] The potential of renewable energy sources is still significantly higher than this. The annual energy potential of renewable energy sources exceeds the total reserves of finite energy sources. Especially solar energy is a promising candidate for renewable energy generation as the sun offers an annual energy potential of 23,000 TWy y^{-1}.[26] The energy provided by one hour sunlight covers the global energy consumed in one year.[28,29] However, the direct use of solar energy is restricted by fluctuations due to the day-night-rhythm, weather changes, and seasons. Due to this, the energy provided by the sun, needs to be converted into storable and transportable forms, *i.e.* chemical fuels such as hydrogen.[29]

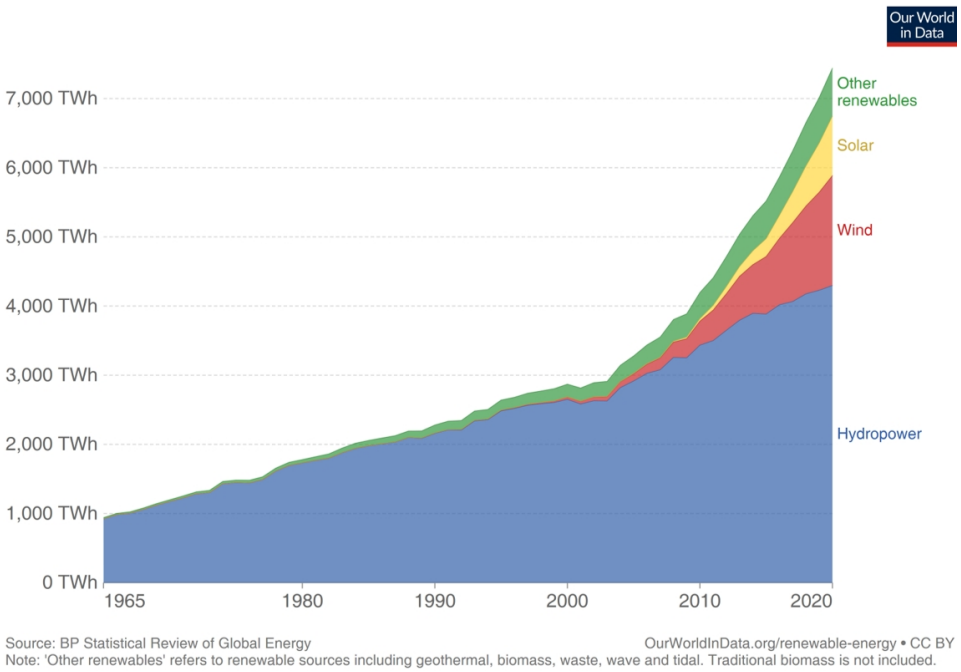

***Figure 3**: Global renewable energy generation from 1965 to 2020. Reprinted with permission of Ritchie et al. (Our World in Data)[20], licensed under CC BY 4.0.*

Hydrogen has the highest energy density by mass compared to other storage methods such as pumped hydroelectric energy storage, batteries, capacitors, or flywheels, but it suffers from a low volumetric energy density.[30] One way to overcome this issue could be the storage of hydrogen in metal hydrides and complex hydrides, which additionally reduces fire risks.[31] Furthermore, other easily transportable chemical fuels such as hydrocarbons, offer higher volumetric energy densities,[30] but suffer from the release of CO_2 upon combustion. In contrast to this, hydrogen forms water upon combustion with oxygen in air and the stored energy is released.[31] Hydrogen can be produced by photocatalytic water splitting, photoelectrochemical processes, or by coupling photovoltaic devices with an electrolyzer as alternative production methods compared to the mainly used steam reforming process based on fossil fuel sources.[32–43] Advantages of photocatalysis are the use of water as an abundant and convenient hydrogen source and the possibility to release formed oxygen into the atmosphere without problems. Fujishima and Honda discovered the light-driven direct splitting of water into its elements hydrogen and oxygen on a TiO_2 semiconductor surface in 1972.[44] Since this time, a lot of effort was put into photocatalysis research, with TiO_2 being the most investigated photocatalyst.[45–47] A detailed discussion of semiconductors and photocatalysis will follow in Chapter 2.2. However, it is important to note here, that the semiconductor material has to fulfill several requirements to be useful in solar-light induced photocatalysis. One of the most important properties is the characteristic band gap of a semiconductor, which has to be small enough that solar light can excite the semiconductor to generate electron-hole pairs. These electron-hole pairs are then used to perform redox reactions in photocatalysis, or can be also used for the generation of electrical power in photovoltaic cells. The photon energy of solar light has to be higher than the band gap of the material, which limits the portion of the solar light usable for photocatalysis with a specific semiconductor. **Figure 4** shows the solar radiation spectra before entering the earth's atmosphere (AM0) and after passing the 1.5 atmospheres (AM1.5).[48] The total energy of the AM0 spectrum emitted by the sun is reduced due to absorption and reflection processes when passing through the atmospheres. Greenhouse gases absorb more than 25 % of the AM0 radiation; the absorption bands of CO_2 and H_2O are especially visible in the IR region.[49,50] Only 5 % of the solar spectrum at the earth's surface belongs to UV-light, 43 % to visible light, and 52 % to

infrared light.[49] Although offering high chemical and physical stability, low cost, and easy availability TiO_2 exhibits a band gap in the range of 3.0 to 3.2 eV and can therefore only absorb UV-light, which limits the theoretical solar-to-hydrogen efficiency of TiO_2 to 1.3 % for anatase and 2.2 % for rutile and therefore the practical application in solar-light harvesting.[51,52] However, the very well studied material properties of TiO_2 makes it to a promising model photocatalyst and tailoring of materials properties can enhanced the light light absorption and photocatalytic activity, *e.g.* nanostructuring or doping.[53–56]

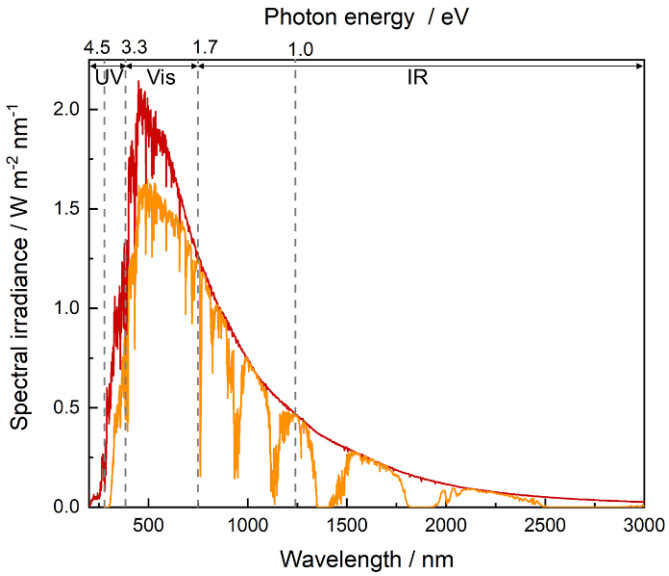

***Figure 4**: Solar radiation spectrum before entering the earth's atmosphere (AM0, red) and the solar spectrum at sea level after passing 1.5 atmospheres (AM1.5, orange) with marked areas of UV, vis, and IR-part of the solar spectrum. Data were taken from Honsberg et al.*[48]

In addition, alternative semiconductor materials have to be found for an efficient application in solar light-induced photocatalysis, which have to be able to harvest a wide range of solar light, thus offering the possibility of highly efficient conversion of solar energy to hydrogen. An absorption edge greater than 420 nm or a band gap smaller than 3 eV are necessary for an efficient harvesting of solar light.[57] Scientists put a lot effort in this and discovered a series of suitable semiconductor materials.[34,58–63] Oxynitride materials have been recognized as one promising group of materials for solar-light induced water splitting, absorbing a wide range of solar light and being suitable for water oxidation and reduction reaction.[57,64–72] Included in this group of materials are also perovskite oxynitrides with the molecular formula $AB(O,N)_3$ (A = La, Ca, Sr, or Ba; B = Nb, Ta or Ti). These materials offer the possibility of fine tuning of physical and chemical properties by ionic doping and substitution due to the higher flexibility of the perovskite structure

compared to a metal oxynitride structure.[57,69,73] Further research on the optimization of such photocatalysts is important for hydrogen production using solar light radiation as an abundant energy source.

Photocatalysis can become then an important part of the world's future energy supply by enabling the decarbonisation of the global energy sector.

2.2 Photocatalysis

In general, chemical reactions that can only occur or proceed faster in the presence of light (photons *hv*) are photochemical processes. Photochemical reactions can be divided into photocatalysis and photosynthesis, which can be distinguished by their change of Gibbs energy ΔG during the reaction. Photocatalytic reactions are exergonic reactions ($\Delta G < 0$) and photosynthetic reactions are endergonic reactions ($\Delta G > 0$).[41,74] Photosynthetic systems can be further distinguished from photocatalytic ones as they additionally have to suppress the back reaction.[74] The degradation of organic pollutants is an example for a photocatalytic process, sacrificial H_2 and O_2 evolution reactions from water can be photosynthetic as well as photocatalytic, whereas the splitting of water into O_2 and H_2 without a sacrificial agent is an example for a photosynthetic reaction.[41,74] However, photochemical processes involving light absorption by semiconductors are most often referred to as photocatalysis and no differentiation is made between photocatalysis and photosynthesis.[74]

Photocatalysis can be further divided into homogenous and heterogeneous photocatalysis, in which educt(s) and photocatalyst are either in the same (homogeneous) or in two different phases (heterogeneous).[41] Examples for homogeneous photocatalysts are polyoxometalates,[75] organic molecules,[41] or metal complexes,[76] whereas photocatalysts for heterogeneous systems are solid semiconductors in either liquid or gaseous medium. This thesis will focus onto heterogeneous photocatalysis with inorganic semiconducting photocatalysts in liquid educts.

Semiconductors exhibit an electronic structure with a valence band (VB) comprised of fully occupied electronic ground states and the conduction band (CB), consisting of fully unoccupied electronic states. The energy difference between the conduction band minimum and the valence band maximum is known as band gap (E_g).[77–80] This band gap

distinguishes semiconductors from metallic conductors, which have overlapping valence and conduction bands (shown in **Figure 5**).[78] Insulators are materials with band gaps above approximately 4 eV, also sometimes referred to as wide-band gap semiconductors.

The half occupied energy level in between the band gap is the so-called Fermi level (E_F).[81,82]

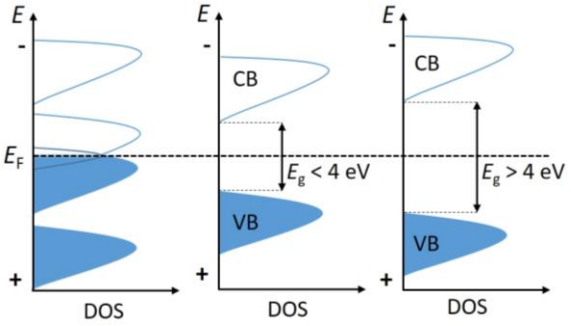

***Figure 5**: Band structure of a metal (left), a semiconductor (middle), and an insulator (right). The occupied states are represented by blue-coloration. The thick dashed line shows the position of the Fermi level (E_F). The band gap (E_g) for a semiconductor and an insulator are given.*

The position of the Fermi level differentiates between the three types of semiconductors, *i.e.* intrinsic, n-type, and p-type semiconductors as shown in **Figure 6**. An ideal intrinsic semiconductor such as silicon has a Fermi level positioned in the middle of the band gap. The excitation of such an intrinsic semiconductor results in identical concentration of electrons and holes.[83] In real semiconductors, impurities and surface defects are always present and can be further introduced by doping, resulting in additional donor or acceptor states. In p-type semiconductors additional acceptor levels are introduced, located above the VB. The majority carriers are therefore holes, the Fermi level is shifted towards the VB. Additional donor levels are introduced in n-type semiconductors resulting in electrons as majority charge carriers and a shift of the Fermi level towards the CB.

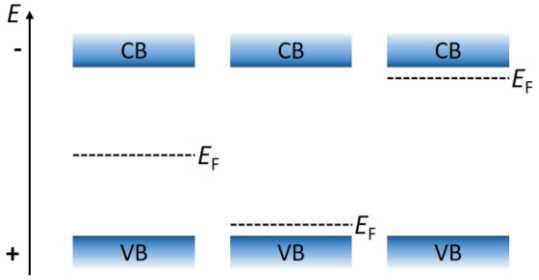

***Figure 6**: Fermi level positions of an intrinsic (left), a p-type (middle), and an n-type (right) semiconductor.*

Most of the commonly used semiconductors are n-type semiconductors with tendencies towards anion deficiencies, as for example ZnO, TiO_2, $BiVO_4$, $Ba_5Ta_4O_{15}$, $MgFe_2O_4$, TaON,

and $BaNbO_2N$.[84–86] Examples for p-type semiconductors with tendencies towards cation deficiencies are CuO and $CaFe_2O_4$.[84,86]

Besides the differentiation between intrinsic, p- and n-type semiconductors, they can be additionally distinguished between direct and indirect semiconductors. Electrons (e^-) can be excited from the VB into the CB of a semiconductor by absorption of photons with an energy equal or larger than E_g leaving holes (h^+) in the VB.[79,80,84] Depending on the electronic position of VB maximum (E_{VB}) and CB minimum (E_{CB}), this transition can be either direct or indirect as represented in **Figure 7**. The optical transitions in direct semiconductors as for example CdS, ZnS, and Ba_2NbO_3N show no change in the wave vector k.[81,87] Transitions in indirect semiconductors such as TiO_2 require a change of k and therefore an additional interaction with phonons, resulting in much larger absorption coefficients for direct semiconductors.[83,88] However, the probability of charge carrier recombination is also higher in direct semiconductors as charge carriers are better separated in indirect semiconductors, resulting in longer charge carrier lifetimes for indirect semiconductors.[88]

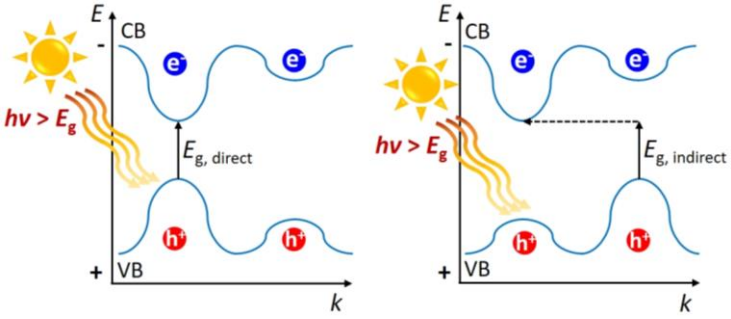

***Figure 7**: Illustration of the optical transition in a direct (left) and indirect (right) semiconductor from valence band maximum to conduction band minimum.*

After excitation in the first step of photocatalysis, photogenerated charge carriers, *i.e.* h^+ and e^-, separate and diffuse to the surface of the semiconductor where they can be used to perform either reduction or oxidation reactions.[84] Electrons promote reduction reaction of adsorbed electron acceptors (A) and holes oxidation reactions of adsorbed electron donors (B) (**Figure 8** left). In overall water splitting, water is oxidized to oxygen and protons are reduced to hydrogen (**Figure 8** right). These reactions can only be performed, if E_{VB} and E_{CB} match the electrochemical potential of the half reaction. For this, E_{VB} needs to be more positive than the oxidation half reaction potential and E_{CB} needs to be located more negative than the potential of the reduction half reaction. Therefore, E_{VB} of a

photocatalyst has to be located more positive than +1.23 V (*vs*. standard hydrogen electrode ((SHE), pH = 0) and E_{CB} has to be more negative than 0 V (*vs.* SHE) to perform overall water splitting.[33,34,71,79] This implies, that the band gap of the photocatalyst additionally has to be larger than 1.23 eV in order to perform overall water splitting. The Gibbs energy for overall water splitting is 237 kJ mol^{-1}, which equals 1.23 eV.[33,34,58,66,71,89–91] Photocatalysts with band gaps of at least 1.8 to 2.2 eV are required for overall water splitting which can be explained by slow kinetics that result in required overpotentials to achieve sufficient reaction rates.[71,92–95]

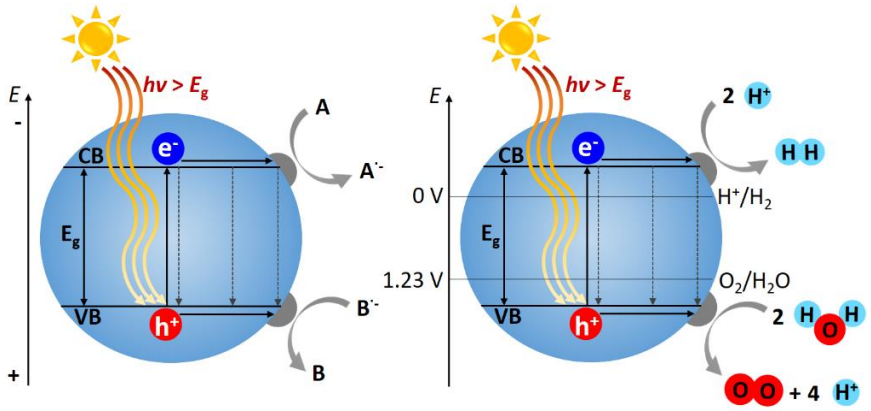

***Figure 8**: Schematic illustration of a photocatalytic reaction with e^- promoting reduction and h^+ oxidation reactions of either an electron acceptor (A) or an electron donor (B) (left). Scheme of overall water splitting as an exemplary photocatalytic redox reaction (right). The dashed lines represent recombination processes. Adapted with permission from Marschall et al.*[84] *Copyright 2013 WILEY-VCH Verlag GmbH & Co. KGaA, Weinheim.*

The efficiency of photocatalytic reactions is reduced by recombination processes that can proceed *via* different mechanisms. Photoexcited charge carriers have a finite lifetime and diffusion length depending on the material, the light intensity as well as on the charge carrier type.[58] The major recombination process of photoexcited charge carriers is the relaxation of photoexcited electrons back into the VB, releasing energy non-radiatively or radiatively in form of heat or photoluminescence.[84] The charge carriers can further undergo bulk recombination at grain boundaries or defects in the crystal structure or surface recombination at the surface of the semiconductor.[79,84] Holes and electrons can be trapped in trap states in the bulk or at the surface of the semiconductor, in mid gap states or in surface states, and recombination can proceed from there. Methods to decrease the charge carrier recombination probability in a photocatalyst are the synthesis of highly crystalline and/or nanostructured materials. A high crystallinity reduces the defect

concentration (recombination centers) in the material, and particle size reduction decreases the diffusion pathway for the photoexcited charge carriers to the surface for the redox reaction.[79,84] Other approaches to reduce the recombination probability is the use of sacrificial agents and co-catalysts as well as the synthesis of heterojunction composites to promote charge carrier separation.[84]

2.2.1 Sacrificial Agents, Co-catalysts and Heterojunction Composites

Sacrificial Agent

Sacrificial agents are either hole or electron scavengers, that consume one kind of photogenerated charge carrier fast, reducing the recombination probability and thus prolonging the charge carrier lifetime of the other not consumed charge carrier, leading to increased activity.[79] Hole scavengers or electron donors used for the sacrificial hydrogen evolution are often organic molecules, thereby alcohols, ethylene diamine tetraacetic acid, and lactic acid are the most important sacrificial agents.[96] Methanol is the most used sacrificial agent for sacrificial hydrogen evolution.[97] Inorganic ions used as sacrificial agents for the sacrificial hydrogen evolution are I^-, S^{2-}/SO_3^{2-}, S^{2-}, SO_3^{2-} Fe^{2+} and Ce^{3+}.[96,98]
Two mechanisms are proposed for the photocatalytic oxidation of methanol, the direct oxidation by photogenerated holes and the indirect oxidation *via* hydroxyl radicals (·OH).[99,100] It could be shown for TiO_2, that the mechanism depends on the adsorbed molecules on the surface and that the indirect oxidation of methanol is most likely the mechanism pursued in aqueous solution.[100] The ·OH radicals, formed by trapping of VB holes, react with methanol by abstracting the hydrogen atom of the C-H bond forming an α-hydroxymethyl radical ($\cdot CH_2OH$).[99,101–104] If no oxygen is present in the reaction solution, an electron is injected from the $\cdot CH_2OH$ radical into the CB of the photocatalyst, resulting in the formation of formaldehyde in a process called (photo)current doubling.[101] This photocurrent doubling was shown to take place for alcohols with α-hydrogen atoms[105], which was also reported for sacrificial hydrogen evolution using $Ba_3Ta_5O_{15}$-$Ba_5Ta_4O_{15}$ composite nanofibers (see **Figure 9**).[6] It is also important that the reduction potential of the radical must be more negative than the CB minimum of the photocatalyst as otherwise, the electron cannot be injected into the CB. But still, an increased hydrogen evolution can be obtained.[6] Besides the photocurrent doubling, an improved charge carrier separation

was obtained for $Ba_3Ta_5O_{15}$-$Ba_5Ta_4O_{15}$ composite nanofibers, which will be discussed later in this section.

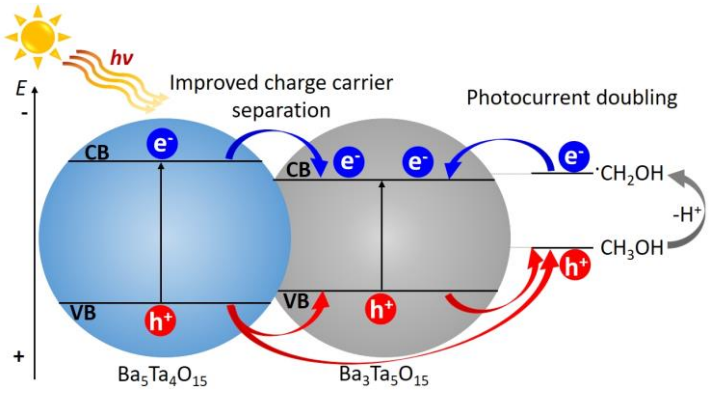

***Figure 9**: Schematic illustration of improved charge carrier separation in $Ba_5Ta_4O_{15}$-$Ba_3Ta_5O_{15}$ composite with photocurrent doubling in the presence of methanol as hole scavenger. Adapted with permission from Bloesser et al.[6] Copyright 2018 American Chemical Society. The formation of the $\cdot CH_2OH$ radical is shown here by direct oxidation of methanol for simplicity.*

Electron scavengers or electron acceptors which can be used for the sacrificial oxygen evolution are Ag^+ or Fe^{3+} and $S_2O_8^{2-}$.[79,99] The most widely employed electron scavenger is Ag^+.[99] All of these electron scavengers have the disadvantage of possible oxygen evolution additional to the oxygen evolution from water oxidation. For example, Ag^+ can be oxidized by holes, forming Ag_2O_2 peroxide, which can be further oxidized, resulting in oxygen evolution.[99] Therefore it cannot be distinguished, which amount of the evolved oxygen is formed *via* direct water oxidation or indirectly from the electron scavenger.[99] Additionally, Ag(0) is deposited on the photocatalyst surface, resulting in absorption changes and blocking of reactive sites, moreover Ag(0) can be catalytically active by itself.

Co-catalysts

A lot of photocatalysts are still not able to produce oxygen or hydrogen only in the presence of a sacrificial agent, an additional decoration with a co-catalyst is necessary.[91] Especially the efficiency of the more challenging oxygen evolution half reaction, as a four electron process could be enhanced by the use of a co-catalyst with low overpotential for the oxygen evolution.[106] Co-catalysts catalyze reactions by lowering the activation energy and the overpotential, provide active sites for the reactions, serve as trapping sites for photogenerated charge carriers, can suppress charge carrier recombination and back reactions, and can also improve the photostability of a photocatalyst.[91,106]

Noble metals such as Pt, Pd, Rh, Ru, Ir, or Au are often used as co-catalysts for the hydrogen evolution reaction, acting as electron sink and additionally as proton reduction site.[84,91,107,108] The efficiency of the electron trapping of noble metals is determined by the difference in the work functions of the metals and the photocatalyst, with a larger work function for the noble metals.[109] A Schottky contact is formed between the metal and the semiconductor, facilitating electron transfer from the semiconductor to the metal as shown in **Figure 10** (top) for an n-type semiconductor.[84,110] The Fermi levels of the metal and the semiconductor equilibrate at the interface, resulting in band bending and the formation of a Schottky barrier. A space charge region forms at the surface of the semiconductor, resulting in depletion of electrons in n-type semiconductors, therefore called a depletion layer.[110] The charge separation is improved as back transfer of electrons is hindered by the Schottky barrier. In p-type semiconductors an accumulation layer is formed as electron transfer is facilitated from the metal to the semiconductor (**Figure 10** bottom).[110,111]

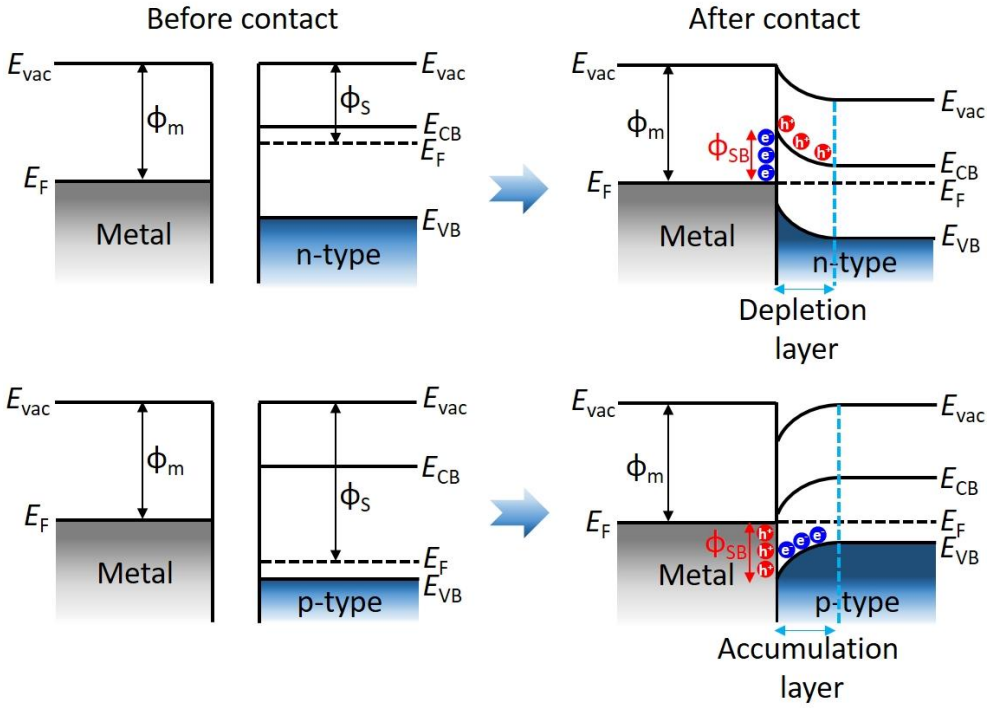

***Figure 10**: Band diagrams of a metal co-catalyst and an n-type (top) and p-type (bottom) semiconductor before contact (left) and in contact under equilibrium with the Schottky barrier Φ_{SB} marked in red. Adapted with permission from Zhang et al.[110] Copyright 2012 American Chemical Society.*

Pt has the largest work function of noble metals and additionally has the lowest activation energy for hydrogen evolution reaction, therefore Pt is the most suitable co-catalyst for the

hydrogen evolution.[91,108,112] Other non-noble metal co-catalysts used for the hydrogen evolution reaction are for example NiO, transition metal disulfides, Ni, Co, Cu, $Ni(OH)_2$, Ni complexes, or artificial molecules such as hydrogenase mimics.[106,113–116]

The most active co-catalysts for the oxygen evolution reaction are RuO_2 and IrO_2.[106] More cost-effective co-catalysts employed for the oxygen evolution reaction are for example CoO_x, Co_3O_4, cobalt-phosphate (Co-Pi), MnO_x, FeO_x, as well as $B_2O_{3-x}N_x$, therein especially Co based co-catalysts receive a lot of attention.[106]

Core-shell Rh-Cr_2O_3 and $Rh_{2-y}Cr_yO_3$ are the most active co-catalysts used for overall water splitting.[106,117] Tested alternatives are for example Cu(II)-Cr(III) mixed oxide nanoparticles and core-shell co-catalysts Ni-NiO, or CrO_x-NiO_y.[106,118–121] Cr_2O_3, NiO, and CrO_x are reported to inhibit the back reaction, *i.e.* the photoreduction of O_2 to water.[106]

The two most employed deposition methods for co-catalysts are *in-situ* photodeposition and impregnation method.[122,123] In the presented studies *in-situ* photodeposition was used for the deposition of Rh-Cr_2O_3 and Pt co-catalyst *via* addition of either an aqueous solution of Na_3RhCl_6, K_2CrO_4, or H_2PtCl_6 to the photocatalyst suspension and subsequent deposition of the corresponding co-catalyst by light irradiation.[1–3] The impregnation method was performed for the deposition of CoO_x *via* dispersion of the photocatalyst in aqueous $Co(NO_3)_2$ solution, evaporation, and heat treatment in NH_3 and air.[2]

Heterojunction Composites

The formation of a heterojunction composite can result in an improved charge carrier separation by charge carrier transfer between the two composite materials, resulting in improved photocatalytic activity as shown in **Figure 9**.[6] Heterojunction composite formation can further enhance the light absorption range by combining a visible light absorbing semiconductor with a non-visible light absorbing material.[84] Furthermore, the stability of a semiconductor material in the composite can be enhanced.[84] Such a heterojunction composite can be either formed between different phases of the same material, *e.g.* between anatase and rutile, or between different photocatalytic materials.

Heterojunction composites of two different components can be divided into three different types shown in **Figure 11**, depending on the VB and CB positions of the components.[84] In a type I heterojunction (**Figure 11**, left) the VB maximum of one semiconductor lies at more positive potential and the CB minimum at more negative potential compared to the other

semiconductor, resulting in accumulation of both electrons and holes in the semiconductor with the smaller band gap and no improvement in the photocatalytic activity. The heterojunction composite of $Ba_5Ta_4O_{15}$-$Ba_3Ta_5O_{15}$ seems to be a type I semiconductor (**Figure 9**), but the difference in the VB position is very small, compared to the difference in the CB minimum position, resulting in an improved charge carrier separation by transfer of photoexcited electrons from the CB of $Ba_5Ta_4O_{15}$ into the CB of $Ba_3Ta_5O_{15}$ and an improved activity.[4,6]

The most used heterojunction composites are type II heterojunctions with optimum stacked band positions of the two semiconductor materials, resulting in efficient charge carrier separation and improved photocatalytic activity (**Figure 11** middle). Here the position of the VB minimum of one semiconductor lies at more positive potential and the CB minimum at less negative potential compared to the other compound, resulting in accumulation of holes in one and electrons in the other semiconductor material.

The charge transfer in type III heterojunctions is similar to that in the type II heterojunctions, only the offset of the VB maximum and CB minimum between the two semiconductors is more intense compared to type II heterojunctions with more negative potentials of both CB and VB of one semiconductor than the CB of the other semiconductor (**Figure 11** right).

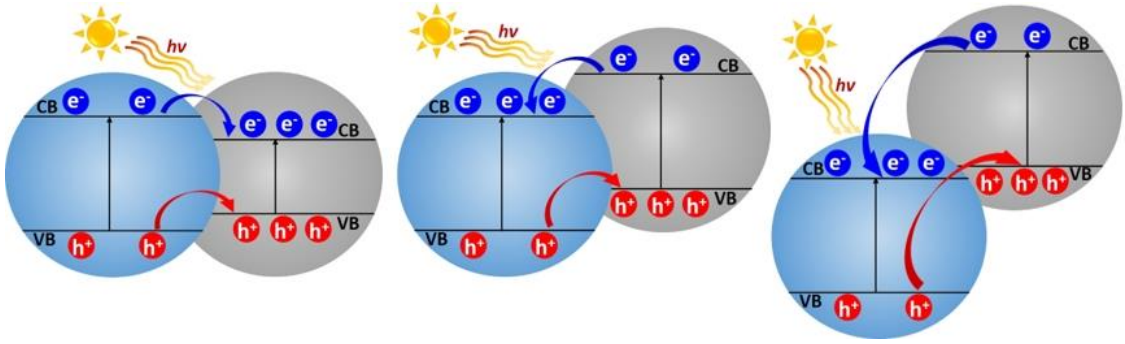

***Figure 11**: Schematic illustration of different kinds of semiconductor heterojunctions with charge transfer; type I (left), type II (middle), and type III (right). Adapted with permission from Marschall et al.*[84] *Copyright 2013 WILEY-VCH Verlag GmbH & Co. KGaA, Weinheim.*

A direct Z-scheme has a comparable structure to that of a type II heterojunction, but the charge carrier separation is different.[124] In this setup, the electrons in the CB of the semiconductor with the higher work function are transferred to the VB of the second semiconductor *via* a redox mediator and recombine there with the holes.[124] The oxidation can proceed at the semiconductor with the higher oxidation ability and reduction at the

second semiconductor with the higher reduction ability, resulting in an optimized redox ability compared to type II heterojunction.

A good interfacial contact between the heterojunction components is required for efficient charge transfer.[125] Examples for type II multiphase heterojunctions are composites of different TiO_2 phases such as TiO_2(B)/anatase or rutile/anatase.[125,126] There are many multicomponent heterojunctions of type II including the most investigated heterojunction CdS/TiO_2 or $MgTa_2O_{6-x}N_y$/TaON.[84,127,128] Stability improvement as well as enhanced light absorption together with improved charge carrier separation was obtained for $Ba_5Ta_4O_{15}/AgVO_3$ heterojunction.[129]

Heterojunctions of n- and p-type semiconductors are especially efficient.[84] Additionally, heterojunction composites of more than two compounds can be prepared. One example is shown in **Figure 12**, a heterojunction composite of $Ba_3Ta_5O_{15}$, $Ba_5Ta_4O_{15}$, and $BaTa_2O_6$. The charge separation in this three component heterojunction is further improved compared to the two component heterojunction $Ba_3Ta_5O_{15}$, $Ba_5Ta_4O_{15}$, resulting in further enhanced photocatalytic activity.[5]

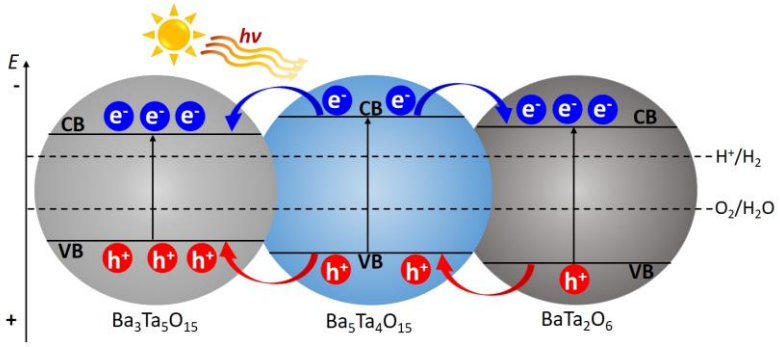

***Figure 12**: Schematic illustration of a heterojunction of $Ba_3Ta_5O_{15}$, $Ba_5Ta_4O_{15}$, and $BaTa_2O_6$ with the corresponding charge transfer. Adapted with permission from Soldat et al.[5], licensed under CC BY 3.0.*

2.2.2 Band Gap Engineering

Although the three component heterojunction $Ba_3Ta_5O_{15}$-$Ba_5Ta_4O_{15}$-$BaTa_2O_6$ showed enhanced activity, it still only absorbs UV-light due to the large band gaps of the three components.[5] Therefore, only a very small part of the solar spectrum (≤5 %) can be absorbed by the single materials as well as by the heterojunction composites. For the absorption of a larger part of the solar spectrum, band gap reduction by band gap engineering is a powerful tool.

There are different approaches to lower the band gap and to obtain visible light absorption as shown in **Figure 13**, either the lifting of the VB (I) or lowering of the CB (II) or the continuous tuning of the VB or/and CB (III) are possible ways to reduce the band gap.[130] For transition metal oxides, shifting the VB maximum towards less positive potentials is the most promising way, as the CB minimum in most semiconductor oxides is only slightly more negative than hydrogen evolution potential and the VB maximum often significantly more positive than oxygen evolution potential.[130]

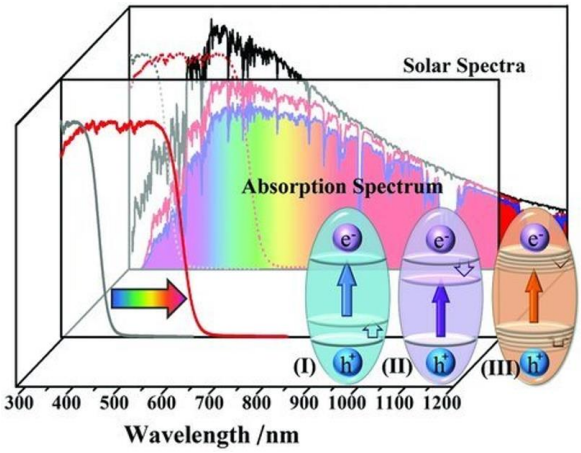

***Figure 13**: Schematic illustration of three different possibilities of band gap engineering. Adapted with permission from Ouyang et al.[131] Copyright 2011 American Chemical Society, adapted version is reprinted with permission from Tong et al.[130].*

The most effective approaches for the lifting of the VB minimum are the doping with 3*d*-transition elements, cations with d^{10} or $d^{10}s^2$ configurations, and non-metal elements.[130] Doping of TiO_2 with different 3*d* transition metal cations such as Cr^{3+}, V^{3+}/V^{4+}, Ta^{5+}, Nb^{5+}, or W^{6+} was investigated and resulted in improved light absorption and photocatalytic activity.[56,132] Also the Ni doping of $InTaO_4$ resulted in visible light absorption and water splitting.[133] However, the 3*d* transition metal doping can also result in increased recombination probability and in suppressed charge carrier transfers due to introduced defects and localized *d*-states in the electronic structure.[130,134,135]

Multi-metal oxides with cations with electronic d^{10} or $d^{10}s^2$ configuration are also interesting, in which additional states are introduced above the VB as for example in $CaBi_2O_4$, where occupied Bi 6*s* states hybridize with O 2*p* orbitals, forming the valence band.[136,137] Other examples are oxides with Ag^+ or Pb^{2+} as well as photocatalysts with Cu^+ or Sn^{2+}, as for example Sn^{2+} exchanged layer titanates or niobates such as $Sn^{2+}/K_4Nb_6O_{17}$ or $Sn^{2+}/Cs_2Ti_6O_{13}$, $Sn_xK_{1-2x}TaWO_6$, or the Sn^{2+} exchanged (111) layered perovskite $Ba_5Nb_4O_{15}$

as well as $CuLaO_2$.[130,138–140] The light absorption of Sn^{2+} exchanged (111) layered perovskite $Ba_5Nb_4O_{15}$ could be enhanced by incorporating Sn $5s^2$ as new VB maximum, reducing the band gap to 2.35 eV for 40 % Sn(II) exchange and visible light activity in the oxygen evolution reaction.[139]

Band gap reduction can be also obtained by doping of non-metal elements, especially with nitrogen or sulfur. The nitrogen doping of the (111) layered perovskite $Ba_5Ta_4O_{15}$ results in the band gap reduction by more than 2 eV, as shown in **Figure 14**, as N 2*p* states hybridize with O 2*p* orbitals, forming the valence band.[141] A reduction of the band gap and enhanced photocatalytic activity by nitrogen doping was also shown for several other metal oxides including TiO_2, ZnO, α-Bi_2O_3, $CsTaWO_6$, $Cs_{0.68}Ti_{1.83}O_4$, and proton-exchanged Dion-Jacobson layered niobate perovskites.[55,142–149]

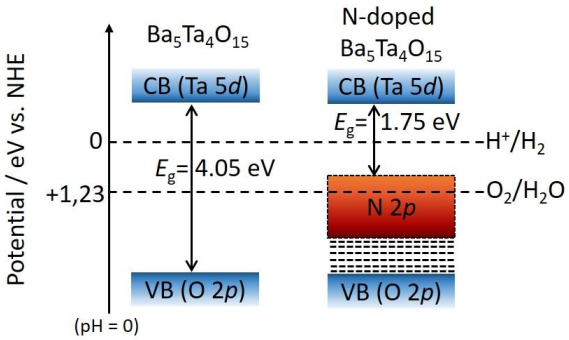

***Figure 14**: Energy diagram of $Ba_5Ta_4O_{15}$ before and after nitrogen doping. Adapted with permission from Mukherji et al.*[141] *Copyright 2011 American Chemical Society.*

The reduction of the band gap of *e.g.* TiO_2, g-C_3N_4, and α-Bi_2O_3 by doping with sulfur was also shown with S 3*p* states that are introduced in the VB.[143,150,151] $CsTaWO_6$ was co-doped with nitrogen and sulfur, resulting in an increase of the VB maximum and decrease of the CB minimum and enhanced photocatalytic activity.[152] The tuning of VB maximum and CB minimum can be achieved continuously by preparation of solid solutions such as β-$AgAl_{1-x}Ga_xO_2$.[130,131]

2.3 Perovskites-Type Metal Oxides and Oxynitrides in Photocatalysis

Perovskite-type metal oxides as well as their derivatives, layered perovskite-type metal oxides, are widely investigated materials in photocatalysis as is illustrated by many review articles.[153–159] They offer structural simplicity and flexibility, high stability, and good photocatalytic efficiency.

The most stable ideal perovskite-type metal oxide with general formula ABO_3 exhibits cubic crystal structure and a tolerance factor of $t = 1$ (**Figure 15 a**).[153,156,160] The B cation is 6-fold coordinated by oxygen, the BO_6 octahedra are corner shared, and the 12-fold oxygen coordinated A cation is located at the center. The A cation can be an alkali or an alkaline earth metal as well as a rare-earth element, while the B cation is a transition metal element. The tolerance factor depends on the ionic radii of A, B, and oxygen and should be between 0.75 and 1 for a stable perovskite.[153,156,160] However, the ideal cubic crystal structure of a perovskite is limited to tolerance factors very close to 1, smaller tolerance factors result in a distortion and orthorhombic (**Figure 15 b**) or rhombohedral symmetry.

Layered perovskite-type metal oxides can be divided into different groups, the Aurivillius perovskites ($(Bi_2O_2)(A_{n-1}B_nO_{3n+1})$), Ruddlesden-Popper perovskites ($A_{n+1}B_nO_{3n+1}$ or $A_2'A_{n-1}B_nO_{3n+1}$), Dion-Jacobson perovskites ($A'[A_{n-1}B_nO_{3n+1}]$), and (110) ($A_nB_nO_{3n+2}$) as well as (111) oriented layered perovskites ($A_{n+1}B_nO_{3n+3}$).[153,154] **Figure 15 c-g** show the crystal structures and exemplary compounds crystallizing in these five types of layered perovskite metal oxides.

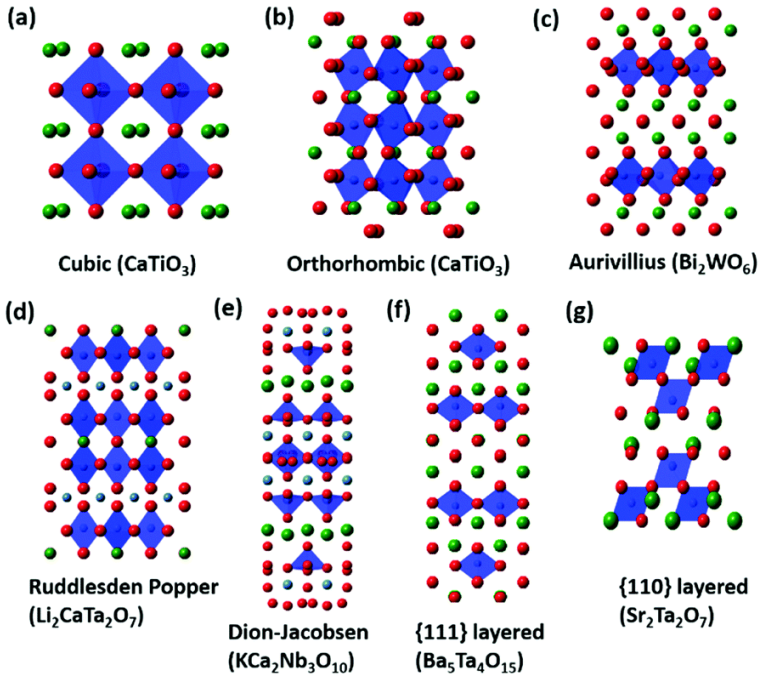

***Figure 15**: Crystal structures of perovskites and layered perovskites (oxygen ions in red, B-site cations in dark blue with corresponding polyhedrons, and A-site cations in green and light blue). Reprinted with permission of Zhang et al.*[153] *Copyright 2016 The Royal Society of Chemistry.*

This thesis focused in the first part on the (111) layered perovskite metal oxides, in detail on $Ba_5Ta_4O_{15}$ and the preparation of photocatalytically more efficient heterojunction

composites with $Ba_3Ta_5O_{15}$ and $BaTa_2O_6$.[1] (111) layered perovskites are known for their very good photocatalytic activity in hydrogen evolution reaction and overall water splitting under UV light irradiation.[155,161–165]

The photocatalytic activity of (111) layered perovskites could be improved by the formation of heterojunctions such as $Sr_5Ta_4O_{15}$-$Sr_2Ta_2O_7$, $Sr_5Ta_4O_{15}$-$Sr_2Ta_2O_7$-$SrTa_4O_{11}$, and the already mentioned $Ba_5Ta_4O_{15}$-$Ba_3Ta_5O_{15}$ and $Ba_5Ta_4O_{15}$-$Ba_3Ta_5O_{15}$-$BaTa_2O_6$.[1,4–6,166] The synthesis of nanosheets and flower-like nanospheres was also shown to improve the photocatalytic activity.[165,167] Visible light absorption together with enhanced activity could be obtained for heterojunction composites $Ba_5Ta_4O_{15}/AgVO_3$ and $Ba_5Ta_4O_{15}$/g-C_3N_4.[129,168]

By substitution of A and B cations by other cations, the electronic and optical properties of (layered) perovskite-type metal oxides can be easily adjusted in a wide range with great influence on the photocatalytic activity of the different perovskite materials, such as the already discussed Sn(II) exchange of the (111) layered perovskite $Ba_5Nb_4O_{15}$.[139,153] Ta substitution by Nb in $Ba_5Ta_4O_{15}$ (111) layered perovskite results in the reduction of the band gap with increasing Nb amount and increasing photocatalytic activity in overall water splitting.[169] Furthermore, perovskite metal oxides offer a wide range of defect engineering by substitution of A or B cations with higher or lower valence, introducing oxygen or A site vancancies. An example for an oxygen deficient perovskite structure is Brownmillerite ($A_2B_2O_5$).[153] Especially aliovalent doping with cations of lower valence, enhances the photocatalytic activity by inhibiting the formation of reduced B cation defect species as for example Ti^{3+} in $SrTiO_3$ by Ga^{3+} doping, or Nb^{4+} in $KNbO_3$ by Zr^{4+} doping.[170,171]

Not only A- and B-site doping with cations, but also doping with non-metal compounds such as nitrogen or sulfur doping is investigated for (layered) perovskite materials, reducing band gaps and enhancing visible light absorption.[141,148,149,153,158,172–174] The second part of this work was focused on the synthesis of nanostructured cubic perovskite oxynitride.[2] Most perovskite oxynitrides exhibit (distorted) cubic perovskite structure, but also a few examples of oxynitrides with layered perovskite structure are known, as for example $Li_2LaTa_2O_6N$, Sr_2TaO_3N, or $K_2Ca_2Ta_3O_9N{\cdot}2\ H_2O$.[175–178] The absorption of a wide range of the visible light and suitable band positions for water splitting as shown in **Figure 16** are promising properties and the reason why perovskite oxynitrides $AB(O,N)_3$ are an interesting

group of materials for visible light water splitting, especially $BaNbO_2N$ with light absorption up to 740 nm.[7,9,175,179–185]

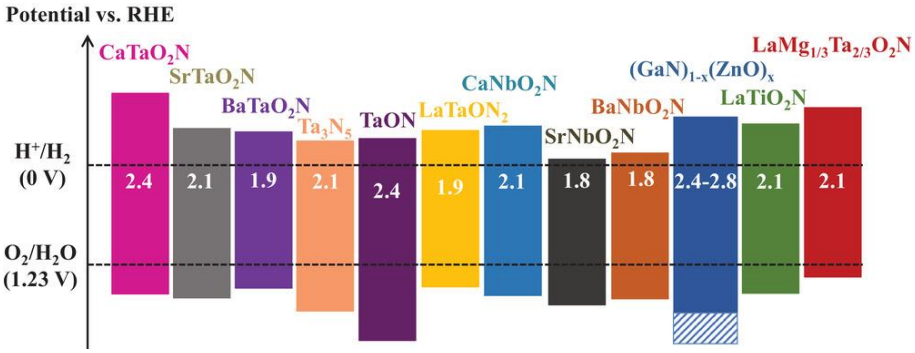

***Figure 16**: Energy diagrams with band gaps for typical (oxy)nitrides. For $(GaN)_{1-x}(ZnO)_x$ a specific range is given represented by the oblique shadow. Reprinted from Dong et al.[186] with data taken from[9,187–196]. Copyright Wiley-VCH GmbH 2021.*

There are different possibilities for the preparation of such perovskite oxynitrides, including the conversion of (111) layered perovskite-type metal oxides or cubic perovskite-type metal oxides by ammonolysis.[7,197–199] During ammonolysis, the precursor materials are heat treated at around 1000 °C in NH_3 gas atmosphere.[175] In case of the conversion of (111) layered perovskite, the absorption edge shifts from the UV range into the visible light range and a change in the crystal structure from (111) layered perovskite crystal structure to the cubic perovskite crystal structure is observed as represented in **Figure 17** for the conversion of $Ba_5Ta_4O_{15}$ to $BaTaO_2N$.[199]

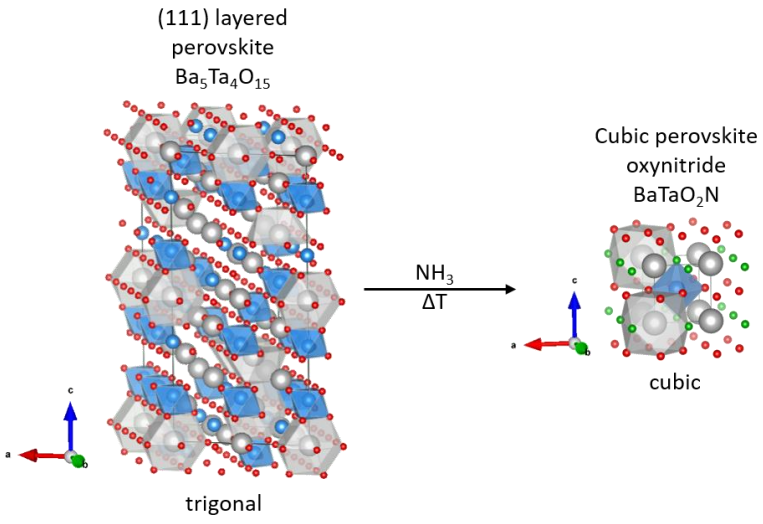

***Figure 17**: Illustration of crystal structure change by ammonolysis of the trigonal (111) layered perovskite metal oxide $Ba_5Ta_4O_{15}$ to the cubic perovskite oxynitride $BaTaO_2N$.[199–201] (Ba ions in gray, Ta ions in blue, and O ions in red with corresponding polyhedrons for Ba (gray) and Ta (blue)).*

Heterojunctions and solid solutions with cubic perovskite oxynitrides are for example $Sr_2Ta_2O_{7-x}N_x$/$SrTaO_2N$, $BaZrO_3$/$BaTaO_2N$, $MgTa_2O_{6-x}N_y$/TaON, Ta_3N_5-nanorods/$BaTaO_2N$, and $BaMg_{1/3}Ta_{2/3}O_{3-x}N_y$/$Ta_3N_5$, with improved activity in sacrificial hydrogen evolution, photoelectrochemical and Z-scheme overall water splitting.[128,196,202–204] A quantum efficiency of 6.8 % at 420 nm for Z-scheme overall water splitting could be achieved for an $MgTa_2O_{6-x}N_y$/TaON heterojunction as hydrogen evolution catalyst with PtO_x-WO_3 as oxygen evolution catalyst and IO_3^-/I^- as redox mediator.

One issue of perovskite oxynitrides is the generation of defects, especially reduced B-site cations, due to the reducing synthesis conditions during ammonolysis. These defects, such as Ti^{3+}, Nb^{4+}, or Ta^{4+} are a major reason for the rather low photocatalytic activity considering the very good visible light absorption, as they act as traps and promote charge carrier recombination.[205–207] Aliovalent doping is an especially important approach for enhancement in photocatalytic efficiency of cubic perovskite oxynitrides, reducing the amount of reduced B-site cation defects.[205,208] Substitution of Nb^{5+} by Ca^{2+} in $BaNbO_2N$ reduces the Nb^{4+} defect concentration and enhances surface hydrophilicity, resulting in improved water oxidation activity, even though the band gap was increased by Ca incorporation.[205] The visible light absorption, crystal structure, and crystal morphology of $BaTaO_2N$ was nearly unchanged by doping 5 % of the aliovalent ions Mg^{2+}, Al^{3+}, Ga^{3+}, Sc^{3+}, or Zr^{4+}, but the photocatalytic activity could be enhanced for all ion doped $BaTaO_2N$ samples compared to the bare $BaTaO_2N$ due to differences in optoelectronic and surface properties.[208] However, it could be also shown, that co-substitution of $BaTaO_2N$ with Al^{3+} and Mg^{2+} results in an increase of the band gap, if more Mg^{2+} is substituted for Ta^{5+}, but still the photocatalytic activity compared to bare $BaTaO_2N$ is enhanced with higher O_2 evolution, especially for higher Mg^{2+} amounts.[209]

It could be further shown, that the photoelectrochemical activity of $BaTaO_2N$ and $BaNbO_2N$ can be enhanced by an additional argon treatment to improve surface crystallinity and reduce defect density.[210,211] Furthermore, facet engineering for better charge carrier separation in perovskite oxynitrides could be an efficient way as it was shown that (100) and (110) co-exposed $BaTaO_2N$ is 10 fold more active in photocatalytic hydrogen production than the only (100) facet exposed $BaTaO_2N$.[212]

2.4 Nanostructuring – Nanofibrous and Porous Photocatalysts

Nanostructuring is a promising way to improve the photocatalytic activity of semiconductor materials due to lowering of the diffusion pathways for photogenerated charge carriers (shown in **Figure 18**) and increasing the surface area. In most cases the recombination probability decreases with smaller particles size.[35]

All photogenerated charge carriers have a finite lifetime and mobility, depending on the charge carrier type, the material, and the light intensity. The range of diffusion is given by the charge carrier diffusion length L_D, which for holes is often shorter than for electrons.[58] Furthermore, L_D of the minority charge carriers decreases with doping of the material. The diameter (in porous materials, the pore wall thickness) of a material should be ideally two times the diffusion pathway of the minority charge carrier additional to the width of the space charge region. This can be fulfilled for nanoparticles, porous materials, as well as for nanofibers.

A high surface area is especially advantageous for photocatalytic degradation of organic compounds since the adsorption of the organic molecule is the most important step in this process.[35] In this regard, especially porous materials with their high surface area can be beneficial due to their mesoporous network, which facilitates the access to the reactive sites at the surface and promotes the diffusion of reactants and products. It is important, that pore size and porosity are adjusted, as too small pore sizes can result in mass transfer restrictions for large molecules inside the pores.[213,214] Particle agglomerates with interparticle pores can also be beneficial due to the so-called antenna mechanism, that describes the increased electron transfer probability to co-catalysts due to the improved diffusion of sacrificial agents through the pores of the agglomerate.[215–217] However, the mechanical stability of such particle agglomerates is lower compared to mesoporous materials with “real” pores, and synthetic modification of such self-assembled networks is not straightforward.[45,103]

In overall water splitting, a highly crystalline material is often more important than a high surface area, as the recombination of photogenerated charge carriers is the most problematic process and high crystallinity results in reduced recombination centers in the material.[35] The amount of defects is often higher in materials, calcined at lower temperatures, which is often the case for materials with high surface areas. Especially

regarding this aspect, it can be beneficial to use nanofibrous or porous materials instead of nanoparticles in overall water splitting, as the photogenerated charge carriers can be spatially better separated in nanofibers and porous materials than in nanoparticles, thus reducing the recombination probability (**Figure 18**).[218] Furthermore, it is possible to prepare highly crystalline metal oxide nanofibers, *e.g.* TiO_2, WO_3, CuO, α-Fe_2O_3, Co_3O_4-CuO, $SrTiO_3$, or (111) layered perovskite nanofibers *via* electrospinning, [6,169,219–226] and highly crystalline ordered or disordered porous metal oxides, *e.g.* TiO_2, Nb_2O_5, ZnO, Ta_2O_5, and $CsTaWO_6$.[214,216,227–234]

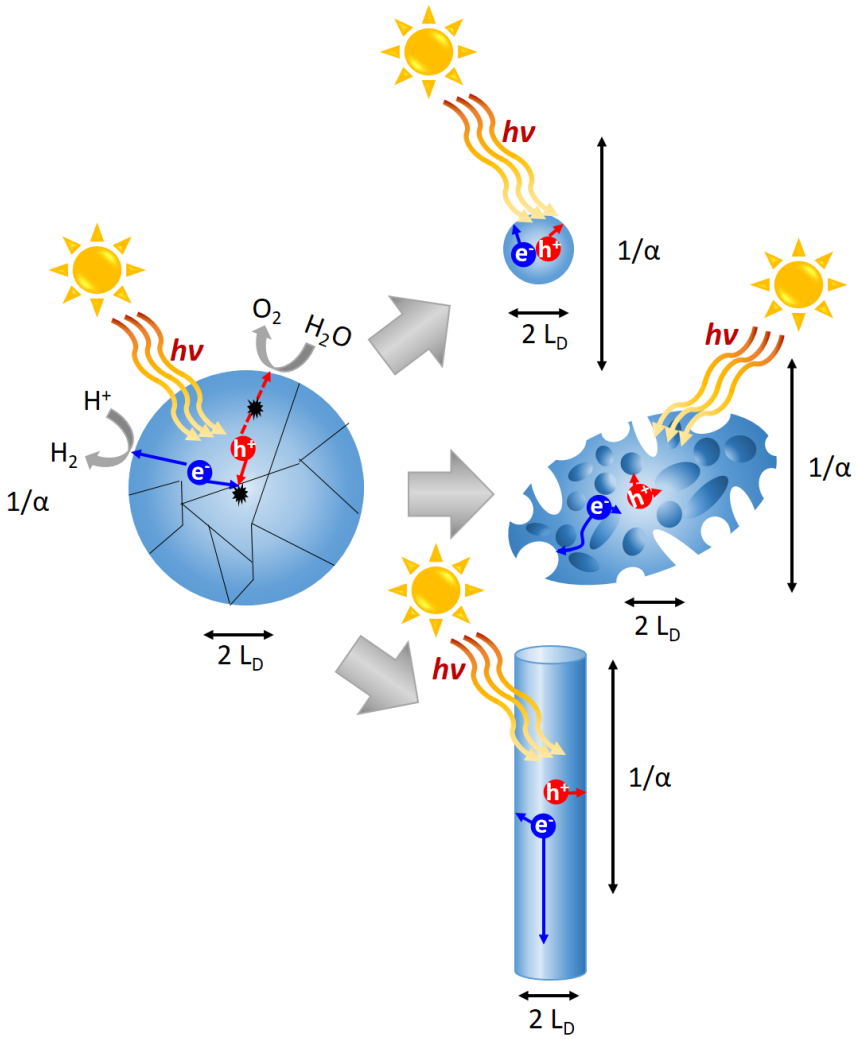

***Figure 18**: Schematic illustration of the effect of size and morphology on the photocatalytic activity; charge transport upon light excitation is shown for a bulk material (left), a nanoparticle (top, right), an unordered porous material (middle, right), and a nanofiber (bottom, right). Additionally, recombination processes at grain boundaries and defects, as well as recombination due to short diffusion length L_D of minority carriers (in this case holes), and the light absorption depth 1/α are shown. Adapted with permission from Kudo et. al. for nanoparticles[35], Copyright 2009 The Royal Society of Chemistry and adapted with permission from Walter et al. for nanofibers[235], Copyright 2010 American Chemical Society.*

For an optimum photocatalytic activity, a good balance between high crystallinity, crystallite size, short diffusion pathways, and high surface area has to be found, depending on the desired photocatalytic reaction and the photocatalyst itself.

Another important aspect is the light penetration depth of the material, which is the distance after which the light intensity is reduced to $1/e$.[58] It equals $1/\alpha$, in which α is the wavelength-dependent absorption coefficient. In photoelectrochemistry, a film thickness of more than 2.3 times $1/\alpha$ is necessary for an absorption of more than 90 % of the incident light.[58] Therefore, free standing nanowires can be beneficial as they offer a short diffusion pathway for the photogenerated charge carriers, and they are long enough for the absorption of light through the whole light penetration depth, as the direction of light absorption and charge carrier collection is decoupled.[235] This can be also beneficial in dispersion, although the light scattering in dispersion is maximal compared to films.[58,218] Compared to nanofibers and nanoparticles, porous photocatalysts can exhibit further enhanced light harvesting due to light reflection and scattering by the pores.[236,237] Besides the high density of active sites and the enhanced light harvesting, porous photocatalysts have the advantage of an easy recovery after the photocatalytic reaction and reusability.[236]

One very important aspect in nanostructuring of photocatalysts is the correlation of morphology and surface area with the photocatalytic activity. Porosity is often correlated with a higher amount of amorphous parts at the pore walls in the material, which can result in a higher recombination probability.[238,239] Therefore, the conversion of amorphous as-synthesized mesoporous photocatalysts to a highly crystalline material while retaining the porous structure is an important part in the synthesis of porous photocatalysts.[240]

One could expect a linear dependency of the surface area and the activity; however, this is most often not applicable.[241] For this, the photocatalytic reaction would have to be carried out under conditions for optimum charge carrier generation and lifetime, low overpotential, and all of the available surface area would have to be accessible.[74,241]

Especially in porous materials, a lot of parameters can influence the activity in such a way, that this correlation is not linear, *e.g.* pore sizes, pore size distribution, the pore origin (interparticular pores or “real” pores), as well as the template nature (hard template or soft template), and of course the material itself. Cherevan *et al.* introduced a methodology to

correlate the relative increase in the surface area to the relative increase in activity in comparison to a non-porous reference.[241] This methodology allowed for the comparison of the data of many articles, as it eradicates many internal parameters of the individual reports and thus enables to correlate the activity increase with the surface area increase. With this, it could be shown, that the pore size and the origin of the pores, *i.e.* interparticular or template derived pores are not the origin for a linear correlation. The activity enhancement rather strongly depends on the type of porogen used in the synthesis with a close to linear correlation for hard template-derived pores compared to soft template engineered ones. This can be explained by a narrower pore size distribution and better defined pores in porous materials obtained by hard templating compared to soft templating.[241] This can be beneficial for reactant and educt diffusion. Furthermore, the type of the material has also a strong influence on the activity enhancement, *e.g.* carbon nitride shows a close to linear correlation; however, TiO_2 and Ta_2O_5 deviate strongly from this.[241]

This report gave a first inside on the influences of material properties on the activity enhancement. However, it is a single-parameter analysis and in nearly all studies, several structural parameters are varied at one time. This can lead to a more pronounced scattering from the linear correlation. Furthermore, the use of a suitable reference material is very important in the research on porous materials.[241] Different synthesis conditions can have a pronounced effect on the activity. It could be suitable to prepare the reference material in the same way as the porous material without using the porogen to have comparable synthesis conditions. Comparable crystallite sizes, crystallinity, defect concentration, as well as phase composition of a reference material are ideal, although the design of such an ideal reference is challenging.[241] Overall, a most suitable reference material has to be selected, and the full characterization of this reference material is very important.

Also other aspects have to be taken into account for future research work on porous materials, including the distribution of co-catalysts in the pores, the adsorption and diffusion of sacrificial agents, products, and educts within the pores, or facet engineering inside the pores, and the influence of these parameter on the photocatalytic activity.[241]

This shows the possibility of property adjustments of porous materials in a wide range for the optimization for their photocatalytic activities.

2.5 Electrospinning of Nanofibers

Electrospinning is one technique for the preparation of nanofibers, which was used in the second study presented in this thesis. It is a simple and versatile technique for the preparation of 1D nanostructured materials such as polymers, ceramics, metal oxides, composites, or carbon nanofibers. Simplified, electrospinning is the continuous stretching of a jet of a highly viscous polymer solution in the presence of an electric field.[242] The first work on electrospinning was a patent invented by Formhals in 1934, who reported about the preparation of artificial filaments by spinning of solutions of cellulose derivatives by applying an electric field between the nozzle and a second electrode.[243] The research interest on electrospinning was first focused on the preparation of polymer nanofiber materials.[244–246] The synthesis of metal oxide nanofibers by electrospinning was first reported in 2002 for alumina-borate oxide nanofibers.[247]

Figure 19 shows a schematic illustration of a basic electrospinning setup with a syringe pump, equipped with a syringe filled with the electrospinning solution and the spinneret (cannula), a high voltage supply, and a collector, in this case a rotating drum.

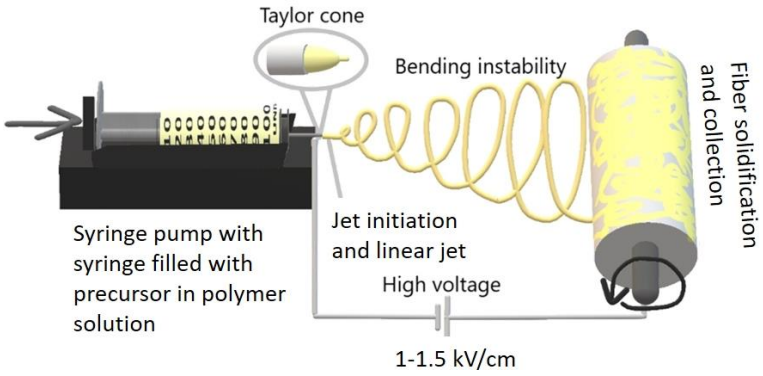

***Figure 19**: Schematic illustration of an electrospinning process.*

In the first step of a sol-gel electrospinning for metal oxide nanofibers, a spinning solution, which is an inorganic sol or a solution consisting of a spinning polymer and a precursor such as an alkoxide, a salt, or polymer precursor needs to be prepared.[248] In a second step the electrospinning process follows. The solution is pumped with a constant rate through the cannula. A high voltage is applied between the cannula and the collector, which is in the

range of 1 to 30 kV, resulting firstly in the formation of a Taylor cone, and secondly in the formation of a liquid jet from the nozzle. This jet elongates, solvent evaporates, and fibers are collected at the collector.[242,248] A humidity and atmosphere control can be necessary in the electrospinning process of metal oxide nanofibers due to moisture or air sensitivity of the precursors controlling the sol-gel process in the jet.[248] The obtained fibers are composite fibers of polymer and precursor. In the third step, the collected fiber mat is calcined to remove the spinning polymer and to crystallize the metal oxide.[248]

More detailed, the spinning process can be divided in four steps, the jet initiation, the rectilinear jet, the bending instabilities and the solidification of the fiber, as represented in **Figure 19**.[249,250] **Figure 20 left** shows processes and forces acting in a Taylor cone in the presence of an electric field.[251–253]

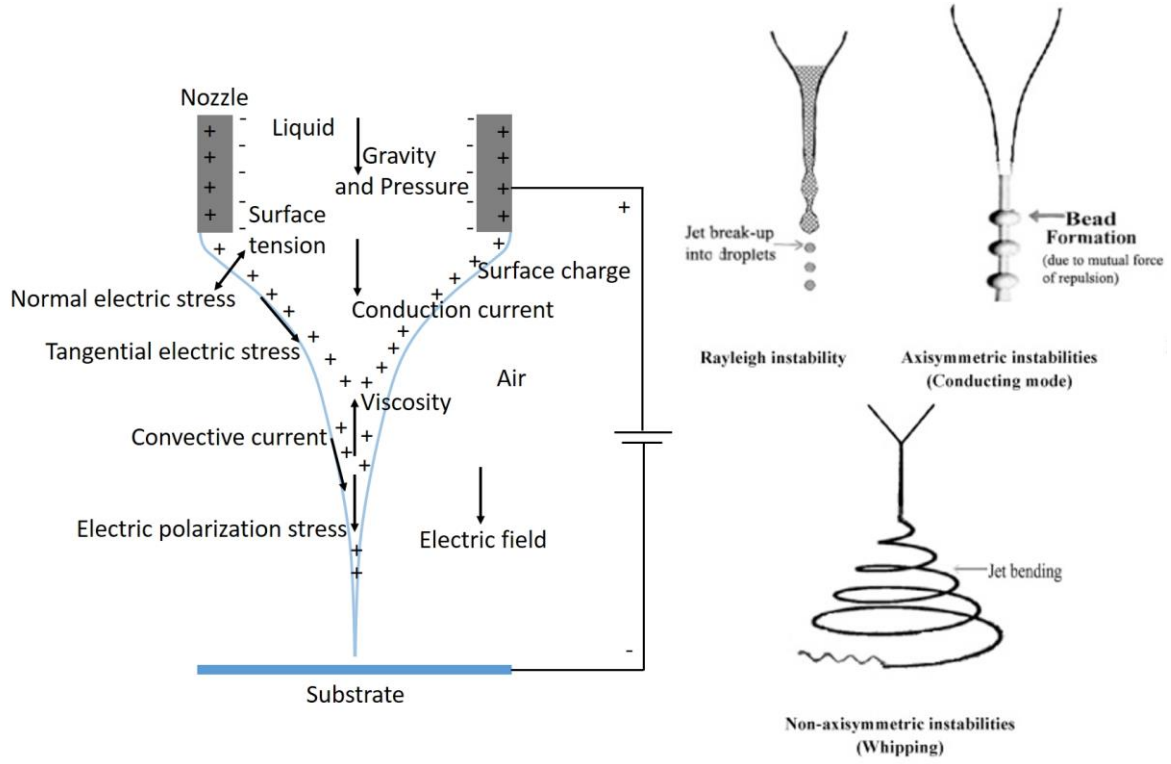

***Figure 20**: Schematic illustrations of processes and forces acting inside a Taylor cone in presence of an electric field (left) (Adapted with permission from Singh et al.[251], licensed under CC BY-NC 3.0 according to Hartman[252] and Aramide et al.[253]) and different modes of jet instabilities in electrospinning (right) (Reprinted with permission from Bagchi et al.[254] Copyright 2015 Elsevier).*

When an electrical field is applied, the positive and negative charges in the spinning solution are separated. The charges opposite to the charge applied to the nozzle are repelled and transfer to the surface of the spinning solution. The repulsive Coulomb

interactions lead to the deformation of the solution at the needle tip. Electrical forces, Coulomb and dielectric forces, are balanced by surface tension and opposite viscous flow.[251] The electric field can be enhanced up to the point where charge repulsion is more intense than the surface tension. At this point, the Taylor cone and a jet form.[250] That jet moves linearly towards the collector with reducing diameter due to solvent evaporation and longitudinal deformation.[249] This rectilinear part of the jet is as long as the bending instabilities become dominant. Then the jet starts whipping as shown in **Figure 20 right** with decreasing jet diameter and increasing loop diameter.[249] Besides the whipping instabilities, other instabilities, *i.e.* Rayleigh and axisymmetric instabilities can occur (**Figure 20 right**).[254,255] The axisymmetric and whipping instabilities are electric field-induced instabilities, which increase with field strength, at the same time the Rayleigh instability is suppressed.[256] On their way to the collector, the nanofibers are solidified, *i.e.* the solvent evaporates, with increasing evaporation rate the thinner the nanofibers are. Then the nanofibers are collected and are calcined.[250]

There are many process parameters in electrospinning that can be adjusted to tailor the properties of the nanofiber material such as the nanofiber diameter or morphology. Bloesser *et al.* tested systematically the influence of the cannula-collector distance, tip-collector voltage, and viscosity on the nanofiber diameter of $Ba_5Ta_4O_{15}$ fibers and could show, that the viscosity of the spinning solution has the most pronounced effect on the fiber diameter.[226] Thereby the viscosity was adjusted *via* the amount of spinning polymer used in the spinning solution. The diameter could be tailored in a range of 100 to 300 nm. These nanofibers were also tested for their photocatalytic activity in overall water splitting and a diameter dependent photocatalytic activity with an optimum nanofiber diameter of 161 nm was found. The same group could prepare the already mentioned heterojunction nanofibers $Ba_5Ta_4O_{15}$-$Ba_3Ta_5O_{15}$ with tailored nanofiber diameter.[6]

Hollow and dense α-Fe_2O_3 nanofibers used as a photoanode could be prepared by the adjustment of the humidity in the electrospinning chamber.[223] 40 % of humidity resulted in dense nanofibers, while 25 % yielded hollow nanofibers. By dispersing indium tin oxide (ITO) nanoparticles in the spinning solution, core-shell α-Fe_2O_3/ITO composite nanofibers could be prepared with a humidity of 25 % in the spinning chamber resulting in improved photoelectrochemical activity. This example also presents that not only polymer or sol-gel

solutions can be electrospun for the preparation of nanofibers, but also particle dispersions as for example shown for TiO_2 nanofibers.[219] Another approach to synthesize hollow or core-shell nanofibers is the coaxial electrospinning, which uses multiple concentric spinnerets to co-spin different electrospinning solution.[257]

One way to gain mesoporosity in nanofibers by electrospinning is the use of different kinds of polymers as for example polyvinylpyrrolidone (PVP) together with polyethylene glycol (PEG). It was shown for Co_3O_4-CuO composite nanofibers, that PVP is responsible for the fiber morphology and PEG introduces the mesoporosity in the nanofibers.[224]

2.6 Preparation of Porous Photocatalysts *via* Sol-Gel Synthesis

The most common used pathways for the synthesis of (ordered) mesoporous materials are the hard- and soft-templating approaches, which use templates as structure directing agents for the formation of the mesoporous network.[214,236] Other synthesis approaches are self-assembly methods, etching processes, or topotactic transitions.[236]

One versatile technique for the preparation of porous materials is the sol-gel synthesis, which allows for the exceptional control of the product's structural and chemical properties.[258–262] Such a sol-gel process starts with the formation of a sol, followed by the formation of a gel.[258,259,263] A sol is a dispersion of colloidal particles with diameters of 1-1000 nm, and a gel is a 3D sponge-like solid network which encapsulates a solvent.[258,259,263] The main reaction processes involved in such a sol-gel process are hydrolysis and condensation reactions (**Figure 21 right**).[258,259,263] The most important approach in sol-gel chemistry is the metal alkoxide route, however a lot of other precursors can be used for the sol-gel preparation method.[259,263,264]

Aerogels are one very interesting group of materials, which are prepared *via* such a sol-gel method. These aerogels offer a very low density, large open pores, as well as high surface areas.[258,262,263,265] Especially the tailoring possibilities of material properties are interesting for photocatalytic applications, as they can be adjusted depending on the desired application. For example, DeSario *et al.* could show by use of intensity-modulated photovoltage and photocurrent spectroscopy that the weight fraction of the precursor during the synthesis of a TiO_2 aerogel has a drastic effect on the electron lifetime and mobility, and thus on the photocatalytic activity in hydrogen generation.[266] With

increasing precursor concentration, an increase in the lifetime of photogenerated electrons could be observed, which correlated with an activity increase in hydrogen evolution. At the same time, the electron mobility decreased, which indicated trapping sites as reactive sites. The oxidative degradation of dichloroacetate depended only weakly on the electron mobility as this reaction is mainly driven by direct hole transfer to the adsorbed chemical. Due to these unique properties of aerogels, the third study in this thesis was focused on TiO_2 aerogels with adjusted material properties.[3]

Figure 21 shows a schematic illustration of the sol-gel synthesis procedure for an aerogel and additional chemical reactions, *i.e.* hydrolysis and condensation reactions, occurring during the synthesis of a, *e.g*. TiO_2, aerogel.[258,259,263]

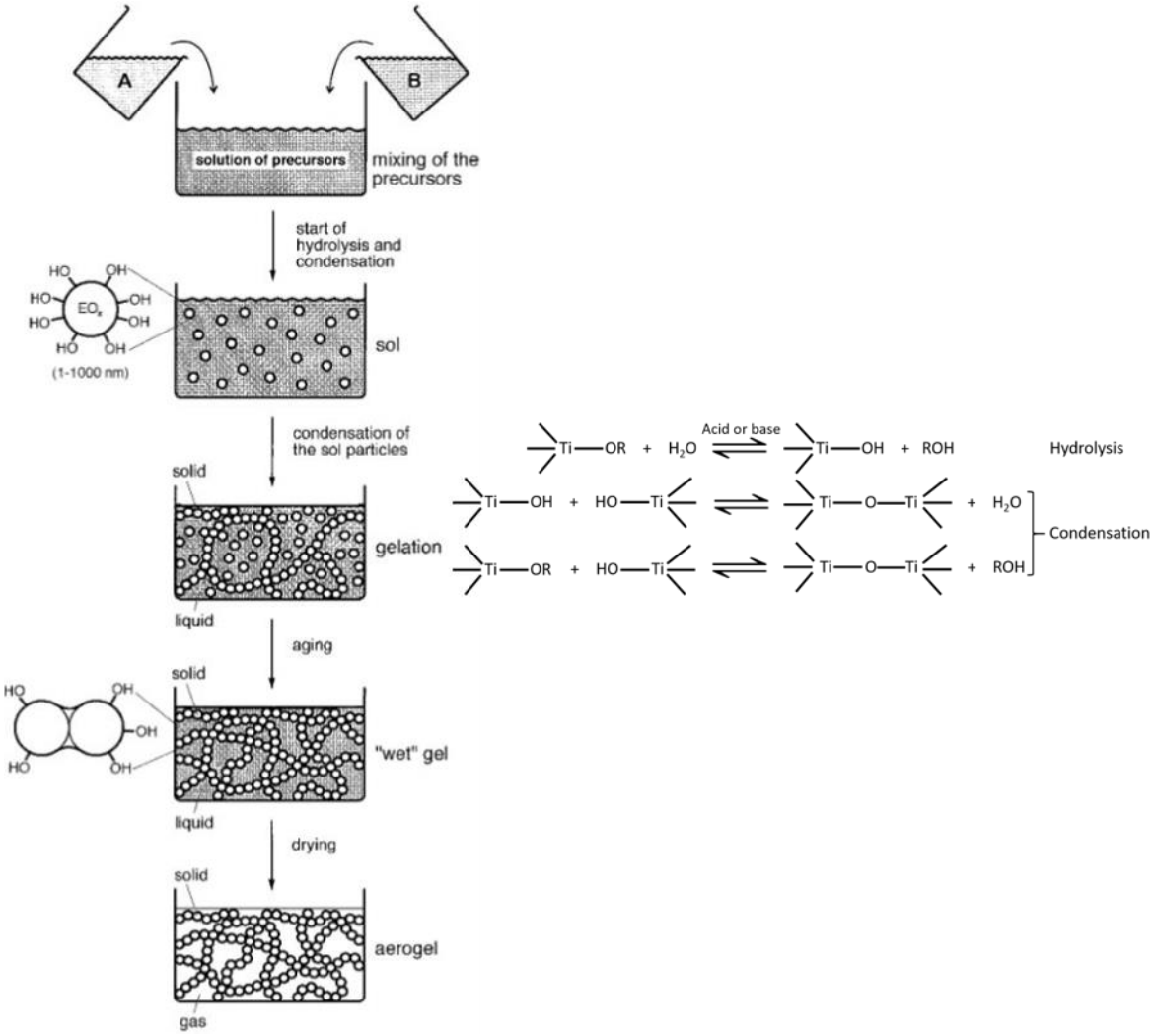

Figure 21*: Schematic illustration of the preparation of aerogels by a sol-gel process (left) (Reprinted with permission from Hüsing et al.*[258]*Copyright 1998 WILEY-VCH Verlag GmbH) and chemical reactions occurring during the sol-gel process of titanium alkoxides.*

The first step in such a sol-gel process is the preparation of the precursor solution. Important parameters in this step are the type and concentration of the precursors, the type of solvent, the ratio between water and alkoxy groups, as well as the temperature and the pH value.[258]

Hydrolysis and condensation of the partially hydrolyzed species follow, and the sol is formed. The condensation reactions further proceed besides the hydrolysis, *i.e*. gelation starts. These condensation reactions can be either water condensation or alcohol condensation reactions **Figure 21 right**.[258,259,263]

The following aging step is an important step for consolidating the wet gel structure by continuous condensation processes, which stop with a spontaneous shrinkage and network densification, depending on time, temperature, pH, and the nature of the aging fluid, which could be shown by *in-situ* nuclear magnetic resonance measurements by Smith *et al*.[258,263,267–269]

The last step in the synthesis of aerogels is the drying process, which can be done by different methods, *e.g.* supercritical drying or freeze-drying.[258,259,263] A conventional evaporation drying often results in a shrinkage of the gel and collapse of the porous network due to capillary forces acting inside the pores.[258,259,263] The resulting product is known as a xerogel with significantly lower surface area and pore volume, and reduced photocatalytic activity compared to aerogels.[54,258,259,263,265] Therefore, other drying methods, *i.e.* supercritical drying or freeze-drying are used to avoid the shrinkage and the occurrence of capillary forces. The used method in the herein presented study was the supercritical drying with CO_2.[3] In this process, the solvent is replaced by supercritical CO_2, thereby preventing capillary stresses due to elimination of liquid-vapor interfaces.[258,259,263]

The temperature of the supercritical drying process can have significant effects on the textural and structural properties of aerogels, as well as on the photocatalytic activity.[54,270] Brodsky *et al.* varied the drying temperature for TiO_2 aerogels in a range of 343 – 473 K.[270] Although the BET surface area of the TiO_2 aerogels remained constant, the specific pore volume increased, and the pore size distribution broadened and shifted towards higher values with increasing drying temperature. Furthermore, crystallization was facilitated by higher drying temperatures.

3 Synopsis

With regard to the ever-growing energy demand, the rise in CO_2 emissions, and the finiteness of carbonaceous fossil fuel reserves, the reduction of energy consumption and the use of renewable energy sources have to play an important role in the upcoming years to diminish the harmful consequences on the world's climate. Besides the contribution of every human being to the reduction of energy consumption, scientists can work on reducing the energy consumption in laboratories, *e.g.* by developing energy efficient syntheses routes with low impact on the environment. Furthermore, the syntheses of highly efficient and stable photocatalysts for solar-light induced water splitting for the generation of clean and renewable hydrogen as an alternative energy carrier as well as an energy efficient synthesis of other important chemicals such as ammonia is very important. This thesis paid attention to these aspects using energy-saving synthesis routes and additionally nanostructuring for the preparation of photocatalysts with focus on hydrogen evolution, overall water splitting, and a first test on ammonia catalytic production.

As introduced, (111) layered perovskites are known for their high photocatalytic activity in the UV range. In the first part of this thesis different synthesis strategies for such (111) layered perovskites were tested, including solid-state reaction, electrospinning of nanofibers, and different citrate route-based synthesis routes. Thereby, an energy saving route for the synthesis of composite materials with (111) layered perovskite $Ba_5Ta_4O_{15}$ as main phase was developed.[1] This first study is based on research published by Marschall *et al*. and Soldat *et al*., who synthesized different barium tantalate composites *via* a citrate route and tested their photocatalytic activity.[4,5] Enhanced activity was found for the $Ba_3Ta_5O_{15}$-$Ba_5Ta_4O_{15}$ composite compared to phase-pure $Ba_5Ta_4O_{15}$ by Marschall *et al*.[4] The improved charge carrier separation in the composite could be verified later by use of transient absorption spectroscopy.[271] Soldat *et al*. prepared more complex multicomponent barium tantalate composites and found the highest photocatalytic activity for the three component composite $Ba_5Ta_4O_{15}$-$Ba_3Ta_5O_{15}$-$BaTa_2O_6$. Therefore, this three component composite was focus of the first study of this thesis. Therein, the citrate route synthesis used in the studies of Marschall and Soldat was optimized energetically. The calcination temperature and reaction time in the citrate route synthesis, used in the named papers are already lower compared to solid-state synthesis. However, we were able to

further optimize this synthesis energetically by systematically adjusting the synthesis parameters, *i.e.* the amount of NH_3 and HNO_3 solution. This resulted in a different extent of the combustion reaction and increasing crystallinity with increasing amounts of NH_3 and HNO_3 solution (**Figure 22 a**). With this, we were able to synthesize a directly crystalline $Ba_5Ta_4O_{15}$-$Ba_3Ta_5O_{15}$-$BaTa_2O_6$ composite at ambient pressure and at comparatively low temperatures. An additional calcination step is not necessary anymore.

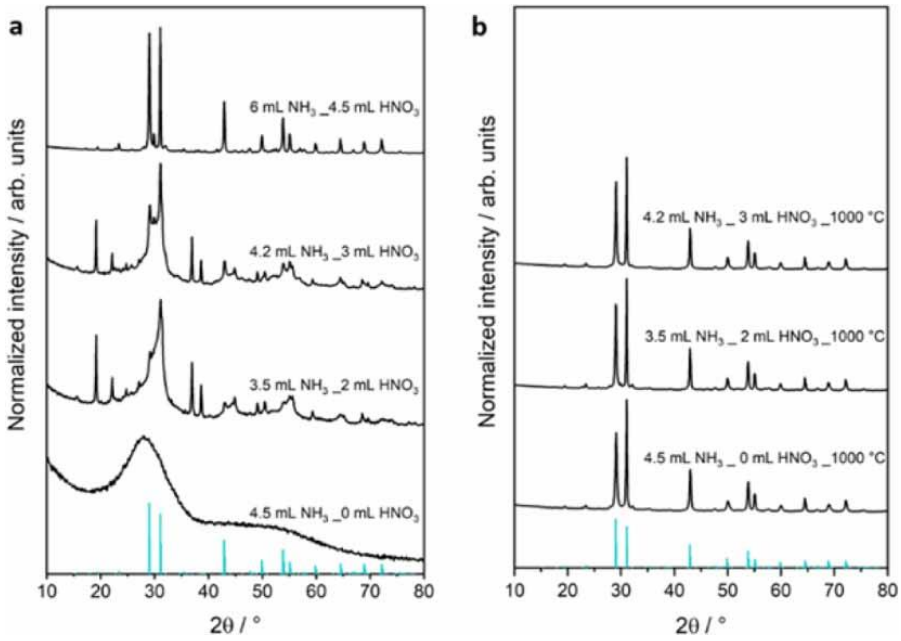

***Figure 22**: XRD patterns of (a) powder precursors depending on NH_3 and HNO_3 amount and of (b) calcined powders. Reference line pattern of $Ba_5Ta_4O_{15}$ (JCPDS 18–0193/JCPDS 72–0631) is shown for comparison.*[1]

Furthermore, the composition of the composite could be tailored with $Ba_5Ta_4O_{15}$ representing the main phase for all samples (**Figure 22 a, b**). The synthesis directly yielding a crystalline product resulted in 12 % of $Ba_3Ta_5O_{15}$ and 12 % of $BaTa_2O_6$, as revealed by Rietveld refinement.

The typical intergrown sheet-like structure of $Ba_5Ta_4O_{15}$, only visible in SEM images after calcination for samples prepared with 0 mL, 2 mL, and 3 mL of HNO_3 was already observable in the non-calcined, directly crystalline sample prepared with 4.5 mL of nitric acid (**Figure 23**). The high crystallinity of this sample could be additionally verified by TEM characterization.

The UV-vis measurements showed the main absorption edge of $Ba_5Ta_4O_{15}$ with 4.3 eV to 4.4 eV for all samples and an additional shoulder related to $Ba_3Ta_5O_{15}$ with a band edge in the range of 3.6 eV to 3.8 eV.

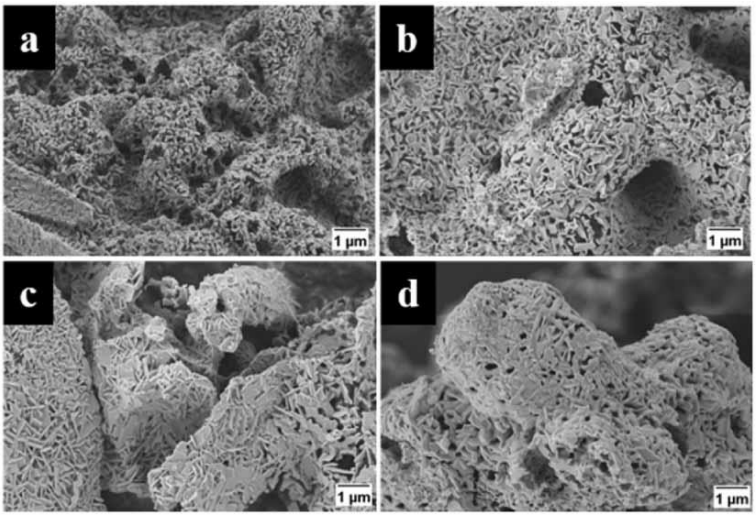

***Figure 23**: SEM images of calcined powder precursors prepared with (a) 0 mL of HNO_3, (b) 2 mL of HNO_3, and (c) 3 mL of HNO_3, compared to (d) the directly crystalline sample prepared with 4.5 mL of HNO_3.*[1]

These composites were tested for their sacrificial hydrogen evolution activity in aqueous methanol solutions, as well as for their overall water splitting activity. Due to the differences of the observed surface areas of the samples, which were in the range of range of 2.5 - 5.4 $m^2\,g^{-1}$ with the smallest surface area for the non-calcined, directly crystalline sample, the gas evolution rates were normalized to the absolute surface area of the samples. Thereby, the non-calcined, directly crystalline sample, showed the highest activity in sacrificial hydrogen and overall water splitting (**Figure 24**). The gas evolution in sacrificial hydrogen evolution without co-catalyst was nearly doubled for the non-calcined sample compared to the calcined samples with 2360 μmol h^{-1} m^{-2} compared to $\sim$ 1380 μmol $h^{-1}\,m^{-2}$ for all calcined samples. This result was in agreement with the results from Rietveld refinement, which revealed a nearly double amount of by-phases in the non-calcined sample compared to the calcined samples. This shows the positive effect of the composite formation on the photocatalytic hydrogen evolution. Rh-Cr_2O_3 co-catalyst was photodeposited on the composites for the overall water splitting experiments. The addition of Rh resulted in an increase of the hydrogen evolution, the deposition of Cr_2O_3 in the expected decrease (**Figure 24 a**). The enhancement after Rh deposition was relatively low compared to the reported increase for phase-pure $Ba_5Ta_4O_{15}$, which was also observed by Soldat *et al.* and can be explained by a more effective charge carrier separation by the composite than charge carrier extraction by co-catalyst from $Ba_5Ta_4O_{15}$.[5]

The overall water splitting experiments showed a typical curve characteristic with a peak in the hydrogen evolution in the beginning of the experiment. This can be explained by oxidation of organic residues, which is supported by the carbon dioxide evolution. After all organic residues are oxidized, the overall water splitting reaction starts and the evolution of oxygen is detected (**Figure 24 b**).

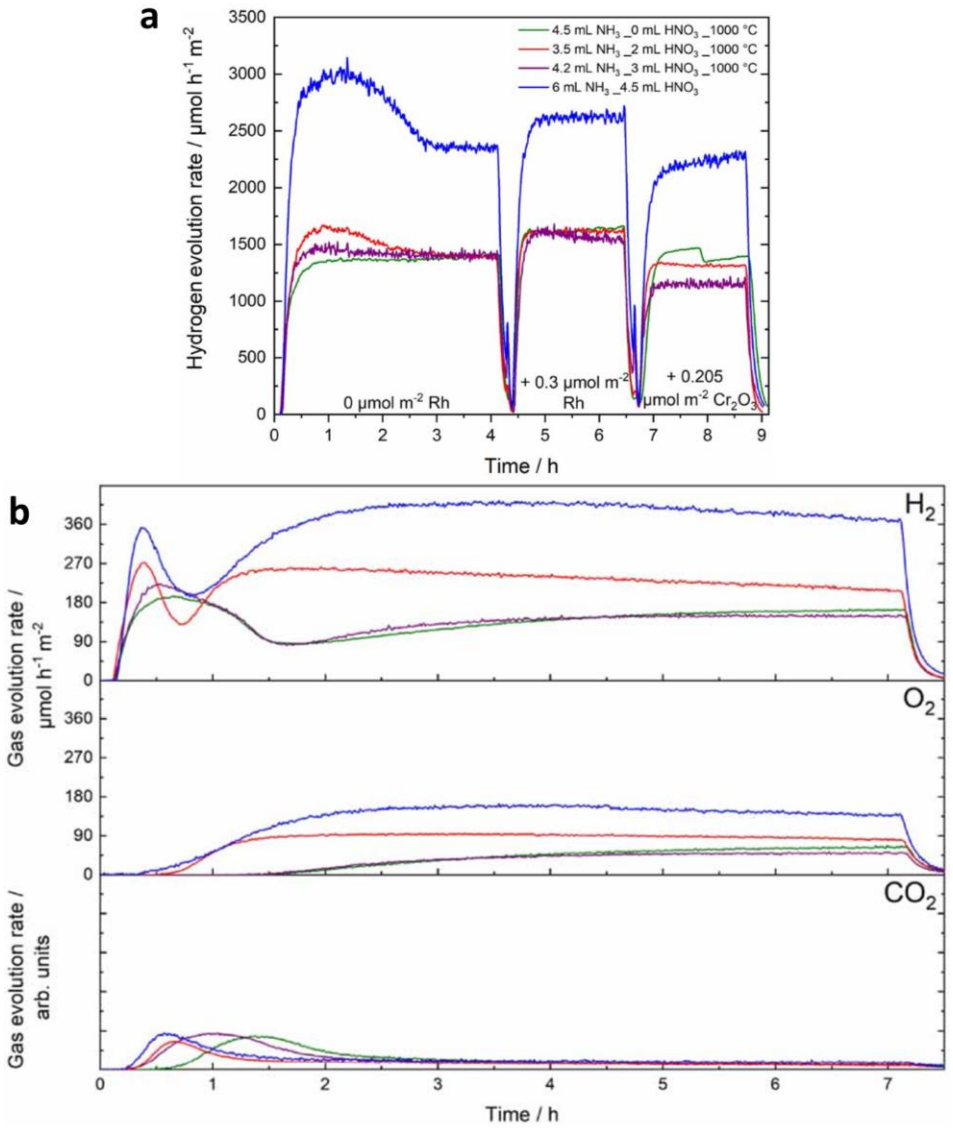

***Figure 24**: (a) Hydrogen evolution curves during photodeposition experiments and (b) hydrogen, oxygen, and carbon dioxide evolution curves in overall water splitting experiments normalized on the absolute surface area.*[1]

A correlation between the amount of $Ba_3Ta_5O_{15}$ in the composite and the activity in the overall water splitting could be found, the higher the $Ba_3Ta_5O_{15}$ concentration, the better is the overall water splitting activity. This further confirmed the improved charge carrier separation in the $Ba_5Ta_4O_{15}$-$Ba_3Ta_5O_{15}$-$BaTa_2O_6$ composites.

This synthesis route combines energy-efficiency and time saving without diminishing the photocatalytic activity, making it an interesting synthesis strategy for many other highly crystalline and highly active semiconductor photocatalysts. Therefore, this synthesis strategy should be also tested for visible-light absorbing photocatalysts.

The prepared $Ba_5Ta_4O_{15}$-$Ba_3Ta_5O_{15}$-$BaTa_2O_6$ composites are highly active in photocatalysis, however, they absorb only UV-light. Therefore, the second study in this thesis was focused on the preparation of visible-light absorbing photocatalysts. Perovskite oxynitrides $AB(O,N)_3$ can be quite easily prepared by ammonolysis of (111) layered perovskites, due to their structural similarity of 6-fold coordinated B cations, corner shared BO_6 octahedra, and the 12-fold oxygen coordinated A cations in both crystal structures (see **Figure 17**). Nanostructuring of such perovskite oxynitrides has not been discussed in detail so far. Often micrometer-sized particles are obtained due to the high temperature of the ammonolysis, thus resulting in small surface areas.[9,10] Therefore, this second study focused on the conversion of nanostructured (111) layered perovskites into their corresponding perovskite oxynitrides while retaining the nanostructure. One possibility to nanostructure photocatalysts and reduce the diffusion pathways of photogenerated charge carriers is the electrospinning of nanofibers. Hildebrandt *et al.* reported the preparation of highly crystalline $Ba_5Nb_4O_{15}$, $Ba_5Ta_4O_{15}$, and $Ba_5Nb_2Ta_2O_{15}$ (111) layered perovskite nanofibers by electrospinning.[169] The calcination temperature can be reduced compared to the solid-state reaction. For example, crystalline $Ba_5Nb_4O_{15}$ nanofibers can already be obtained at a calcination temperature of 800 to 900 °C. Bloesser *et al*. reported about the electrospinning of $Ba_5Ta_4O_{15}$ and $Ba_5Ta_4O_{15}$-$Ba_3Ta_5O_{15}$ nanofibers with tailored fiber diameters.[6,226] These results were the starting point for the second project of this thesis. **Figure 25** shows an illustration representing the aim of the second study. The idea was to electrospin (111) layered perovskite nanofibers with tailored fiber diameters and to convert them *via* ammonolysis to the corresponding perovskite oxynitride, retaining the nanofiber morphology.

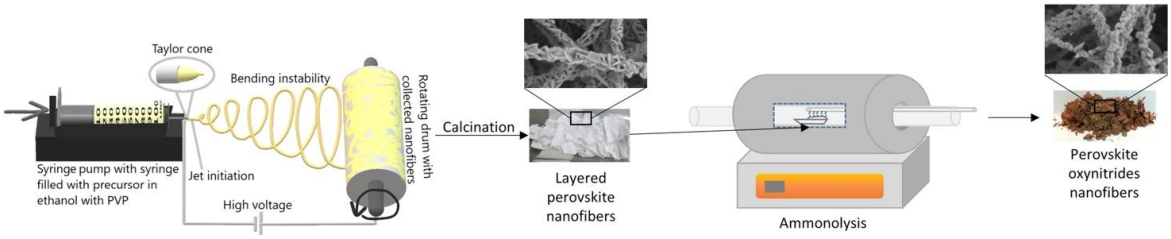

***Figure 25**: Schematic illustration of the synthesis strategy for perovskite oxynitride nanofibers.*

$Ba_5Nb_4O_{15}$ (111) layered perovskite nanofibers with tailored nanofiber diameters were electrospun and converted *via* ammonolysis. The nanofiber morphology was retained and the nanofiber diameter could be adjusted in a range of 135 up to 215 nm (**Figure 26**).

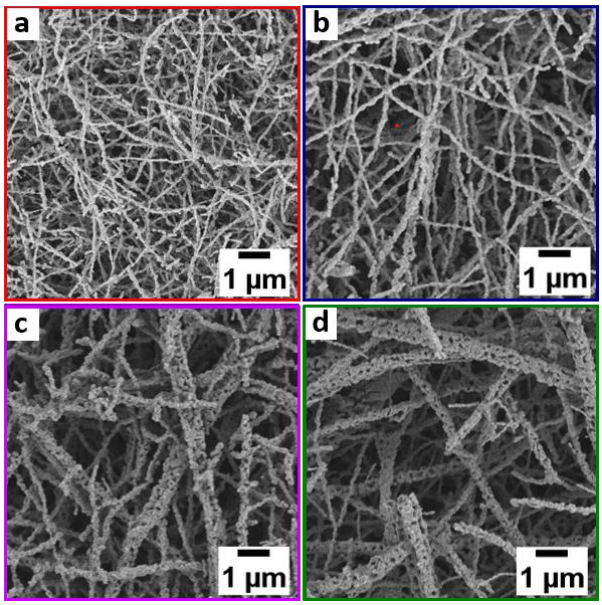

***Figure 26**: SEM images of converted perovskite oxynitride nanofibers with diameters of (a) 135 nm, (b) 156 nm, (c) 194 nm, and (d) 213 nm.*[2]

The XRD pattern revealed in the first instance a complete conversion of the layered perovskite nanofibers. However, a thorough characterization, including Rietveld refinement, revealed the formation of a novel $BaNbO_2N$-Ba_2NbO_3N perovskite oxynitride composite (**Figure 27**). This was only detectable by an asymmetric tailing of the XRD reflections towards lower diffraction angles.

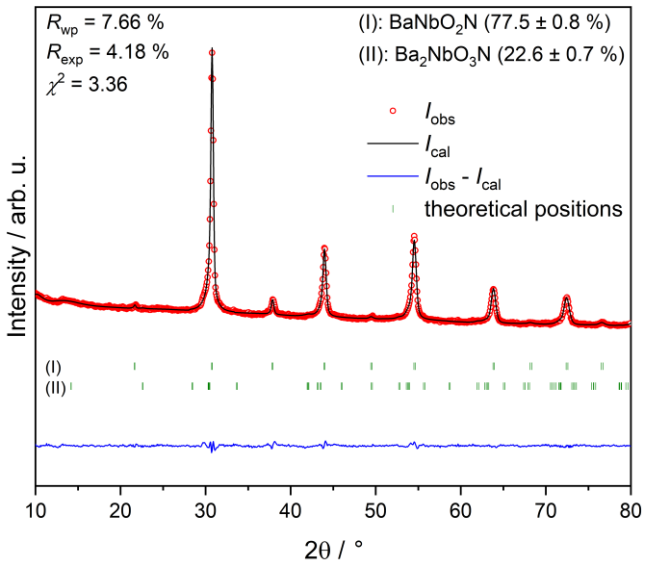

***Figure 27**: Rietveld refinement of converted perovskite oxynitride nanofibers with 156 nm.*[2]

Storing the $BaNbO_2N$-Ba_2NbO_3N perovskite oxynitride composite at ambient conditions resulted in the formation of $BaCO_3$ and simultaneous reduction in the amount of Ba_2NbO_3N as also revealed by Rietveld refinement. Suemoto *et al*. had comparably showed the decomposition to $SrCO_3$ for the isostructural Sr_2TaO_3N.[177] The amount of $BaCO_3$ in the $BaNbO_2N$-Ba_2NbO_3N composite nanofibers was in the range of 4-7 wt. %, that of Ba_2NbO_3N was in the range of 16-23 wt. %, and $BaNbO_2N$ represented the main phase with 71-78 wt. %.

XPS, EDX, and EA measurements revealed a slight barium excess, a nitrogen deficiency, and oxygen excess in the nanofibers due to surface oxidation.

UV-vis measurements further supported the results of a $BaNbO_2N$-Ba_2NbO_3N composite formation and revealed a reduction of the band edge by more than 2.0 eV from 3.9 eV for $Ba_5Nb_4O_{15}$ to 1.8 eV for the converted nanofiber composites for the indirect transition (**Figure 28**). $BaNbO_2N$ is an indirect semiconductor with band edge of approximately 1.8 eV.[184,206] Based on theoretical calculations Ba_2NbO_3N is a direct semiconductor with a band gap of 2.0 to 2.13 eV.[87]

Band edges obtained for the direct transition were slightly higher with 2.6 to 2.8 eV. However, calculated band edges are often smaller than measured ones as it is also applicable for $BaNbO_2N$ with a calculated band edge of 1.4 eV to 1.6 eV.[272]

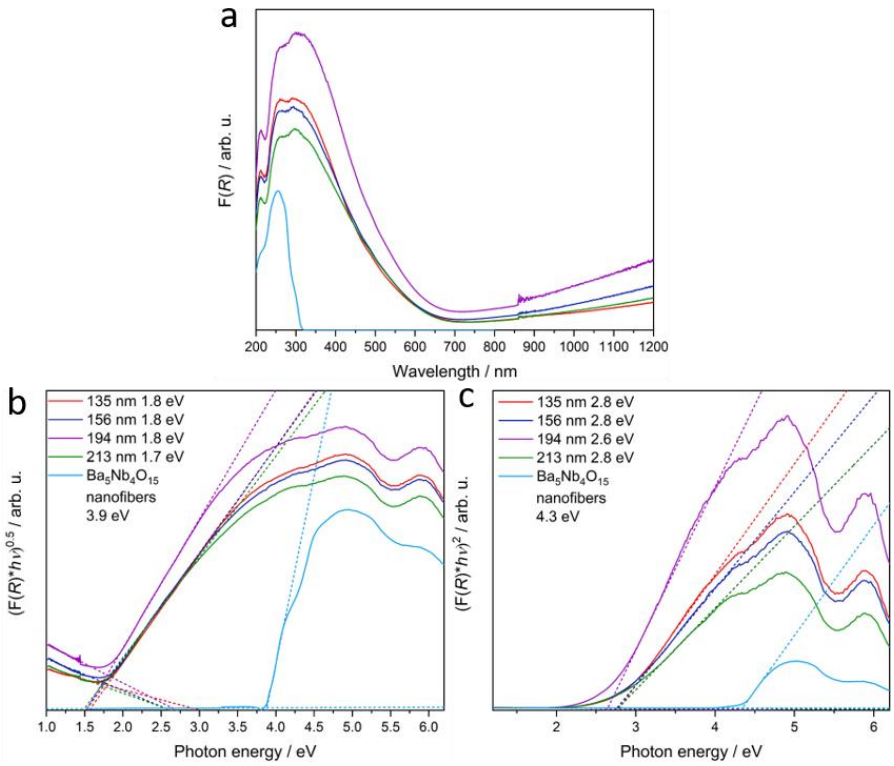

***Figure 28**: (a) Kubelka-Munk UV-vis spectra, (b) indirect, and (c) direct Tauc plots of converted $BaNbO_2N$-Ba_2NbO_3N nanofiber samples and $Ba_5Nb_4O_{15}$ nanofibers.*[2]

The $BaNbO_2N$-Ba_2NbO_3N composite nanofibers were tested for their photocatalytic hydrogen and oxygen generation under irradiation with a 500 W doped Hg lamp ($\lambda > 300$ nm). All nanofibers were able to produce hydrogen at a rate of ~1.0 µmol h^{-1} m^{-2} without the addition of co-catalyst (**Figure 29**). After addition of an optimized amount of Pt co-catalyst, a diameter-dependent hydrogen evolution activity was obtained with an optimum nanofiber diameter of 213 nm with a hydrogen evolution rate of 3.1 µmol h^{-1} m^{-2}.

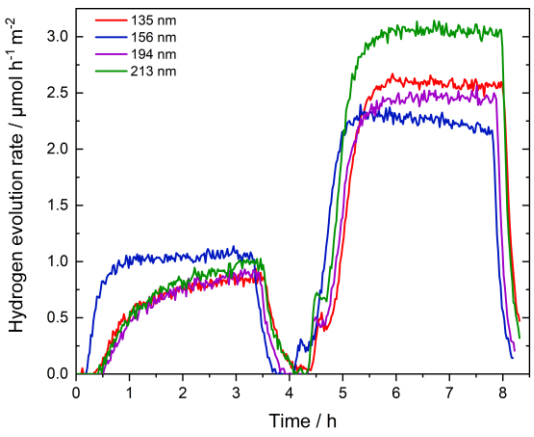

***Figure 29**: Hydrogen evolution curves of converted $BaNbO_2N$-Ba_2NbO_3N nanofibers normalized to absolute surface area.*[2]

A reported CoO_x impregnation method with subsequent calcination steps in ammonia and air was performed for the deposition of oxygen evolution co-catalysts.[273] This resulted in the formation of $CoNbO_4$ and hexagonal $Ba_4Nb_2O_9$. These $CoNbO_4$ decorated nanofiber samples were tested for their oxygen evolution activity (**Figure 30**). Again, diameter-dependent evolution rates were obtained with an optimum nanofiber diameter of 213 nm with an evolution rate of 41.3 µmol m^{-2} in 2 hours.

Photocatalytic measurements with a 300 W Xe lamp equipped with an AM1.5G filter on the most active nanofiber sample with 213 nm did not show any gas evolution, although the samples absorb a wide range of the visible light. This can be explained by the lower photon flux compared to the Hg immersion lamp.

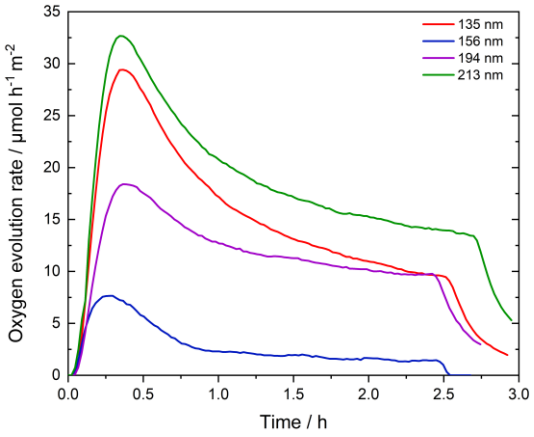

***Figure 30**: Oxygen evolution curves of converted $BaNbO_2N$-Ba_2NbO_3N nanofibers normalized to absolute surface area.*[2]

Overall water splitting measurements on the most active sample decorated with Pt and $CoNbO_4$ under irradiation of a 500 W doped Hg lamp resulted in only small gas evolution rates with the highest evolution rate for nitrogen, suggesting a preference for decomposition of the sample under these conditions. Compared to this, only negligible amounts of nitrogen were detected in the sacrificial hydrogen and oxygen evolution experiments.

Further investigations in the future on the reasons for the low photocatalytic activity under solar-light irradiation and the diameter dependent activity should be performed to optimize synthesis conditions for optimum photocatalytic activity. Nevertheless, this synthesis route can be used for the synthesis of other nanostructured perovskite oxynitrides and is a starting point to establish other novel nanostructuring strategies for perovskite oxynitrides.

Besides electrospinning, other nanostructuring strategies can be similarly or even more effective to improve photocatalytic activities. One of them is the generation of mesoporosity, *i.e.* in aerogels. Aerogels are 3D nanostructures of interconnected porous networks with ultra-low density and high surface areas.[258,274] They are an interesting group of materials, as they offer the possibility to tailor surface area and crystallinity in a wide range.[11,12] The high surface area and presumably high amount of reactive sites, as well as short diffusion pathways for the minority charge carriers and an improved charge carrier separation are advantageous for photocatalytic applications.[12,266,275] One of the most investigated semiconductor materials for photocatalysis, including in the form of aerogels, is TiO_2.[43,46,47,52,214,260] This metal oxide was used in the third study of this thesis, which was focused on the photocatalytic hydrogen evolution and electron storage ability of mesoporous TiO_2 aerogels. This third study paid also much attention to the ability of the synthesized TiO_2 aerogels to store photoexcited electrons, which can be used for later dark reduction reactions. The group of Bahnemann *et al.* performed different reduction reactions with such stored photoelectrons in TiO_2, *e.g.* reduction reaction with silver ions, gold ions, oxygen, hydrogen peroxide, and viologen compounds.[276–279] A very promising reduction reaction using stored photoexcited electrons is the nitrogen reduction reaction for the production of ammonia, which was first reported by Bahnemann *et al.* in 2011 for stored electrons in TiO_2.[280] This reaction can pave the way to an energy efficient and decentralized production of ammonia, which is commonly produced *via* the extremely energy intensive Haber-Bosch process. Ammonia is the second most produced chemical in the world and it's industrial production *via* the Haber-Bosch process causes 2 % of the annual global energy consumption, 3-5 % of the natural gas consumption, and 1.6 % of the global CO_2 emissions.[281] Therefore, sustainable processes, such as electrocatalysis or photocatalysis have to be established to reduce the energy consumption and avoid the release of CO_2. For nitrogen reduction reaction using stored photoexcited electrons, materials with high electron storage ability and the possibility to use these electrons for the reduction reaction are needed. For this, we tested TiO_2 aerogels with their high surface area. It is already known, that electrons in TiO_2 are trapped close to the surface of the material and that Ti^{3+} states are formed, which show a characteristic dark blue coloration, *i.e.* a broad absorption at a maximum of 650 nm.[276,277,280,282] Furthermore, it was reported

by Panayotov *et al.*, that TiO_2 aerogels offer a higher density of photoexcited electrons compared to TiO_2 nanoparticles.[12] These characteristics are the reason for the use of TiO_2 aerogels as they seem to be promising materials for electron storage and future applications in on-demand reduction reactions.

The TiO_2 aerogels were prepared *via* a novel acid catalyzed sol-gel synthesis with subsequent supercritical drying (see in **Figure 31**). The aerogels were used as-synthesized and were also calcined at temperatures of 300, 400, and 500 °C. It was possible to reduce the aging time from more than 40 days down to 7 days compared to reported literature.[283]

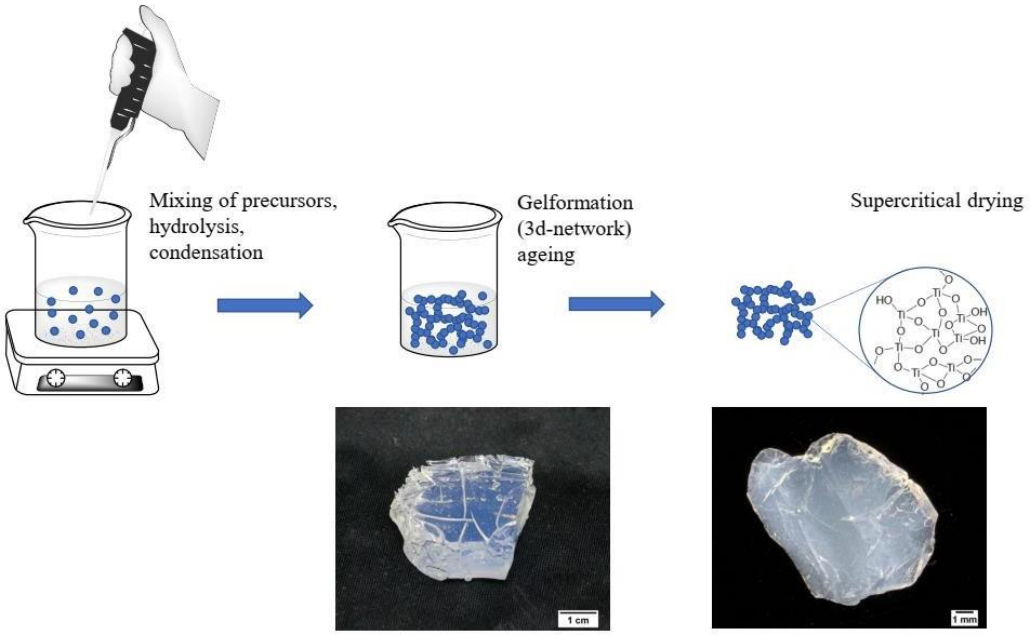

***Figure 31**: Schematic presentation of synthesis procedure and images of TiO_2 wet gel (left) and aerogel (right).*[3]

With this synthesis, a semi-crystalline as-synthesized TiO_2 aerogel could be obtained with 10 wt. % of crystalline anatase TiO_2. This semi-crystalline character was confirmed by TEM measurements. The calcined TiO_2 aerogels did all exhibit anatase crystal structure as can be seen in **Figure 32**.

Physisorption measurements revealed a decrease of the specific surface area from 600 $m^2 g^{-1}$ for the as-synthesized aerogel down to 92 $m^2 g^{-1}$ for the aerogel calcined at 500 °C.

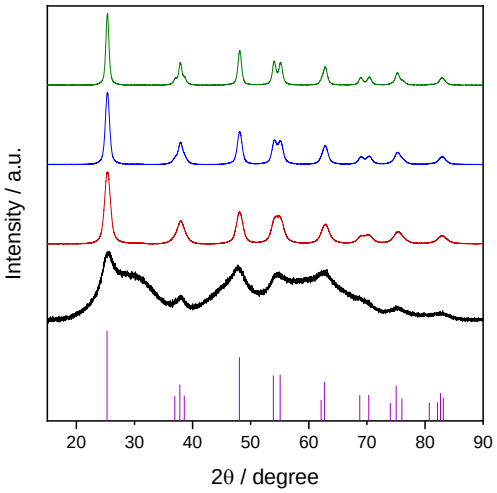

***Figure 32**: XRD patterns of the as-synthesized TiO_2 aerogel (black) and aerogels calcined at 300 °C (red), 400 °C (blue) and 500 °C (green). Reference line pattern of anatase TiO_2 (PDF-21-1272) is shown for comparison. Normalized data to the range 0 to 100 related to the highest signal.*[3]

These aerogels were first tested for their sacrificial hydrogen evolution activity by irradiation with a 300 W Xe lamp (**Figure 33**). The hydrogen evolution activity without co-catalyst decreased with increasing surface area. This can be explained by the better crystallinity of the calcined aerogels. At the same time, a color-change of the dispersions from colorless to blueish was observed after irradiation. This blueish coloration was more intense the higher the surface area of the TiO_2 aerogel and is an indication for a Ti^{3+} state formation and storage of electrons. The addition of an aqueous H_2PtCl_6 solution to the dispersions *in the dark* resulted in the evolution of hydrogen without light irradiation, due to the reduction of Pt^{4+} to Pt^0 and the formation of a Schottky contact. The coloration of the dispersion disappeared at the same time. The intensity of that hydrogen evolution peak was the higher, the darker the dispersion. This was a further indication that the as-synthesized aerogel has the best electron storage ability. This better ability to store electrons can be explained by the high surface area and presumably highest amount of surface defects (due to the lack of heat treatment), in which photoexcited electrons are trapped as has been reported by Ikeda *et al.*[284]

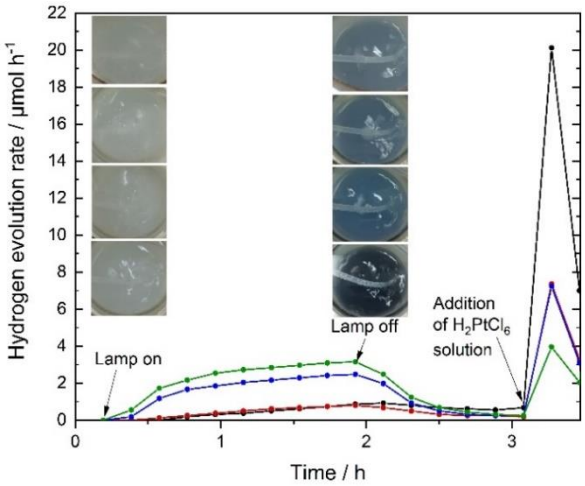

***Figure 33**: Hydrogen evolution rates over time of the as-synthesized (black) and calcined TiO_2 aerogels, 300 °C (red), 400 °C (blue), 500 °C (green); Measured without co-catalyst for the first 100 min; then measured with 0.0076 µmol m^{-2} Pt as co-catalyst (≙ 0.1 wt.-% for the as-synthesized sample) for approx. 30 min without irradiation. The photographs show the dispersions before irradiation, and after 100 min irradiation with 500 °C, 400 °C, 300 °C and as-synthesized sample from top to bottom.*[3]

The amount of the stored electrons was quantified *via* the reduction reaction of Pt^{4+} to Pt^0 in the dark and a high resolution detection of the evolved hydrogen *via* online mass spectrometer, including commercial anatase nanoparticles for comparison (**Figure 34)**. The amount of evolved hydrogen increased as expected with increasing surface area and decreasing calcination temperature of the TiO_2 aerogels.

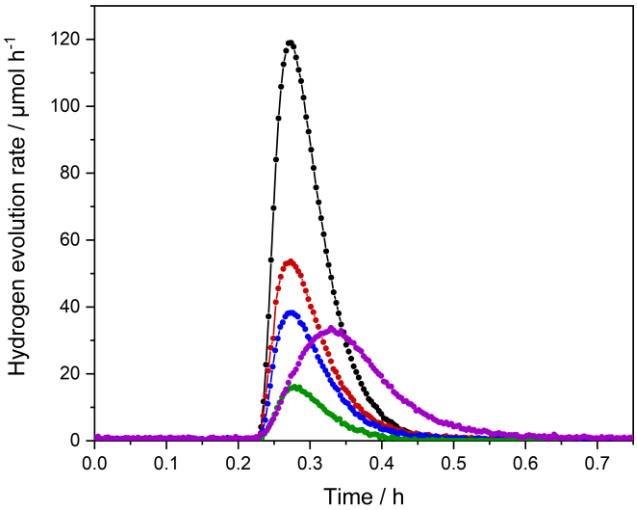

***Figure 34**: Hydrogen evolution rates in the dark for the quantification of stored electrons in the as-synthesized (black), 300 °C (red), 400 °C (blue), and 500 °C (green) TiO_2 aerogel and in commercial anatase (purple) for comparison. The samples were irradiated for 100 min and it was waited that H_2 evolution was 0 µmol h^{-1} (this time was set to 0 h here), for a stable baseline for curve integration, then Pt solution was added after 0.2 h to reach 0.1 wt.-% and the hydrogen evolution was measured until no evolution was detected anymore.*[3]

The amount of stored electrons was determined by the integration of the hydrogen evolution peak. It were 22 µmol of electrons for the as-synthesized aerogel and decreased for the calcined aerogels down to 4.8 µmol of stored electrons for the 500 °C calcined sample. The commercial anatase nanoparticles stored 13 µmol of electrons, which was in the same range as the 300 °C calcined aerogel, which has only around half of the surface area of the commercial anatase. The as-synthesized TiO_2 aerogel stored 1.7 times more electrons than the commercial anatase nanoparticles. The 500 °C calcined TiO_2 aerogel stored only 0.22 times electrons compared to the as-synthesized aerogel, however it showed 4 times higher hydrogen evolution activity. This shows that the properties of aerogels can be tailored and optimized depending on their desired application.

Additionally, absorbance measurements of the TiO_2 aerogel dispersions before and after irradiation showed the characteristic broad absorption of Ti^{3+} with a maximum at approximately 600 nm. The absorption increase after irradiation was decreasing with increasing calcination temperature, further supporting the results that the electron storage ability decreases with the calcination temperature.

It could be concluded from the results that the as-synthesized aerogel offers the best ability to store photoexcited electrons. Experiments on the influence of the methanol concentration on the electron storage ability showed, that the amount of stored electrons depends on the methanol concentration and increases with increasing concentration.

The use of such TiO_2 aerogels with high electron storage ability in subsequent dark nitrogen reduction reaction could be of high interest as introduced. Therefore, the as-synthesized TiO_2 aerogel was also tested for the ability to reduce nitrogen. For this, it was first charged as usual under Argon, the lamp was subsequently turned off, and then nitrogen was flushed trough the dispersion for several hours instead of Argon. Afterwards, a salicylate test was performed, which showed a positive test result with the formation of 5 µg L^{-1} of ammonia. This result paves the way for future research on the optimization of photocatalytic nitrogen reduction and other reduction reactions with such aerogels.

4 References

[1] A. Hofmann, M. Weiss, R. Marschall, *J. Phys. Energy* **2021**, *3*, 014002.

[2] A. Hofmann, M. Weiss, J. Timm, R. Marschall, *Adv. Mater. Interfaces* **2021**, *8*, 2100813.

[3] A. Rose, A. Hofmann, P. Voepel, B. Milow, R. Marschall, *ChemRxiv* **2022**, DOI 10.26434/chemrxiv-2021-vxkpq-v3.

[4] R. Marschall, J. Soldat, M. Wark, *Photochem. Photobiol. Sci.* **2013**, *12*, 671.

[5] J. Soldat, R. Marschall, M. Wark, *Chem. Sci.* **2014**, *5*, 3746.

[6] A. Bloesser, R. Marschall, *ACS Appl. Energy Mater.* **2018**, *1*, 2520.

[7] T. Hisatomi, C. Katayama, Y. Moriya, T. Minegishi, M. Katayama, H. Nishiyama, T. Yamada, K. Domen, *Energy Environ. Sci.* **2013**, *6*, 3595.

[8] J. Seo, M. Nakabayashi, T. Hisatomi, N. Shibata, T. Minegishi, M. Katayama, K. Domen, *J. Mater. Chem. A* **2019**, *7*, 493.

[9] M. Hojamberdiev, E. Zahedi, E. Nurlaela, K. Kawashima, K. Yubuta, M. Nakayama, H. Wagata, T. Minegishi, K. Domen, K. Teshima, *J. Mater. Chem. A* **2016**, *4*, 12807.

[10] T. Yamada, Y. Murata, S. Suzuki, H. Wagata, S. Oishi, K. Teshima, *J. Phys. Chem. C* **2018**, *122*, 8037.

[11] P. A. DeSario, J. J. Pietron, D. H. Taffa, R. Compton, S. Schünemann, R. Marschall, T. H. Brintlinger, R. M. Stroud, M. Wark, J. C. Owrutsky, D. R. Rolison, *J. Phys. Chem. C* **2015**, *119*, 17529.

[12] D. A. Panayotov, P. A. DeSario, J. J. Pietron, T. H. Brintlinger, L. C. Szymczak, D. R. Rolison, J. R. Morris, *J. Phys. Chem. C* **2013**, *117*, 15035.

[13] "NASA: Climate Change and Global Warming," can be found under https://climate.nasa.gov/, accessed 2022-07-11, **2022**.

[14] J. Cook, N. Oreskes, P. T. Doran, W. R. L. Anderegg, B. Verheggen, E. W. Maibach, J. S. Carlton, S. Lewandowsky, A. G. Skuce, S. A. Green, D. Nuccitelli, P. Jacobs, M. Richardson, B. Winkler, R. Painting, K. Rice, *Environ. Res. Lett.* **2016**, *11*, 048002.

[15] C. P. Morice, J. J. Kennedy, N. A. Rayner, J. P. Winn, E. Hogan, R. E. Killick, R. J. H. Dunn, T. J. Osborn, P. D. Jones, I. R. Simpson, *J. Geophys. Res. Atmos.* **2021**, *126*, 1.

[16] T. Wei, S. Yang, J. C. Moore, P. Shi, X. Cui, Q. Duan, B. Xu, Y. Dai, W. Yuan, X. Wei, Z. Yang, T. Wen, F. Teng, Y. Gao, J. Chou, X. Yan, Z. Wei, Y. Guo, Y. Jiang, X. Gao, K. Wang, X. Zheng, F. Ren, S. Lv, Y. Yu, B. Liu, Y. Luo, W. Li, D. Ji, J. Feng, Q. Wu, H. Cheng, J. He, C. Fu, D. Ye, G. Xu, W. Dong, *Proc. Natl. Acad. Sci.* **2012**, *109*, 12911.

[17] B. Ekwurzel, J. Boneham, M. W. Dalton, R. Heede, R. J. Mera, M. R. Allen, P. C. Frumhoff, *Clim. Change* **2017**, *144*, 579.

[18] K. O. Yoro, M. O. Daramola, in *Adv. Carbon Capture* (Ed.: G. Nisbet), Elsevier, **2020**, pp. 3–28.

[19] P. Friedlingstein, M. W. Jones, M. O'Sullivan, R. M. Andrew, D. C. E. Bakker, J. Hauck, C. Le Quéré, G. P. Peters, W. Peters, J. Pongratz, S. Sitch, J. G. Canadell, P. Ciais, R. B. Jackson, S. R. Alin, P. Anthoni, N. R. Bates, M. Becker, N. Bellouin, L. Bopp, T. T. T. Chau, F. Chevallier, L. P. Chini, M. Cronin, K. I. Currie, B. Decharme, L. M. Djeutchouang, X. Dou, W. Evans, R. A. Feely, L. Feng, T. Gasser, D. Gilfillan, T. Gkritzalis, G. Grassi, L. Gregor, N. Gruber, Ö. Gürses, I. Harris, R. A. Houghton, G. C. Hurtt, Y. Iida, T. Ilyina, I. T. Luijkx, A. Jain, S. D. Jones, E. Kato, D. Kennedy, K. K. Goldewijk, J. Knauer, J. I. Korsbakken, A. Körtzinger, P. Landschützer, S. K. Lauvset,

N. Lefèvre, S. Lienert, J. Liu, G. Marland, P. C. McGuire, J. R. Melton, D. R. Munro, J. E. M. S. Nabel, S. I. Nakaoka, Y. Niwa, T. Ono, D. Pierrot, B. Poulter, G. Rehder, L. Resplandy, E. Robertson, C. Rödenbeck, T. M. Rosan, J. Schwinger, C. Schwingshackl, R. Séférian, A. J. Sutton, C. Sweeney, T. Tanhua, P. P. Tans, H. Tian, B. Tilbrook, F. Tubiello, G. R. Van Der Werf, N. Vuichard, C. Wada, R. Wanninkhof, A. J. Watson, D. Willis, A. J. Wiltshire, W. Yuan, C. Yue, X. Yue, S. Zaehle, J. Zeng, *Earth Syst. Sci. Data* **2022**, *14*, 1917.

[20] H. Ritchie, M. Roser, P. Rosado, "Energy," can be found under https://ourworldindata.org/energy, accessed 2022-07-07, **2020**.

[21] *Bp Statistical Review of World Energy 2022, 71th Edition*, London, **2022**.

[22] H. Rodhe, *Science* **1990**, *248*, 1217.

[23] "Increase in atmospheric methane set another record during 2021 | National Oceanic and Atmospheric Administration," can be found under https://www.noaa.gov/news-release/increase-in-atmospheric-methane-set-another-record-during-2021, accessed 2022-07-07, **2022**.

[24] United Nations, *ADOPTION OF THE PARIS AGREEMENT - Paris Agreement*, Paris, **2015**.

[25] H. Ritchie, M. Roser, P. Rosado, "CO_2 and Greenhouse Gas Emissions," can be found under https://ourworldindata.org/co2-and-other-greenhouse-gas-emissions, accessed 2022-07-07, **2020**.

[26] M. Perez, R. Perez, *Sol. Energy Adv.* **2022**, *2*, 100014.

[27] M. Perez, R. Perez, *UPDATE 2015-A FUNDAMENTAL LOOK AT SUPPLY SIDE ENERGY RESERVES FOR THE PLANET*, **2015**.

[28] N. S. Lewis, G. Crabtree, A. J. Nozik, M. R. Wasielewski, P. Alivisatos, H. Kung, J. Tsao, E. Chandler, W. Walukiewicz, M. Spitler, R. Ellingson, R. Overend, J. Mazer, M. Gress, J. Horwitz, C. Ashton, B. Herndon, L. Shapard, R. M. Nault, *Basic Research Needs for Solar Energy Utilization. Report of the Basic Energy Sciences Workshop on Solar Energy Utilization, April 18-21, 2005*, **2005**.

[29] N. S. Lewis, D. G. Nocera, *Proc. Natl. Acad. Sci.* **2006**, *103*, 15729.

[30] T. R. Cook, D. K. Dogutan, S. Y. Reece, Y. Surendranath, T. S. Teets, D. G. Nocera, *Chem. Rev.* **2010**, *110*, 6474.

[31] J. Graetz, *Chem. Soc. Rev.* **2009**, *38*, 73.

[32] K. Shimura, H. Yoshida, *Energy Environ. Sci.* **2011**, *4*, 2467.

[33] Z. Wang, C. Li, K. Domen, *Chem. Soc. Rev.* **2019**, *48*, 2109.

[34] F. E. Osterloh, *Chem. Mater.* **2008**, *20*, 35.

[35] A. Kudo, Y. Miseki, *Chem. Soc. Rev.* **2009**, *38*, 253.

[36] K. Roel van de, M. Grätzel, *Photoelectrochemical Hydrogen Production*, Springer US, Boston, MA, **2012**.

[37] C. Moon, B. Shin, *Discov. Mater.* **2022**, *2*, 5.

[38] M. Ahmed, I. Dincer, *Int. J. Hydrogen Energy* **2019**, *44*, 2474.

[39] S. Ardo, D. Fernandez Rivas, M. A. Modestino, V. Schulze Greiving, F. F. Abdi, E. Alarcon Llado, V. Artero, K. Ayers, C. Battaglia, J.-P. Becker, D. Bederak, A. Berger, F. Buda, E. Chinello, B. Dam, V. Di Palma, T. Edvinsson, K. Fujii, H. Gardeniers, H. Geerlings, S. M. H. Hashemi, S. Haussener, F. Houle, J. Huskens, B. D. James, K. Konrad, A. Kudo, P. P. Kunturu, D. Lohse, B. Mei, E. L. Miller, G. F. Moore, J. Muller, K. L. Orchard, T. E. Rosser, F. H. Saadi, J.-W. Schüttauf, B. Seger, S. W. Sheehan, W. A. Smith, J. Spurgeon, M. H. Tang, R. van de Krol, P. C. K. Vesborg, P. Westerik, *Energy*

Environ. Sci. **2018**, *11*, 2768.
[40] G. Colón, *Appl. Catal. A Gen.* **2016**, *518*, 48.
[41] D. Ravelli, D. Dondi, M. Fagnoni, A. Albini, *Chem. Soc. Rev.* **2009**, *38*, 1999.
[42] A. Ibhadon, P. Fitzpatrick, *Catalysts* **2013**, *3*, 189.
[43] M. Ni, M. K. H. Leung, D. Y. C. Leung, K. Sumathy, *Renew. Sustain. Energy Rev.* **2007**, *11*, 401.
[44] A. Fujishima, K. Honda, *Nature* **1972**, *238*, 37.
[45] J. Schneider, M. Matsuoka, M. Takeuchi, J. Zhang, Y. Horiuchi, M. Anpo, D. W. Bahnemann, *Chem. Rev.* **2014**, *114*, 9919.
[46] Q. Guo, C. Zhou, Z. Ma, X. Yang, *Adv. Mater.* **2019**, *31*, 1901997.
[47] K. Nakata, A. Fujishima, *J. Photochem. Photobiol. C Photochem. Rev.* **2012**, *13*, 169.
[48] C. B. Honsberg, S. G. Bowden, "Photovoltaics Education Website," can be found under https://www.pveducation.org/, accessed 2022-07-18, **2019**.
[49] O. Kruse, J. Rupprecht, J. H. Mussgnug, G. C. Dismukes, B. Hankamer, *Photochem. Photobiol. Sci.* **2005**, *4*, 957.
[50] M. Iqbal, *An Introduction to Solar Radiation*, Elsevier, **1983**.
[51] Z. Li, W. Luo, M. Zhang, J. Feng, Z. Zou, *Energy Environ. Sci.* **2013**, *6*, 347.
[52] S. Banerjee, S. C. Pillai, P. Falaras, K. E. O'Shea, J. A. Byrne, D. D. Dionysiou, *J. Phys. Chem. Lett.* **2014**, *5*, 2543.
[53] J. Kwon, K. Choi, M. Schreck, T. Liu, E. Tervoort, M. Niederberger, *ACS Appl. Mater. Interfaces* **2021**, *13*, 53691.
[54] S. K. Parayil, R. J. Psota, R. T. Koodali, *Int. J. Hydrogen Energy* **2013**, *38*, 10215.
[55] C. Burda, Y. Lou, X. Chen, A. C. S. Samia, J. Stout, J. L. Gole, *Nano Lett.* **2003**, *3*, 1049.
[56] K. E. Karakitsou, X. E. Verykios, *J. Phys. Chem.* **1993**, *97*, 1184.
[57] R.-J. Xie, H. T. Bert Hintzen, *J. Am. Ceram. Soc.* **2013**, *96*, 665.
[58] F. E. Osterloh, *Chem. Soc. Rev.* **2013**, *42*, 2294.
[59] B. Ohtani, *J. Photochem. Photobiol. C Photochem. Rev.* **2010**, *11*, 157.
[60] R. Abe, *J. Photochem. Photobiol. C Photochem. Rev.* **2010**, *11*, 179.
[61] K. Maeda, K. Domen, in *Theor. Comput. Chem.*, Elsevier, **2007**, pp. 301–315.
[62] K. Domen, J. N. Kondo, M. Hara, T. Takata, *Bull. Chem. Soc. Jpn.* **2000**, *73*, 1307.
[63] K. Maeda, *J. Photochem. Photobiol. C Photochem. Rev.* **2011**, *12*, 237.
[64] K. Maeda, K. Domen, *MRS Bull.* **2011**, *36*, 25.
[65] M. Ahmed, G. Xinxin, *Inorg. Chem. Front.* **2016**, *3*, 578.
[66] T. Takata, C. Pan, K. Domen, *Sci. Technol. Adv. Mater.* **2015**, *16*, 033506.
[67] A. Fuertes, *Mater. Horizons* **2015**, *2*, 453.
[68] K. Maeda, K. Teramura, N. Saito, Y. Inoue, H. Kobayashi, K. Domen, *Pure Appl. Chem.* **2006**, *78*, 2267.
[69] S. Jiang, Y. Liu, J. Xu, *Mater. Adv.* **2021**, *2*, 1190.
[70] T. Takata, C. Pan, K. Domen, *ChemElectroChem* **2016**, *3*, 31.
[71] Y. Moriya, T. Takata, K. Domen, *Coord. Chem. Rev.* **2013**, *257*, 1957.
[72] Y. Wu, P. Lazic, G. Hautier, K. Persson, G. Ceder, *Energy Environ. Sci.* **2013**, *6*, 157.
[73] S. Pokrant, A. E. Maegli, G. L. Chiarello, A. Weidenkaff, *Chimia* **2013**, *67*, 162.
[74] F. E. Osterloh, *ACS Energy Lett.* **2017**, *2*, 445.
[75] S. Kim, H. Park, W. Choi, *J. Phys. Chem. B* **2004**, *108*, 6402.
[76] S. Fukuzumi, Y.-M. Lee, W. Nam, *Coord. Chem. Rev.* **2018**, *355*, 54.
[77] L. Zhang, J. Ran, S.-Z. Qiao, M. Jaroniec, *Chem. Soc. Rev.* **2019**, *48*, 5184.
[78] P. Zrazhevskiy, M. Sena, X. Gao, *Chem. Soc. Rev.* **2010**, *39*, 4326.

[79] A. Kudo, Y. Miseki, *Chem. Soc. Rev.* **2009**, *38*, 253.
[80] X. Chen, S. Shen, L. Guo, S. S. Mao, *Chem. Rev.* **2010**, *110*, 6503.
[81] H. Kisch, *Angew. Chemie Int. Ed.* **2013**, *52*, 812.
[82] A. M. Rahman, *Am. Acad. Sci. Res. J. Eng. Technol. Sci.* **2014**, *7*, 50.
[83] V. Parmon, *J. Photochem. Photobiol. A Chem.* **2002**, *4*, 91.
[84] R. Marschall, *Adv. Funct. Mater.* **2014**, *24*, 2421.
[85] J. Seo, M. Nakabayashi, T. Hisatomi, N. Shibata, T. Minegishi, M. Katayama, K. Domen, *J. Mater. Chem. A* **2019**, *7*, 493.
[86] H. Raebiger, S. Lany, A. Zunger, *Phys. Rev. B* **2007**, *76*, 045209.
[87] Y. Cen, J. Shi, M. Zhang, M. Wu, J. Du, W. Guo, Y. Zhu, *J. Colloid Interface Sci.* **2019**, *546*, 20.
[88] T. Wang, B. Daiber, J. M. Frost, S. A. Mann, E. C. Garnett, A. Walsh, B. Ehrler, *Energy Environ. Sci.* **2017**, *10*, 509.
[89] A. A. Ismail, D. W. Bahnemann, *Sol. Energy Mater. Sol. Cells* **2014**, *128*, 85.
[90] T. Takata, J. Jiang, Y. Sakata, M. Nakabayashi, N. Shibata, V. Nandal, K. Seki, T. Hisatomi, K. Domen, *Nature* **2020**, *581*, 411.
[91] J. Yang, D. Wang, H. Han, C. Li, *Acc. Chem. Res.* **2013**, *46*, 1900.
[92] B. A. Pinaud, J. D. Benck, L. C. Seitz, A. J. Forman, Z. Chen, T. G. Deutsch, B. D. James, K. N. Baum, G. N. Baum, S. Ardo, H. Wang, E. Miller, T. F. Jaramillo, *Energy Environ. Sci.* **2013**, *6*, 1983.
[93] S. A. Razek, M. R. Popeil, L. Wangoh, J. Rana, N. Suwandaratne, J. L. Andrews, D. F. Watson, S. Banerjee, L. F. J. Piper, *Electron. Struct.* **2020**, *2*, 023001.
[94] C. Zhao, Z. Chen, R. Shi, X. Yang, T. Zhang, *Adv. Mater.* **2020**, *32*, 1907296.
[95] P. Niu, J. Dai, X. Zhi, Z. Xia, S. Wang, L. Li, *InfoMat* **2021**, *3*, 931.
[96] Q. Li, X. Li, J. Yu, in *Interface Sci. Technol.*, Elsevier B.V., **2020**, pp. 313–348.
[97] G. L. Chiarello, E. Selli, in *Adv. Hydrog. Prod. Storage Distrib.*, Elsevier, **2014**, pp. 216–247.
[98] G. Zhang, W. Zhang, J. Crittenden, D. Minakata, Y. Chen, P. Wang, *J. Renew. Sustain. Energy* **2014**, *6*, 033131.
[99] J. Schneider, D. W. Bahnemann, *J. Phys. Chem. Lett.* **2013**, *4*, 3479.
[100] C. Wang, H. Groenzin, M. J. Shultz, *J. Am. Chem. Soc.* **2004**, *126*, 8094.
[101] N. Hykaway, W. M. Sears, H. Morisaki, S. R. Morrison, *J. Phys. Chem.* **1986**, *90*, 6663.
[102] C. Wang, J. Rabani, D. W. Bahnemann, J. K. Dohrmann, *J. Photochem. Photobiol. A Chem.* **2002**, *148*, 169.
[103] C. Wang, R. Pagel, D. W. Bahnemann, J. K. Dohrmann, *J. Phys. Chem. B* **2004**, *108*, 14082.
[104] L. Sun, J. R. Bolton, *J. Phys. Chem.* **1996**, *100*, 4127.
[105] S. Yamagata, S. Nakabayashi, K. M. Sancier, A. Fujishima, *Bull. Chem. Soc. Jpn.* **1988**, *61*, 3429.
[106] J. Ran, J. Zhang, J. Yu, M. Jaroniec, S. Z. Qiao, *Chem. Soc. Rev.* **2014**, *43*, 7787.
[107] S. Sakthivel, M. V. Shankar, M. Palanichamy, B. Arabindoo, D. W. Bahnemann, V. Murugesan, *Water Res.* **2004**, *38*, 3001.
[108] C. Li, J.-B. Baek, *ACS Omega* **2020**, *5*, 31.
[109] J. Yang, D. Wang, H. Han, C. Li, *Acc. Chem. Res.* **2013**, *46*, 1900.
[110] Z. Zhang, J. T. Yates, *Chem. Rev.* **2012**, *112*, 5520.
[111] W. Mönch, *Electronic Properties of Semiconductor Interfaces*, Springer Verlag Berlin Heidelberg GmbH, Berlin, Heidelberg, **2004**.

[112] K. Chang, X. Hai, J. Ye, *Adv. Energy Mater.* **2016**, *6*, 1502555.
[113] H. Kato, A. Kudo, *Chem. Phys. Lett.* **1998**, *295*, 487.
[114] H. Kato, A. Kudo, *Catal. Letters* **1999**, *58*, 153.
[115] P. D. Tran, L. Xi, S. K. Batabyal, L. H. Wong, J. Barber, J. S. Chye Loo, *Phys. Chem. Chem. Phys.* **2012**, *14*, 11596.
[116] W. J. Foo, C. Zhang, G. W. Ho, *Nanoscale* **2013**, *5*, 759.
[117] K. Maeda, K. Teramura, D. Lu, N. Saito, Y. Inoue, K. Domen, *Angew. Chemie Int. Ed.* **2006**, *45*, 7806.
[118] K. Maeda, T. Ohno, K. Domen, *Chem. Sci.* **2011**, *2*, 1362.
[119] K. Domen, A. Kudo, T. Onishi, N. Kosugi, H. Kuroda, *J. Phys. Chem.* **1986**, *90*, 292.
[120] K. Han, T. Kreuger, B. Mei, G. Mul, *ACS Catal.* **2017**, *7*, 1610.
[121] C. T. K. Thaminimulla, T. Takata, M. Hara, J. N. Kondo, K. Domen, *J. Catal.* **2000**, *196*, 362.
[122] T. Kawawaki, Y. Kataoka, S. Ozaki, M. Kawachi, M. Hirata, Y. Negishi, *Chem. Commun.* **2021**, *57*, 417.
[123] M. Carraro, A. Sartorel, F. M. Toma, F. Puntoriero, F. Scandola, S. Campagna, M. Prato, M. Bonchio, *Photocatalysis*, Springer-Verlag Berlin Heidelberg GmbH, Berlin, Heidelberg, **2011**.
[124] J. Low, C. Jiang, B. Cheng, S. Wageh, A. A. Al-Ghamdi, J. Yu, *Small Methods* **2017**, *1*, 1700080.
[125] P. Voepel, M. Weiss, B. M. Smarsly, R. Marschall, *J. Photochem. Photobiol. A Chem.* **2018**, *366*, 34.
[126] D. O. Scanlon, C. W. Dunnill, J. Buckeridge, S. A. Shevlin, A. J. Logsdail, S. M. Woodley, C. R. A. Catlow, M. J. Powell, R. G. Palgrave, I. P. Parkin, G. W. Watson, T. W. Keal, P. Sherwood, A. Walsh, A. A. Sokol, *Nat. Mater.* **2013**, *12*, 798.
[127] N. Serpone, E. Borgarello, M. Grätzel, *J. Chem. Soc., Chem. Commun.* **1984**, 342.
[128] S. Chen, Y. Qi, T. Hisatomi, Q. Ding, T. Asai, Z. Li, S. S. K. Ma, F. Zhang, K. Domen, C. Li, *Angew. Chemie Int. Ed.* **2015**, *54*, 8498.
[129] K. Wang, X. Wu, G. Zhang, J. Li, Y. Li, *ACS Sustain. Chem. Eng.* **2018**, *6*, 6682.
[130] H. Tong, S. Ouyang, Y. Bi, N. Umezawa, M. Oshikiri, J. Ye, *Adv. Mater.* **2012**, *24*, 229.
[131] S. Ouyang, J. Ye, *J. Am. Chem. Soc.* **2011**, *133*, 7757.
[132] H. Yamashita, Y. Ichihashi, M. Takeuchi, S. Kishiguchi, M. Anpo, *J. Synchrotron Radiat.* **1999**, *6*, 451.
[133] Z. Zou, J. Ye, K. Sayama, H. Arakawa, *Nature* **2001**, *414*, 625.
[134] W. Choi, A. Termin, M. R. Hoffmann, *J. Phys. Chem.* **1994**, *98*, 13669.
[135] D. Wang, J. Ye, T. Kako, T. Kimura, *J. Phys. Chem. B* **2006**, *110*, 15824.
[136] J. Tang, Z. Zou, J. Ye, *Angew. Chemie Int. Ed.* **2004**, *43*, 4463.
[137] W. T. Fu, *Phys. C Supercond.* **1995**, *250*, 67.
[138] Y. Hosogi, H. Kato, A. Kudo, *J. Phys. Chem. C* **2008**, *112*, 17678.
[139] S. O'Donnell, A. Smith, A. Carbone, P. A. Maggard, *Inorg. Chem.* **2022**, *61*, 4062.
[140] S. Saadi, A. Bouguelia, A. Derbal, M. Trari, *J. Photochem. Photobiol. A Chem.* **2007**, *187*, 97.
[141] A. Mukherji, C. Sun, S. C. Smith, G. Q. Lu, L. Wang, *J. Phys. Chem. C* **2011**, *115*, 15674.
[142] W. Yu, J. Zhang, T. Peng, *Appl. Catal. B Environ.* **2016**, *181*, 220.
[143] J. Shang, Y. Gao, W.-C. Hao, X. Jing, H.-J. Xin, L. Wang, H.-F. Feng, T.-M. Wang, *Chinese Phys. B* **2014**, *23*, 038103.
[144] W. Wang, M. Chen, D. Huang, G. Zeng, C. Zhang, C. Lai, C. Zhou, Y. Yang, M. Cheng,

L. Hu, W. Xiong, Z. Li, Z. Wang, *Compos. Part B Eng.* **2019**, *172*, 704.
[145] W. Wang, M. O. Tadé, Z. Shao, *Prog. Mater. Sci.* **2018**, *92*, 33.
[146] A. Mukherji, R. Marschall, A. Tanksale, C. Sun, S. C. Smith, G. Q. Lu, L. Wang, *Adv. Funct. Mater.* **2011**, *21*, 126.
[147] G. Liu, L. Wang, C. Sun, X. Yan, X. Wang, Z. Chen, S. C. Smith, H.-M. Cheng, G. Q. Lu, *Chem. Mater.* **2009**, *21*, 1266.
[148] S. Chen, J. Yang, C. Ding, R. Li, S. Jin, D. Wang, H. Han, F. Zhang, C. Li, *J. Mater. Chem. A* **2013**, *1*, 5651.
[149] N. Kulischow, M. Ade, M. Weiss, R. Marschall, *Photochem. Photobiol. Sci.* **2022**, *1*, 1.
[150] T. Umebayashi, T. Yamaki, H. Itoh, K. Asai, *Appl. Phys. Lett.* **2002**, *81*, 454.
[151] G. Liu, P. Niu, C. Sun, S. C. Smith, Z. Chen, G. Q. (Max) Lu, H.-M. Cheng, *J. Am. Chem. Soc.* **2010**, *132*, 11642.
[152] R. Marschall, A. Mukherji, A. Tanksale, C. Sun, S. C. Smith, L. Wang, G. Q. (Max) Lu, *J. Mater. Chem.* **2011**, *21*, 8871.
[153] G. Zhang, G. Liu, L. Wang, J. T. S. Irvine, *Chem. Soc. Rev.* **2016**, *45*, 5951.
[154] Y. Hu, L. Mao, X. Guan, K. A. Tucker, H. Xie, X. Wu, J. Shi, *Renew. Sustain. Energy Rev.* **2020**, *119*, 109527.
[155] Y. Miseki, H. Kato, A. Kudo, *Energy Environ. Sci.* **2009**, *2*, 306.
[156] Z. Ma, Y. Wang, Y. Lu, H. Ning, J. Zhang, *Energy Technol.* **2021**, *9*, 2001019.
[157] V.-H. Nguyen, H. H. Do, T. Van Nguyen, P. Singh, P. Raizada, A. Sharma, S. S. Sana, A. N. Grace, M. Shokouhimehr, S. H. Ahn, C. Xia, S. Y. Kim, Q. Van Le, *Sol. Energy* **2020**, *211*, 584.
[158] E. Grabowska, *Appl. Catal. B Environ.* **2016**, *186*, 97.
[159] P. Kanhere, Z. Chen, *Molecules* **2014**, *19*, 19995.
[160] V. M. Goldschmidt, *Naturwissenschaften* **1926**, *14*, 477.
[161] O. Harumi, K. Kiyoung, K. Asuka, T. Ikuharu, F. Hirotaka, S. Yoshihisa, I. Hayao, M. Takako, T. Kenji, *Chem. Lett.* **2005**, *34*, 822.
[162] Y. Miseki, H. Kato, A. Kudo, *Chem. Lett.* **2006**, *35*, 1052.
[163] T.-G. Xu, C. Zhang, X. Shao, K. Wu, Y.-F. Zhu, *Adv. Funct. Mater.* **2006**, *16*, 1599.
[164] J. Soldat, G. W. Busser, M. Muhler, M. Wark, *ChemCatChem* **2016**, *8*, 153.
[165] S. Park, H. J. Song, C. W. Lee, S. W. Hwang, I. S. Cho, *ACS Appl. Mater. Interfaces* **2015**, *7*, 21860.
[166] F. Sun, P. Wang, Z. Yi, M. Wark, J. Yang, X. Wang, *Catal. Sci. Technol.* **2018**, *8*, 3025.
[167] D. Xu, W. Shi, C. Xu, S. Yang, H. Bai, C. Song, B. Chen, *J. Mater. Res.* **2016**, *31*, 2640.
[168] E. Hua, G. Liu, G. Zhang, X. Xu, *Dalt. Trans.* **2018**, *47*, 4360.
[169] N. C. Hildebrandt, J. Soldat, R. Marschall, *Small* **2015**, *11*, 2051.
[170] T. Takata, K. Domen, *J. Phys. Chem. C* **2009**, *113*, 19386.
[171] I. Mondal, M. Srikanth, K. Srinivasu, Y. Soujanya, U. Pal, *J. Phys. Chem. C* **2017**, *121*, 2597.
[172] F.-F. Li, D.-R. Liu, G.-M. Gao, B. Xue, Y.-S. Jiang, *Appl. Catal. B Environ.* **2015**, *166–167*, 104.
[173] M. Lv, X. Sun, S. Wei, C. Shen, Y. Mi, X. Xu, *ACS Nano* **2017**, *11*, 11441.
[174] Z. Ma, Y. Li, Y. Lv, R. Sa, Q. Li, K. Wu, *ACS Appl. Mater. Interfaces* **2018**, *10*, 39327.
[175] S. G. Ebbinghaus, H.-P. Abicht, R. Dronskowski, T. Müller, A. Reller, A. Weidenkaff, *Prog. Solid State Chem.* **2009**, *37*, 173.
[176] S. Esmaeilzadeh, J. Grins, T. Hörlin, *Mater. Sci. Forum* **2000**, *325–326*, 11.
[177] Y. Suemoto, Y. Masubuchi, Y. Nagamine, A. Matsutani, T. Shibahara, K. Yamazaki, S.

Kikkawa, *Inorg. Chem.* **2018**, *57*, 9086.
[178] Y. Tang, K. Kato, T. Oshima, H. Mogi, A. Miyoshi, K. Fujii, K. Yanagisawa, K. Kimoto, A. Yamakata, M. Yashima, K. Maeda, *Inorg. Chem.* **2020**, *59*, 11122.
[179] K. Maeda, M. Higashi, B. Siritanaratkul, R. Abe, K. Domen, *J. Am. Chem. Soc.* **2011**, *133*, 12334.
[180] A. Kasahara, K. Nukumizu, T. Takata, J. N. Kondo, M. Hara, H. Kobayashi, K. Domen, *J. Phys. Chem. B* **2003**, *107*, 791.
[181] J. Xu, C. Pan, T. Takata, K. Domen, *Chem. Commun.* **2015**, *51*, 7191.
[182] M. Higashi, K. Domen, R. Abe, *J. Am. Chem. Soc.* **2013**, *135*, 10238.
[183] F. Oehler, S. G. Ebbinghaus, *Solid State Sci.* **2016**, *54*, 43.
[184] T. Yamada, Y. Murata, S. Suzuki, H. Wagata, S. Oishi, K. Teshima, *J. Phys. Chem. C* **2018**, *122*, 8037.
[185] J. Seo, T. Hisatomi, M. Nakabayashi, N. Shibata, T. Minegishi, M. Katayama, K. Domen, *Adv. Energy Mater.* **2018**, *8*, 1800094.
[186] B. Dong, J. Cui, Y. Qi, F. Zhang, *Adv. Mater.* **2021**, *33*, 2004697.
[187] Y. Wang, S. Jin, X. Sun, S. Wei, L. Chen, X. Xu, *Appl. Catal. B Environ.* **2019**, *245*, 10.
[188] Y. Wang, S. Wei, X. Xu, *Appl. Catal. B Environ.* **2020**, *263*, 118315.
[189] R. Wang, Y. Wang, S. Chang, S. Jin, Y. Shao, X. Xu, *J. Catal.* **2020**, *390*, 57.
[190] S. Balaz, S. H. Porter, P. M. Woodward, L. J. Brillson, *Chem. Mater.* **2013**, *25*, 3337.
[191] W.-J. Chun, A. Ishikawa, H. Fujisawa, T. Takata, J. N. Kondo, M. Hara, M. Kawai, Y. Matsumoto, K. Domen, *J. Phys. Chem. B* **2003**, *107*, 1798.
[192] G. Lin, R. Wang, T. Cao, L. Yuan, X. Xu, *Inorg. Chem. Front.* **2020**, *7*, 2629.
[193] N. Kosem, Y. Honda, M. Watanabe, A. Takagaki, Z. P. Tehrani, F. Haydous, T. Lippert, T. Ishihara, *Catal. Sci. Technol.* **2020**, *10*, 4042.
[194] G. Lin, X. Xu, *ACS Sustain. Chem. Eng.* **2020**, *8*, 9641.
[195] Z. Pan, T. Hisatomi, Q. Wang, S. Chen, M. Nakabayashi, N. Shibata, C. Pan, T. Takata, M. Katayama, T. Minegishi, A. Kudo, K. Domen, *ACS Catal.* **2016**, *6*, 7188.
[196] Y. Pihosh, V. Nandal, T. Minegishi, M. Katayama, T. Yamada, K. Seki, M. Sugiyama, K. Domen, *ACS Energy Lett.* **2020**, *5*, 2492.
[197] J. Seo, Y. Moriya, M. Kodera, T. Hisatomi, T. Minegishi, M. Katayama, K. Domen, *Chem. Mater.* **2016**, *28*, 6869.
[198] S. Ramaraj, J. Seo, *J. Energy Chem.* **2022**, *68*, 529.
[199] M. Hojamberdiev, M. F. Bekheet, E. Zahedi, H. Wagata, J. J. M. Vequizo, A. Yamakata, K. Yubuta, A. Gurlo, K. Domen, K. Teshima, *Dalt. Trans.* **2016**, *45*, 12559.
[200] A. Jain, S. P. Ong, G. Hautier, W. Chen, W. D. Richards, S. Dacek, S. Cholia, D. Gunter, D. Skinner, G. Ceder, K. A. Persson, *APL Mater.* **2013**, *1*, 011002.
[201] Materials Project, "mp-1227303: BaTaNO2 (Tetragonal, P4/mmm, 123)," can be found under https://materialsproject.org/materials/mp-1227303/, from database version v2021.11.10, accessed 2022-08-22, **2021**.
[202] W. Zeng, Y. Bian, S. Cao, Y. Ma, Y. Liu, A. Zhu, P. Tan, J. Pan, *ACS Appl. Mater. Interfaces* **2018**, *10*, 21328.
[203] T. Matoba, K. Maeda, K. Domen, *Chem. - A Eur. J.* **2011**, *17*, 14731.
[204] J. Cui, Y. Qi, B. Dong, L. Mu, Q. Ding, G. Liu, M. Jia, F. Zhang, C. Li, *Appl. Catal. B Environ.* **2019**, *241*, 1.
[205] S. Wei, S. Jin, G. Pan, Z. Li, G. Liu, X. Xu, *J. Am. Ceram. Soc.* **2019**, *102*, 6194.
[206] B. Siritanaratkul, K. Maeda, T. Hisatomi, K. Domen, *ChemSusChem* **2011**, *4*, 74.
[207] M. Matsukawa, R. Ishikawa, T. Hisatomi, Y. Moriya, N. Shibata, J. Kubota, Y. Ikuhara,

K. Domen, *Nano Lett.* **2014**, *14*, 1038.
[208] M. Hojamberdiev, R. Vargas, Z. C. Kadirova, K. Kato, H. Sena, A. G. Krasnov, A. Yamakata, K. Teshima, M. Lerch, *ACS Catal.* **2022**, *12*, 1403.
[209] M. Hojamberdiev, R. Vargas, Z. C. Kadirova, K. Teshima, M. Lerch, *Mater. Adv.* **2022**, DOI 10.1039/D2MA00611A.
[210] J. Seo, M. Nakabayashi, T. Hisatomi, N. Shibata, T. Minegishi, M. Katayama, K. Domen, *J. Mater. Chem. A* **2019**, *7*, 493.
[211] J. Seo, M. Nakabayashi, T. Hisatomi, N. Shibata, T. Minegishi, K. Domen, *ACS Appl. Energy Mater.* **2019**, *2*, 5777.
[212] Y. Luo, S. Suzuki, Z. Wang, K. Yubuta, J. J. M. Vequizo, A. Yamakata, H. Shiiba, T. Hisatomi, K. Domen, K. Teshima, *ACS Appl. Mater. Interfaces* **2019**, *11*, 22264.
[213] J. Niu, J. Albero, P. Atienzar, H. García, *Adv. Funct. Mater.* **2020**, *30*, 1908984.
[214] W. Zhou, H. Fu, *ChemCatChem* **2013**, *5*, 885.
[215] T. A. Kandiel, R. Dillert, L. Robben, D. W. Bahnemann, *Catal. Today* **2011**, *161*, 196.
[216] A. A. Ismail, D. W. Bahnemann, L. Robben, V. Yarovyi, M. Wark, *Chem. Mater.* **2010**, *22*, 108.
[217] A. A. Ismail, D. W. Bahnemann, I. Bannat, M. Wark, *J. Phys. Chem. C* **2009**, *113*, 7429.
[218] N. Lu, M. Zhang, X. Jing, P. Zhang, Y. Zhu, Z. Zhang, *ENERGY Environ. Mater.* **2022**, DOI 10.1002/eem2.12338.
[219] C. Wessel, R. Ostermann, R. Dersch, B. M. Smarsly, *J. Phys. Chem. C* **2011**, *115*, 362.
[220] S. Chuangchote, J. Jitputti, T. Sagawa, S. Yoshikawa, *ACS Appl. Mater. Interfaces* **2009**, *1*, 1140.
[221] H. Lee, M. Kim, D. Sohn, S. H. Kim, S.-G. Oh, S. S. Im, I. S. Kim, *RSC Adv.* **2017**, *7*, 6108.
[222] M. Einert, T. Weller, T. Leichtweiß, B. M. Smarsly, R. Marschall, *ChemPhotoChem* **2017**, *1*, 326.
[223] M. Einert, R. Ostermann, T. Weller, S. Zellmer, G. Garnweitner, B. M. Smarsly, R. Marschall, *J. Mater. Chem. A* **2016**, *4*, 18444.
[224] A. C. Pradhan, T. Uyar, *ACS Appl. Mater. Interfaces* **2017**, *9*, 35757.
[225] C.-Q. Li, S.-S. Yi, D. Chen, Y. Liu, Y.-J. Li, S.-Y. Lu, X.-Z. Yue, Z.-Y. Liu, *J. Mater. Chem. A* **2019**, *7*, 17974.
[226] A. Bloesser, P. Voepel, M. O. Loeh, A. Beyer, K. Volz, R. Marschall, *J. Mater. Chem. A* **2018**, *6*, 1971.
[227] W. Zhou, F. Sun, K. Pan, G. Tian, B. Jiang, Z. Ren, C. Tian, H. Fu, *Adv. Funct. Mater.* **2011**, *21*, 1922.
[228] D. M. Antonelli, J. Y. Ying, *Angew. Chemie Int. Ed. English* **1995**, *34*, 2014.
[229] J. Lee, M. Christopher Orilall, S. C. Warren, M. Kamperman, F. J. DiSalvo, U. Wiesner, *Nat. Mater.* **2008**, *7*, 222.
[230] E. Hosono, T. Tokunaga, S. Ueno, Y. Oaki, H. Imai, H. Zhou, S. Fujihara, *Cryst. Growth Des.* **2012**, *12*, 2923.
[231] A. S. Cherevan, S. Robbins, D. Dieterle, P. Gebhardt, U. Wiesner, D. Eder, *Nanoscale* **2016**, *8*, 16694.
[232] T. Grewe, H. Tüysüz, *J. Mater. Chem. A* **2016**, *4*, 3007.
[233] T. Weller, J. Sann, R. Marschall, *Adv. Energy Mater.* **2016**, *6*, 1600208.
[234] T. Weller, L. Deilmann, J. Timm, T. S. Dörr, P. A. Beaucage, A. S. Cherevan, U. B. Wiesner, D. Eder, R. Marschall, *Nanoscale* **2018**, *10*, 3225.
[235] M. G. Walter, E. L. Warren, J. R. McKone, S. W. Boettcher, Q. Mi, E. A. Santori, N. S. Lewis, *Chem. Rev.* **2010**, *110*, 6446.

[236] J. H. Pan, H. Dou, Z. Xiong, C. Xu, J. Ma, X. S. Zhao, *J. Mater. Chem.* **2010**, *20*, 4512.
[237] G. K. Mor, O. K. Varghese, M. Paulose, K. Shankar, C. A. Grimes, *Sol. Energy Mater. Sol. Cells* **2006**, *90*, 2011.
[238] D. Gu, F. Schüth, *Chem. Soc. Rev.* **2014**, *43*, 313.
[239] B. Ohtani, Y. Ogawa, S. Nishimoto, *J. Phys. Chem. B* **1997**, *101*, 3746.
[240] J. N. Kondo, K. Domen, *Chem. Mater.* **2008**, *20*, 835.
[241] A. S. Cherevan, L. Deilmann, T. Weller, D. Eder, R. Marschall, *ACS Appl. Energy Mater.* **2018**, *1*, 5787.
[242] D. Li, Y. Xia, *Adv. Mater.* **2004**, *16*, 1151.
[243] A. Formhals, *PROCESS AND APPARATUS FOR PREPARING ARTIFICIAL THREADS*, **1930**, 1,975,504; Serial No. 500, 283.
[244] J. Doshi, D. H. Reneker, *J. Electrostat.* **1995**, *35*, 151.
[245] D. H. Reneker, I. Chun, *Nanotechnology* **1996**, *7*, 216.
[246] A. Frenot, I. S. Chronakis, *Curr. Opin. Colloid Interface Sci.* **2003**, *8*, 64.
[247] H. Dai, J. Gong, H. Kim, D. Lee, *Nanotechnology* **2002**, *13*, 674.
[248] D. Li, J. T. McCann, Y. Xia, M. Marquez, *J. Am. Ceram. Soc.* **2006**, *89*, 1861.
[249] S. Agarwal, A. Greiner, J. H. Wendorff, *Prog. Polym. Sci.* **2013**, *38*, 963.
[250] G. Cadafalch Gazquez, Electrospinning as a Tool for Fabricating Functional Ceramics, University of Twente, **2016**.
[251] S. K. Singh, A. Subramanian, *RSC Adv.* **2020**, *10*, 25022.
[252] R. P. A. Hartman, Electrohydrodynamic Atomization in the Cone-Jet Mode. From Physical Modeling to Powder Production., Technische Universiteit Delft, **1998**.
[253] B. Aramide, A. Kothandaraman, M. Edirisinghe, S. N. Jayasinghe, Y. Ventikos, *Langmuir* **2019**, *35*, 10203.
[254] S. Bagchi, R. Brar, B. Singh, C. Ghanshyam, *J. Electrostat.* **2015**, *78*, 68.
[255] Lord Rayleigh, *Proc. London Math. Soc.* **1878**, *s1-10*, 4.
[256] M. M. Hohman, M. Shin, G. Rutledge, M. P. Brenner, *Phys. Fluids* **2001**, *13*, 2201.
[257] X. Qin, in *Electrospun Nanofibers*, Elsevier, **2017**, pp. 41–71.
[258] N. Hüsing, U. Schubert, *Angew. Chemie Int. Ed.* **1998**, *37*, 22.
[259] D. A. Ward, E. I. Ko, *Ind. Eng. Chem. Res.* **1995**, *34*, 421.
[260] M. Schneider, A. Baiker, *Catal. Today* **1997**, *35*, 339.
[261] M. A. Cauqui, J. M. Rodríguez-Izquierdo, *J. Non. Cryst. Solids* **1992**, *147–148*, 724.
[262] J. Fricke, A. Emmerling, in *Chem. Spectrosc. Appl. Sol-Gel Glas. Struct. Bond.* (Eds.: R. Reisfeld, C.K. JJørgensen), Springer Verlag, Berlin, Heidelberg, **1992**, pp. 37–87.
[263] M. Schneider, A. Baiker, *Catal. Rev.* **1995**, *37*, 515.
[264] R. Moussaoui, K. Elghniji, M. ben Mosbah, E. Elaloui, Y. Moussaoui, *J. Saudi Chem. Soc.* **2017**, *21*, 751.
[265] G. M. Pajonk, *Appl. Catal.* **1991**, *72*, 217.
[266] P. A. DeSario, J. J. Pietron, D. H. Taffa, R. Compton, S. Schünemann, R. Marschall, T. H. Brintlinger, R. M. Stroud, M. Wark, J. C. Owrutsky, D. R. Rolison, *J. Phys. Chem. C* **2015**, *119*, 17529.
[267] D. M. Smith, R. Deshpande, C. J. Brinker, W. L. Earl, B. Ewing, P. J. Davis, *Catal. Today* **1992**, *14*, 293.
[268] P. J. Davis, C. Jeffrey Brinker, D. M. Smith, *J. Non. Cryst. Solids* **1992**, *142*, 189.
[269] D. M. Smith, C. L. Glaves, P. J. Davis, C. Jeffrey Brinker, *MRS Proc.* **1988**, *121*, 657.
[270] C. J. Brodsky, E. I. Ko, *J. Mater. Chem.* **1994**, *4*, 651.
[271] J. Schneider, K. Nikitin, M. Wark, D. W. Bahnemann, R. Marschall, *Phys. Chem. Chem.*

Phys. **2016**, *18*, 10719.
[272] H. Wolff, R. Dronskowski, *J. Comput. Chem.* **2008**, *29*, 2260.
[273] F. Zhang, A. Yamakata, K. Maeda, Y. Moriya, T. Takata, J. Kubota, K. Teshima, S. Oishi, K. Domen, *J. Am. Chem. Soc.* **2012**, *134*, 8348.
[274] S. Alwin, X. Sahaya Shajan, *Mater. Renew. Sustain. Energy* **2020**, *9*, 7.
[275] M. L. Anderson, R. M. Stroud, C. A. Morris, C. I. Merzbacher, D. R. Rolison, *Adv. Eng. Mater.* **2000**, *2*, 481.
[276] H. H. Mohamed, R. Dillert, D. W. Bahnemann, *J. Phys. Chem. C* **2011**, *115*, 12163.
[277] H. H. Mohamed, R. Dillert, D. W. Bahnemann, *Chem. - A Eur. J.* **2012**, *18*, 4314.
[278] H. H. Mohamed, R. Dillert, D. W. Bahnemann, *J. Photochem. Photobiol. A Chem.* **2011**, *217*, 271.
[279] H. H. Mohamed, R. Dillert, D. W. Bahnemann, *J. Photochem. Photobiol. A Chem.* **2012**, *245*, 9.
[280] H. H. Mohamed, C. B. Mendive, R. Dillert, D. W. Bahnemann, *J. Phys. Chem. A* **2011**, *115*, 2139.
[281] K. Wang, D. Smith, Y. Zheng, *Carbon Resour. Convers.* **2018**, *1*, 2.
[282] D. Bahnemann, A. Henglein, J. Lilie, L. Spanhel, *J. Phys. Chem.* **1984**, *88*, 709.
[283] S. Sadrieyeh, R. Malekfar, *J. Non. Cryst. Solids* **2017**, *457*, 175.
[284] S. Ikeda, N. Sugiyama, S. Murakami, H. Kominami, Y. Kera, H. Noguchi, K. Uosaki, T. Torimoto, B. Ohtani, *Phys. Chem. Chem. Phys.* **2003**, *5*, 778.

5 Individual Contribution to Joint Publications

In this chapter, the contributions of all authors to each publication, presented in the following chapters, will be specified. Corresponding author of all presented publications is Prof. Dr. Roland Marschall.

5.1 Publication 1

"Fast low temperature synthesis of layered perovskite heterojunctions for overall water splitting"

Anja Hofmann, Morten Weiss, Roland Marschall*

published in Journal of Physics: Energy published by IOP Publishing Ltd.

Impact factor Journal of Physics: Energy (2021): 7.528

J. Phys. Energy **2021**, *3*, 014002

https://doi.org/10.1088/2515-7655/abc07a

I synthesized all samples and performed XRD, UV-vis, Raman, DRIFT, and SEM characterization as well as photocatalytic experiments. Furthermore, I wrote the first draft of the manuscript. Dr. Morten Weiss performed Rietveld refinements, wrote the Rietveld refinement part, and proofread the manuscript. Prof. Dr. Roland Marschall supervised the work, gave scientific advice, and corrected the manuscript. Dr. Jana Timm and Christopher Simon, who are acknowledged in the manuscript, performed Kr physisorption and TEM measurements, respectively. My contribution to the publication is approximately 70 %.

5.2 Publication 2

"Perovskite-type oxynitride nanofibers performing photocatalytic oxygen and hydrogen generation"

Anja Hofmann, Morten Weiss, Jana Timm, Roland Marschall*

published in Advanced Materials Interfaces published by Wiley-VCH GmbH.

Impact factor Advanced Materials Interfaces (2021): 6.389

Adv. Mater. Interfaces **2021**, *8*, 2100813

https://doi.org/10.1002/admi.202100813

I prepared the samples and characterized them by XRD, UV-vis, SEM, and EDX. Furthermore, I conducted the photocatalytic measurements and wrote the first draft of the manuscript. Dr. Jana Timm performed the Kr physisorption and EA measurements, was involved in writing and correcting of the manuscript, and contributed to the scientific discussion. Dr. Morten Weiss did the Rietveld refinements and performed the XPS measurements, and XPS data interpretation. He also wrote the XPS part and did proofreading of the manuscript. Prof. Dr. Roland Marschall supervised the work, gave scientific advice, and corrected the manuscript. Lena Geiling and Christopher Simon performed TG-MS and TEM measurements, respectively. They are acknowledged in the work. My contribution to the manuscript is approximately 65 %.

5.3 Publication 3

"Photocatalytic activity and electron storage capability of TiO_2 aerogels with adjustable surface area"

Alexandra Rose[§], Anja Hofmann[§], Pascal Voepel, Barbara Milow, Roland Marschall[*]

§: These authors contributed equally to the manuscript.

Published in ChemRxiv, Cambridge: Cambridge Open Engage published by Cambridge University Press.

Rose *et al. ChemRxiv*, DOI: 10.26434/chemrxiv-2021-vxkpq-v3, 2022

10.26434/chemrxiv-2021-vxkpq-v3

Alexandra Rose synthesized the samples and characterized them *via* XRD, and SEM, and organized the post-photocatalytic characterization together with Pascal Voepel. I performed the UV-vis and all photocatalysis measurement. Alexandra Rose and I wrote the together the first draft of the manuscript. Barbara Milow and Pascal Voepel, supervised the work at the DLR, and Roland Marschall supervised the work at the University of Bayreuth.

All gave scientific advice and corrected the manuscript. Judith Zander, who is acknowledged in the manuscript, supported the nitrogen reduction reaction measurements, Lion Schumacher and Jonas Jungmann performed XRD and physisorption measurements of the commercial anatase nanoparticles, and Markus Heyer supported the supercritical drying. Dr. Peter Mechnich and Alexander Francke supported the X-ray quantitative phase analysis. They are all acknowledged in the manuscript. My contribution to the manuscript is approximately 40 %.

6 Fast Low Temperature Synthesis of Layered Perovskite Heterojunctions for Overall Water Splitting

6.1 Main manuscript

Anja Hofmann[1], Morten Weiss[1] and Roland Marschall[1]

Published 6 November 2020 • © 2020 The Author(s). Published by IOP Publishing Ltd,

Citation Anja Hofmann *et al* 2021 *J. Phys. Energy* **3** 014002

Author emails roland.marschall@uni-bayreuth.de

Author affiliations [1] Department of Chemistry, University of Bayreuth, 95447, Bayreuth, Germany

https://doi.org/10.1088/2515-7655/abc07a

Keywords: low temperature synthesis, (111) layered perovskite, heterojunction, overall water splitting

Abstract

The $Ba_5Ta_4O_{15}$-$Ba_3Ta_5O_{15}$-$BaTa_2O_6$ heterojunction was synthesized for the first time at ambient pressure and mild temperatures without further need of calcination. By systematically adjusting the synthesis parameters, the composition of the composite could be tailored. Detailed Rietveld refinement revealed the highest amount of by-phases for the non-calcined sample with around 12% of $Ba_3Ta_5O_{15}$ and 12% of $BaTa_2O_6$, respectively. $Ba_5Ta_4O_{15}$ represented the main phase for all samples. The non-calcined heterojunction showed the highest activity in photocatalytic hydrogen production with 2360 μmol $h^{-1}m^{-2}$ corresponding to 1180 μmol h^{-1} without any co-catalyst. A Rh-Cr_2O_3 co-catalyst was photodeposited on all samples depending on the surface area for overall water splitting. All samples were active in overall water splitting. This novel synthesis strategy paves the way towards a general low-cost and energy-saving synthesis route to achieve highly crystalline and highly active metal oxide semiconductor photocatalysts.

1. Introduction

Since the beginning of research in photocatalytic hydrogen production and overall water splitting, many semiconductor materials have been investigated as possible photocatalyts [1–5]. One group of materials are (111) layered perovskites $A_5B_4O_{15}$(A = Ba, Sr; M = Nb, Ta) [6–10]. They are highly active in photocatalytic water splitting under UV light due to their layered crystal structure, which offers additional reaction sites in the interlayers [6, 11].

The photocatalytic activity of the wide-band gap material $Ba_5Ta_4O_{15}$ can be improved for example *via* ammonolysis [12, 13], or by formation of heterojunctions such as $Ba_5Ta_4O_{15}$-$AgVO_3$[14], and $Ba_5Ta_4O_{15}$-g-C_3N_4[15], thereby gaining visible-light absorption properties.

Different synthesis strategies for semiconductor materials such as $Ba_5Ta_4O_{15}$ are known, the most used is the solid state reaction due to its simplicity [3, 16, 17]. However, the necessary high reaction temperatures and times result in the formation of large particle sizes in the range of several micrometres, and therefore very low surface areas. For example, $Ba_5Ta_4O_{15}$ requires 24 h at 1150 °C synthesis time and temperature, which is highly energy-consuming [17].

Alternative synthesis methods for layered perovskites $A_5M_4O_{15}$ are the flux-assisted method [13, 18], hydrothermal synthesis [14, 15, 19, 20], the polymerisable complex method [7–9], electrospinning [21–23], sol-gel synthesis [24, 25], as well as a citrate synthesis route [26, 27]. Such synthesis methods need either high temperatures, high pressures, long reaction times or additional calcination steps.

For example, $Ba_5Ta_4O_{15}$[26] and the multicomponent heterojunctions $Ba_5Ta_4O_{15}$-$Ba_3Ta_5O_{15}$ and $Ba_5Ta_4O_{15}$-$Ba_3Ta_5O_{15}$-$BaTa_2O_6$[27] were prepared by adjustment of the precursor ratios in a citrate synthesis route. Powder precursors obtained in this syntheses need to be calcined to obtain the final crystalline products. The heterojunctions showed an improved photocatalytic activity compared to phase-pure $Ba_5Ta_4O_{15}$[27]. The formation of the three-component heterojunction $Ba_5Ta_4O_{15}$-$Ba_3Ta_5O_{15}$-$BaTa_2O_6$ resulted in a 70% higher gas evolution rate in overall water splitting measurements with Rh-Cr_2O_3 as co-catalyst as compared to pure $Ba_5Ta_4O_{15}$. An improved charge separation and extended lifetime of electrons due to the electron injection from the·CH_2OH radical into the conduction band of $Ba_3Ta_5O_{15}$ (photocurrent doubling), revealed by laser flash photolysis experiments on $Ba_5Ta_4O_{15}$-$Ba_3Ta_5O_{15}$ and $Ba_5Ta_4O_{15}$ in N_2-methanol atmosphere, was

shown to be the reason for the enhanced photocatalytic activity. Trapped electrons accumulate in the system. In case of the phase-pure $Ba_5Ta_4O_{15}$, the $\cdot CH_2OH$ radical acts as recombination centre. Without methanol, no difference in the decay behaviour could be found [28]. A comparison of the photocatalytic activity to phase-pure $Ba_3Ta_5O_{15}$ *via* citrate synthesis route is hitherto not reported, which can be explained with the complex synthesis of $Ba_3Ta_5O_{15}$ reported by Feger *et al*. This synthesis is highly energy-consuming as a pressed pellet of $Ba_5Ta_4O_{15}$, Ta_2O_5, and Ta needs to be sealed with $BaCl_2$ in a tantalum ampule and heat treated at 1640 °C for 12 h [29].

The group of Marschall synthesized $Ba_5Ta_4O_{15}$, $Ba_5Nb_4O_{15}$, and $Ba_5Nb_2Ta_2O_{15}$ nanofibers by electrospinning [21]. Later they were able to adjust the diameter of $Ba_5Ta_4O_{15}$ nanofibers and $Ba_5Ta_4O_{15}$-$Ba_3Ta_5O_{15}$ heterojunction nanofibers and showed also an improved activity for the $Ba_5Ta_4O_{15}$-$Ba_3Ta_5O_{15}$ heterojunction compared to phase-pure $Ba_5Ta_4O_{15}$ nanofibers. An intense interfacial contact and improved charge carrier separation together with the photocurrent doubling effect were shown to be the reason for the improved photocatalytic activity in the composite nanofibers, which was demonstrated by variation of sacrificial hole scavengers [22, 23].

Even in electrospinning a calcination step is needed to decompose the used spinning polymer and to crystallize the layered perovskite nanofiber materials. In the citrate synthesis route as well as in the electrospinning, the calcination temperatures are comparably low and reaction times are shorter—compared to solid state reaction—resulting in reduced particle sizes and a better energy efficiency of these two synthesis methods. Energy efficiency is one of the 12 principles of green chemistry in designing new reaction processes [30]. Synthesis at ambient conditions is one possible way to reduce the energy consumption of chemical syntheses.

Since the composite materials $Ba_5Ta_4O_{15}$-$Ba_3Ta_5O_{15}$ and $Ba_5Ta_4O_{15}$-$Ba_3Ta_5O_{15}$-$BaTa_2O_6$ have been shown to be much more active in photocatalysis than phase-pure $Ba_5Ta_4O_{15}$, we have developed a faster and more facile synthesis route for such composites. We present an optimized citrate synthesis route followed by combustion, which allows the synthesis of $Ba_5Ta_4O_{15}$-$Ba_3Ta_5O_{15}$-$BaTa_2O_6$ heterojunctions at ambient pressure and at comparatively low temperatures without further need of calcination. This was achieved by systematically adjusting the intensity of the combustion reaction. The photocatalytic activity of the

synthesized powders in hydrogen evolution and overall water splitting experiments were investigated. A non-calcined sample showed a higher photocatalytic activity compared to the powders synthesized with an additional calcination step, despite having the smallest surface area. The reason for this is the optimized composition of the heterojunction, resulting in improved charge carrier separation.

We think that this synthesis route could be an energy efficient way to synthesize many other semiconductor materials without diminishing the photocatalytic activity.

2. Experimental section

2.1. Materials preparation

The heterojunctions were prepared *via* a citrate synthesis route, using an adapted synthesis of Marschall *et al*[26]. 0.7058 g EDTA (99.4%, Alfa Aesar) and 0.6283 g citric acid monohydrate (Bernd Kraft) were dissolved in 60 ml water by adding different amounts of ammonia solution (25%,VWR) (either 3.5 ml, 4.2 ml, 4.5 ml or 6 ml). Afterwards different amounts (2 ml, 3 ml, or 4 ml) of conc. nitric acid (65%, Bernd Kraft) were added. The synthesis with 4.5 ml ammonia solution was done without addition of nitric acid. To stabilize the highest oxidation state of Ta, 5 ml hydrogen peroxide (30%, Fisher Scientific) were added. 0.9344 g $Ta(OEt)_5$(99.99%, abcr) were dissolved in 6 ml abs. ethanol (99.5%, Acros Organics) and were added in portions while heating the solution to 90 °C. 0.7514 g $Ba(NO_3)_2$(99.95%, Alfa Aesar) dissolved in 10 ml water, were added in small portions. In all cases, except the synthesis without addition of nitric acid, a clear solution was obtained. The volume of the solution was reduced to approx. 10 ml and then transferred in a heating mantel, where the entire solvent was evaporated. The obtained powders were completely black if no nitric acid was added with an increasing amount of white powder with increasing amounts of used ammonia solution and nitric acid. The powder precursors with dark components were grinded completely and were calcined at 1000 °C for 10 h (5 °C min^{-1}) in air. In the case of the sample, prepared with 6 ml ammonia solution and 4.5 ml nitric acid, the obtained white powder was used without further calcination.

2.2. Methods of characterization

Powder x-ray diffraction (XRD) patterns were recorded on a PANalytical Empyrean with a Pixcel 1D detector using Cu K_α in a 2θ range of 10–80°. The divergence slit was fixed to 0.5° and an anti-scatter slit of 1° was used. Rietveld refinements were performed with the program Fullprof [31]. Instrumental broadening was determined with a LaB_6 standard (NIST SRM 660 c). Reflections were modelled with an Thompson-Cox-Hastings pseudo-Voigt function [32] and the background was approximated with a Chebychev polynomial. Rietveld refinements were based on the crystal structure information published by Hojamberdiev *et al* for $Ba_5Ta_4O_{15}$[13], Feger *et al* for $Ba_3Ta_5O_{15}$[29], Ling *et al* for hexagonal (h) $Ba_4Ta_2O_9$[33], and Galasso *et al* for orthorhombic (o) $BaNb_2O_6$, which is isostructural to $BaTa_2O_6$[34]. Simulated diffraction patterns were also calculated with Fullprof.

Raman spectra were recorded using a LABRAM I from Horiba Jobin Yvon with a HeNe 632.817 nm laser with a laser power of 20 mW, equipped with an Olympus BX41 microscope (50x magnification).

Diffuse reflectance FTIR spectra were measured on a Bruker alpha II spectrometer equipped with a DRIFT module using a gold standard for measuring background spectra.

A PerkinElmer Lambda 750 UV/VIS/NIR spectrometer, equipped with a Praying-Mantis mirror unit from Harrick was used to record the diffuse reflectance spectra using a spectralon pellet as white standard. The spectra were converted into absorption spectra using Kubelka-Munk function; bandgaps were estimated using Tauc-Plots.

Krypton physisorption data were collected at 77 K in the p/p^0 range of 0.05–0.3 (fixed p^0: 2.63 Torr) by using an Anton Paar QuantaTec ASiQ-MP-MP-AG setup. Specific surface area was determined by BET (Brunauer–Emmet–Teller) method. The samples were degassed at 200 °C for 3 h with subsequent testing of complete degassing.

Scanning electron microscopy (SEM) images were recorded with a Zeiss LEO 1530 at the Bavarian Polymer Institute (BPI) KeyLab Electron and Optical microscopy. An acceleration voltage of 3 kV was set and the working distance was chosen between 6 mm and 8 mm with an aperture set to 30 μm.

Transmission electron microscopy (TEM) was carried out using a JEOL JEM-2200FSat an acceleration voltage of 200 kV at the BPI KeyLab Electron and Optical microscopy.

2.3. Photocatalytic reactions

2.3.1. Hydrogen evolution and photodepostion of Rh-Cr_2O_3 co-catalyst

For the hydrogen evolution experiments, a dispersion of 200 mg photocatalyst in 550 ml water and 50 ml methanol was used. The photocatalyst was dispersed at 30 °C for 15 min in an ultrasonic bath. The dispersion was filled into a homemade double-walled inner-irradiation glass reactor with a quartz glass housing for the lamp and was stirred with 250 rpm. A 700 W Hg mid-pressure lamp (Peschl UV-Consulting) set to 500 W was placed in an inlet of double walled quartz glass. The reactor was cooled to 10 °C with a thermostat (LAUDA RP845). The whole system was flushed with Ar 5.0 with 100 ml min^{-1} using a Bronkhorst mass flow controller for approximately 1 h to remove residual air. The gas evolution was detected online using a mass spectrometer (Hiden HPR-20 Q/C). During the experiment oxygen, hydrogen and carbon dioxide were detected. The gas evolution was measured for 4 h to investigate the activity without any co-catalyst deposited.

After 4 h the lamp was shortly switched off to add an aqueous solution of Na_3RhCl_6 (99.999%, Sigma Aldrich) through a rubber sealing. The amount was adjusted, depending on the surface area of the used photocatalyst to achieve an Rh co-catalyst loading of 0.3 μmol m^{-2} for all samples. Before the addition, the stirring speed was raised to 500 rpm to ensure a uniform distribution of the co-catalyst. After stirring for 10 min the stirring speed was set back to 250 rpm and the lamp was switched on again for 2 h. Then, an aqueous solution of K_2CrO_4 (99.5%, Sigma Aldrich) was added in the same way resulting in Cr_2O_3 amount of 0.205 μmol m^{-2}. After two more hours, the reaction was stopped. The sedimented samples were centrifuged and thoroughly washed with water and dried at 80 °C.

2.3.2. Overall water splitting

100 mg of the recovered photocatalyst with Rh-Cr_2O_3 co-catalyst were dispersed in 600 ml water in the same reactor system as described above. The system was flushed overnight with 50 ml min^{-1} Ar before the experiment. The reaction conditions were the same as in the photodeposition experiments. The gas evolution was measured for 7.5 h.

3. Results and discussion

3.1. Characterization

All prepared samples were thoroughly characterized before and after photocatalytic experiments. Since a stoichiometric amount of $Ba(NO_3)_2$ was used in the synthesis, the heterojunction $Ba_5Ta_4O_{15}$-$Ba_3Ta_5O_{15}$ should be formed as presented by Marschall *et al*[26]. As can be seen in the XRD patterns in figure 1(a), the crystallinity of the obtained powders after combustion increases with increasing amounts of ammonia solution and nitric acid. If no nitric acid is used, a completely amorphous powder is obtained. In contrast to this, a crystalline powder precursor is obtained even without calcination if 6 ml ammonia solution and 4.5 ml of nitric acid are used in the synthesis. XRD pattern confirms formation of heterojunctions with $Ba_5Ta_4O_{15}$ as majority phase with several reflections belonging to impurity phases. Reflections of the main phase are in accordance with reference pattern of $Ba_5Ta_4O_{15}$ (JCPDS 18–0193/JCPDS 72–0631). Lower amounts of ammonia solution and nitric acid, result in lower crystallinity of the obtained powders. Table S1 (available online at http://stacks.iop.org/JPENERGY/3/014002/mmedia) gives an overview of the assignment of the reflections of the powder precursors obtained with 4.2 ml of ammonia solution and 3.5 ml of ammonia solution, respectively, to each phase.

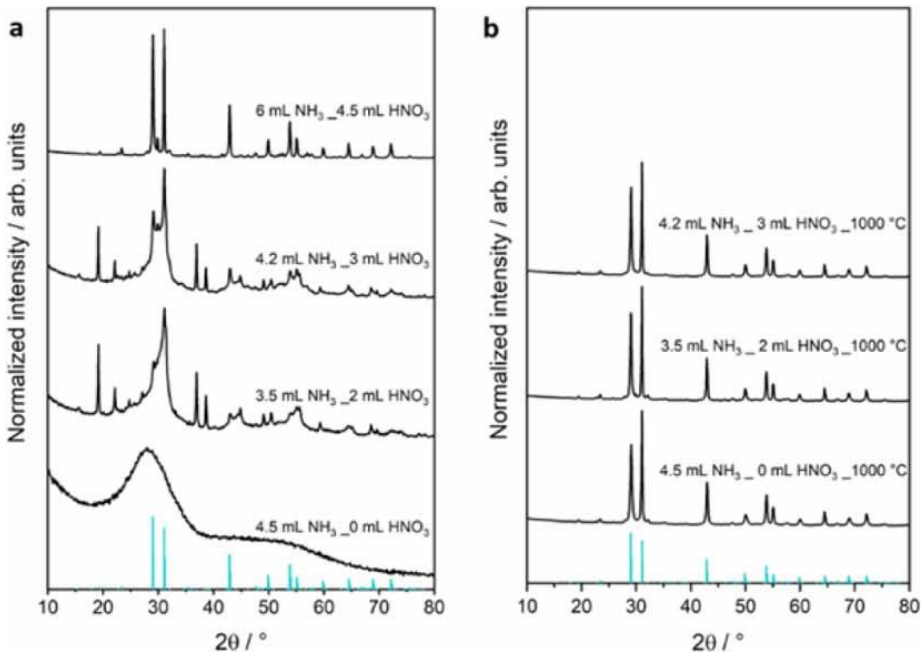

Figure 1. *XRD patterns of (a) powder precursors, and (b) calcined powders. Reference line pattern of $Ba_5Ta_4O_{15}$ is shown for comparison.*

The increasing crystallinity with increasing amounts of ammonia solution and nitric acid can be explained by the formation of ammonium nitrate during the synthesis. The ammonium nitrate ignites when most of the solvent is evaporated, which is comparable to auto-combustion methods shown before in the literature [35–37]. The more ammonium nitrate is formed, the higher the temperature will become during combustion, resulting in a higher crystallinity of the obtained powder. As no ammonium nitrate can be formed in the synthesis without nitric acid, the combustion proceeds at significantly lower temperature and an amorphous product is obtained instead. Images made of the obtained powder precursors (figures S1(a)–(d)) show an increasing amount of white material with an increasing amount of ammonium nitrate in the synthesis. As expected, the optical impression of the increasing amount of white sample can be verified by reflection measurements (figure S1(e)). With increasing amounts of used ammonia solution and nitric acid, the reflection increases, therefore supporting the optical impression.

After calcination of the powders prepared with 0 ml, 2 ml and 3 ml of nitric acid, XRD confirms the formation of $Ba_5Ta_4O_{15}$ as main phase with small amounts of by-phases for all calcined samples (figure 1(b)). Identification of the impurity phases is complicated by the small amounts and the similar diffraction patterns of most $Ba_xTa_yO_z$ phases. In order to unambiguously identify the samples, we have calculated simulated diffraction patterns for 90 wt.% $Ba_5Ta_4O_{15}$ with each 10 wt.% of $Ba_3Ta_5O_{15}$, orthorhombic (o) $BaTa_2O_6$ and hexagonal (h) $Ba_4Ta_2O_9$ (figure S2). These calculations take into account similar reflection broadening of all phases—due to crystallite size and micro-strain—and preferred orientation of $Ba_5Ta_4O_{15}$ as the experimental patterns in figure 1. By comparing the experimental and simulated diffraction patterns, the impurity phases could be reliably identified: all four samples consist of $Ba_5Ta_4O_{15}$ as majority phase and $BaTa_2O_6$(o) and $Ba_3Ta_5O_{15}$ as impurity phases. The sample synthesised with 4.2 ml ammonia solution and 3 ml nitric acid has additional small reflections that can be assigned to $Ba_4Ta_2O_9$(h). No reflections belonging to hexagonal $BaTa_2O_6$ or monoclinic $Ba_4Ta_2O_9$ could be observed.

In order to obtain a reliable quantification of relative phase content, Rietveld refinements were performed (figure 2). The synthesis without nitric acid results in the highest amount of $Ba_5Ta_4O_{15}$ (94.2%) and a combined 5.8% of $BaTa_2O_6$ (o) and $Ba_3Ta_5O_{15}$. An increasing amount of nitric acid—and thus a more intense combustion—results in a

higher content of the two minority phases; however, no clear preference between those two phases is discernible. The sample synthesised without nitric acid also has the smallest mean crystallite size with 47 nm as compared to the other samples with 76 nm (3.5 ml/2 ml), 64 nm (4.2 ml/3 ml), and 70 nm (6 ml/4.5 ml).

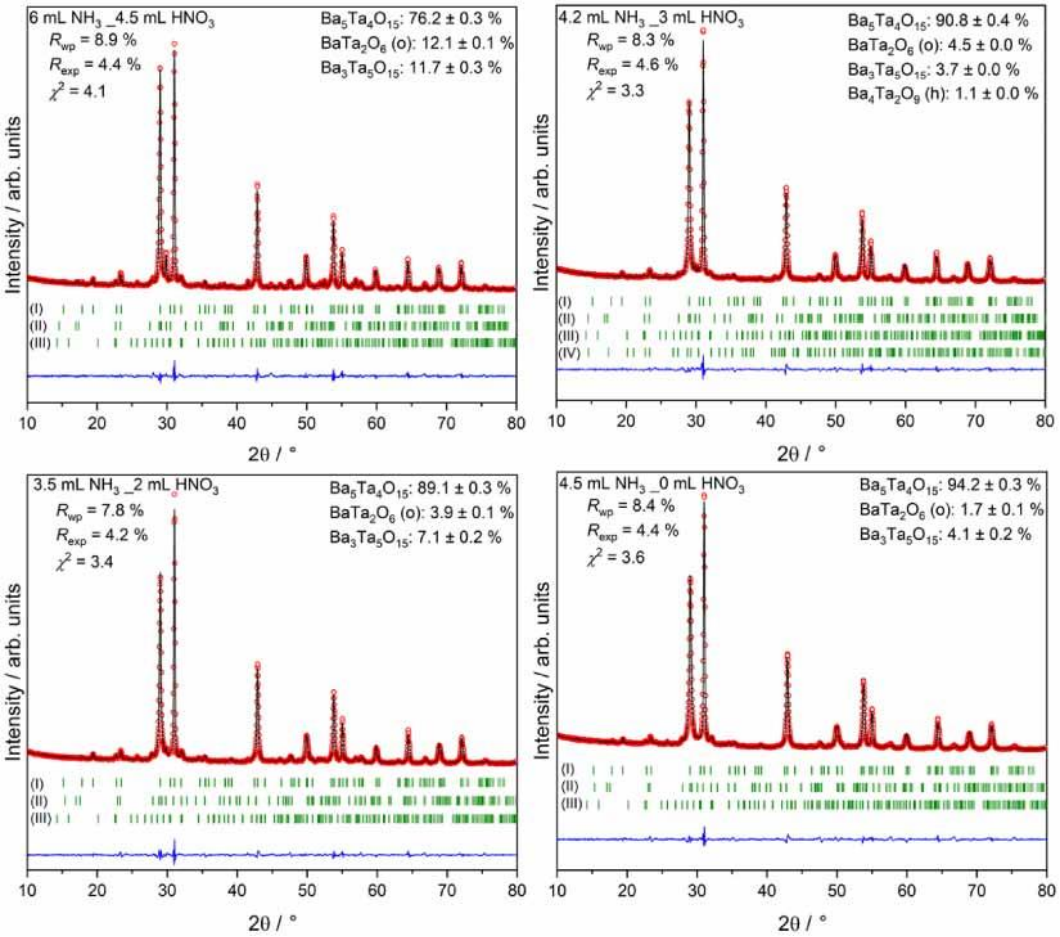

Figure 2. *Rietveld refinements of all four samples; red circles indicate measurement points, the black line is the calculated pattern, the blue line is the difference curve and the green dashes indicate theoretical reflection positions: (I) $Ba_5Ta_4O_{15}$, (II) $BaTa_2O_6$ (o), (III) $Ba_3Ta_5O_{15}$, and (IV) $Ba_4Ta_2O_9$ (h).*

The SEM images of the powder precursors in figure 3 show the typical intergrown sheet-like structure of $Ba_5Ta_4O_{15}$ for the non-calcined sample prepared with 4.5 ml nitric acid. The other samples show a smooth dense structure. After calcination, all samples exhibit the intergrown sheet-like structure (figure 4).

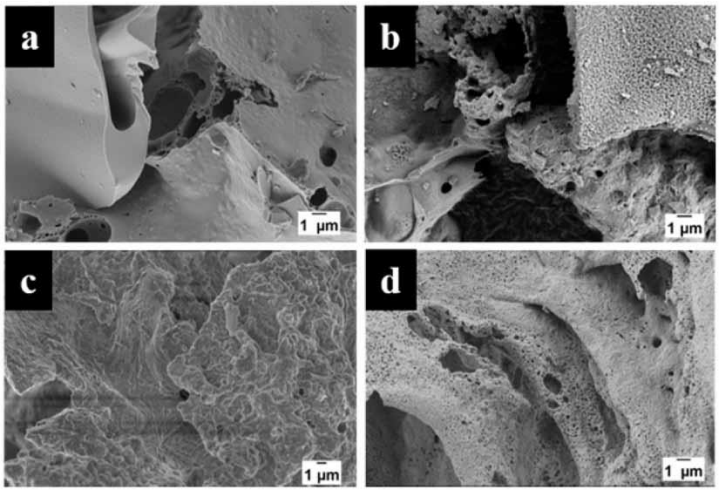

Figure 3. *SEM images of powder precursors prepared with (a) 0 ml HNO_3, (b) 2 ml HNO_3, (c) 3 ml HNO_3, and (d) 4.5 ml HNO_3.*

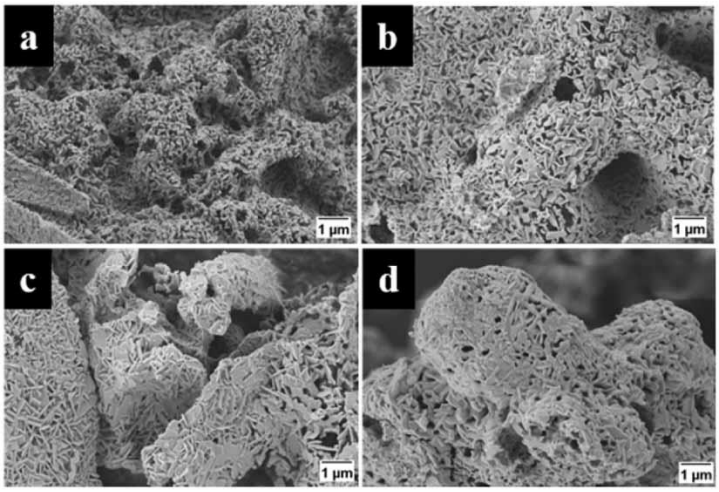

Figure 4. *SEM images of calcined powders initially prepared with (a) 0 ml HNO_3, (b) 2 ml HNO_3, and (c) 3 ml HNO_3, compared to (d) the non-calcined powder precursor prepared with 4.5 ml HNO_3.*

TEM images confirm the formation of a highly crystalline heterojunction for the non-calcined sample (figure 5(a)). Since the lattice plane distances for $Ba_5Ta_4O_{15}$, $Ba_3Ta_5O_{15}$, and $BaTa_2O_6$ are very similar, it is not possible to assign the visible lattice planes to either compound of the heterojunction unambiguously, even in high-resolution TEM (figure 5). Nevertheless, the TEM images confirm the intense interfacial contact between the crystallites of the heterojunction for optimum charge transport, already without calcination. The calcined powder prepared with 2 ml nitric acid was also investigated for comparison (figure 5(b)), showing similarly very high crystallinity and an intense interfacial contact between crystallites. A close contact between the components is crucial for good charge separation [38] and enhanced photocatalytic activity.

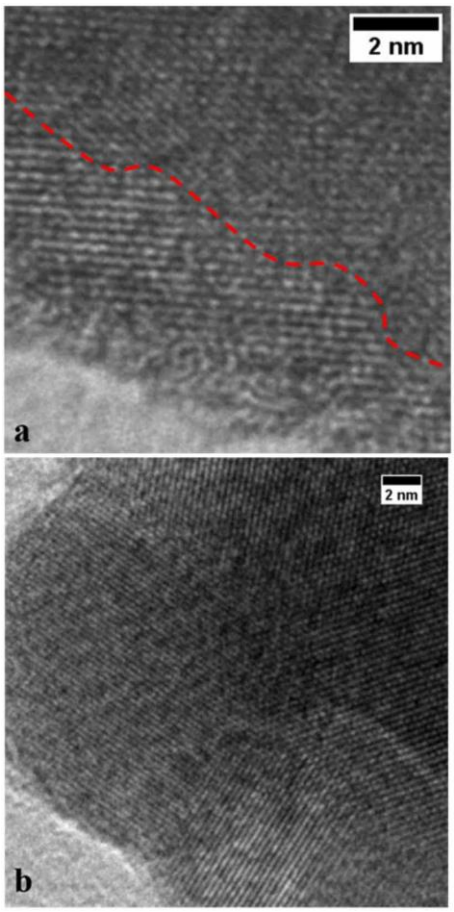

Figure 5. *TEM images of (a) the non-calcined powder and (b) the calcined powder prepared with 2 ml HNO_3.The red dashed line in (a) shows the borderline between two crystallites.*

Raman spectra of the synthesized heterojunctions are shown in figure 6(a), the main Raman bands are in agreement to the reported Raman spectra of $Ba_5Ta_4O_{15}$ in the literature [39, 40]. The DRIFT spectra in figure 6(b) are also in consistence with the reported spectra of $Ba_5Ta_4O_{15}$ [23, 39]. As expected, $BaCO_3$ and $Ba(NO_3)_2$ bands can be identified additionally in Raman and DRIFT spectra at 1059 cm^{-1}, 1046 cm^{-1} and in the range of 1400 cm^{-1}–1800 cm^{-1}. The formation of small amounts of $BaCO_3$ was already shown before in the synthesis of $Ba_5Ta_4O_{15}$ and $Ba_5Ta_4O_{15}$-$Ba_3Ta_5O_{15}$ nanofibers [21, 23]. Samples prepared with 2 ml of nitric acid, 3 ml of nitric acid, and the non-calcined sample exhibit additionally Raman bands, which are in correspondence with the Raman spectra of orthorhombic $BaTa_2O_6$ [41]. The intensity variation of these bands confirms the fractions of orthorhombic $BaTa_2O_6$ obtained from Rietveld refinement for the samples. An assignment of Raman bands to $Ba_3Ta_5O_{15}$ is not possible as no reference spectrum could be found and no unassigned Raman bands are present in the spectra.

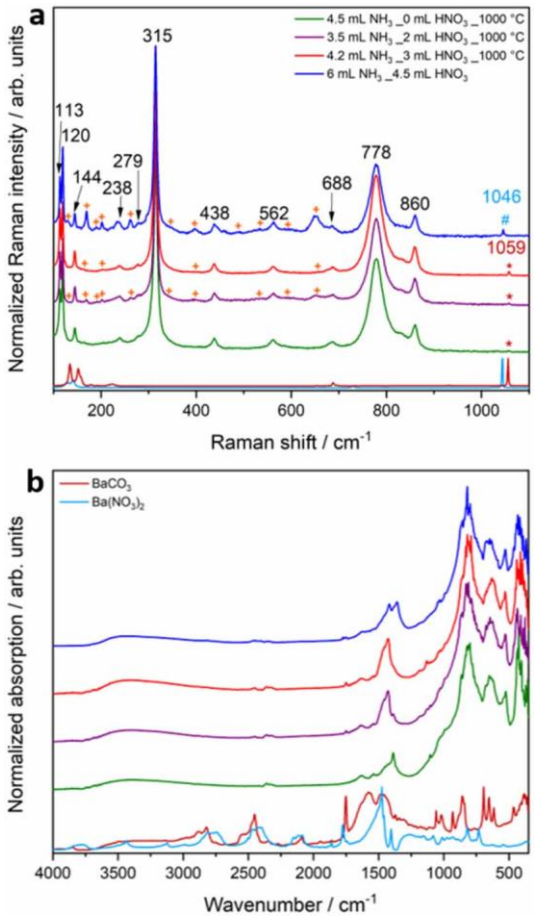

Figure 6. *Raman spectra (a) and DRIFT spectra (b) of calcined powders and non-calcined sample. The colour code is identical in a and b. Measured commercial $BaCO_3$ and $Ba(NO_3)_2$ references are shown for comparison. Black numbered bands correspond to Raman bands of $Ba_5Ta_4O_{15}$. The light blue mark correspond to Raman band of $Ba(NO_3)_2$, red marked bands to $BaCO_3$, and orange marked bands correspond to Raman bands of orthorhombic $BaTa_2O_6$.*

Tauc plots and absorption spectra (figure 7) confirm the formation of heterojunctions, as a clear shoulder at lower energy is visible additionally to the main absorption edge. The main absorption edge can be attributed to $Ba_5Ta_4O_{15}$ and is in the range of 4.3 eV to 4.4 eV for all samples. The small shoulder is related to $Ba_3Ta_5O_{15}$ and the band gaps are in the range of 3.6 eV to 3.8 eV for all samples. Estimated band gaps are in consistence with literature values [12, 21, 22, 26, 27]. A clear identification of $BaTa_2O_6$ and $Ba_4Ta_2O_9$ out of the UV–Vis spectra is not possible as the band gap of orthorhombic $BaTa_2O_6$ is overlaid by the smaller band gap of $Ba_3Ta_5O_{15}$ and as the amount of hexagonal α-$Ba_4Ta_2O_9$ is too small with 1%. Reported band gaps of orthorhombic $BaTa_2O_6$ are in the range of 4.1 eV [42] and 4.2 eV [27].

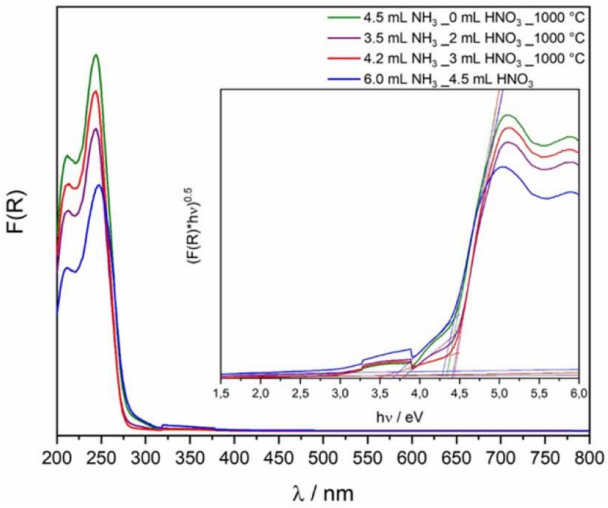

Figure 7. *Kubelka–Munk UV–Vis spectra and Tauc-Plots (inset) of synthesized heterojunctions.*

Additionally to the two absorption edges of the heterojunction, a small absorption giving a band gap of 2.9 eV is visible in the Tauc plots of the synthesized materials. This absorption can be attributed to oxygen vacancy defects in the material as it was calculated for Ta_2O_5[43].

Table 1 summarizes the estimated band gaps and measured surface areas of the materials. The surface areas are in the range of 2.5 m^2g^{-1}–5.4 m^2g^{-1}. Thereby, the non-calcined $Ba_5Ta_4O_{15}$-$Ba_3Ta_5O_{15}$-$BaTa_2O_6$ heterojunction exhibits the smallest surface area. The values are comparable to $Ba_5Ta_4O_{15}$-$Ba_3Ta_5O_{15}$ heterojunction synthesized by a citrate route in literature [27].

Table 1. *Band gaps and BET surface areas of synthesized heterojunctions.*

Sample	Calcination temperature/°C	Band gaps/eV	BET surface area/m^2 g^{-1}
4.5 ml NH3 _0 ml HNO3	1000	3.8/4.3	3.3
3.5 ml NH_3 _2 ml HNO_3	1000	3.8/4.4	5.4
4.2 ml NH_3 _3 ml HNO_3	1000	3.6/4.4	4.7
6 ml NH_3 _4.5 ml HNO_3	as-syn	3.7/4.3	2.5

3.2. Photocatalytic results and post-photocatalytic characterization

To investigate the photocatalytic activity of the synthesized heterojunctions, hydrogen evolution and overall water splitting under UV-light from water with and without methanol were measured.

3.2.1. Hydrogen evolution and photodeposition results

All synthesized heterojunctions are able to generate hydrogen from water/methanol mixture without addition of a co-catalyst (figure S3). Steady state was reached after approximately 3.5 h with hydrogen evolution rates ranging from 930 μmol h^{-1} up to 1493 μmol h^{-1} for the calcined samples. The non-calcined heterojunction shows comparable photocatalytic activity to the calcined samples with an evolution rate of 1180 μmol h^{-1}. A direct comparison of these results is difficult due to the differences of the observed surface areas of the samples and thus the presumable differences in the number of reaction sites. To exclude this influence, the hydrogen evolution rate was normalized to the absolute surface area of the samples. The resulting hydrogen evolution curves are shown in figure 8.

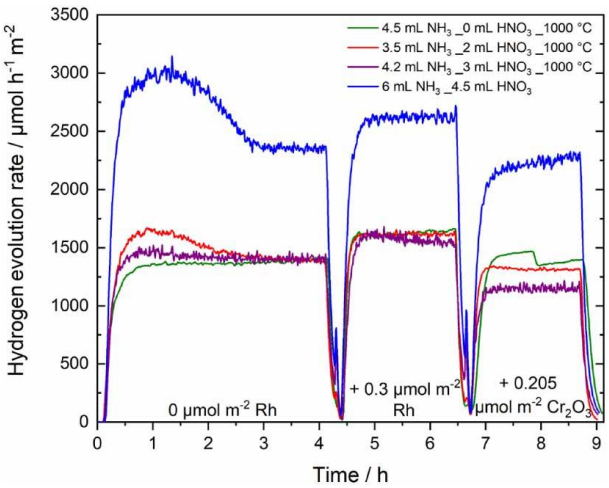

Figure 8. *Hydrogen evolution curves during photodeposition experiments, normalized on absolute surface area.*

The non-calcined sample—with the smallest surface area and therefore the presumably smallest number of reaction sites—shows the highest activity per hour and surface area. The hydrogen evolution diminishes strongly from the non-calcined sample with 2360 μmol h^{-1} m^{-2} to the calcined samples, which altogether show a highly similar evolution rate of ~ 1380 μmol $h^{-1}m^{-2}$.

These results correlate with the obtained results from the Rietveld refinements. The non-calcined sample has, with 11.7% of $Ba_3Ta_5O_{15}$ and 12.1% of $BaTa_2O_6$, the highest fraction of by-phases. The overall amount of by-phases in the other samples are in the range of 5.8% up to 11%. The nearly doubled amount of evolved hydrogen therefore

correlates with the amount of by-phases, showing the positive effect of heterojunctions in photocatalytic hydrogen evolution.

For later overall water splitting experiments, a Rh-Cr_2O_3 co-catalyst was photodeposited on the heterojunctions. The enhancement of the stirring speed during the addition of co-catalyst solution is the reason for the two peaks in the hydrogen evolution rates in figure 8. A quite low activity enhancement of all samples after addition of 0.3 μmol m^{-2} Rh co-catalyst is detected, which was already shown before and can be explained by the greater impact of heterojunction formation on charge carrier separation than Rh co-catalyst decoration [27]. As expected, the photodeposition of Cr_2O_3 results in a decrease of photocatalytic activity. Exemplarily, TEM images of sample prepared with 2 ml nitric acid were recorded and show the photodeposited Rh-Cr_2O_3 co-catalyst (figure S4). Additional detection of Rh and Cr in XPS was impossible (not shown) with the small amounts of co-catalyst deposited in this work [22].

All samples were characterized after photodeposition (figure S5): XRD characterization (figure S5(a)) reveals no changes in the crystal structure of all samples, diffuse reflectance UV/vis spectra show no changes in the band gaps (figure S5(b), table S2). Small changes in the DRIFT spectra (figure S5(c)) can be seen. The bands for carbonates and nitrates are lower in intensity after photodeposition for all samples. Parts of the residual barium carbonate and barium nitrate from synthesis dissolve during the photocatalysis. Additionally, bands of organic residues from the photodeposition process are visible. Raman spectra (figure S5(d)) are comparable to the spectra before photodeposition.

3.2.2. Overall water splitting results

Overall water splitting experiments were performed with the Rh-Cr_2O_3 decorated heterojunctions (figure S6). All prepared samples show activity in overall water splitting experiments with typical curve characteristics shown before [22]. The strong peak in the hydrogen evolution at the beginning of the measurements is due to organic residues in the samples, which are still present after photodeposition experiments as the DRIFT spectra revealed for all samples (figure S5(c)). The additional detection of carbon dioxide evolution in the beginning of the overall water splitting experiments verifies this fact, as it shows also a strong peak at the beginning of the curves. After nearly all residual carbonate is oxidized,

the evolution of carbon dioxide nearly stops and the water splitting reaction starts, as also indicated by the increase in oxygen evolution.

All samples show a hydrogen and oxygen evolution with ratios larger than 2:1, which can be explained still by residual carbonates, as the carbon dioxide evolution never stops completely. The hydrogen evolution varies from 112 μmol h^{-1} for the most active sample prepared with 3.5 ml of ammonia solution and 2 ml nitric acid to 55 μmol h^{-1} for the sample prepared without nitric acid (figure S6). The non-calcined sample shows again a comparable activity to the calcined samples with 92 μmol h^{-1}.

Again, it has to be taken into account that the surface area of the prepared samples varies and needs to be excluded to give a clear statement about the effect of the different amounts of by-phases in the synthesized samples. Normalizing the evolution rates with respect to absolute surface area again, the non-calcined sample offers the best activity with 368 μmol $h^{-1}m^{-2}$ hydrogen evolution rate (figure 9).

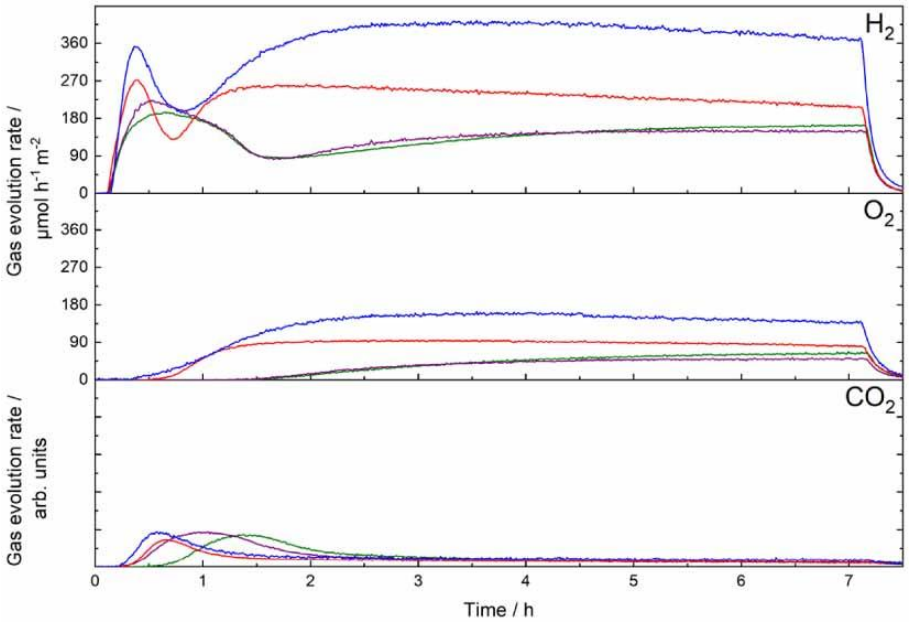

Figure 9. *Overall water splitting hydrogen, oxygen and carbon dioxide evolution curves during overall water splitting experiments, normalized on absolute surface area. Colour code is identical to figure 8.*

The activity of the samples in overall water splitting correlates with the amount of $Ba_3Ta_5O_{15}$ in the synthesized composites. The higher the amount of $Ba_3Ta_5O_{15}$ estimated by Rietveld refinement, the better is the activity in overall water splitting. This clearly confirms the improved charge separation in $Ba_5Ta_4O_{15}$-$Ba_3Ta_5O_{15}$-$BaTa_2O_6$ heterojunctions.

Roughly calculated band position from literature [26, 27] confirm this, as the conduction band of $Ba_5Ta_4O_{15}$ is slightly more negative than the conduction band of $Ba_3Ta_5O_{15}$ and $BaTa_2O_6$. Therefore, the photoexcited electrons are transferred from the conduction band of $Ba_5Ta_4O_{15}$ to the conduction bands of $Ba_3Ta_5O_{15}$ and $BaTa_2O_6$ and recombination with the holes in $Ba_5Ta_4O_{15}$ is reduced. The improved charge carrier separation for the $Ba_5Ta_4O_{15}$-$Ba_3Ta_5O_{15}$ heterojunction was already shown by transient absorption measurements in the literature [28]. A characterization of all samples with XRD, Raman, DRIFT, and UV–Vis after overall water splitting experiments reveals no changes in these samples (figure S7). The DRIFT spectra still show bands of organic residues, carbonates and nitrates after the overall water splitting experiments. The bands for carbonates and nitrates show only very small decrease compared to measurements before the overall water splitting. Most intense reduction of these bands can be seen in case of the non-calcined sample.

4. Conclusion

The $Ba_5Ta_4O_{15}$-$Ba_3Ta_5O_{15}$-$BaTa_2O_6$ heterojunction was prepared with a new and fast low temperature, energy efficient synthesis under ambient pressure conditions without further need of calcination. The photocatalytic activity of this non-calcined material was comparable or even better in hydrogen production without any co-catalyst and in overall water splitting after Rh-Cr_2O_3 deposition compared to samples prepared with an additional calcination step. In times of ever-growing energy demand, this energy efficient fast synthesis could be a new way for the synthesis of other crystalline and defined semiconductor materials without diminishing the photocatalytic activity.

Acknowledgments

We thank Dr. Jana Timm for Kr physisorption measurements, and for fruitful discussions. Furthermore, we would like to thank Christopher Simon (all University of Bayreuth, Germany) for TEM measurements. Additionally, we thank the BPI KeyLab Electron and Optical Microscopy for the possibility to use the Zeiss Leo 1530 and JEOL JEM-2200FS.

References

[1] Osterloh F E 2008 *Chem. Mater.* **20** 35–54
[2] Kudo A and Miseki Y 2009 *Chem. Soc. Rev.* **38** 253–78
[3] Chen X, Shen S, Guo L and Mao S S 2010 *Chem. Rev.* **110** 6503–70
[4] Kubacka A, Fern´andez-García M and Col´on G 2012 *Chem. Rev.* **112** 1555–614
[5] Ismail A A and Bahnemann D W 2014 *Sol. Energy Mater. Sol. Cells* **128** 85–101
[6] Harumi O, Kiyoung K, Asuka K, Ikuharu T, Hirotaka F, Yoshihisa S, Hayao I, Takako M and Kenji T 2005 *Chem. Lett.* **34** 822–3
[7] Yoshioka K, Petrykin V, Kakihana M, Kato H and Kudo A 2005 *J. Catal.* **232** 102–7
[8] Miseki Y, Kato H and Kudo A 2006 *Chem. Lett.* **35** 1052–3
[9] Miseki Y, Kato H and Kudo A 2009 *Energy Environ. Sci.* **2** 306–14
[10] Wu D, Zhang X, Jing Y, Zhao X and Zhou Z 2016 *Nano Energy* **28** 390–6
[11] Kim J, Hwang D W, Kim H G, Bae S W, Lee J S, Li W and Oh S H 2005 *Top. Catal.* **35** 295–303
[12] Mukherji A, Sun C, Smith S C, Lu G Q and Wang L 2011 *J. Phys. Chem.* C **115** 15674–8
[13] Hojamberdiev M, Bekheet M F, Zahedi E, Wagata H, Vequizo J J M, Yamakata A, Yubuta K, Gurlo A, Domen K and Teshima K 2016 *Dalton. Trans.* **45** 12559–68
[14] Wang K, Wu X, Zhang G, Li J and Li Y 2018 *ACS Sustain. Chem. Eng.* **6** 6682–92
[15] Hua E, Liu G, Zhang G and Xu X 2018 *Dalton Trans.* **47** 4360–7
[16] Takanabe K and Domen K 2012 *ChemCatChem* **4** 1485–97
[17] Galasso F and Katz L 1961 *Acta Crystallogr.* **14** 647–50
[18] Yamada T, Murata Y, Wagata H, Yubuta K and Teshima K 2016 *Cryst. Growth Des.* **16** 3954–60
[19] Xu T G, Zhang C, Shao X, Wu K and Zhu Y F 2006 *Adv. Funct. Mater.* **16** 1599–607
[20] Xu D, Shi W, Xu C, Yang S, Bai H, Song C and Chen B 2016 *J. Mater. Res.* **31** 2640–8
[21] Hildebrandt N C, Soldat J and Marschall R 2015 *Small* **11** 2051–7
[22] Bloesser A, Voepel P, Loeh M O, Beyer A, Volz K and Marschall R 2018 *J. Mater. Chem.* A **6** 1971–8
[23] Bloesser A and Marschall R 2018 *ACS Appl. Energy Mater.* **1** 2520–5
[24] Huang J J, Hsiao Y J, Fang T H and Chen T H 2012 *J. Sol-Gel Sci. Technol.* **62** 75–78
[25] Hsiao Y J, Chang Y H, Chang Y S and Fang T H 2007 *J. Am. Ceram. Soc.* **90** 2287–90
[26] Marschall R, Soldat J and Wark M 2013 *Photochem. Photobiol. Sci.* **12** 671–7
[27] Soldat J, Marschall R and Wark M 2014 *Chem. Sci.* **5** 3746–52
[28] Schneider J, Nikitin K, Wark M, Bahnemann D W and Marschall R 2016 *Phys. Chem. Chem. Phys.* **18** 10719–26
[29] Feger C R and Ziebarth R P 1995 *Chem. Mater.* **7** 373–8
[30] Anastas P and Eghbali N 2010 *Chem. Soc. Rev.* **39** 301–12
[31] Rodríguez-Carvajal J 1993 *Phys. B: Phys. Condens. Matter.* **192** 55–69
[32] Thompson P, Cox D E and Hastings J B 1987 *J. Appl. Cryst.* **20** 79–83
[33] Ling C D, Avdeev M, Kharton V V, Yaremchenko A A, Macquart R B and Hoelzel M 2010 *Chem. Mater.* **22** 532–40
[34] Galasso F, Layden G and Ganung G 1968 *Mater. Res. Bull.* **3** 397–407
[35] Li Y, Xue L, Fan L and Yan Y 2009 *J. Alloys Compd.* **478** 493–7
[36] Yue Z, Zhou J, Li L, Zhang H and Gui Z 2000 *J. Magn. Magn. Mater.* **208** 55–60
[37] Ge L, Zhou W, Ran R, Shao Z and Liu S 2008 *J. Alloys Compd.* **450** 338–47

[38] Kho Y K, Iwase A, Teoh W Y, M¨adler L, Kudo A and Amal R 2010 *J. Phys. Chem.* C **114** 2821–9
[39] Kemmler-Sack S, Treiber U and Fadini A 1979 *Z. Anorg. Allg. Chem.* **453** 157–62
[40] Massa N E, Pagola S, Carbonio R E, Alonso J A, Rasines I, Polla G and Leyva G 1996 *Proc. SPIE Spectrosc. Stud. Supercond*. **2696** 302–12
[41] Repelin Y, Husson E, Dao N Q and Brusset H 1980 *Mater. Res. Bull.* **15** 985–93
[42] Kato H and Kudo A 1998 *Chem. Phys. Lett.* **295** 487–92
[43] Lee J, Lu W D and Kioupakis E 2017 *Nanoscale* **9** 1120–7

6.2 Supporting Information

Supplementary information to

Fast low temperature synthesis of layered perovskite heterojunctions for overall water splitting

Anja Hofmann, Morten Weiss, and Roland Marschall*

Department of Chemistry, University of Bayreuth, 95447 Bayreuth, Germany

*E-mail: roland.marschall@uni-bayreuth.de

***Table 1**: Peak positions of phases in powder precursors prepared with 4.2 mL NH_3 and 3.5 mL NH_3. Used reference patterns are $Ba_5Ta_4O_{15}$ (JCPDS 72-0631), $Ba(NO_3)_2$ (COD 153-2290), $Ba_3Ta_5O_{15}$ (JCPDS 83-0713), and $BaTa_2O_6$ (JCPDS 20-0146).*

Sample	2 Θ / °	(hkl) phase
4.2 mL NH_3_3 mL HNO_3 /	15.58 / 15.59	(002) $Ba_5Ta_4O_{15}$
3.5 mL NH_3_2 mL HNO_3	23.34 / 23.34	(012) $Ba_5Ta_4O_{15}$
	29.10 / 29.12	(013) $Ba_5Ta_4O_{15}$
	31.09 / 31.11	(110) $Ba_5Ta_4O_{15}$
	35.55 / 35.65	(104) $Ba_5Ta_4O_{15}$
	43.00 / 43.02	(203) $Ba_5Ta_4O_{15}$
	44.09 / 44.09	(114) $Ba_5Ta_4O_{15}$
	47.88 / 47.82	(024) $Ba_5Ta_4O_{15}$
	50.00 / 49.94	(106) $Ba_5Ta_4O_{15}$
	50.12 / 50.12	(115) $Ba_5Ta_4O_{15}$
	50.79 / 50.79	(122) $Ba_5Ta_4O_{15}$
	53.91 / 53.94	(123) $Ba_5Ta_4O_{15}$
	55.10 / 55.10	(300) $Ba_5Ta_4O_{15}$
	58.01 / 57.95	(214) $Ba_5Ta_4O_{15}$

	59.95 / 59.95	(026) $Ba_5Ta_4O_{15}$
	64.49 / 64.56	(220) $Ba_5Ta_4O_{15}$
	68.92 / 68.86	(216) $Ba_5Ta_4O_{15}$
	69.11 / 69.05	(305) $Ba_5Ta_4O_{15}$
	72.21 / 72.32	(313) $Ba_5Ta_4O_{15}$
	73.17 / 72.93	(224) $Ba_5Ta_4O_{15}$
4.2 mL NH_3_3 mL HNO_3	19.16 / 19.16	(111) $Ba(NO_3)_2$
3.5 mL NH_3_2 mL HNO_3	22.15 / 22.12	(020) $Ba(NO_3)_2$
	24.79 / 24.76	(021) $Ba(NO_3)_2$
	27.12 / 27.12	(121) $Ba(NO_3)_2$
	36.94 / 36.94	(131) $Ba(NO_3)_2$
	38.64 / 38.68	(222) $Ba(NO_3)_2$
	44.85 / 44.85	(040) $Ba(NO_3)_2$
	49.12 / 49.08	(133) $Ba(NO_3)_2$
	50.44 / 50.44	(024) $Ba(NO_3)_2$
	55.63 / 55.63	(242) $Ba(NO_3)_2$
	59.31 / 59.31	(151) $Ba(NO_3)_2$
	65.14 / 65.11	(044) $Ba(NO_3)_2$
	68.51 / 68.47	(153) $Ba(NO_3)_2$
	69.62 / 69.58	(244) $Ba(NO_3)_2$
	73.96 / 74.03	(062) $Ba(NO_3)_2$
	77.12 / 77.16	(353) $Ba(NO_3)_2$
	78.18 / 78.27	(262) $Ba(NO_3)_2$
4.2 mL NH_3_3 mL HNO_3 /	22.55 / 22.59	(001) $Ba_3Ta_5O_{15}$
3.5 mL NH_3_2 mL HNO_3	25.75 / 25.65	(320) $Ba_3Ta_5O_{15}$
	27.70 / 27.79	(211) $Ba_3Ta_5O_{15}$
	31.97 / 31.97	(420) $Ba_3Ta_5O_{15}$
	34.62 / -	(321) $Ba_3Ta_5O_{15}$

	36.51 / -	(510) $Ba_3Ta_5O_{15}$
	41.95 / -	(530) $Ba_3Ta_5O_{15}$
	45.60 / -	(620) $Ba_3Ta_5O_{15}$
	45.99 / -	(002) $Ba_3Ta_5O_{15}$
	48.63 / 48.63	(630) $Ba_3Ta_5O_{15}$
	51.67 / 51.72	(312) $Ba_3Ta_5O_{15}$
	56.86 / 56.79	(711) $Ba_3Ta_5O_{15}$
	56.98 / 57.14	(422) $Ba_3Ta_5O_{15}$
	60.90 / -	(820) $Ba_3Ta_5O_{15}$
	66.72 / -	(622) $Ba_3Ta_5O_{15}$
	71.26 / -	(712) $Ba_3Ta_5O_{15}$
4.2 mL NH_3_3 mL HNO_3	17.55 / -	(020) $BaTa_2O_6$
3.5 mL NH_3_2 mL HNO_3	22.75 / 22.71	(220) $BaTa_2O_6$
	23.37 / 23.35	(310) $BaTa_2O_6$
	26.15 / -	(030) $BaTa_2O_6$
	27.66 / 27.55	(202) $BaTa_2O_6$
	29.17 / 29.18	(400) $BaTa_2O_6$
	29.30 / 29.31	(022) $BaTa_2O_6$
	30.07 / 30.19	(230) $BaTa_2O_6$
	34.11 / -	(420) $BaTa_2O_6$
	37.56 / 37.56	(510) $BaTa_2O_6$
	38.17 / 38.25	(203) $BaTa_2O_6$
	39.55 / 39.52	(023) $BaTa_2O_6$
	41.69 / 41.73	(303) $BaTa_2O_6$
	46.37 / -	(403) $BaTa_2O_6$
	47.00 / -	(531) $BaTa_2O_6$
	47.51 / -	(004) $BaTa_2O_6$
	51.55 / -	(540) $BaTa_2O_6$

	52.06 / 52.15	(700) $BaTa_2O_6$
	52.69 / 52.69	(304) $BaTa_2O_6$

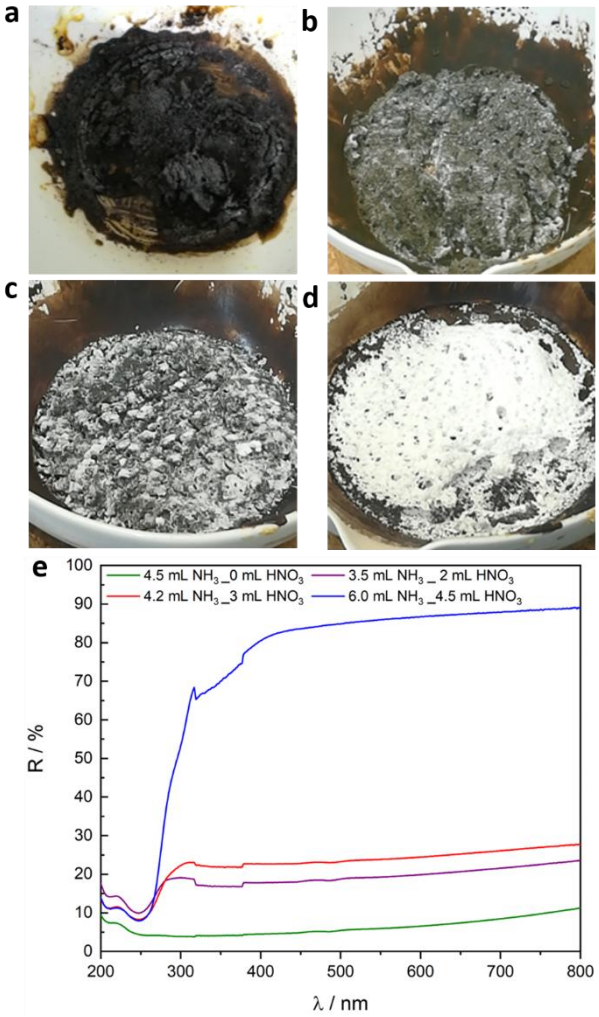

***Figure S 1**:(a-d) Images of synthesized powder precursors, synthesized with (a) 0 mL HNO_3, (b) 2 mL HNO_3, (c) 3 mL HNO_3, and (d) 4.5 mL HNO_3 and (e) reflection measurements of powder precursors, synthesized with different amounts of ammonia solution and concentrated nitric acid.*

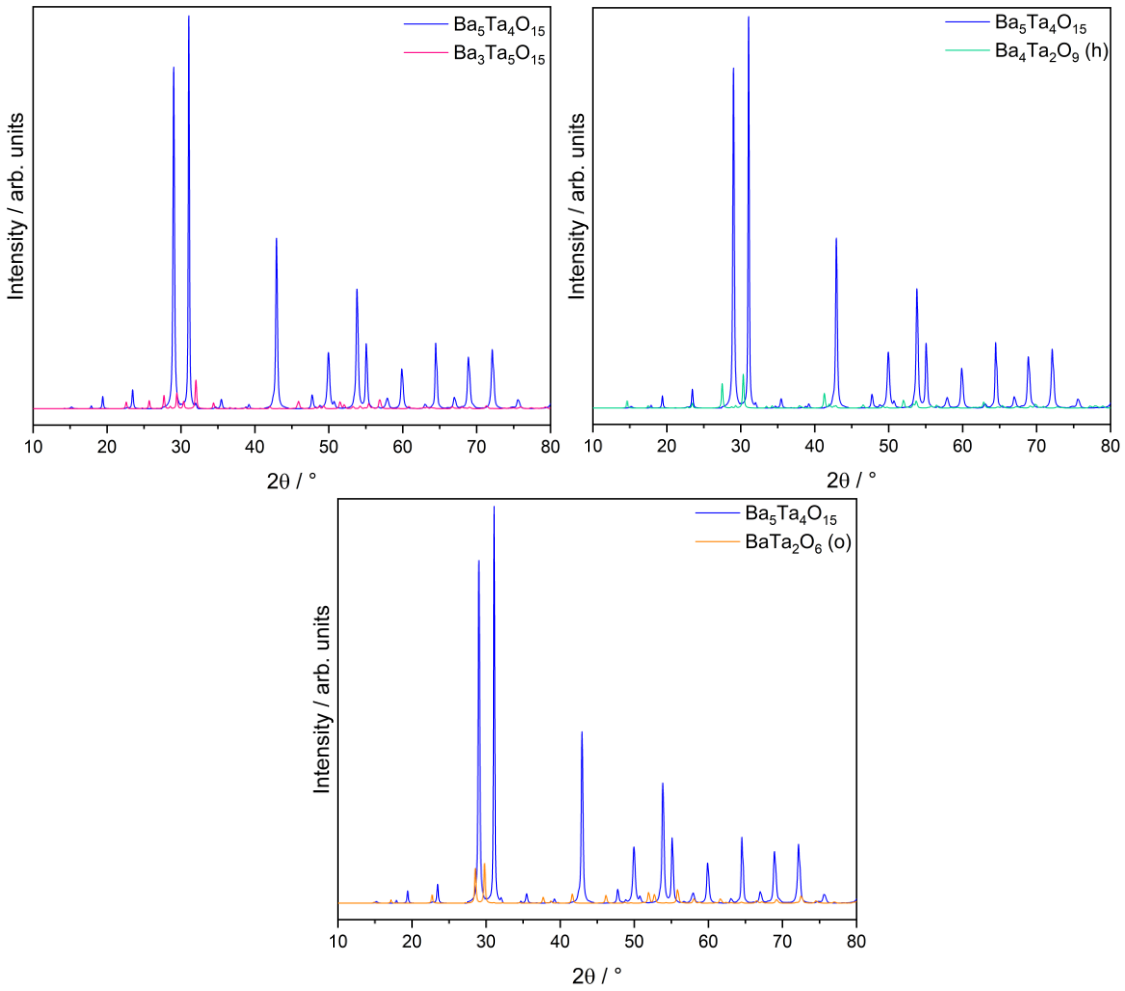

***Figure S 2**: Simulated XRD patterns of 90 wt.% $Ba_5Ta_4O_{15}$ with 10 wt.% $Ba_3Ta_5O_{15}$ (upper left), 10 wt.% $Ba_4Ta_2O_9$ (h) (upper-right) and 10 wt.% $BaTa_2O_6$ (o) (lower centre).*

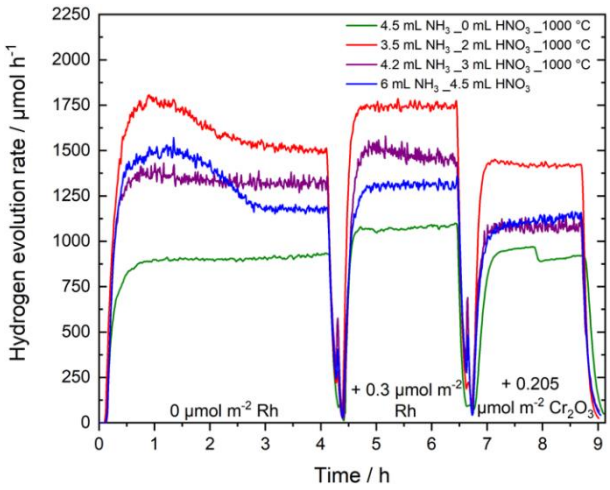

***Figure S 3**: Hydrogen evolution curves of 200 mg synthesized heterojunctions in water/methanol during photodeposition experiments.*

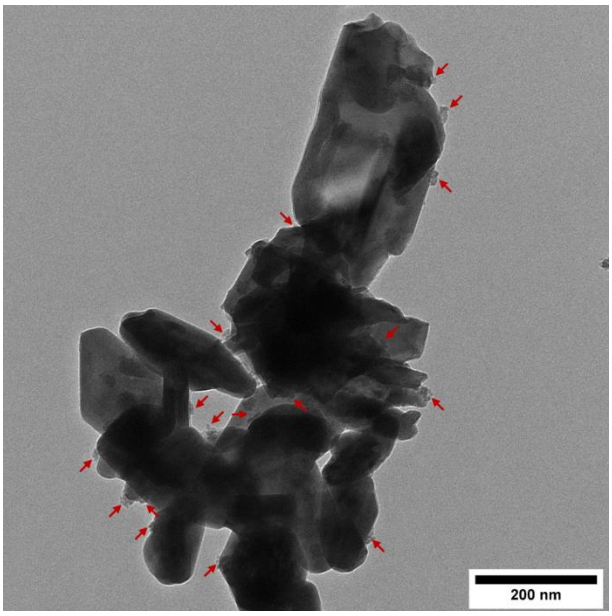

***Figure S 4**: TEM images of Rh-Cr_2O_3 co-catalyst on surface of photocatalyst prepared with 3.5 mL NH_3 and 2 mL HNO_3. Red arrows show areas with co-catalyst.*

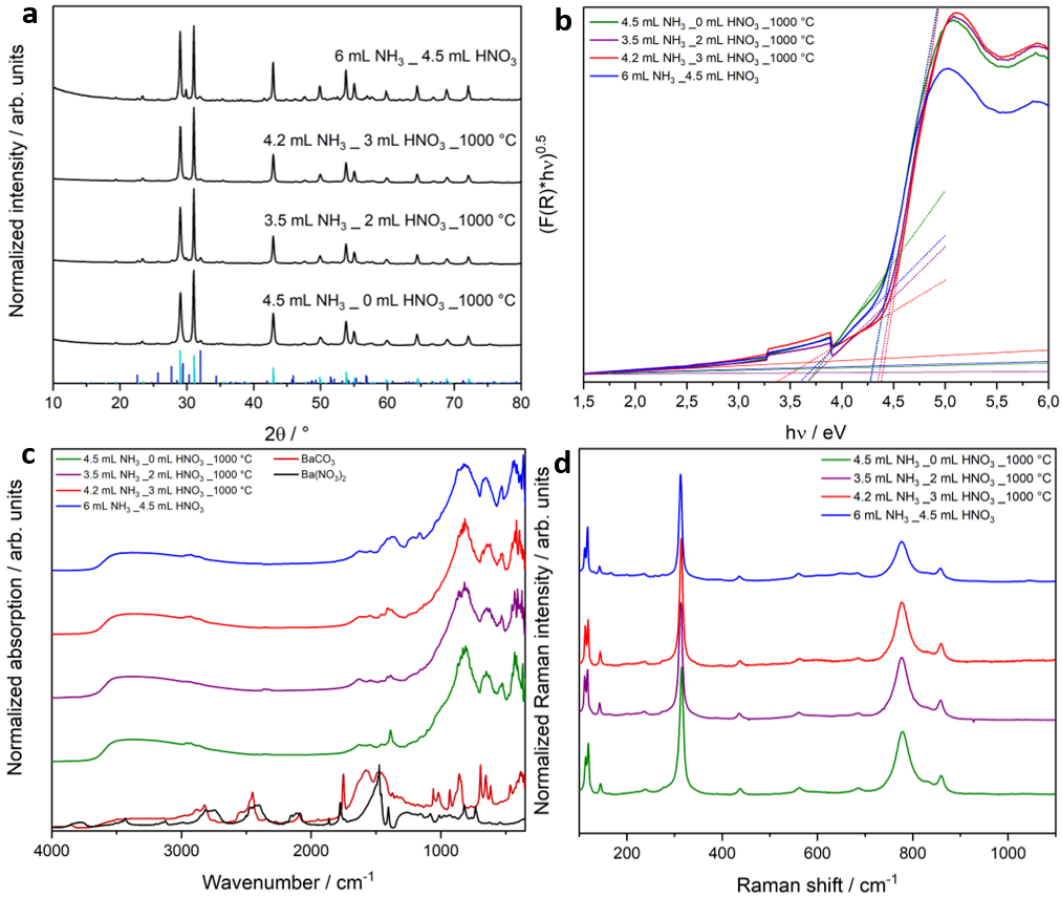

***Figure S 5**: (a) XRD patterns, (b) Tauc Plots,(c) DRIFT spectra, and (d) Raman spectra of samples after photodeposition experiments.*

***Table S 2**: Estimated band gaps after photodeposition experiments*.

Sample post photodeposition	Band gaps / eV
4.5 mL NH_3 _0 mL HNO_3	3.8 / 4.3
3.5 mL NH_3 _2 mL HNO_3	3.8 / 4.4
4.2 mL NH_3 _3 mL HNO_3	3.7 / 4.4
6 mL NH_3 _4.5 mL HNO_3	3.7 / 4.3

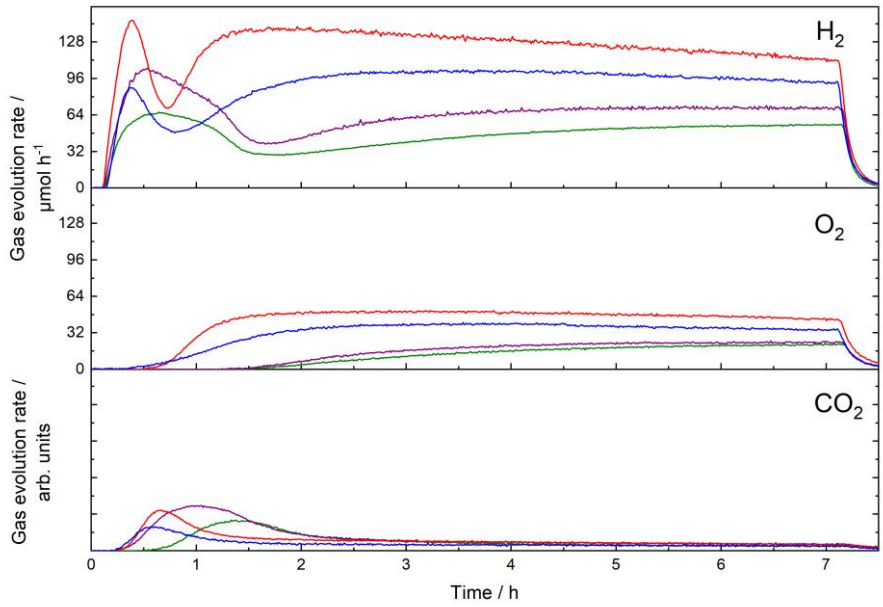

***Figure S 6**: Overall water splitting gas evolution rates for hydrogen, oxygen, and carbon dioxide using 100 mg of photodeposited heterojunctions. The color code is identical to **Figure S 3**.*

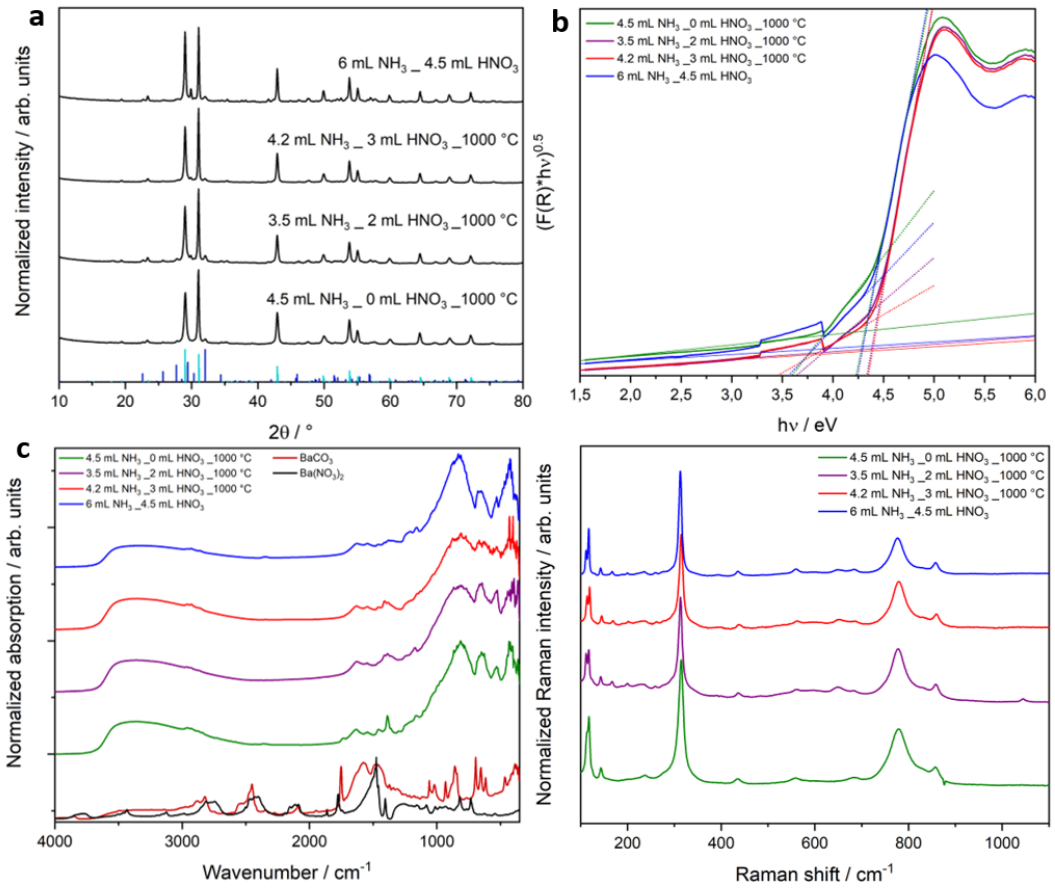

***Figure S 7**: (a) XRD patterns, (b) Tauc Plots,(c) DRIFT spectra, and (d) Raman spectra of samples after overall water splitting experiments.*

***Table S 4**: Estimated band gaps after overall water splitting experiments.*

Sample post overall water splitting	Band gaps / eV
4.5 mL NH_3 _0 mL HNO_3	3.9 / 4.3
3.5 mL NH_3 _2 mL HNO_3	3.9 / 4.4
4.2 mL NH_3 _3 mL HNO_3	3.8 / 4.4
6 mL NH_3 _4.5 mL HNO_3	3.8 / 4.3

7 Perovskite-Type Oxynitride Nanofibers Performing Photocatalytic Oxygen and Hydrogen Generation

7.1 Main Manuscript

Anja Hofmann, Morten Weiss, Jana Timm, Roland Marschall*

Citation Hofmann *et al Adv. Mater. Interfaces* 2021, *8*, 2100813

Author affiliations Department of Chemistry University of Bayreuth Universitätsstraße 30, 95447 Bayreuth, Germany

Author emails roland.marschall@uni-bayreuth.de

https://doi.org/10.1002/admi.202100813

Abstract

$Ba_5Nb_4O_{15}$ nanofibers with tailored nanofiber diameters are prepared *via* electrospinning, and treated in ammonia gas to synthesize niobate oxynitride nanofibers. Most importantly, the nanofibers retain their fiber morphology during ammonolysis, and the nanofiber diameter of the converted fibers can be adjusted. Only a thorough characterization, including detailed Rietveld refinements, can reveal that the ammonolysis of $Ba_5Nb_4O_{15}$ results not only in $BaNbO_2N$, but also generates Ba_2NbO_3N as additional oxynitride phase. Such $BaNbO_2N$–Ba_2NbO_3N composite nanofibers with adjusted nanofiber diameters are applied in photocatalytic water oxidation and hydrogen generation. After decoration with $CoNbO_4$ or Pt cocatalyst, the materials show a diameter-dependent photocatalytic activity, respectively, with an optimum nanofiber diameter. The presented synthesis demonstrates a novel sol–gel-derived possibility for nanostructuring of oxynitrides, which can pave the way for new synthesis strategies of nanostructured complex oxynitrides.

1 Introduction

Due to ever-growing energy demand, research for generating renewable, clean hydrogen by using solar-light-induced water splitting becomes more important. The most crucial part

of an (solar-light driven) efficient water splitting process is a suitable catalyst/cocatalyst system: any photocatalytically active material is highly dependent on band positions and optical bandgap. First, the band positions of the semiconducting photocatalyst have to be suitable for water splitting. Further, to achieve a high solar-to-hydrogen efficiency a semiconductor has to absorb a wide range of visible light. Perovskite-oxynitrides $AB(O,N)_3$ (A = La, Ca, Sr, or Ba; B = Ti, Ta, Nb) are fulfilling these requirements.[1-4] $BaNbO_2N$ ($Pm3m$),[5, 6] for example, shows superior visible-light absorption up to 740 nm, corresponding to a bandgap of 1.7 to 1.8 eV, compared to other perovskite oxynitrides, and suitable band positions for water oxidation and reduction.[7-11] For comparison, other oxynitrides such as $SrNbO_2N$ with an absorption edge at 700 nm,[1] $BaTaO_2N$ at 660 nm,[4] $LaTiO_2N$ at 600 nm,[2] and $CaTaO_2N$ at 510 nm[3] show less pronounced visible-light absorption. This makes $BaNbO_2N$ a very interesting semiconductor material for visible-light photocatalytic and photoelectrochemical water splitting.[8-10, 12-14] $BaNbO_2N$ can be synthesized by different synthesis routes, solid-state reaction route by ammonolysis of a mixture of $BaCO_3$ and Nb_2O_5 is one prominent example.[5, 6, 13, 15, 16] Odahara *et al.* synthesized $BaNbO_2N$ by an intense exothermic and explosive reaction without the need of a nitridation step.[17] Other routes include an additional step with the synthesis of an oxide precursor, such as $BaNbO_3$ or the layered perovskite $Ba_5Nb_4O_{15}$ or an amorphous oxide precursor, which is subsequently nitrided.[7, 9-14, 18, 19] Hojamberdiev *et al.* prepared $BaNbO_2N$ crystals *via* a NH_3-assisted flux-growth approach by ammonolysis of a mixture of $BaCO_3$ and Nb_2O_5 and KCl.[8] Hisatomi *et al.* showed a faster ammonia flow and a higher barium to niobium ratio in the precursor results in a suppressed niobium reduction.[13] Furthermore, they reported an increase in the photocatalytic activity by using precursors prepared *via* a soft chemistry route, compared to a mixture of $BaCO_3$ and Nb_2O_5 due to a lower nitridation temperature.[13] A nitridation of size-controlled $Ba_5Nb_4O_{15}$ crystals in micrometer size was reported by Yamada *et al.* and they assumed that the differences in photocatalytic activity can be assigned to competitive effects of crystallinity and anion deficiency in the prepared size-controlled $BaNbO_2N$.[10]

All aforementioned syntheses—excluding the explosive reaction—include a nitridation step at high temperature (1023 to 1273 K), which often leads to micrometer-sized particles and therefore small surface areas with resulting poor catalyst-reactant contact-areas. The

catalyst surface could be increased by nanostructuring. The already mentioned, necessary high temperatures hamper the classical nanostructuring routes *via* surfactants or templated sol–gel chemistry. An advanced technique to overcome the problem of rapid crystal growth is electrospinning, which is very often used in polymer science, but is also suitable for the preparation of metal oxides such as $Ba_5Nb_4O_{15}$ and $Ba_5Ta_4O_{15}$.[20, 21] The advantage of using electrospinning is the resulting fiber morphology after the spinning process. Even the required crystallization preserves the fiber morphology.[20] Furthermore, it is possible to synthesize metal oxides such as $Ba_5Nb_4O_{15}$ with a reduced temperature (800–900 °C) compared to the solid-state reaction synthesis (up to 1500 °C).[20, 22] Moreover, the nanofiber diameter of the resulting oxide can be tuned by adjusting the viscosity of the spinning solution, as reported for $Ba_5Ta_4O_{15}$ nanofibers and $Ba_5Ta_4O_{15}$–$Ba_3Ta_5O_{15}$ composite nanofibers.[21, 23] Bloesser *et al.* were able to show a nanofiber diameter dependent activity in photocatalytic overall water splitting for $Ba_5Ta_4O_{15}$ with an optimum nanofiber diameter of 161 nm.[21]

Here, we present the first study to prepare diameter-controlled oxynitride nanofibers of $BaNbO_2N$ by electrospinning. We combine the reported positive effect of a Ba/Nb ratio >1[13] with the positive effect of the electrospinning to boost the photocatalytic activity of $BaNbO_2N$. Fully crystalline $Ba_5Nb_4O_{15}$ nanofibers with adjusted diameters are synthesized *via* sol–gel electrospinning, and converted to corresponding $BaNbO_2N$ nanofibers. Morphology and detailed bulk and surface analysis of the prepared $BaNbO_2N$ samples are provided, showing the formation of a Ba_2NbO_3N–$BaNbO_2N$ composite. The nanofiber morphology and diameter retain nicely during the nitridation of the $Ba_5Nb_4O_{15}$ nanofibers. Diameter-dependent hydrogen and oxygen evolution results are presented, and overall water splitting activity is investigated on the most active sample.

2 Results and Discussion

2.1 Characterization

Scanning electron microscopy (SEM) images of the nitrided nanofibers (N-NFs) of different diameter are shown in **Figure** 1. All samples still exhibit the nanofiber morphology after the ammonolysis of $Ba_5Nb_4O_{15}$ precursor nanofibers. Figure S1 of the Supporting Information shows for one exemplary sample that the main nanofiber morphology stays the same

during ammonolysis, but the sheet-like structure of the particles in layered perovskite $Ba_5Nb_4O_{15}$ nanofibers changes to smaller particles during the conversion to $BaNbO_2N$, which was already reported before for La_2TiO_2N.[10, 24] This proves that the nanofiber morphology is retained during the conversion of the $Ba_5Nb_4O_{15}$ precursor nanofibers. Similar results are known for hydrothermally grown $SrTaO_2N$.[25] Additionally, the nanofiber diameter of our obtained N-NF can be adjusted by tailoring the diameter of the $Ba_5Nb_4O_{15}$ precursor nanofibers. The diameter of the N-NF increases from 135 up to 213 nm with an increasing amount of polymer used for the electrospinning of the $Ba_5Nb_4O_{15}$ precursor nanofibers.

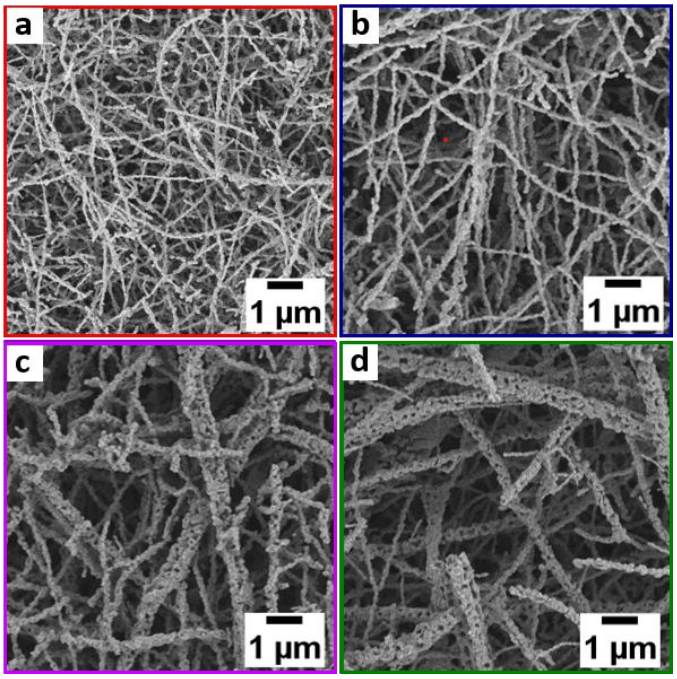

Figure 1 *SEM images of N-NF with nanofiber diameters of a) 135 nm, b) 156 nm, c) 194 nm, and d) 213 nm.*

Figure S2 of the Supporting Information displays the corresponding nanofiber diameter distributions for the investigated samples. Krypton physisorption measurements were performed to gain information about the specific Brunauer–Emmet–Teller (BET) surface area of the N-NF for photocatalytic characterization measurements. **Table** 1 gives an overview of the nanofiber diameters and the BET surface areas depending on the amount of polyvinylpyrrolidone (PVP) used in the electrospinning process of the precursor $Ba_5Nb_4O_{15}$ nanofibers. The BET surface areas for all four N-NF samples are overall comparable with slightly increasing values upon decreasing nanofiber diameter of 6.9 up to 8.1 $m^2 g^{-1}$.

***Table 1**. Nanofiber diameter and BET surface area of $Ba_5Nb_4O_{15}$ nanofibers and converted N-NF depending on the amount of PVP used for electrospinning*

Amount of PVP [mg]	Average nanofiber diameter of $Ba_5Nb_4O_{15}$ [nm]	Average nanofiber diameter of N-NF [nm]	BET surface area [$m^2\ g^{-1}$]
200	109 ± 39	135 ± 44[a)]	8.2[b)]
300	157 ± 58	156 ± 61[a)]	7.1[b)]
400	169 ± 80	194 ± 109[a)]	7.0[b)]
500	209 ± 81	213 ± 121[a)]	6.9[b)]

[a)]Diameters of every N-NF sample measured and distribution estimated to get average diameter of mixed sample; [b)]Mixed sample measured with Kr physisorption.

For the investigation of the bulk material, detailed X-ray diffraction (XRD) analysis was performed. XRD patterns of N-NF directly after ammonolysis are shown in **Figure** 2. No reflections belonging to the precursor nanofibers $Ba_5Nb_4O_{15}$ are present in all four nanofiber samples, therefore suggesting the successful conversion to phase pure $BaNbO_2N$. Furthermore, no reflections attributable to barium oxide are present in the XRD patterns, which is why an additional washing step was not performed, which is mostly done in other reported syntheses to remove excess BaO.[8-12]

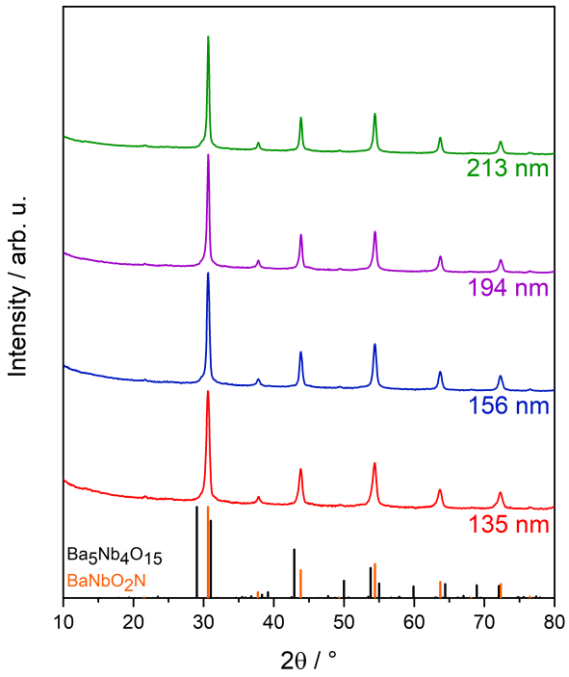

***Figure 2** XRD patterns of N-NF with nanofiber diameter of 135 nm (red), 156 nm (blue), 194 nm (purple), and 213 nm (green). Calculated reference pattern of $Ba_5Nb_4O_{15}$ (black, COD 96-230-0161) and $BaNbO_2N$ (orange, COD 01-078-1456 and Fujii et al.[6]) are shown for comparison.*

At careful observation, the XRD reflections of $BaNbO_2N$ exhibit asymmetric tailing toward lower diffraction angles, which has been ascribed to possible defect formation within the perovskite lattice.[26] However, a single-phase Rietveld refinement of $BaNbO_2N$ (with asymmetry assumption) is not satisfactory, as can be seen in Figure S3 of the Supporting Information. Additionally, Suemoto *et al.* showed the emergence of Sr_2TaO_3N for $SrTaO_2N$—which is isostructural with $BaNbO_2N$—if the Sr/Ta ratio is ≥1.2.[26] Ba_2NbO_3N was therefore included within the Rietveld refinements resulting in satisfactory quality of the data, although Rietveld refinements are still complicated due to reflection broadening and closely overlapping reflections, which is shown in Figure S4 of the Supporting Information. Quantitative analysis of a selected sample directly after ammonolysis in **Figure 3**—nanofibers with 156 nm diameter—shows $BaNbO_2N$ as majority phase (77.5 wt%) and 22.6 wt% Ba_2NbO_3N as secondary phase. This is a very important result, since at a first glance no by-phase can be observed in the XRD patterns in Figure 2. Such detailed phase analysis shall be very important for other ammonolysis reactions and oxynitride formations as well.

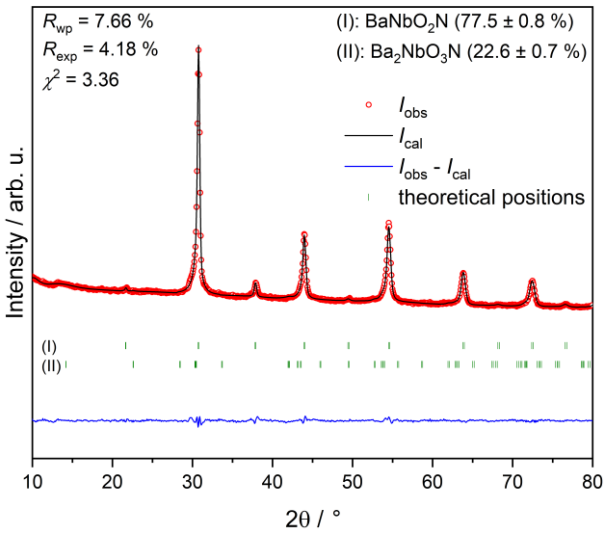

Figure 3 *Rietveld refinement of N-NF with a diameter of 156 nm directly after ammonolysis.*

Selected area electron diffraction (SAED) and visible lattice planes in **Figure 4** confirm the formation of a highly crystalline fiber sample. Due to very similar lattice planes of $BaNbO_2N$ and Ba_2NbO_3N it is not possible to assign them to one of the two oxynitrides unambiguously. Stacking faults in the $BaNbO_2N$–Ba_2NbO_3N nanofibers, which were shown by Suemoto *et al.*,[26] cannot be found.

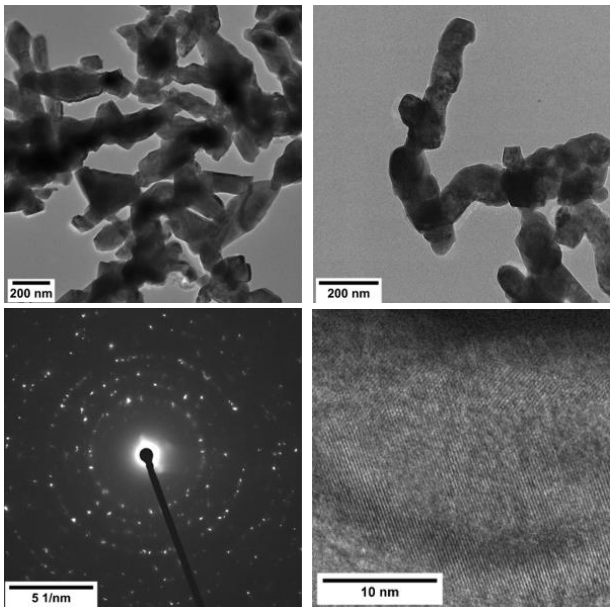

Figure 4 *Transmission electron microscopy (TEM) images and SAED pattern of N-NF with 135 nm diameter.*

XRD analysis of the N-NF samples stored for a few weeks shows additional reflections in the XRD pattern, which can be assigned to $BaCO_3$ (Figure S5, Supporting Information). Rietveld refinements of these samples in **Figure** 5 show amounts of 4–7 wt% of $BaCO_3$ and additionally, similar (71–78 wt%) amounts of $BaNbO_2N$, whereas the amounts of Ba_2NbO_3N have been decreasing (16–23 wt%) compared to samples measured directly after ammonolysis. We therefore consider it highly likely that it is indeed Ba_2NbO_3N and not the main phase $BaNbO_2N$, which is decomposing here with time. Suemoto *et al.* showed the decomposition of isostructural Sr_2TaO_3N toward $SrCO_3$ after exposure to humidity at ambient conditions,[26] which also corroborates the presence of Ba_2NbO_3N in samples here. Crystallite sizes for $BaNbO_2N$ in the four mixed sample batches range from 25 to 35 nm, as compared to 5–7 nm for Ba_2NbO_3N and 25–28 nm for $BaCO_3$ and can be considered highly consistent.

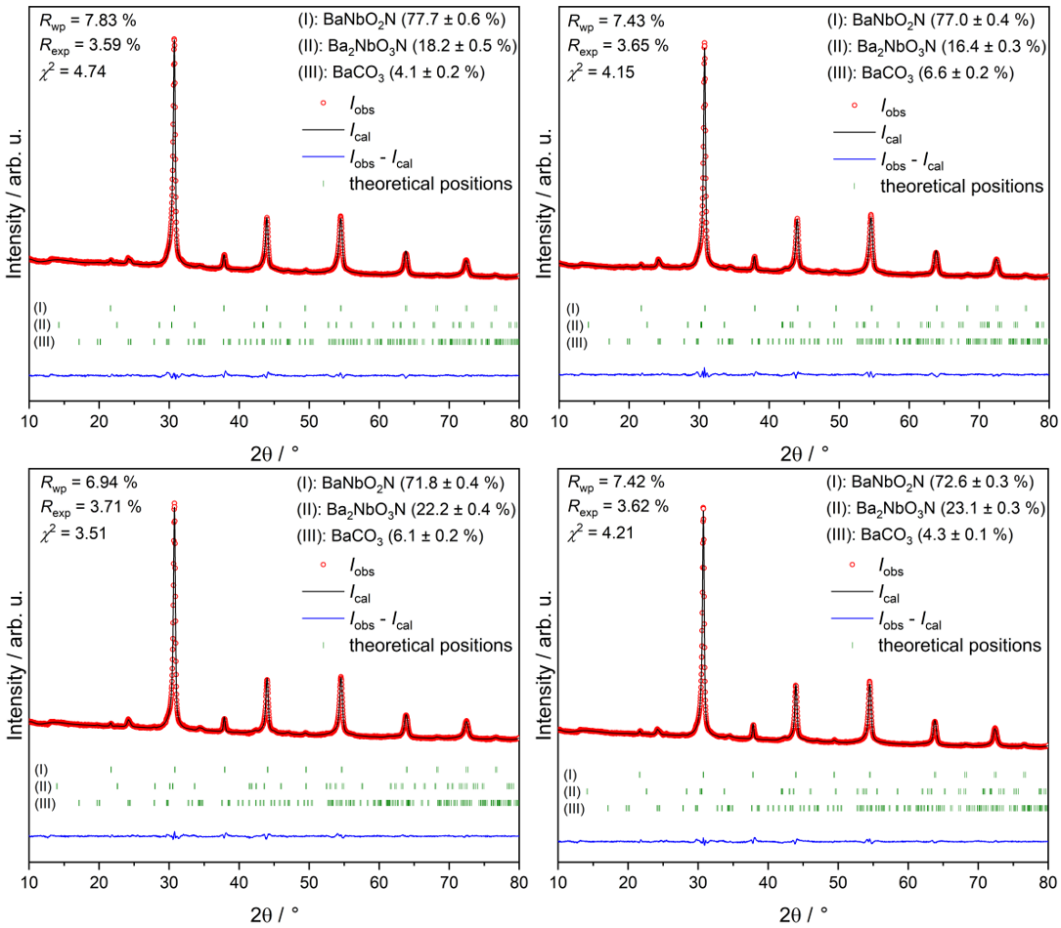

Figure 5 *Rietveld refinements of all four stored N-NF samples with nanofiber diameter of (upper left) 135 nm, (upper right) 156 nm, (lower left) 194 nm, and (lower right) 213 nm.*

The comparison of diffuse reflectance infrared Fourier transform (DRIFT) spectra of N-NF directly after the ammonolysis and after storage shows the formation of carbonate species in the samples after storage, which are not present in the samples directly after ammonolysis (Figure S6, Supporting Information). This further underlines the results from XRD analysis.

X-ray photoelectron spectroscopy (XPS) analysis was performed on the thinnest nanofibers stored for a few weeks after ammonolysis. Survey XPS data in Figure S7 of the Supporting Information show a surface elemental distribution of 13.5 at% Ba, 10.9 at% Nb, 41.5 at% O, 5.4 at% N, and 28.6 at% C. No other impurities besides the always-present adventitious carbon could be detected. Compared to the nominal stoichiometry, the surface has a slight Ba excess and a severe N deficiency and O excess, respectively.

Energy-dispersive X-ray (EDX) analysis gives Ba/Nb ratios in the same range of 1.23 to 1.26, which is highly similar to the Ba/Nb ratio as in the $Ba_5Nb_4O_{15}$ precursor nanofibers

with 1.25. The determined Ba excess further underlines the result of the XRD analysis. A slight Ba excess is expected if Ba_2NbO_3N is formed as by-product and no Ba is evaporated during the ammonolysis process.

Elemental analysis was performed for determination of the exact nitrogen amount in the converted nanofiber samples. The nitrogen content of all four N-NF samples stored is in a comparable range of 3.23 to 3.39 wt%. The theoretical value of nitrogen in the samples was calculated by taking the phase composition obtained by quantitative Rietveld analysis (Figure 5) into account, leading to a theoretical value of 4.4 to 4.5 wt%, the samples showing a slight nitrogen deficiency. The nitrogen deficiency—corresponding with slight oxygen excess—can be explained by surface oxidation shown by XPS analysis (**Figure** 6): the Nb 3d signals are highly complex with four different components with binding energies (for Nb $3d_{5/2}$) of 206.3 eV (32.2%), 205.1 eV (64.3%), 203.3 eV (1.6%), and 202.0 eV (2.0%). The first (206.3 eV) can be ascribed to Nb(V) oxides.[27, 28]

The second peak (205.1 eV) has sometimes also been ascribed to a not specified Nb^{4+} state.[11] However, the values in the literature reported for Nb^{4+}, *i.e.*, niobium(IV) oxide NbO_2 are at higher binding energies than the herein measured value.[28-31] We thus attribute this signal to $BaNbO_2N$, since the measured value is highly similar to those reported for niobium oxynitride NbON.[32-34]

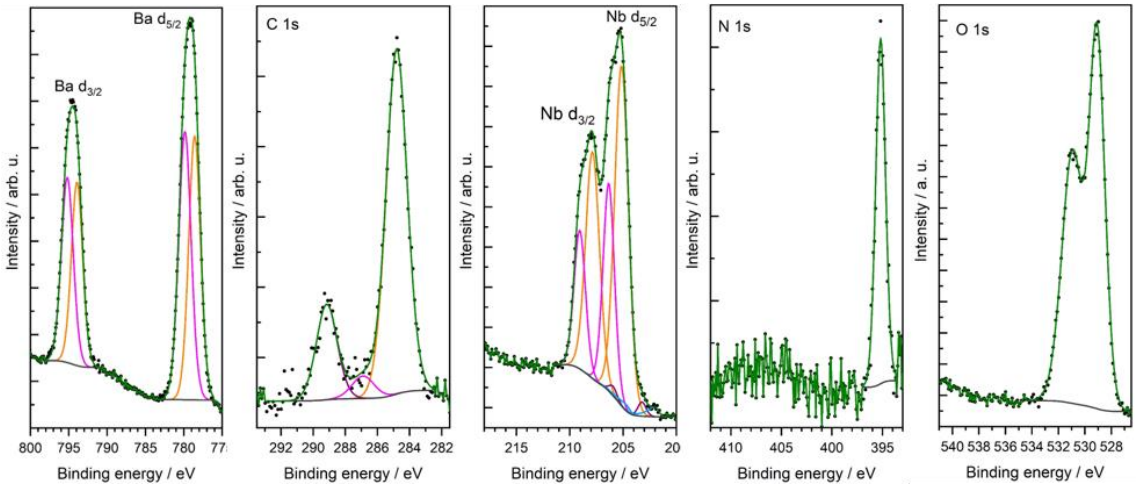

Figure 6 *High-resolution XP spectra of Ba 3d signals (left), C 1s signals (middle left), Nb 3d signals (middle), N 1s signal (middle right), and O 1s signals (right) for nanofiber sample with diameter of 135 nm after storage. Black circles indicate the measurements points, blue line the background, green line the envelope curve, and orange, pink, light blue, and purple lines the fitting curves.*

The third and far smaller component (203.3 eV) can be ascribed to niobium nitride NbN,[27, 32, 33, 35] which seems to form in a small amount during ammonolysis. The fourth component (202.0 eV) can be assigned to elemental Nb, which is likewise formed.[27, 28, 35, 36] Although the oxynitride component is by far the most prevalent, the existence of a substantial Nb(V) oxide component indicates that the oxynitride is unstable and oxidized, which would also explain the N deficiency inferred from the survey spectra.

High-resolution XP spectra of the Ba 3d region show two separate peaks for both $3d_{5/2}$ and $3d_{3/2}$ signals, the respective binding energies are 778.2 and 779.9 eV for the $3d_{5/2}$ signal. The first can be ascribed to mixed Ba oxides, whereas the latter is typical for $BaCO_3$,[27, 37] which has been observed before on Ba containing perovskites.[37] The corresponding C 1s signal has been observed at 289.2 eV, whereas the other C 1s peaks are typical for adventitious carbon.

The N 1s spectrum consists of a single signal at 395.2 eV, which is lower than normally observed for nitrides, but highly similar to reported binding energies for niobium oxynitride NbON and $BaNbO_2N$.[19, 27, 38]

The O 1s spectrum consists of minimum two different components but could be also fitted with up to six components. An unambiguous analysis is thus not possible as all fittings would be of good quality (not shown).

The temperature stability was further investigated by thermogravimetric analysis coupled with online mass spectrometry (TG-MS) in a temperature range of 200 to 1000 °C in synthetic air (Figure S8, Supporting Information): a slight mass loss can be observed up to 200 °C with an increase in the MS signal of H_2O (m/z = 18). Adsorbed water on the oxynitride surface desorbs in this temperature range. Afterward, the mass increases up to 600 °C, which can be assigned to the oxidation of the barium niobium oxynitride, followed by a stepwise decrease of the mass up to a temperature of 850 °C. A peak in the MS signal assigned to CO_2 (m/z = 44) is detected in the temperature range of 500 up to 800 °C, which can be assigned to the decomposition of the formed $BaCO_3$. The stepwise decrease of the mass is due to the release of nitrogen. This could not be detected *via* MS since synthetic air was used as carrier gas. The curve progression is in good agreement with TG-MS curves of $SrNbO_2N$ measured in an atmosphere with 20% oxygen.[39]

Optical properties were analyzed by diffuse reflectance measurements, which were converted to Kubelka–Munk spectra and Tauc plots for bandgap estimation (**Figure** 7). The conversion of $Ba_5Nb_4O_{15}$ nanofibers to $BaNbO_2N$–Ba_2NbO_3N nanofibers leads to a visible light absorption compared to UV light-only absorption for the precursor nanofibers. This corresponds to a decrease of the indirect bandgap from 3.9 eV for $Ba_5Nb_4O_{15}$ to ≈1.8 eV for the converted nanofiber composite samples. Since the resulting material consists of a composite, the term bandgap is not fully correct here, but the shift in the absorption edge by more than 2 eV is very prominent. All four samples exhibit absorption edges at 1.7 to 1.8 eV, which is in correspondence to the reported literature.[7-11, 13, 16, 18, 14] The first derivation of the reflectance spectra in Figure S9 of the Supporting Information shows that the main absorption edge shows only one maximum, therefore only of $BaNbO_2N$. A clear attribution of the very small absorption maxima at 495 nm cannot be given. Furthermore, Cen *et al.* performed theoretical calculations on the electronic structure of Ba_2NbO_3N and showed that this Ruddlesden–Popper perovskite is a direct semiconductor material with a theoretical bandgap of 2.0 to 2.13 eV with decreasing bandgap going from one layered to three layered Ba_2NbO_3N.[40] Therefore direct bandgaps of the samples were also estimated (Figure 7). Absorption edges are all in the range of 2.6 to 2.8 eV, compared to 4.3 eV for the precursor nanofibers. This is slightly higher than the value obtained from theoretical calculations of the Ruddlesden–Popper perovskite Ba_2NbO_3N, which is also the case for the indirect bandgap of $BaNbO_2N$, which has been calculated to be 1.4 to 1.6 eV.[41] Resulting from this, it can be concluded that the diffuse reflectance analysis confirms the presence of $BaNbO_2N$–Ba_2NbO_3N composite nanofibers.

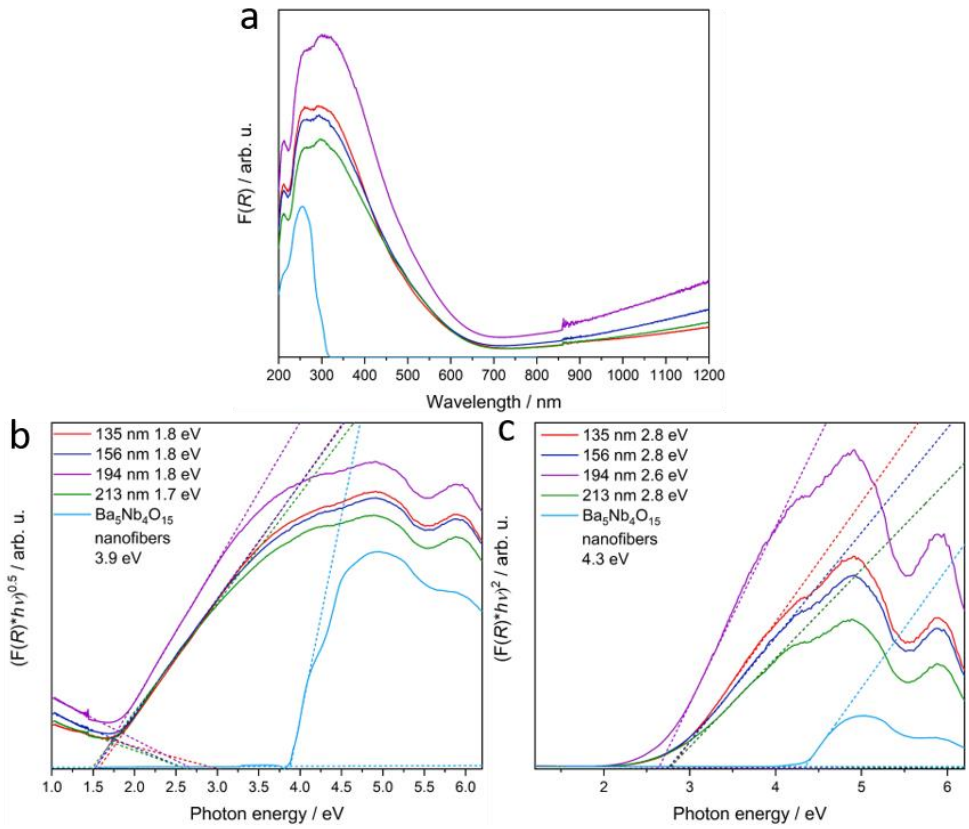

Figure 7 *a)Kubelka–Munk UV–vis spectra, b) indirect Tauc plots, and c) direct Tauc plot of $BaNbO_2N$–Ba_2NbO_3N nanofiber batches with 135 nm (red), 156 nm (dark blue), 194 nm (purple), and 213 nm (green) and of $Ba_5Nb_4O_{15}$ nanofibers (light blue) for comparison.*

2.2 Photocatalytic Hydrogen and Oxygen Evolution Results and Post-Photocatalytic Characterization

Photocatalytic hydrogen and oxygen evolution experiments were performed with $BaNbO_2N$–Ba_2NbO_3N nanofibers of different diameters after storage, to investigate their photocatalytic activity and the potential influence of the nanofiber diameter. A doped mercury lamp in a borosilicate housing was used, which cuts off all light intensity smaller than 300 nm (Figure S10, Supporting Information).

For the hydrogen evolution reaction, the nanofiber samples were dispersed in a mixture of water and methanol as sacrificial agent, the hydrogen evolution rate was measured with and without cocatalyst. The optimum amount of Pt cocatalyst was estimated on one exemplary sample by a stepwise photodeposition of Pt until no further increase in the hydrogen evolution rate could be detected, and was determined to be 0.5 wt% (Figure S11, Supporting Information). This amount was then recalculated respective to the absolute surface area, resulting in 3.66 µmol m^{-2} Pt; this amount was used for the further hydrogen

evolution measurements of all samples. The surface specific loading with cocatalyst was shown to be very important for the comparison of photocatalytic activities of nanostructured materials.[21, 42]

All nanofiber samples are able to produce hydrogen without the addition of cocatalyst, as can be seen in the first 3 h of the measurement (**Figure** 8). The hydrogen evolution rate without addition of a cocatalyst is 0.8 to 1.0 µmol h^{-1} for all four nanofiber samples and is therefore comparable. After Pt decoration, the fiber samples with the highest and smallest diameter and surface area show the same rate with 2.8 µmol h^{-1} (Figure 8 left).

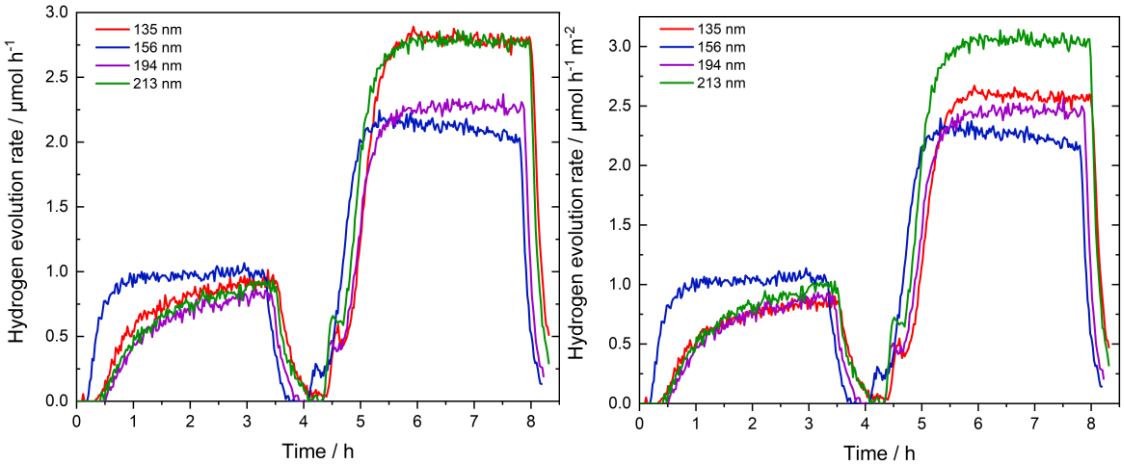

Figure 8 *Hydrogen evolution curves of $BaNbO_2N$–Ba_2NbO_3N after storage with diameters of 135 nm (red), 156 nm (blue), 194 nm (purple), and 213 nm (green) non-normalized (left) and normalized on absolute surface area (right), without cocatalyst in the first 3 h and with Pt as cocatalyst in the second 3 h. Lamp was turned off after 3.25 to 3.5 h and on again after 4.0 to 4.25 h for cocatalyst addition and off after 7.75 to 8.0 h.*

To exclude the influence of surface area and investigate the activity dependence solely on fiber diameter, Figure 8 right shows the hydrogen evolution curves, normalized on absolute surface area to compensate for the influence of different numbers of active sites due to differences in surface area. This conversion was recently reviewed as being very important for nanostructured and porous materials with high specific surface area, for the evaluation of the real influence of specific surface area enhancement.[43] Here, since the influence of the fiber diameter shall be discussed, the absolute surface area is taken into account by this normalization.

The evolution rates without cocatalyst are still in the same range for all samples. The hydrogen evolution rate increases two- to threefold after the addition of Pt. The most

pronounced increase to 3.1 µmol h^{-1} m^{-2} is obtained for the nanofiber sample with the largest nanofiber diameter of 213 nm, followed by the sample with the smallest diameter with 2.6 µmol h^{-1} m^{-2}.

This trend is now different compared to the non-normalized rate, since by using the same catalyst mass a different surface area is in contact with the electrolyte. This indicates that surface area and diameter, as expected, both have an influence on the activity. The thickest oxynitride nanofibers show the highest activity, likely due to structural or morphological differences as we reported before for diameter-adjusted $Ba_5Ta_4O_{15}$ nanofibers.[21] The nitrogen evolution was also tracked in these experiments to investigate the degradation of samples and shows only maximum values of 0 to 0.4 µmol h^{-1} (not shown).

Characterization of the samples after the hydrogen evolution reaction shows a less pronounced tailing of the reflections of $BaNbO_2N$ in the XRD patterns, no $BaCO_3$ reflections are visible anymore (Figure S12, Supporting Information). Single-Rietveld refinements of $BaNbO_2N$ (with asymmetric assumption) are in all four cases satisfying (Figure S13, Supporting Information), which confirm that indeed Ba_2NbO_3N decomposes and not $BaNbO_2N$. The Kubelka–Munk spectra show comparable absorption edges for all samples, demonstrating that $BaNbO_2N$ is not decomposed during the hydrogen evolution reaction (Figure S12, Supporting Information). This can be further underlined by elemental analysis after hydrogen evolution reaction with comparable values of 3.2 to 3.3 wt% nitrogen and only the small amounts of nitrogen gas, which are detected during photocatalytic reaction. Exemplary SEM image of nanofibers with diameter of 213 nm after hydrogen evolution reaction (Figure S14, Supporting Information) shows small nanofiber pieces, which can be explained by the sample preparation (ultrasonication) and stirring during the reaction time.

Additionally, the activity of the composite samples regarding oxygen evolution reaction was tested. Since it was already reported that $BaNbO_2N$ is not able to produce oxygen without the addition of a cocatalyst,[7, 14] CoO_x was deposited as cocatalyst *via* an impregnation method followed by subsequent annealing in ammonia and air following literature.[44] However, XRD pattern after the deposition shows additional reflections, which can be assigned to $CoNbO_4$ and hexagonal $Ba_4Nb_2O_9$ (**Figure** 9). The appearance of additional reflections after the deposition process was already reported before for

$BaTaO_2N$, however has not been assigned to cobalt containing phases before, but to amorphous Co species instead.[45]

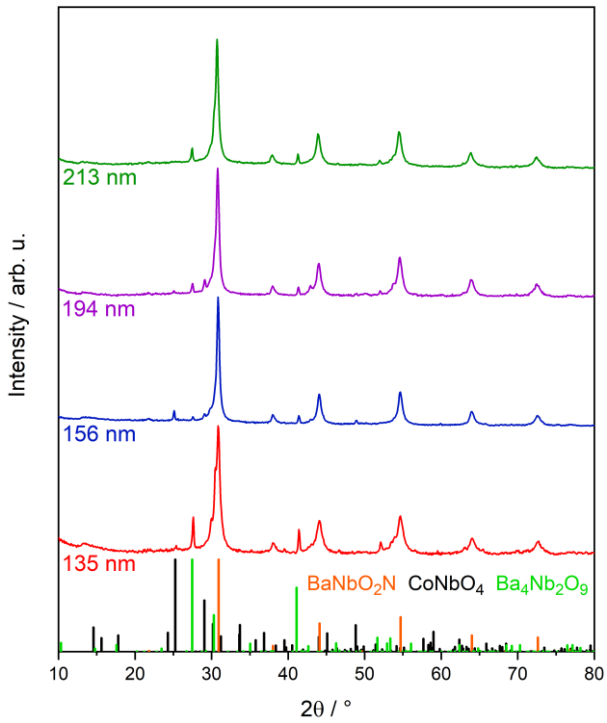

Figure 9 *XRD pattern after $CoNbO_4$ deposition on $BaNbO_2N$–Ba_2NbO_3N nanofiber batches with 135 nm (red), 156 nm (blue), 194 nm (purple), and 213 nm (green) diameter. Calculated reference pattern of $BaNbO_2N$ (orange, COD 01-078-1456 and Fujii et al.[6]), $CoNbO_4$ (black, ICDS 98-001-6377), and $Ba_4Nb_2O_9$ (light green, COD 96-400-1053) are shown for comparison.*

These $CoNbO_4$-decorated samples were then dispersed in water together with La_2O_3 as pH buffer (pH ≈ 8) for the oxygen evolution reaction, and the oxygen evolution was measured with the same setup as was used for the hydrogen evolution. Cobalt loadings of 1 or 2 wt% were tested on one sample (156 nm diameter) in water with silver nitrate as sacrificial agent (Figure S11, Supporting Information). Co loading of 2 wt% resulted in higher oxygen evolution amounts when the first 2 h were considered, thus it was used as loading for all nanofiber samples. Without the addition of silver nitrate as sacrificial agent, only small amounts of 0 to 0.4 µmol oxygen and 0.3 µmol to 0.7 µmol nitrogen were detected for all samples (not shown). After the addition of silver nitrate as sacrificial agent, a pronounced increase in oxygen evolution could be observed. **Figure** 10 shows the oxygen evolution after the addition of silver nitrate for all four $CoNbO_4$ decorated nanofiber composite samples: all samples produce oxygen. The activity trends regarding the nanofiber diameter is comparable to the results of the hydrogen evolution reaction (Figure 8 left). The nanofibers

with lowest and highest diameter and surface area show the highest activity with 22.7 and 23.0 µmol oxygen evolution (Figure 10 left). After normalization to absolute surface area (Figure 10 right), the nanofibers with the highest fiber diameter clearly exhibit the highest activity with 32.7 µmol h^{-1} m^{-2} in maximum, followed by the fibers with the smallest diameter with 29.5 µmol h^{-1} m^{-2}. Nanofibers with 194 nm exhibit a maximum of 18.4 µmol h^{-1} m^{-2} and fibers with 156 nm in diameter show the lowest rate with 7.7 µmol h^{-1} m^{-2} in maximum. Nitrogen evolution rates after addition of silver nitrate were comparably negligible as before, showing that the oxynitride samples are stable against decomposition (not shown). Due to the fact, that a comparison of the maxima in the oxygen evolution rates is not that precise, the absolute amount of oxygen in the first 2 h after addition of silver nitrate was calculated by integration. **Table** 2 summarizes these values and the evolution rates of the hydrogen evolution reaction depending on the nanofiber diameter for the non-normalized and to absolute surface area normalized data.

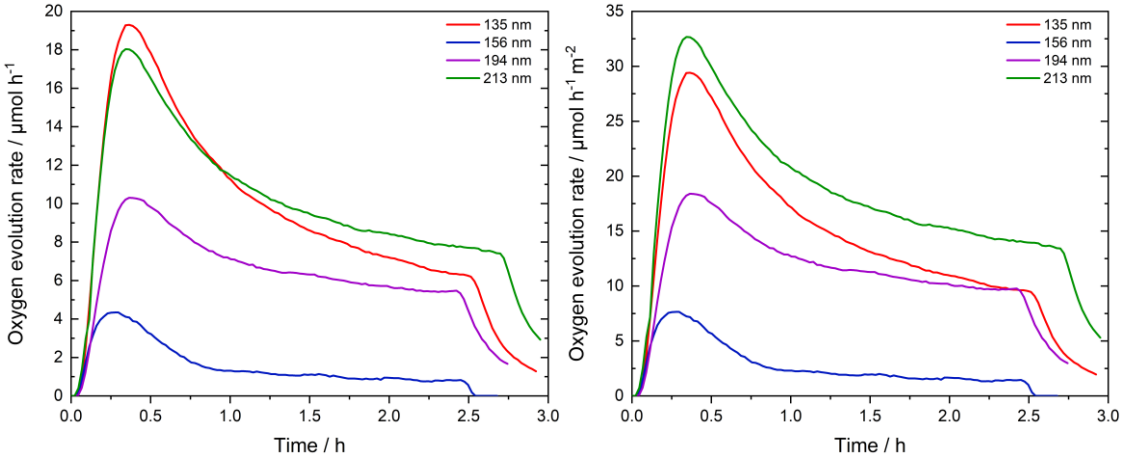

Figure 10 *Oxygen evolution curves of $CoNbO_4$ deposited $BaNbO_2N$–Ba_2NbO_3N samples after storage with diameters of 135 nm (red), 156 nm (blue), 194 nm (purple), and 213 nm (green) non-normalized (left) and normalized on absolute surface area (right). Lamp turned off after 2.5 to 2.75 h.*

Sample characterization after the oxygen evolution reaction *via* XRD characterization is not shown, due to the high amount of La_2O_3 added as buffer, which severely compromises the analysis of XRD patterns. Moreover, silver deposited during the oxygen evolution reaction precludes diffuse reflectance measurements.

Table 2. *Hydrogen evolution rates and amount of oxygen evolved in oxygen evolution reaction depending on the nanofiber diameter, non-normalized and normalized on absolute surface area*

Nanofiber diameter [nm]	Hydrogen evolution rate[a] [µmol h^{-1}]	Hydrogen evolution rate[a] [µmol h^{-1} m^{-2}]	Oxygen evolution[b] [µmol]	Oxygen evolution[b] [µmol m^{-2}]
135	0.9[c]/2.8[d]	0.8[c]/2.6[d]	22.7[b]	34.6[b]
156	1.0[c]/2.0[d]	1.1[c]/2.2[d]	3.7[b]	6.5[b]
194	0.8[c]/2.3[d]	0.9[c]/2.4[d]	14.3[b]	25.3[b]
213	0.9[c]/2.8[d]	1.0[c]/3.1[d]	23.0[b]	41.3[b]

[a]Steady-state value; [b]Amount of oxygen in the first 2 h after $AgNO_3$ addition, calculated by integration; [c]Evolution rate without cocatalyst deposited; [d]Evolution rate with 3.66 µmol m^{-2} Ptdeposited.

Comparing these results with regards to the influence of nanofiber diameters with the diameter-dependent study of photocatalytic water splitting on $Ba_5Ta_4O_{15}$ nanofibers, the trend in the activities is different: after optimization of the cocatalyst loading, a 161 nm as optimum diameter was reported, followed by comparable values for thicker nanofibers with 228 nm and smallest fiber diameter with 109 nm.[21] Comparable to this, the activities in the present study first decrease with decreasing fiber diameters but then increase again for fibers with the smallest diameter of 135 nm. One reason for the higher activities of the thinnest and the thickest oxynitride nanofiber composites—compared to fibers of the layered perovskite—could be the competitive effects of crystallinity and anion deficiency in the nitridation process of $BaNbO_2N$ with different micrometer sizes postulated by Yamada *et al.*[10]

Hydrogen and oxygen evolution reactions with a 300 W Xe lamp equipped with an AM1.5G filter on the most active nanofiber sample with 213 nm with cocatalyst surprisingly did not show any gas evolution, in contrast to reported visible light activity of $BaNbO_2N$.[7-9, 13, 19] This will be investigated in the future.

Finally, overall water splitting activity was investigated on the most active sample (213 nm diameter). For this, Pt was first photodeposited on the sample and afterward cobalt was deposited *via* the impregnation method. The gas evolution is shown in Figure S15 of the Supporting Information. Only very small amounts of gas could be detected. The decomposition process of the sample, forming N_2 seems to be preferred. Comparing hydrogen and oxygen evolution values, slightly more oxygen is evolved, although a 2:1 ratio of hydrogen to oxygen is expected in overall water splitting. This in correspondence to the

significant lower hydrogen evolution activity compared to the oxygen evolution activity with cocatalyst deposited. Instead of the reduction of protons, it seems that the photocatalyst itself is decomposed in pure water. XRD pattern after overall water splitting experiment in Figure S16 of the Supporting Information shows reflections belonging to $BaNbO_2N$ with a reduced tailing, which confirms the results of the decomposition of Ba_2NbO_3N from XRD patterns after hydrogen evolution reaction. Furthermore, the additional reflections after CoO_x deposition are not visible anymore, indicating, that these phases are not stable under the overall water splitting conditions.

3 Conclusion

The conversion of electrospun $Ba_5Nb_4O_{15}$ nanofibers with adjusted diameters *via* an ammonolysis reaction led to the formation of oxynitride nanofibers with retained nanofiber morphology. Moreover, the nanofiber diameter was adjusted in a range of 135 up to 213 nm. Most importantly, only very detailed material characterization revealed that the resulting oxynitride is actually a novel $BaNbO_2N$–Ba_2NbO_3N composite, and not sole $BaNbO_2N$. A diameter-dependent photocatalytic hydrogen and oxygen evolution activity could be shown with an optimum nanofiber diameter of 213 nm. Pt and $CoNbO_4$ cocatalyst deposited fibers with optimum diameter exhibited a performance of 3.1 µmol h^{-1} m^{-2} in hydrogen evolution and 41.3 µmol m^{-2} in oxygen evolution reaction. The influence of Ba_2NbO_3N on photocatalytic activity has to be investigated in the future. Nevertheless, this novel approach of nanostructuring semiconductors for ammonolysis reactions could be a way to synthesize other photocatalytically active oxynitride semiconductors with beneficial nanostructures.

4 Experimental Section

Chemicals

Barium(II) ethylhexanoate (98%, Sigma-Aldrich), niobium(V) ethoxide (99.9%, abcr, used as a 0.24 m solution in absolute ethanol (extra dry, 99.5%, AcrosOrganics), PVP (MW = 1 300 000, Alfa Aesar), tetrahydrofuran (technical grade, VWR), lanthanum oxide (99.9%, Strategic Elements), hydrogen hexachloroplatinate(IV) hydrate (99.995%, Carl Roth), cobalt(II) nitrate hexahydrate (99%, abcr), silver nitrate (99.8-100.5%, VWR), and

methanol (99.9%, Fisher chemical). Lanthanum oxide was heated to 600 °C for 10 h before usage. All other chemicals were used as received.

Synthesis of $Ba_5Nb_4O_{15}$ Nanofibers as Precursors for $BaNbO_2N$ Nanofibers

$Ba_5Nb_4O_{15}$ nanofibers were synthesized according to the route reported by Hildebrandt *et al.*, and nanofiber diameters were adjusted as shown by Bloesser *et al.*[20, 21] For one batch of $Ba_5Nb_4O_{15}$ nanofibers, 890 mg of barium(2-ethylhexanoate) was dissolved in 3 mL of THF and 7 mL of a 0.24 $Nb(OEt)_5$ solution in absolute ethanol was added. Then, 200 to 500 mg of PVP were added and the solution was stirred until a clear spinning solution was obtained. The solution was filled in a syringe equipped with a cannula with an inner diameter of 0.8 mm and a flat-cut tip, and placed in a syringe pump for the electrospinning process in a home-made electrospinning chamber. The humidity in the chamber was set to 30%, the distance between the tip of the cannula and the rotating drum collector to 15 cm, a potential of +18 kV at the cannula and −2 kV at the collector was applied, and the solution was pumped with a rate of 0.3 mL min^{-1}. The obtained fibers were calcined at 1173 K for 10 h (heating rate of 5 K min^{-1}) in a muffle furnace in air for removal of the spinning polymer and crystallization of $Ba_5Nb_4O_{15}$.

Synthesis of $BaNbO_2N$ Nanofibers

The $BaNbO_2N$ nanofibers were prepared by an ammonolysis reaction of the synthesized $Ba_5Nb_4O_{15}$ precursor nanofibers. $Ba_5Nb_4O_{15}$ nanofibers were placed in a quartz boat and were annealed in an NH_3 flow of 60 mL min^{-1} at 1273 K for 20 h in a tube furnace. The heating was performed in an Ar flow with a heating rate of 10 K min^{-1} and the sample was also cooled down in Ar flow to room temperature. To obtain enough material for the photocatalytic characterization of the $BaNbO_2N$ nanofibers, two to three charges were mixed after thorough characterization.

Characterization Methods

SEM images were recorded with a Zeiss LEO 1530. All samples were sputtered with 1 to 2 nm Pt using a Cressington Sputter Coater 208 HR. An acceleration voltage of 3 kV was applied with an aperture set to 30 µm. For EDX analysis an UltraDry-EDX detector

(ThermoFisher Scientific NS7) was used, the voltage was set to 20 kV, and the aperture to 60 µm. For each sample, the Ba/Nb ratio was averaged from measurements of several areas.

TEM images were recorded with a JEOL JEM-2200FS EFTEM equipped with Schottky FEG and In-Column Omega Energyfilter from JEOL operated at 200 kV. Prior the measurement, 1 to 2 mg of the sample were suspended in 1 mL of ethanol (AcrosOrganics, extra dry, 99.5%). Then, 4 µL of the suspension was dropped on a carbon film coated Cu TEM grid (200 Mesh). TEM images were processed using ImageJ.

XRD was measured on an Empyrean diffractometer (Malvern PANalytical) with a PixCel 1D detector using Cu Kα radiation. Rietveld refinements were performed using the program Fullprof with a Thompson-Cox-Hastings pseudo-Voigt function with asymmetry as profile function and a Chebychev polynomial for background approximation.[46] Instrumental broadening was determined with a LaB_6 standard (NIST SRM660c). Due to the similar mass attenuation coefficients and the small crystallite sizes microabsorption was neglected. Information about the crystal structure for refinements were taken from Fujii *et al.* for $BaNbO_2N$,[6] Clarke *et al.* for Ba_2NbO_3N (adjusted accordingly),[47] and Antao and Hassan for $BaCO_3$.[48] Theoretical diffraction patterns were calculated using Diamond (Crystal Impact). Information about the crystal structure were taken from Cernik *et al.* for $Ba_5Nb_4O_{15}$,[49] Lehmann and Müller-Buschbaum for $CoNbO_4$,[50] and Ling *et al.* for h-$Ba_4Nb_2O_9$.[51]

DRIFT spectra were collected using a Bruker Alpha II with interchangeable measurement modules.

XPS was measured on a VersaProbe III Scanning XPS Microprobe from Physical Electronics PHI using monochromatic Al Kα radiation and a beam diameter of 100 µm. Survey spectra were recorded with a pass energy of 224 eV and a step size of 0.8 eV, whereas high-resolution spectra were recorded with a pass energy of 26 eV and a step size of 0.1 eV; integration time was 50 ms in both cases. The sample was flooded with slow-moving electrons and argon ions during measurement to prevent surface charging. The sample was not argon sputter cleaned prior to measurement to prevent reduction of the surface. Data analysis was performed using CasaXPS; Shirley backgrounds and Gaussian–Lorentzian (GL30) peak-shapes were used for ionic components and asymmetric

LA(1.2,5,12) peak-shapes for metallic Nb. For charge correction, the C 1s signal was set to 284.8 eV.

TG analysis in synthetic air was performed with a Netzsch Jupiter STA 449C thermobalance, which was additionally coupled with a Netzsch Aeolos QMS 403C quadrupol MS for recording gaseous compounds, *i.e.*, H_2O (18), N_2 (28), and CO_2 (44).

Krypton physisorption measurements at 77 K were recorded with ASiQ-MP-MP-AG setup (Anton Paar QuantaTec, Boynton Beach, USA). Prior to the measurement the samples were degassed for 3 h at 200 °C in vacuum. The data analysis was done using the BET model *via* software ASiQwin (Anton Paar QuantaTec, Boynton Beach, USA). The saturation pressure p_0 was kept constant at 2.63 Torr.

Elemental analysis (C, H, N, S) was measured with a Unicube from Elementar with sulfanilamide as the standard. Precise quantities of samples between 2 and 4 mg were placed in a tin boat and sealed prior to the measurement. To ensure the complete combustion of the samples, the combustion tube was heated up to 1143 °C in O_2/Ar atmosphere. The detection of completely oxidized gas species was done *via* thermal conductivity system.

A PerkinElmer Lambda 750 UV/vis/NIR spectrometer, equipped with a Praying-Mantis mirror unit from Harrick was used to record the diffuse reflectance with step size of 1 nm. A spectralon pellet was used as white standard. The spectra were converted into absorption spectra using Kubelka–Munk function; bandgaps were estimated using Tauc plots.

Lamp spectra were measured with a Flame spectrometer from Ocean Insight.

Photocatalytic Hydrogen Evolution Experiments

Ultrapure water was used for all hydrogen evolution reactions. A dispersion of 132 mg photocatalyst in 550 mL water and 50 mL methanol was prepared with ultrasonication for 15 min. The dispersion was filled into a homemade double-walled inner-irradiation glass reactor with a borosilicate housing for the lamp and was stirred with 200 rpm. A 700 W Z4 doped Hg mid-pressure lamp (Peschl UV-Consulting) set to 500 W was used, the lamp spectra are shown in Figure S10 of the Supporting Information. The temperature was set to 10 °C with a thermostat (LAUDA RP845) and the whole system was flushed with 100 mL

min^{-1} Ar 5.0 using a Bronkhorst mass flow controller for several hours to remove residual air. The gas evolution was detected online using a mass spectrometer (Hiden HPR-20 Q/C). During the experiment oxygen, hydrogen, nitrogen, and carbon dioxide were detected. To find the optimum in Pt cocatalyst loading different amounts of Pt were in situ photodeposited on one exemplary nanofiber sample by a stepwise addition of an aqueous solution of H_2PtCl_6 through a rubber sealing. After 2.5 h without any Pt codeposited, Pt loading was adjusted until the detected hydrogen evolution rate did not improve further by shortly switching off the lamp and adding a defined amount of Pt to the dispersion and turning the lamp on again. Every photodeposition step took around 1 h. The optimum Pt loading was then used for all other hydrogen evolution reactions and was adjusted, depending on the surface area of the used nanofiber sample. For the measurements of the nanofiber samples with varying diameter, the gas evolution was measured for ≈3 h to investigate the activity of the nanofiber samples without any cocatalyst deposited. Afterward the lamp was shortly switched off to add an aqueous solution of H_2PtCl_6 through a rubber sealing. The sedimented samples were centrifuged and dried at 80 °C.

Hydrogen evolution reaction with 300 W solar simulator using a Xe lamp (Quantum Design) equipped with an AM1.5G filter was conducted on the most active sample in a top-irradiated reaction vessel. Measurements were performed at 20 °C, the system was also flushed with Ar before measurement. For the measurement 68 mg of the photocatalyst was dispersed in a mixture of 135 mL water and 15 mL methanol. Gas evolution was also detected online with MS.

Deposition of Cobalt-Based Cocatalyst

The deposition was performed *via* an impregnation method reported by Zhang *et al.*[39] An appropriate amount aqueous solution of $Co(NO_3)_2{\cdot}6H_2O$ (490 mg L^{-1}) was added to the synthesized nanofiber sample and the water was then evaporated at 100 °C under stirring. The obtained solid was placed in a quartz boat, was annealed in a NH_3 flow (200 mL min^{-1}) at 973 K (heating rate 10 K min^{-1}) for 1 h and was cooled down in an Ar flow in a tube furnace. The sample was afterward heated for 1 h at 473 K in air in a muffle furnace.

Photocatalytic Oxygen Evolution Experiments

Ultrapure water was used for all oxygen evolution reactions (cleaned with a pure water system of VWR (A series), total organic carbon (TOC) = 2 ppb). A dispersion of 80 mg of the CoO_x deposited photocatalyst and 160 mg La_2O_3 as pH buffer in 600 mL water was prepared with an ultrasonication step for 15 min. The dispersion was filled into the same reactor, conditions and lamp kept the same as for the hydrogen evolution reaction (details see above). Oxygen evolution rate in first hours was detected without addition of sacrificial agent. Then the lamp was shortly switched off and 3 m $AgNO_3$ solution was added through a rubber sealing to reach a concentration of 0.01 m. After all gases evolution rates reached zero again, the lamp was switched on again and the gas evolution was detected for further 2.5 h. As only a negligible amount of gases was formed without $AgNO_3$, only the gas evolution curves after the addition of $AgNO_3$ are shown and time was set to zero, when gas evolution reached 0 after $AgNO_3$ addition.

Oxygen evolution reaction was performed with Xe-lamp on the most active sample (65 mg) with the same conditions as already mentioned in the hydrogen evolution part, but instead of methanol silver nitrate was used as sacrificial agent (10×10^{-3} m) and La_2O_3 (130 mg) was added as pH buffer.

Overall Water Splitting Experiment

Ultrapure water (TOC = 2 ppb) was used for Pt photodeposition and overall water splitting experiment. Overall water splitting was tested on the most active sample in hydrogen and oxygen evolution reactions. First 3.66 µmol m^{-2} Pt was photodeposited on 136 mg of the sample as described above with photodeposition time of 1 h. After this, the sample was directly evaporated to dryness, washed thoroughly with water, and dried. Then CoO_x was deposited *via* impregnation method. For overall water splitting, 96 mg of the Pt-CoO_x deposited nanofiber sample was immersed in 600 mL water with 15 min ultrasonication and filled in the same reactor as for hydrogen and oxygen evolution reaction. Reaction conditions and used lamp were also the same. The system was flushed with Ar overnight to remove any residual air. The gas evolution was then detected for 3 h. Gas evolution in the first 15 min can be attributed to small contaminations. Lamp was turned on after gas evolution rate was zero again after 20 min and measurement was performed for 3 h.

Acknowledgements

The authors thank Christopher Simon for TEM measurements and Lena Geiling (all University of Bayreuth, Germany) for TG-MS measurements. Furthermore, the authors thank the Keylab Device Engineering at the Bavarian Polymer Institute, University Bayreuth for use of the XPS. Additionally, the authors thank the BPI KeyLab Electron and Optical Microscopy for use of the Zeiss Leo 1530 and JEOL JEM-2200FS.

Open access funding enabled and organized by Projekt DEAL.

Conflict of Interest

The authors declare no conflict of interest.

Data Availability Statement

Research data are not shared.

Keywords

ammonolysis, electrospinning, nanofibers, oxynitride, photocatalysis

References

[1] K. Maeda, M. Higashi, B. Siritanaratkul, R. Abe, K. Domen, *J. AM. CHEM. Soc.* **2011**, *133*, 12334.
[2] A. Kasahara, K. Nukumizu, T. Takata, J. N. Kondo, M. Hara, H. Kobayashi, K. Domen, *J. Phys. CHEM. B* **2003**, *107*, 791.
[3] J. Xu, C. Pan, T. Takata, K. Domen, *CHEM. COMMUN.* **2015**, 51, 7191.
[4] M. Higashi, K. Domen, R. Abe, *J. AM. CHEM. Soc*. **2013**, *135*, 10238.
[5] F. Pors, R. Marchand, Y. Laurent, P. Bacher, G. Roult, *Mater. Res. Bull*. **1988**, *23*, 1447.
[6] K. Fujii, K. Shimada, M. Yashima, *J. CERAM. Soc. Jpn*. **2017**, *125*, 808.
[7] F. Oehler, S. G. Ebbinghaus, *Solid State Science*, Elsevier Masson SAS, Amsterdam **2016**, pp. 43–48.
[8] M. Hojamberdiev, E. Zahedi, E. Nurlaela, K. Kawashima, K. Yubuta, M. Nakayama, H. Wagata, T. Minegishi, K. Domen, K. Teshima, *J. Mater. CHEM. A* **2016**, *4*, 12807.
[9] T. Hisatomi, C. Katayama, Y. Moriya, T. Minegishi, M. Katayama, H. Nishiyama, T. Yamada, K. Domen, *Energy Environ. Sci.* **2013**, *6*, 3595.
[10] T. Yamada, Y. Murata, S. Suzuki, H. Wagata, S. Oishi, K. Teshima, *J. Phys. CHEM. C* **2018**, *122*, 8037.
[11] J. Seo, T. Hisatomi, M. Nakabayashi, N. Shibata, T. Minegishi, M. Katayama, K. Domen, *Adv. Energy Mater*. **2018**, *8*, 1800094.
[12] J. Seo, M. Nakabayashi, T. Hisatomi, N. Shibata, T. Minegishi, M. Katayama, K. Domen, *J. Mater. CHEM. A* **2019**, *7*, 493.

[13] T. Hisatomi, C. Katayama, K. Teramura, T. Takata, Y. Moriya, T. Minegishi, M. Katayama, H. Nishiyama, T. Yamada, K. Domen, *CHEMSUSCHEM* **2014**, *7*, 2016.
[14] B. Siritanaratkul, K. Maeda, T. Hisatomi, K. Domen, *CHEMSUSCHEM* **2011**, *4*, 74.
[15] Y. Il Kim, E. Lee, *J. CERAM. Soc. Jpn.* **2011**, *119*, 371.
[16] Y. Il Kim, P. M. Woodward, K. Z. Baba-Kishi, C. W. Tai, *CHEM. Mater*. **2004**, *16*, 1267.
[17] J. Odahara, A. Miura, N. C. Rosero-Navarro, K. Tadanaga, *Inorg*. *CHEM*. **2018**, *57*, 24.
[18] J. Seo, Y. Moriya, M. Kodera, T. Hisatomi, T. Minegishi, M. Katayama, K. Domen, *CHEM. Mater*. **2016**, *28*, 6869.
[19] S. Wei, S. Jin, G. Pan, Z. Li, G. Liu, X. Xu, *J. AM. CERAM. Soc*. **2019**, *102*, 6194.
[20] N. C. Hildebrandt, J. Soldat, R. Marschall, *SMALL* **2015**, *11*, 2051.
[21] A. Bloesser, P. Voepel, M. O. Loeh, A. Beyer, K. Volz, R. Marschall*, J. Mater. CHEM. A* **2018**, *6*, 1971.
[22] S. Pagola, G. Polla, G. Leyva, M. T. Casais, J. A. Alonso, R. Rasines, R. E. Carbinio, *Mater. Sci. FORUM* **1996**, *819*, 228.
[23] A. Bloesser, R. Marschall, *ACS Appl. Energy Mater*. **2018**, *1*, 2520.
[24] K. Kawashima, M. Hojamberdiev, H. Wagata, K. Yubuta, S. Oishi, K. Teshima, *Cryst. Growth Des*. **2015**, *15*, 333.
[25] M. Davi, F. Schrader, T. Scholz, Z. Ma, A. Rokicinska, R. Dronskowski, P. Kustrowski, A. Slabon, *ACS Appl. Nano Mater.* **2018**, *1*, 869.
[26] Y. Suemoto, Y. Masubuchi, Y. Nagamine, A. Matsutani, T. Shibahara, K. Yamazaki, S. Kikkawa, *Inorg. CHEM*. **2018**, *57*, 9086.
[27] J. F. Moulder, W. F. Stickle, P. E. Sobol, K. D. Bomben, *Handbook of X-Ray Photoelectron Spectroscopy*, Physical Electronics Division, Perkin-Elmer Corporation, Eden Prairie, MN, USA **1993**.
[28] M. K. Bahl, *J. Phys. CHEM. Solids* **1975**, *36*, 485.
[29] Z. Yang, X. Lu, W. Tan, J. Zhao, D. Yang, Y. Yang, Y. He, K. Zhou*, Appl. Surf. Sci.* **2018**, *439*, 1119.
[30] Z. Weibin, W. Weidong, W. Xueming, C. Xinlu, Y. Dawei, S. Changle, P. Liping, W. Yuying, B. Li, *Surf. Interface Anal*. **2013**, *45*, 1206.
[31] D. D. Sarma, C. N. R. Rao*, J. Electron Spectros. Relat. PHENOM*. **1980**, 20, 25.
[32] A. Darlinski, J. Halbritter, *Surf. Interface Anal*. **1987**, *10*, 223.
[33] A. Darlinski, J. Halbritter, *Z. Anal. CHEM*. **1987**, *329*, 266.
[34] K. S. Havey, J. S. Zabinski, S. D. Walck, *Thin Solid FILMS* **1997**, *303*, 238.
[35] S. Badrinarayanan, S. Sinha*, J. Appl. Phys*. **1991**, *69*, 1141.
[36] D. Simon, C. Perrin, P. Baillif, C. R. *Acad. Sci. Paris, Ser. C* **1976**, *283*, 241.
[37] M. C. Blanco López, G. Fourlaris, B. Rand, F. L. Riley, *J. AM. CERAM. Soc.* **1999**, *82*, 1777.
[38] B. S. Shaheen, A. M. Hafez, B. Murali, A. R. Kirmani, A. Amassian, O. F. Mohammed, N. K. Allam*, Sol. Energy Mater. Sol. Cells* **2016**, *151*, 149.
[39] A. Rachel, S. G. Ebbinghaus, M. Güngerich, P. J. Klar, J. Hanss, A. Weidenkaff, A. Reller, *THERMOCHIM. Acta* **2005**, *438*, 134.
[40] Y.-l. Cen, J.-j. Shi, M. Zhang, M. Wu, J. Du, W.-h. Guo, Y.-h. Zhu, *J. Colloid Interface Sci.* **2019**, *546*, 20.
[41] H. Wolff, R. Dronskowski, *J. COMPUT. CHEM*. **2008**, *29*, 2260.
[42] A. Hofmann, M. Weiss, R. Marschall, *J. Phys. Energy* **2021**, *3*, 014002.
[43] A. S. Cherevan, L. Deilmann, T. Weller, D. Eder, R. Marschall, *ACS Appl. Energy Mater.* **2018**, *1*, 5787.

[44] F. Zhang, A. Yamakata, K. Maeda, Y. Moriya, T. Takata, J. Kubota, K. Teshima, S. Oishi, K. Domen*, J. AM. CHEM. Soc.* **2012**, *134*, 43.
[45] H. Okamoto, M. Kodera, T. Hisatomi, M. Katayama, T. Minegishi, K. Domen, *Catal. Today* **2020**, *354*, 204.
[46] J. Rodríguez-Carvajal, *Phys. B* **1993**, *192*, 55.
[47] S. J. Clarke, K. A. Hardstone, C. W. Michie, M. J. Rosseinsky, *CHEM. Mater*. **2002**, *14*, 2664.
[48] S. M. Antao, I. Hassan*, Phys. CHEM. Miner.* **2007**, *34*, 573.
[49] R. J. Cernik, M. Barwick, F. Azough, R. Freer, *J. Appl. Crystallogr*. **2007**, *40*, 749.
[50] U. Lehmann, H. Müller-Buschbaum, *Z. Anorg. Allg. CHEM*. **1980**, *471*, 85.
[51] C. D. Ling, M. Avdeev, R. Kutten, V. V. Kharton, A. A. Yaremchenko, S. Fialkova, N. Sharma, R. B. Macquart, M. Hoelzel, M. Gutmann, *CHEM. Mater*. **2009**, *21*, 3853.

7.2 Supporting Information

Supporting Information for Adv. Mater. Interfaces,

DOI:10.1002/admi.202100813

Perovskite-Type Oxynitride Nanofibers Performing Photocatalytic Oxygen and Hydrogen Generation

Anja Hofmann, Morten Weiss, Jana Timm, and Roland Marschall*

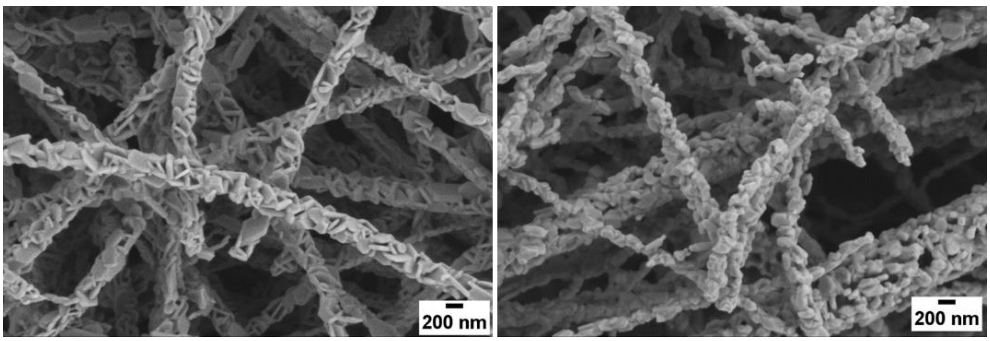

Figure SI 1. *SEM images of electospun $Ba_5Nb_4O_{15}$ nanofibers before (left) and after conversion to $BaNbO_2N$ nanofibers (right).*

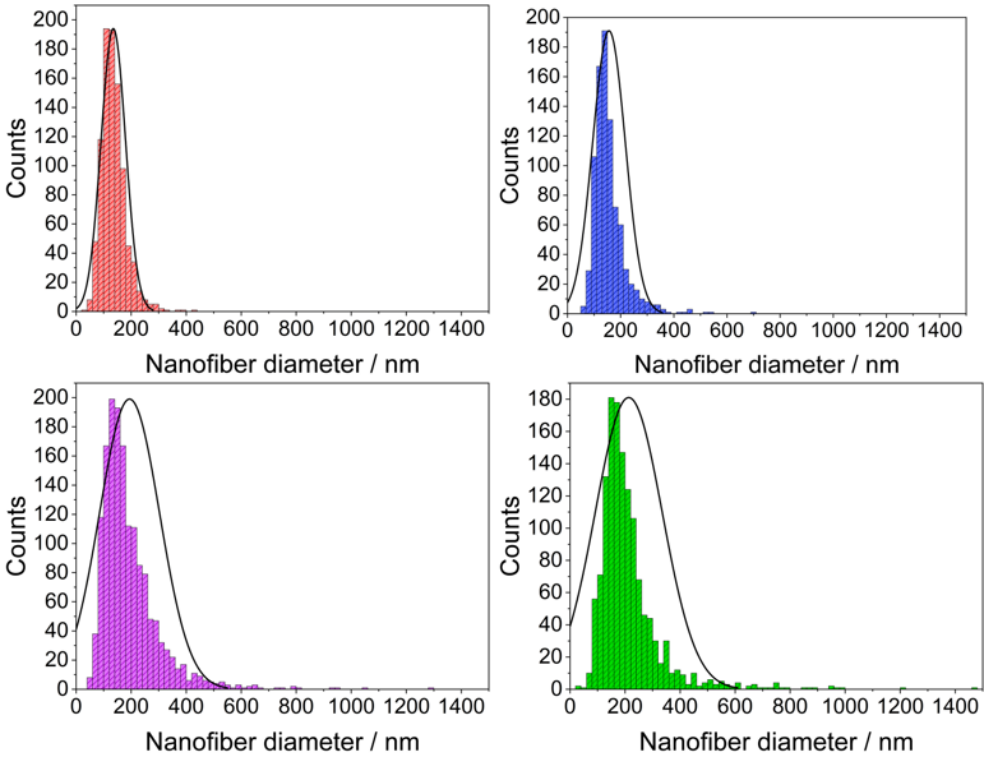

Figure SI 2. *Nanofiber diameter distributions of $BaNbO_2N$ nanofibers with mean diameter of 135 nm (red), 156 nm (blue), 194 nm (purple) and 213 nm (green).*

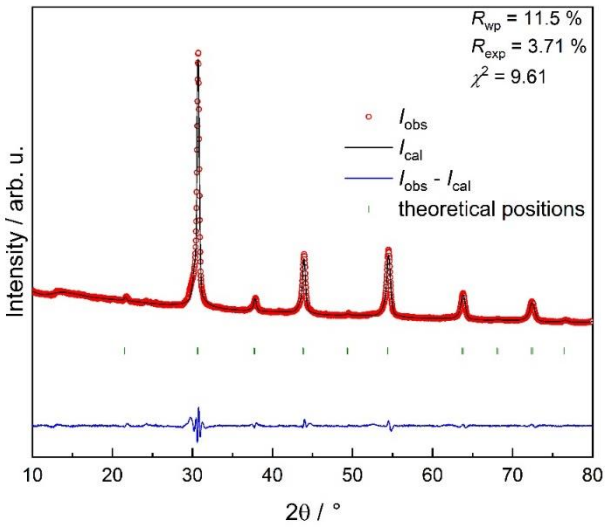

Figure SI 3. *Single-Rietveld refinement with asymmetry on nanofibers with 213 nm diameter.*

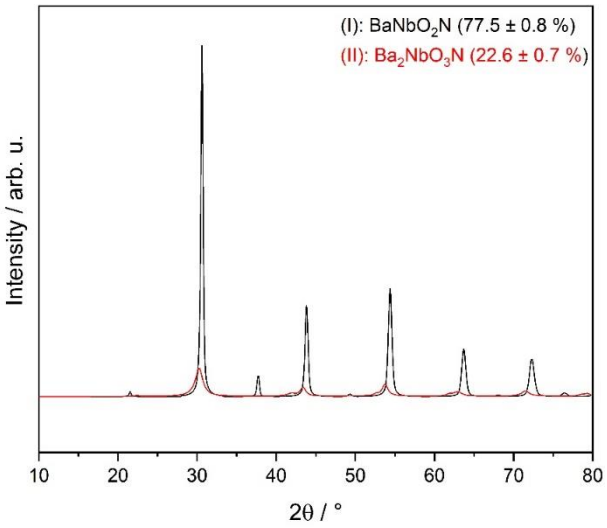

Figure SI 4. *Simulated XRD pattern showing the combination of $BaNbO_2N$ (black) and Ba_2NbO_3N (red) XRD pattern obtained from Rietveld refinement of XRD pattern shown in* ***Figure 4****.*

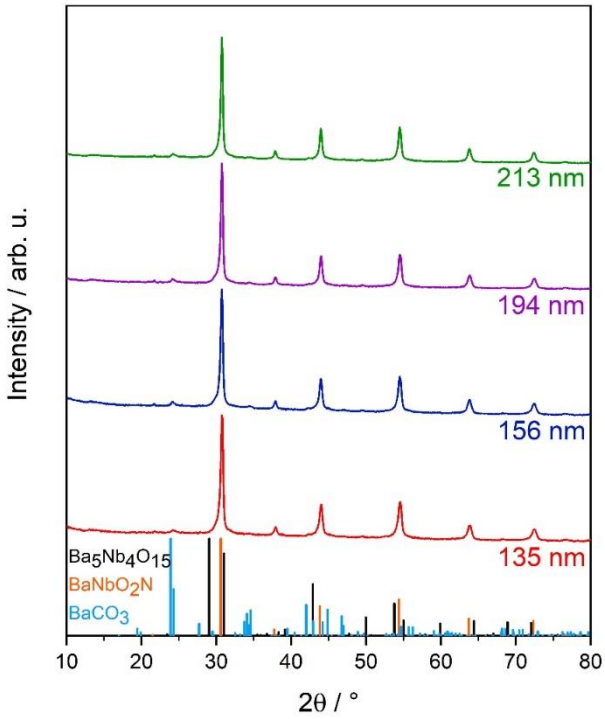

Figure SI 5. *XRD patterns of $BaNbO_2N$-Ba_2NbO_3N after storage with nanofiber diameter ranging from 135 nm to 213 nm. Calculated reference pattern of Ba5Nb4O15 (black, COD 96-230-0161), BaCO3 (light blue, COD 96-901-0929), and BaNbO2N (orange, COD 01-078-1456 and Fujii et al.[6]) are shown for comparison*

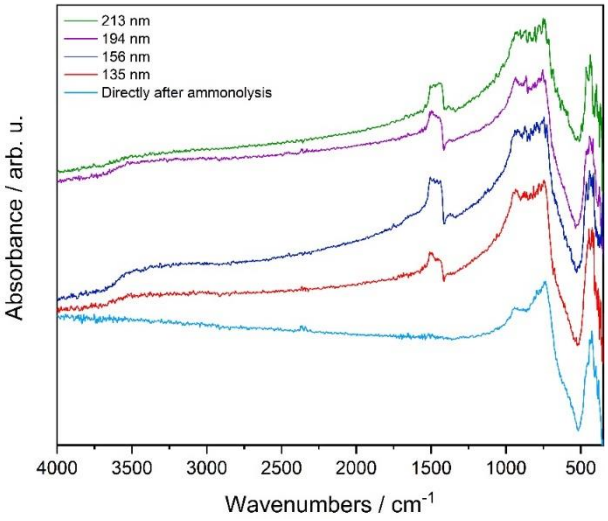

Figure SI 6. *DRIFT spectra of stored $BaNbO_2N$-Ba_2NbO_3N nanofibers with 135 nm (red), 156 nm (blue), 194 nm (purple), and 213 nm (green) diameter in comparison to an $BaNbO_2N$-Ba_2NbO_3N nanofiber sample with 213 nm diameter directly after ammonolysis.*

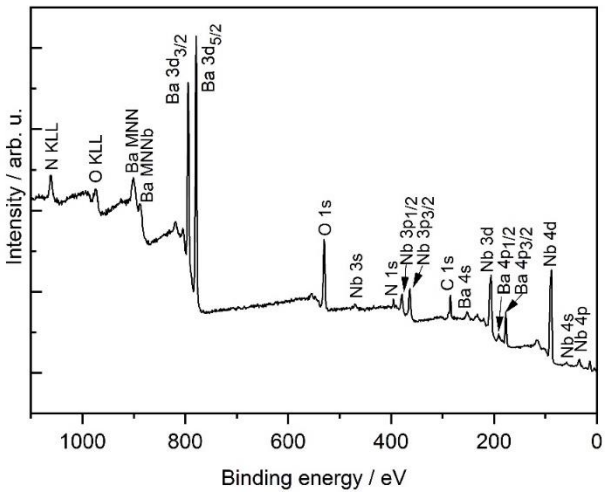

Figure SI 7. *Survey XP spectrum of $BaNbO_2N$-Ba_2NbO_3N nanofiber sample with diameter of 135 nm after storage at ambient conditions.*

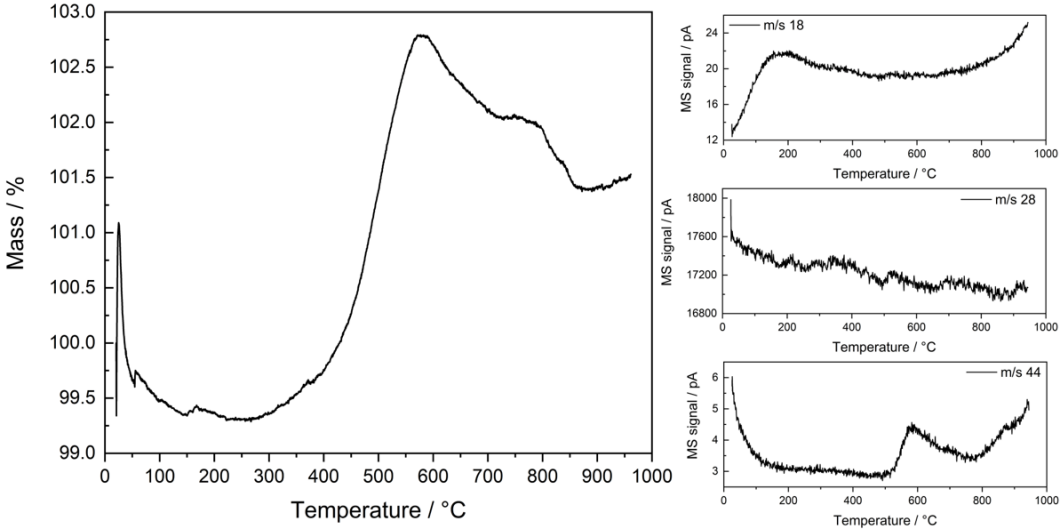

Figure SI 8. *TG measurement of $BaNbO_2N$-Ba_2NbO_3N batch nanofibers with diameter of 135 nm (left) and H_2O (m/z = 18) (upper right), N_2 (m/z = 28) (middle right), and CO_2 (m/z = 44) (lower right) evolution during TG measurements monitored via mass spectrometry.*

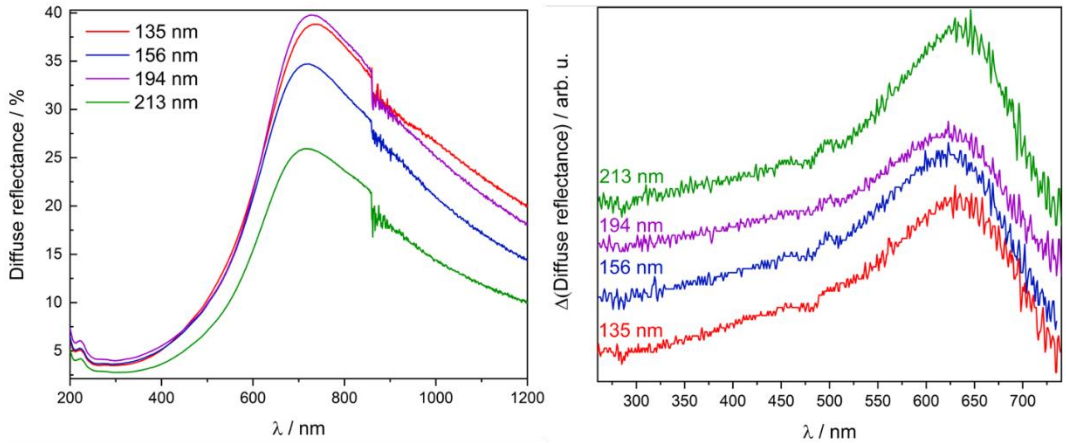

Figure SI 9. *Diffuse reflectance spectra (left) and first derivation of diffuse reflectance spectra (right) of stored $BaNbO_2N$-Ba_2NbO_3N nanofibers with 135 nm (red), 156 nm (blue), 194 nm (purple), and 213 nm (green) diameter.*

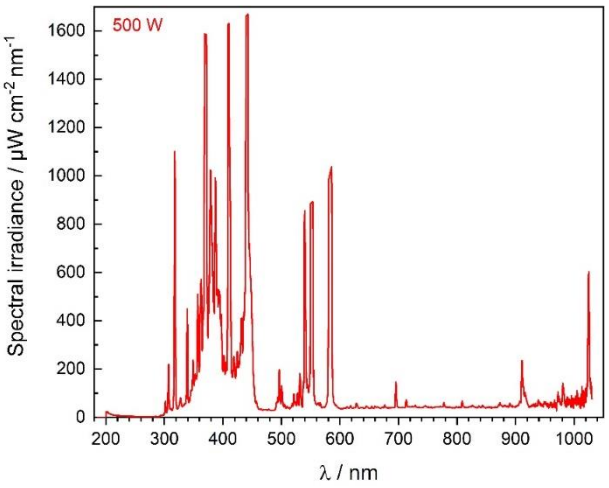

Figure SI 10. *Lamp spectra of Z4 Hg lamp set to 500 W, main peaks cutted due to saturation of the detector.*

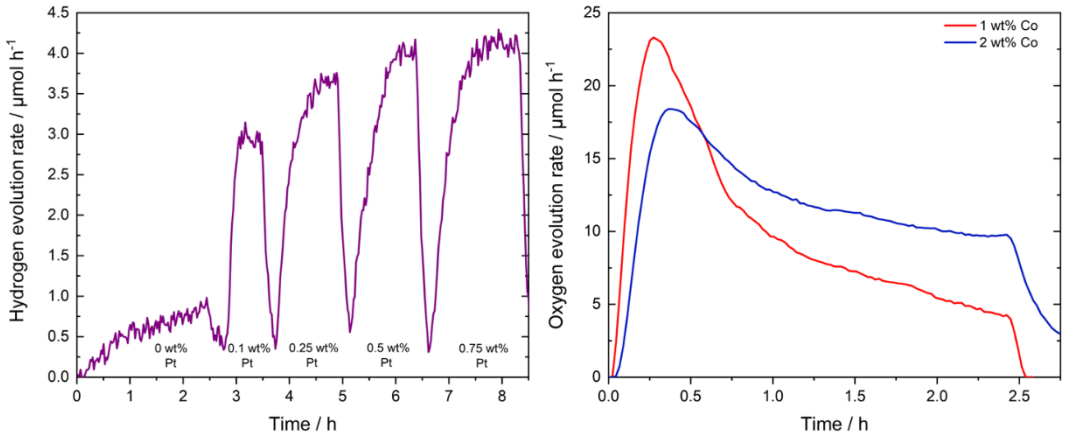

Figure S 11. *Hydrogen evolution during Pt photodeposition test for optimal Pt-loading (left) and oxygen evolution on CoO_x impregnated $BaNbO_2N$-Ba_2NbO_3N sample with 1 wt.-% and 2 wt.-% Co for test of optimal Co loading (right). Lamp was turned off after 2.5, 3.5, 4.75, 6.25, and 8.25 hours and on after 2.75, 3.75, 5.0, and 6.5 hours for co-catalyst addition (left). Lamp was turned off after 2.5 hours (right).*

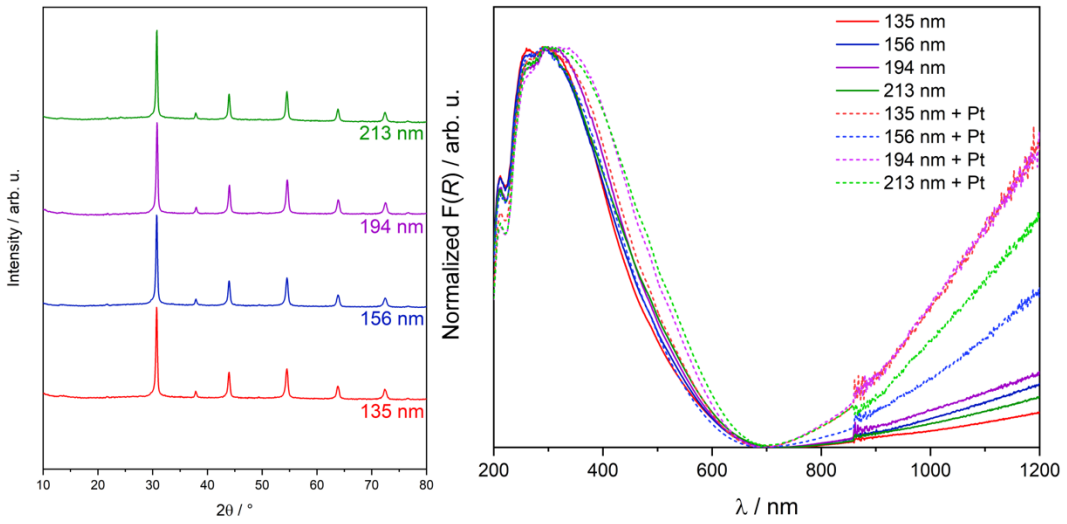

Figure SI 12. *XRD pattern (left) of nanofibers with 135 nm (red), 156 nm (blue), 194 nm (purple), and 213 nm (green) diameter after hydrogen evolution experiments and Kubelka-Munk spectra (right) of nanofibers before (solid line) and after (dotted line) hydrogen evolution experiments.*

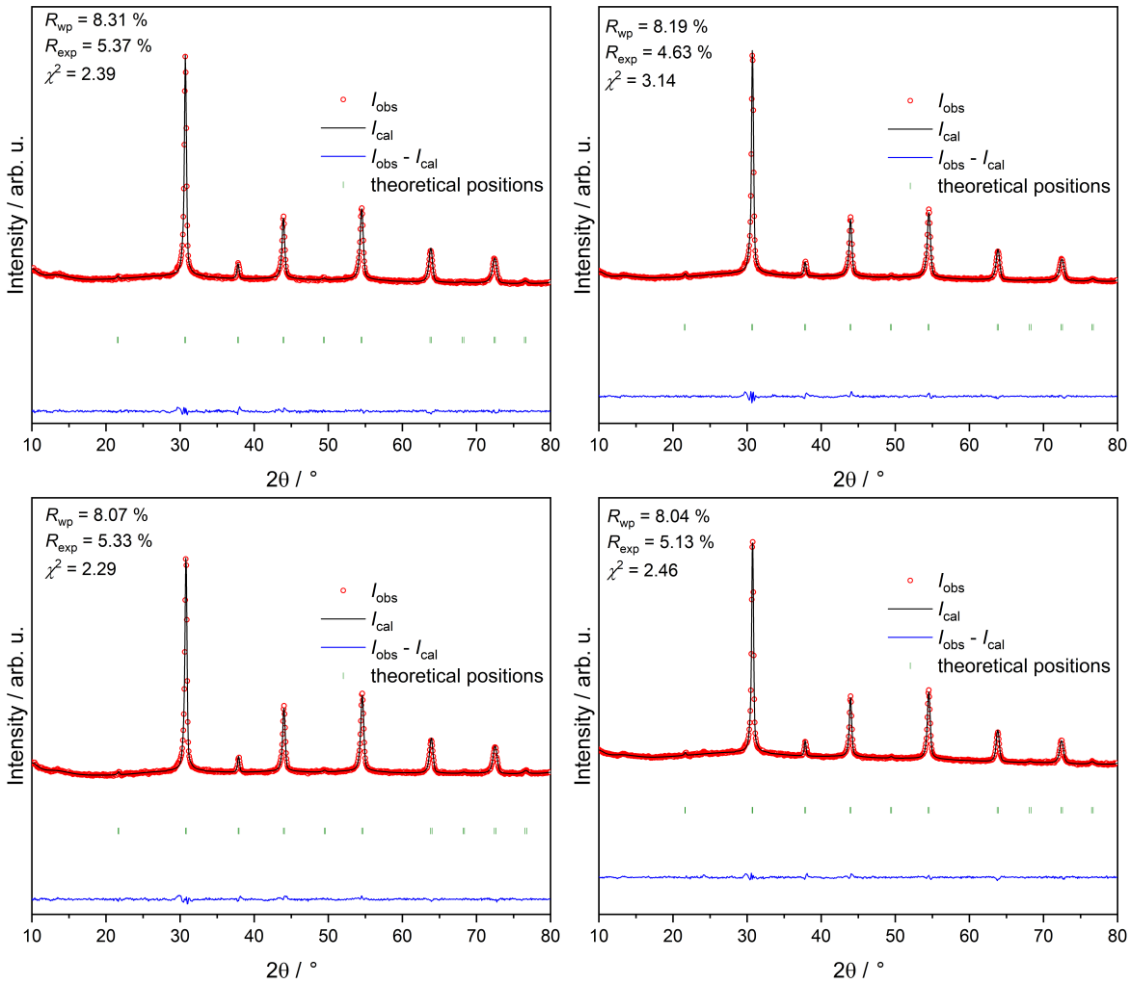

Figure SI 13. *Rietveld refinements of all four N-NF samples after hydrogen evolution reaction with nanofiber diameter of (upper left) 135 nm, (upper right) 156 nm, (lower left) 194 nm, and (lower right) 213 nm.*

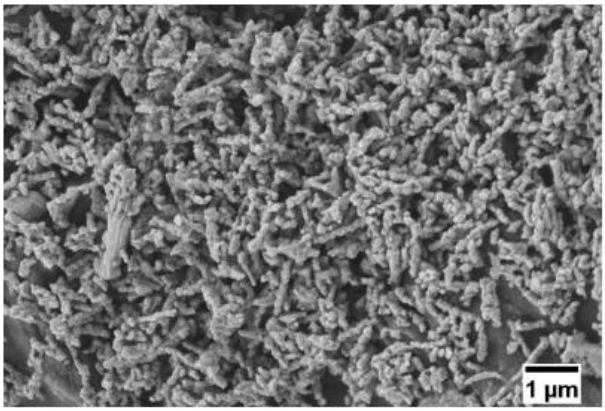

Figure S14. *SEM image of nanofibers with diameter of 213 nm after hydrogen evolution reaction.*

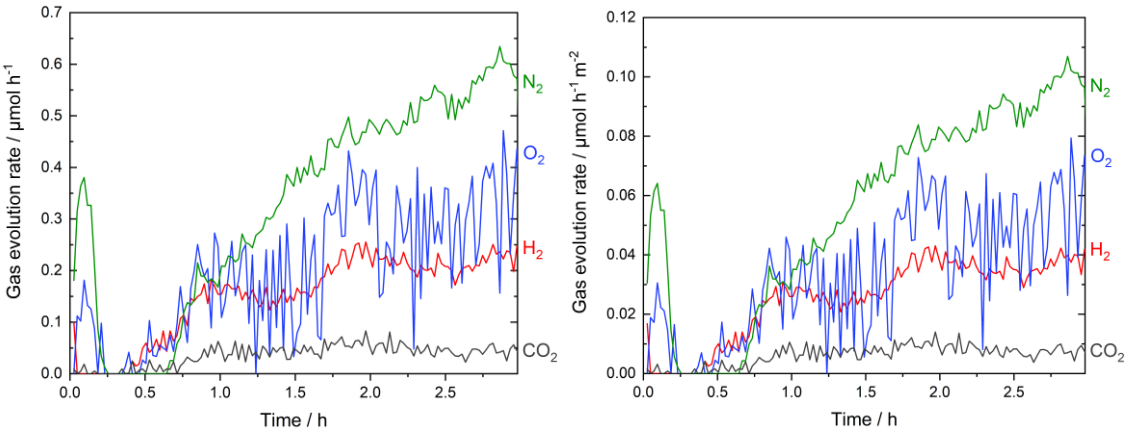

Figure SI 15. *Left: Gas evolution curves in overall water splitting, H_2 (red), O_2 (blue), N_2 (green) and CO_2 (gray) on Pt-CoO_x deposited $BaNbO_2N$-Ba_2NbO_3N nanofiber sample with 213 nm diameter; right: normalized on absolute surface area.*

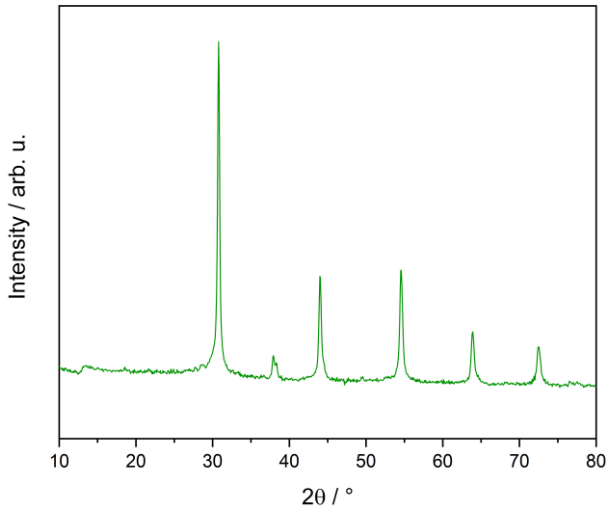

Figure S16. *XRD pattern of nanofibers with diameter of 213 nm after overall water splitting experiment.*

8 Photocatalytic Activity and Electron Storage Capability of TiO_2 Aerogels with Adjustable Surface Area

8.1 Main Manuscript

Alexandra Rose[a,§], Anja Hofmann[b,§], Pascal Voepel[a], Barbara Milow[a], Roland Marschall[b,*]

§: These authors contributed equally to the manuscript.

Published 08 July 2022 in ChemRxiv, Cambridge: Cambridge Open Engage. Published by Cambridge University Press, licensed under Attribution-NonCommercial-NoDerivatives 4.0 International license.

Citation: Rose *et al. ChemRxiv*, DOI: 10.26434/chemrxiv-2021-vxkpq-v3, 2022

Author affiliations [a] German Aerospace Center, Institute of Materials Research, Aerogels and Aerogel composites, Linder Höhe, Köln 51147, Germany

[b] Department of Chemistry, University of Bayreuth, Universitätsstraße 30, Bayreuth 95447, Germany

Author emails: roland.marschall@uni-bayreuth.de

10.26434/chemrxiv-2021-vxkpq-v3

Keywords: TiO_2 aerogel, Electron storage, Photocatalysis, Hydrogen production, Nitrogen reduction

Abstract

Mesoporous TiO_2 aerogels with surface area larger than 600 $m^2 g^{-1}$ have been prepared *via* acid-catalyzed sol-gel synthesis and supercritical drying. Varying temperature treatment in air results in changes in the morphology of the aerogels and their specific surface area. Interestingly, the ability to store photogenerated electrons in the surface states of the aerogels upon illumination of dispersions in water-methanol mixtures increases with lower calcination temperature. Additionally, the extent of electron storage capability also depends on hole scavenger concentration. Increasing the calcination temperature to 500 °C results in decreased surface area and electron storage capability, however in increased hydrogen evolution rates. Finally, nitrogen reduction to ammonia in the dark is performed with photogenerated stored electrons in TiO_2 aerogels, separating the charge carrier photogeneration from the dark reduction reaction.

Introduction

Aerogels are unique 3D mesoporous materials of interconnected porous networks which exhibit high surface areas, open pores and low densities.[1,2] The sol-gel process is a prominent technique to synthesize such aerogels, since it is a simple method and requires no complex setup. Several synthesis parameters can be varied to control the nanoscale structure and physicochemical properties.[3,4] It has been demonstrated that high surface areas could be obtained in amorphous titania aerogels based on chloride and alkoxide precursors followed by hydrolysis and condensation reaction forming a wet gel[5,6] which is further dried e.g. supercritically to prevent the porous structure to collapse.[1] The ability to control the sol-gel process for synthesizing aerogels is a powerful tool for designing a suitable and efficient catalyst. A high specific surface area and open porosity of aerogels favors the adsorption and diffusion of reactants, therefore offers many active reaction sites and their accessibility for photocatalytic reactions.[7] The interconnected network of nanoparticles offers additionally long diffusion pathways for photogenerated electrons.

Aerogels were reported as suitable catalysts for photocatalytic applications, *e.g.* degradation of dyes or organic substances and hydrogen evolution.[8–12] Especially, TiO_2 and composite aerogels are high potential materials for efficient photocatalysis, due to reactive sites and improved charge separation.[13,14] The polymorphic forms of TiO_2, and morphological and structural characteristics were reported as crucial factors for photocatalysis. Different synthesis procedures for TiO_2 aerogels are reported in literature, to improve synthesis parameters and consequently the morphological and structural characteristics with regard to photocatalytic hydrogen evolution. Parayil *et al.* investigated the synthesis parameters using alkoxide precursors for TiO_2 aerogel synthesis *via* high temperature supercritrical drying.[15] Luna *et al.* reported TiO_2 aerogels assembled from crystalline pre-formed nanoparticles which showed an efficient hydrogen generation.[8] Recently, Niederberger *et. al.* presented similar titania-based aerogels and their ability for hydrogen production based on water/methanol vapours.[16] TiO_2-Pt composites were reported by Lin *et al*. and Puskelova *et al.*[17,18] They described the dependency of the hydrogen evolution rate on the Pt particle size and loading on TiO_2, reflecting the number of reactive sites. With intensity-modulated photovoltage spectroscopy and photocurrent spectroscopy measurements on TiO_2 aerogels, synthesized with different weight fractions

of sol-gel precursors, DeSario *et al.* were able to show that trapping sites are the reactive sites in photocatalytic hydrogen generation.[13] This could be concluded due to differences in lifetime and mobility of photogenerated electrons. Hydrogen generation increased with increased sol-gel precursor concentration. By use of UV-Vis and EPR spectroscopy, Di Iorio *et al.* found an improved electron storage capacity for TiO_2 ethanolic sols with an increase of titanium to water molar ratio.[19] Panayotov *et al.* reported that photogenerated electron-hole pairs in TiO_2 aerogels are more efficiently separated compared to commercial TiO_2 nanoparticles and that the density of excited-state electrons is higher in these aerogels.[14] Besides the discussed aerogel structure, the crystal structure also has an influence on the charge carrier lifetime. Sachs *et al.* performed transient absorption spectroscopy measurements on the most commonly used TiO_2 crystals phases, *i.e.* rutile and anatase. They found a faster recombination rate for the rutile crystal phase and that for both polymorphs, the surface recombination is the most important factor for the charge carrier lifetime.[20] There are several examples in the literature which report the storage of photoexcited electrons in semiconductor materials, and the use of these stored electrons for reduction reactions. Bahnemann *et al.* reported the trapping of electrons close to the surface of colloidal TiO_2 with the formation of Ti^{3+} states in presence of a hole scavenger, which was characterized by a broad absorption with a maximum at 650 nm.[21] They performed further investigation on the electron storage of TiO_2. By employing the stopped flow technique and UV-Vis spectroscopy, they investigated the reduction reaction of the stored electrons with silver ions[22], gold ions[23], and other electron acceptors in detail.[24,25] In 2011, they showed for the first time that photoexcited electrons stored in TiO_2 can reduce nitrogen.[26] Since then, reports about the electron storage of different materials[27] including WO_3,[28,29] copper complexes,[30] and carbon nitrides[31] were published. In case of cyanamide-functionalized polymeric networks of heptazine units, 4-methylbenzyl alcohol was necessary as hole acceptor to store electrons in the material. In contrast to this, an aqueous methanol solution with a concentration of 0.02 mol L^{-1} is already enough to extract photoexcited holes and to store photoexcited electrons in TiO_2.[26] The addition of a co-catalyst like Pt or other metal co-catalysts to a photocatalyst storing photoexcited electrons in aqueous solution, lead to the formation of hydrogen.[22,23,31,32] There are also some reports on the storage of photoexcited electrons in photoelectrodes. Amal *et al.* showed

for WO_3 photoelectrodes, that higher calcination lead to improved crystallinity, but lower electron storage. The photocatalytic H_2 evolution activity also increased as long as the contact between WO_3 and the substrate was sufficient.[33] They presented in another work, that WO_3 films can be charged using an electrolyte with alkali cations and that this charges can be used in dark conditions.[28] These films could be also recharged. Kamat *et al.* showed, that photocatalytically deposited Ag on TiO_2 lead to an improved photoelectrochemical performance with about two times higher photocurrent of TiO_2/Ag films compared to none modified TiO_2 films.[34] The authors explained this improved activity by capturing of photogenerated electrons and the more negative Fermi level. They also found a dependency of electron storage on the amount of deposited Ag with an optimum capacity at 8.6 µM for a suspension with 5.8 mM TiO_2. They quantified the stored electrons by titration with methylene blue and found that the electron storage is the best for Ag modified TiO_2 compared to none, Au, and Pt modified TiO_2.

In the present work, we report a detailed investigation on the photocatalytic and electron storage properties of mesoporous TiO_2 aerogels prepared *via* a novel modified acid catalyzed sol-gel synthesis with subsequent supercritical drying and different heat treatments in air. All prepared TiO_2 aerogels exhibit the anatase crystal structure to exclude the influence of a composite formation on the photocatalytic activity and electron storage ability of the aerogels. The influence of the physical properties, especially the surface area and crystallinity, on the ability to store electrons in water-methanol slurry and on hydrogen evolution are discussed in detail. Quantification experiments of the stored electrons via reduction reaction in the dark will be presented. Methanol concentration-dependent measurements on samples with high electron storage ability are presented furthermore. We show the possibility of electron storage optimization by adjustment of crystallinity, surface area, and concentration of sacrificial agent, for which TiO_2 aerogel materials offer the possibility for tailoring surface area and crystallinity in a wide range. *Via* an experiment for nitrogen reduction in the dark yielding ammonia, using such stored electrons as a possible ammonia-on-demand application for the herein synthesized aerogels a highly promising application besides hydrogen generation is presented.

Experimental Section

Chemicals

Titanium (IV) tetraisopropoxide (98%, Merck), hydrochloric acid (37%, ACS reagent, Sigma Aldrich), ethanol (Chemcolute, denatured with MEK, IPA, and Bitrex, 99.8%), methanol (99.9%, Fisher chemical), hexachloroplatinate (IV) hydrate (99.995%, Carl Roth), Hombikat UV 100 (99%, Sachtleben Chemie) were used as received.

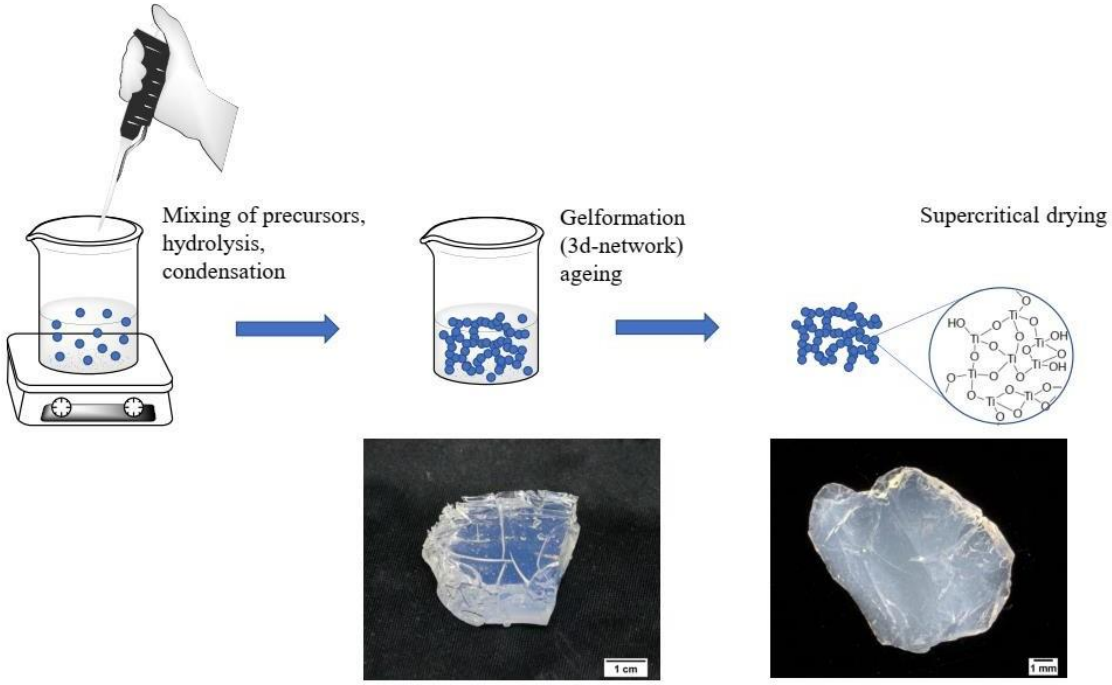

Scheme 1. *Schematic presentation of synthesis procedure and images of TiO_2 wet gel (left) and aerogel (right).*

TiO_2 aerogel synthesis (Scheme 1)

TiO_2 gels were prepared with acid (HCl) catalyzed sol-gel method using titanium (IV) isopropoxide (TTIP) as precursor. The molar ratio of TTIP/ethanol/acid/water was kept constant 1 : 26 : 0.1 : 4. A solution containing TTIP in ethanol (EtOH) was prepared under magnetic stirring at 0 °C. Hydrochloric acid was added after few minutes. Deionized water was added dropwise to the solution. A gel formed after few minutes. Gels were aged for 7 days at 50 °C, then washed in isopropanol four times and dried with CO_2 at supercritical conditions (60 °C, 115 bar, flow rate 15-20 kg/h). As formed aerogels, excluding as-synthesized aerogel, were thermally treated in air at 300 °C, 400 °C, and 500 °C for 10 h (heating rate 10 K min^{-1}).

Characterization

XRD measurements were performed on a Bruker D8 Advance X-ray diffractometer using Cu-Kα radiation source and Lynxeye XE-T detector. The diffraction data were collected in the range of 15-90° 2θ with a step size of 0.01°. The crystallite sizes were estimated using Bruker EVA software by calculating the integral breadth from XRD pattern. Phase quantification and determination of amorphous/crystalline phase was performed by the Rietveld method implemented in Topas using CeO_2 as internal standard.

The specific surface area was determined via N_2 physisorption measurements at 77 K on a Micromeritics 3Flex instrument in a partial pressure range of $0.05 < p/p_0 < 0.3$ using the Brunauer-Emmett-Teller (BET) method. The total pore volume of the samples was obtained from the N_2 desorption isotherms at a partial pressure of 0.98, and the pore size distribution was obtained using Barrett-Joyner-Halenda (BJH) model. Prior to physisorption analysis, the samples were outgassed at 60 °C for 12 h on a Micromeritics VacPrep Gas Adsorption Sample Preparation Device.

SEM images were taken with a Zeiss Ultra 55 electron microscope using an accelerating voltage of 3 kV. The samples were coated with platinum using a Baltec sputter coater prior to measuring.

TEM analysis was performed with a Philips Tecnai F30 operated at 300 kV. D-spacing was determined from TEM images using ImageJ.

A PerkinElmer Lambda 750 UV/vis/NIR spectrometer, equipped with a Praying-Mantis mirror unit from Harrick, was used to record the diffuse reflectance of the powdered aerogels with a step size of 1 nm. The used white standard was a spectralon pellet. The spectra were converted into absorption spectra using Kubelka-Munk function. Tauc plots were used to estimate the band gaps. For the estimation of the absorbance of the dispersions, the spectrometer was equipped with an integrating sphere, and the dispersion was stirred during the measurements of the diffuse reflectance. The spectra were converted to absorbance spectra. Three measurements were performed for every point and error was determined.

Photocatalytic test experiments

For all photocatalytic experiments ultrapure water with TOC = 2 ppb was used. The

experiments were conducted with a 300 W Xe lamp (Quantum Design) in a top-irradiated glass reaction vessel. Measurements were all performed at 20 °C (ECO RE 1050G (Lauda) thermostat) under stirring. The system was flushed with argon 5.0 before the measurements to remove residual air. Detection of the evolved hydrogen was performed every 11 minutes using a GC2014 gas chromatograph from Shimadzu, equipped with a shin carbon ST column (Restek) and a thermal conductivity detector, using argon 5.0 as carrier gas. The argon 5.0 flow rate for the measurements was set to 25 mL min^{-1} with a Bronkhorst mass flow controller.

The hydrogen evolution experiments with Pt photodeposition were carried out with 100 mg aerogel sample dispersed in a mixture of 135 mL water and 15 mL methanol. The dispersion was irradiated for 100 min without co-catalyst. The lamp was turned off and it was waited until no hydrogen evolution was detected anymore, then an aqueous solution of hexachloroplatinate (IV) hydrate was added via rubber sealing without opening the reactor to reach 0.0076 µmol m^{-2}. The lamp was turned on again after the hydrogen evolution peak, and the sample was irradiated for another 100 min. Afterwards the lamp was turned off, and it was waited that the hydrogen evolution was zero. Another amount of hexachloroplatinate (IV) hydrate was added to the calcined aerogel dispersion to reach the same amount of 0.1 wt.-% Pt as for the as-synthesized aerogel sample. The dispersions of the calcined aerogel samples were irradiated again for 100 min, the lamp was turned off and the measurements were stopped after no hydrogen evolution was detected. Photographs of all dispersions were taken before the measurement and after each irradiation step. The samples with Pt deposited were washed with isopropanol three times and centrifuged at 1500 rpm. Then they were dried with CO_2 at supercritical conditions. XRD measurements were performed as described above to determine any changes on the sample.

For the experiments to detect the absorbance of the dispersions, 100 mg of the aerogel sample were dispersed in a mixture of 135 mL of water and 15 mL methanol. After flushing with argon 5.0, a sample of approximately 2.5 mL dispersion was taken and filled in an argon flushed closed cuvette, and the diffuse reflectance was measured in a PerkinElmer Lambda 750 UV/vis/NIR spectrometer, equipped with an integrating sphere under stirring. The aerogel dispersions were afterwards irradiated for 100 min. 2.5 mL of the blueish

dispersion was filled in an argon flushed cuvette and the diffuse reflectance was measured immediately, 30 minutes, and 110 min after the sample was taken.

For the experiments of the dependency of the electron storage ability on the methanol concentration, 100 mg of the as-synthesized aerogel sample were dispersed in 150 mL aqueous methanol solutions with different methanol concentrations ranging from 0.02 mol L^{-1} up to 19.7 mol L^{-1}. The dispersions were irradiated for 100 min. Photographs of the dispersions were taken directly after the irradiation.

For the nitrogen reduction reaction, 100 mg of the as-synthesized aerogel was dispersed in 150 mL of 2.5 mol L-1 aqueous methanol solution. The dispersion was irradiated for 100 min under the same conditions as for the absorbance detection measurements, the argon 5.0 flow rate was set to 50 mL min-1. After the irradiation under argon 5.0, the carrier gas was switched to N_2. The flow rate was set to 50 mL min^{-1} N_2 for 7 h for the nitrogen reduction reaction in the dark. Afterwards a salicylate test was performed to determine the yield of NH_3 quantitatively.[35]

Electron quantification experiments

Electron quantification via Pt^{4+} reduction and hydrogen evolution was performed in the same reactor as described above. The reaction parameters were kept constant to the hydrogen evolution experiments. The argon 5.0 flow rate was set to 100 mL min^{-1}, and the hydrogen gas evolution was detected online using a mass spectrometer (Hiden HPR-20 Q/C) every 13 seconds. The samples were irradiated for 100 min, it was waited until no hydrogen evolution from that irradiation was detected anymore (this time was set to zero). Then 0.1 wt.-% Pt was added to the dispersion *via* a rubber sealing without opening the reactor and it was waited until no hydrogen evolution in the dark was detected anymore.

Results and Discussion

Sample Characterization

The synthesized TiO_2 gel (Scheme 1 left photograph) shows a transparent appearance. After supercritical drying the as-synthesized TiO_2 aerogel (Scheme 1 right photograph) turned into a very light, brittle and translucent aerogel. The translucency in the visible range indicates a small particle size and homogeneous pore distribution,[36] which is confirmed by

the physisorption results shown in **Figure 2**.

X-ray diffraction (XRD) patterns of the as-synthesized and calcined TiO_2 aerogels are shown in **Figure 1.** It can be observed that surprisingly the as-synthesized TiO_2 aerogel (please see *Experimental Section* for details) is semi-crystalline. The broad diffraction peaks represent a high amorphous content, but the main reflections at 25.28° and 48.05° *2θ* agree with the main reflections of anatase TiO_2 (PDF-21-1272). TiO_2 nanostructures which are synthesized using TTIP were reported to be crystalline (anatase) when ambiently dried or dried at e.g. 60°C.[37,38] However, in our case, the TiO_2 gels were, supercritically dried, which generally as reported in literature lead to amorphous aerogels. Varying the synthesis conditions *e.g* type or amount of catalyst, without any addition/assembly of preformed crystalline TiO_2 nanoparticles, the resulting aerogels were reported to be amorphous or only very few crystallites were found.[5,6,8,16,39]

The degree of crystallinity was determined with Rietveld refinement using an internal standard, that indicated a significant crystalline content of TiO_2 anatase in the as-synthesized aerogel (**Table 1**). The degree of crystallinity of the as-synthesized TiO_2 aerogel could be due to the temperature and pressure during the supercritical drying process. It was reported by Moussaoui *et al.* that the drying conditions, such as high temperature, have an impact on the crystalline structure.[40]

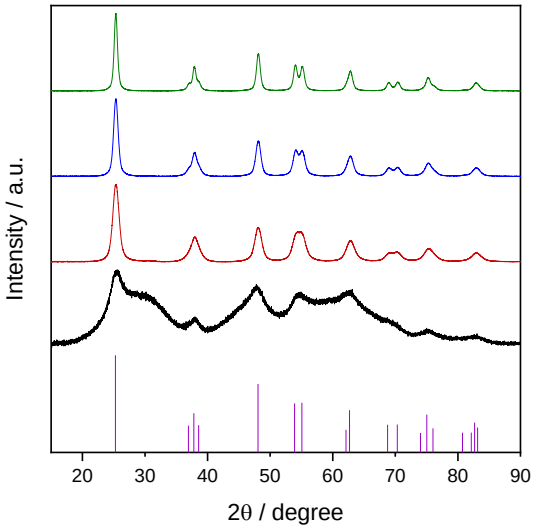

Figure 1. *XRD patterns of the as-synthesized TiO_2 aerogel (black) and aerogels calcined at 300 °C (red), 400 °C (blue) and 500 °C (green). Reference line pattern of anatase TiO_2 (PDF-21-1272) is shown for comparison. Normalized data to the range 0 to 100 related to the highest signal.*

The heat-treated TiO_2 aerogels at 300°C, 400°C and 500°C show reflections which can be

assigned to the TiO_2 anatase crystal structure. No reflections can be assigned to TiO_2 rutile crystal structure, which is ideal for photocatalytic applications, since rutile is usually less active.[41] According to literature, anatase is the most likely occurring crystal structure at the applied calcination temperatures.[6] The anatase-rutile phase transition was reported to occur at temperatures between 400-800 °C.[3] The XRD pattern of the calcined aerogel at 500 °C exhibits well-defined and better resolved reflections compared to the calcined aerogels at 300 °C and 400 °C, respectively. This indicates that the crystallinity increases with the calcination temperature. The crystallite sizes of the aerogels were estimated for (101) preferred oriented anatase TiO_2 in the range of 23°-28° *2*θ. They increase with calcination temperature from 4 nm for the as-synthesized TiO_2 aerogel to 13 nm for TiO_2 aerogel calcined at 500 °C (**Table 1**).

In order to study the influence of the calcination temperature on the degree of crystallinity of TiO_2 aerogels, Rietveld refinement was applied on the XRD data of the prepared samples (**Table 1**). The semi-crystalline structure of the as-synthesized TiO_2 aerogel was confirmed with a maximum crystalline content of approx. 10 wt.%. For calcination temperatures of 300°C-500°C the TiO_2 sample was completely crystallized forming anatase.

Table 1. *Rietveld analysis of the prepared TiO_2 aerogel samples.*

	TiO_2 crystalline phase/anatase wt.%	TiO_2 amorphous phase wt.%	Crystallite size / nm
as-synthesized	10	90	4
300 °C	100	0	7
400 °C	100	0	10
500 °C	100	0	13

The adsorption and desorption isotherms of the as-synthesized and heat-treated TiO_2 aerogels are presented in **Figure 2**. They exhibit a type IVa isotherm with H1 hysteresis loop according to the IUPAC classifications indicating a mesoporous material.[42] The desorption path is in thermodynamic equilibrium and different to the adsorption path, leading to hysteresis which is associated with delayed capillary condensation during adsorption.[43,44] The type H1 hysteresis loop and the steep adsorption branch indicate a uniform and narrow pore size distribution. The adsorbed volume of nitrogen increases strongly at a relative pressure of p/p^0=0.6 for the as-synthesized TiO_2 aerogel before it reaches a plateau,

indicating capillary condensation and saturation. For the heat-treated TiO_2 aerogels the steep adsorption branch occurs at higher relative pressures, in particular the higher the calcination temperature the higher the relative pressure for the increase of adsorbed volume. This indicates larger pores after higher calcination temperatures. This is in good agreement with the pore size distribution shown in **Figure 2 (inset)**.

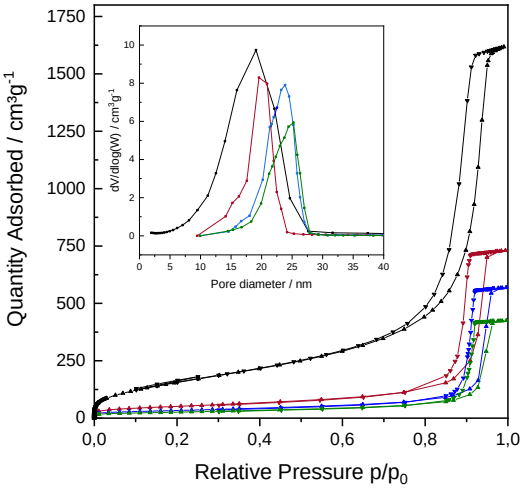

Figure 2. *N_2 physisorption isotherms and BHJ pore size distribution (inset) for the as-synthesized and heat-treated TiO_2 aerogels; as- synthesized TiO_2 aerogel (black) and aerogels calcined at 300 °C (red), 400 °C (blue) and 500 °C (green).*

Table 2. *Nitrogen physisorption results and band gaps of the prepared TiO_2 aerogel samples.*

	BET surface area / $m^2\ g^{-1}$	Cumulative pore volume / $cm^3\ g^{-1}$	Average pore diameter / nm	Band gap/ eV
as-synthesized	600	2.5	19	3.5
300 °C	184	1.1	20	3.3
400 °C	118	0.9	24	3.3
500 °C	92	0.7	25	3.2

A narrow pore size distribution was obtained for the as-synthesized and heat-treated TiO_2 aerogels, whereby the pore size distribution is slightly narrower and the BJH-derived average pore size shifts to larger pore sizes for the heat-treated samples. This is in good agreement with the location of hysteresis loops, which occur at higher relative pressure and in a narrower pressure range for higher calcination temperatures. This can be explained by smaller mesopores (approx. 5-15 nm) which coalesced with larger mesopores (approx. 20 nm). The reduced number of smaller mesopores could also explain the decreased surface area after heat-treatment, as smaller pores contribute more to higher surface

areas.[6]

The physisorption results are summarized in **Table 2**. It shows the effect of calcination temperature on the specific surface area and cumulative pore volume. The as-synthesized TiO_2 aerogel exhibits high specific surface area and pore volume of 600 m^2/g and 2.5 cm^3/g, respectively. The supercritical drying process preserves the mesoporous structure of the as-synthesized TiO_2 aerogel leading to the observed high values. Similar results have been reported in literature by Sadrieyeh *et al.*, however the aging time could be reduced from >40 days to 7 days during synthesis here, achieving a stable and translucent TiO_2 aerogel.[6] As expected, the surface area as well as the pore volume decrease for the heat-treated TiO_2 aerogel at 300 °C. The surface area and pore volume show a further decrease for the TiO_2 aerogels heat-treated at 400 °C and 500 °C, indicating a decrease in porosity. This is in accordance with the results reported in literature for calcined aerogel samples.[6] Even though the calcination of the TiO_2 aerogel reduced the specific surface area and porosity, both are higher compared to conventional bulk anatase, and therefore it is beneficial using the investigated sol-gel synthesis conditions and supercritical drying for TiO_2 aerogel synthesis.[6]

Figure 3 shows the SEM images of the different TiO_2 aerogels at two different magnifications. The as-synthesized sample (a) shows mainly a smooth surface. The high magnification SEM image (b) shows small, nearly spherical interconnected particles which form an open porous network. This is highlighted with dotted lines in **Figure 3b**. **Figure 3** c-h show the SEM images of the heat-treated TiO_2 aerogels at 300 °C, 400 °C and 500 °C. The images show also a smooth uniform surface of the samples, however the porosity of the samples decreases with higher calcination temperature, which is visible through the fewer and larger voids/pores between the particles and denser appearance of the microstructure. The particles become larger with higher calcination temperature and seem to be arranged more densely.

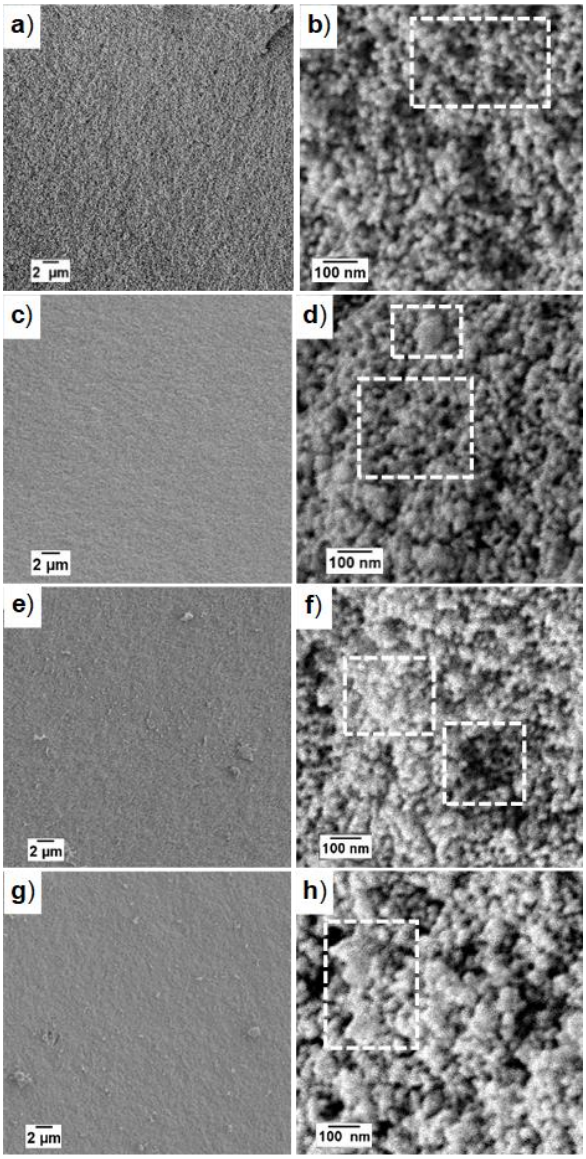

Figure 3. *SEM images of the a-b) as-synthesized aerogel, c-d) calcined aerogel at 300 °C, e-f) calcined aerogel at 400 °C, g-h) calcined aerogel at 500 °C, at lower (5.000x) and higher (100.000x) magnification.*

In **Figure 3d** small pores are still visible but also larger particles at 300 °C calcination temperature compared to the as-synthesized sample. The effect of higher calcination temperature leading to larger pores and denser microstructure gets clearly visible at 400 °C calcination temperature in the highlighted areas in **Figure 3f**. The particle size increases at 500 °C calcination temperature, which is highlighted in **Figure 3h**. These results are in good agreement with the N_2 physisorption results in **Figure 2** and **Table 2**.The as-synthesized TiO_2 aerogel was further analyzed using TEM, to confirm the observed semi-crystalline structure. **Figure 4** shows the TEM images of the as-synthesized TiO_2 aerogel at different

magnifications. Amorphous particles and nanocrystals can be observed. This is in good agreement with the XRD results shown in **Figure 1**, where a semi-crystalline structure was assumed. The TEM image shows the interconnected particles and nanocrystals in the porous network. It can be assumed that the particles in the aerogel network are connected by chemical means, rather than physical connection as in P25 nanopowder. This is advantageous for photocatalytic hydrogen evolution, as this could improve the separation of charge carriers. It was reported that the interconnected structure of TiO_2 nanocrystals offers better charge carrier delocalization compared to TiO_2 nanoparticle aggregates, e.g. P25 which are physically connected.[17,45] The inset in **Figure 4** shows the d-spacing which was estimated 0.35 nm for the observed nanocrystals. This fits to the (101)-oriented anatase TiO_2 phase and confirms the semi- crystalline nature of the as-synthesized TiO_2 aerogel.

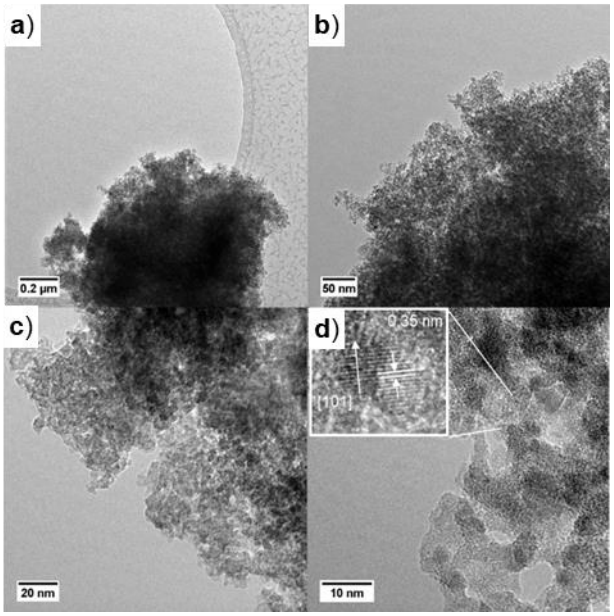

Figure 4. *TEM images of as-synthesized TiO_2 aerogel, a) 12.000x, b) 39.000x, c) 115.000x, d) 295.000x, the inset is a local enlargement of TiO_2 nanocrystal.*

The size of the nanocrystals was estimated approx. 4-6 nm, which is slightly larger compared to the calculated grain size from XRD pattern (approx. 4 nm). This partial crystallinity is confirmed via basic Rietveld refinement. The amount of amorphous phase is decreased via heat treatment from initial 10 wt.% for the as-synthesized aerogel to none (within the boundaries of the error).

Absorption spectra in diffuse reflectance were recorded to characterize the optical

properties of the TiO_2 aerogels. Diffuse reflectance spectra was converted to Kubelka-Munk spectra and Tauc plots for band gap estimation (**Figure S1**). **Table 2** shows the estimated band gaps of the aerogel samples. The bandgap of the untreated TiO_2 aerogel is with 3.5 eV slightly higher than the bandgap of the calcined aerogels with 3.2 to 3.3 eV, which was expected as it is a partially amorphous sample. For all aerogels, only one sharp absorption edge at 340 to 375 nm is visible in the UV-vis spectra, indicating that no by-phases are formed. The estimated bandgaps are in correspondence with the reported literature values for anatase TiO_2 with 3.2 eV.[45,46]

Photocatalytic electron storage and hydrogen generation

Photocatalytic experiments were performed with all TiO_2 aerogel samples to investigate the influence of the physicochemical properties of the aerogels on the electron storage capability and photocatalytic activity (**Figure 5**). For this, 100 mg aerogel were dispersed in 150 mL of a 2.5 mol L^{-1} aqueous methanol solution, and were irradiated with a 300 W Xe lamp (see *Experimental Section*). The samples were first irradiated for 100 minutes without a co-catalyst. Then the lamp was turned off to show that the hydrogen evolution is really a photocatalytic effect, indicated by a decrease in the hydrogen evolution rate as no more charge carriers are generated. The color change of the dispersions is shown in the graph (**Figure 5**) going from a colorless dispersion to a blueish colored dispersion after irradiation. Enlarged versions of the photographs are given additionally in the *Supporting information* (**Figure S2** SI). This blue coloration is an indication of the storage of electrons and formation of Ti^{3+} states.[22,24,26,47] Their recombination is inhibited due to the use of methanol as hole scavenger, reacting fast with photogenerated holes to be oxidized.[21]

The intensity of the blue color decreases with increasing calcination temperature of the aerogels, and therefore also with the surface area of the TiO_2 aerogel samples. Meanwhile, the amounts of detected hydrogen are very low (below 10 µmol h^{-1}), as expected for unmodified TiO_2. Indeed, the sample with the smallest surface area - calcined at 500 °C - offers the best hydrogen evolution rate up to 3.2 µmol h^{-1}. It can be assumed that besides the improved crystallinity confirmed by XRD, the interconnection of the TiO_2 nanocrystals in the aerogels improves by higher calcination temperature, which is advantageous for the photocatalytic hydrogen production, as the charge carrier separation seems to be

improved. This finding is comparable to results by Amal *et al.* on WO_3 photoelectrodes, where higher calcination lead to improved crystallinity, better charge transportation (lower electron storage) and therefore higher photocatalytic H_2 evolution.[33] The heat-treatment can also reduce the amount of bulk defects, which are recombination centers. Kong *et al.* reported a reduced bulk to surface defect ratio and increased photocatalytic activity for TiO_2 nanocrystals, which were calcined compared to TiO_2 nanocrystals, which were prepared without a calcination step.[48]

After the lamp was switched off and the hydrogen evolution went to zero due to no more charge carrier generation, an aqueous H_2PtCl_6 solution was added to the blueish dispersions *via* rubber sealing (to keep the inert atmosphere in the reactor), to achieve Pt decoration *via* subsequent photodeposition. However, even without light irradiation but few seconds after the addition of the co-catalyst precursor solution, the coloration of the dispersion disappeared. At the same time, a sharp peak in the hydrogen evolution rate was detected in all four cases even without light irradiation (sharp peak after 3 hours in Figure 5). The intensity of this hydrogen evolution peak without light irradiation has the same trend as the intensity of the blueish color of the dispersion: The darker the dispersion before H_2PtCl_6 addition, the higher the hydrogen evolution peak after the addition, up to 20 µmol h^{-1} if a gas chromatograph is used for the detection of hydrogen every ~11 min.

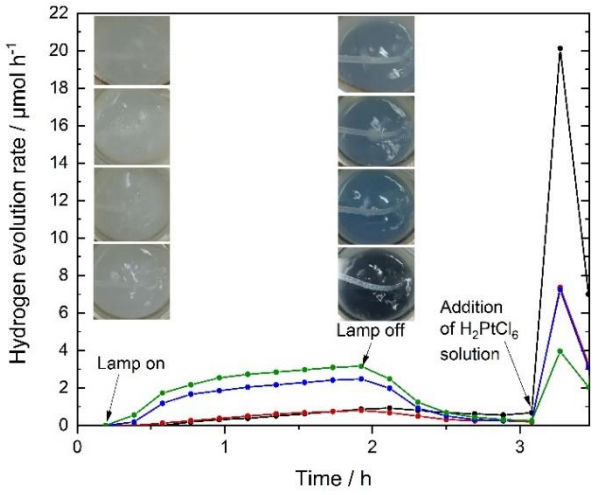

Figure 5. *Hydrogen evolution rates over time of the as-synthesized (black) and calcined TiO_2 aerogels, 300 °C (red), 400 °C (blue), 500 °C (green); Measured without co-catalyst for the first 100 min; measured with 0.0076 µmol m^{-2} Pt as co-catalyst (≙ 0.1 wt.-% for the as-synthesized sample) for approx. 30 min without irradiation. The photographs show the dispersions before irradiation, and after 100 min irradiation with 500 °C, 400 °C, 300 °C and as-synthesized sample from top to bottom.*

This hydrogen evolution rate peak can be explained by the photogenerated and stored electrons in the aerogel sample being used to form metallic Pt clusters on the TiO_2 aerogels upon H_2PtCl_6 reduction. After all Pt ions are reduced and formed Pt metal nanoparticles, a Schottky contact is formed between Pt and TiO_2, upon which the excess stored electrons in the aerogels are transferred to the Pt metal particles, were they are used to reduce protons to hydrogen acting as co-catalysts. This is then detected as the sharp peak in the hydrogen evolution rate curve. This kind of mechanism was already reported before for different metal co-catalyst deposition on TiO_2.[22,23,47,49] The intensity of this peak is therefore - beneath the intensity of the blue color – an indication for the amount of stored electrons. Furube *et al.* reported an improved charge carrier separation by Pt deposition on TiO_2 by use of transient absorption spectroscopy, which additionally explains the enhancement of the hydrogen evolution rate.[50]

The electron storage capability of the aerogels can be related to their physicochemical properties. The as- synthesized partially amorphous sample with the highest surface area can store the most electrons indicated by the most intense blue coloration. Ikeda *et al.* reported that electrons are trapped at defective sites in TiO_2 e.g. oxygen vacancies, which are mainly located at the surface of TiO_2. They state that the quantity of accumulated electrons represents the number of defective sites.[51] The as-synthesized aerogel can therefore store the most photocharged electrons due to the highest surface area and presumably highest amount of surface defects, due to its low heat treatment. An increase in the heat treatment and decrease in surface area results in a decreased amount of stored electrons.

In case of the semi-crystalline as-synthesized TiO_2 aerogel, more electrons are stored in the material and are not used for the hydrogen evolution, as can be seen in the coloration of the dispersion. This is an indication that the electrons are trapped in surface defects and not in bulk defects, where electrons would recombine with holes. Surface defects are on the one hand charge carrier traps and on the other hand adsorption sites for methanol as hole scavenger.[48] Electrons are trapped, recombination is prevented by the fast and efficient reaction of the holes with methanol, which makes the untreated aerogel the best electron storage material in this study. Heat treatment seems to reduce the amount of surface defects and bulk defects leading to reduced electron storage, but improved charge carrier

separation and hydrogen evolution.

The dependence on the heat treatment of the aerogel can be seen also in the photocatalytic hydrogen evolution rates after co-catalyst deposition (**Table 3**). After the deposition of the co-catalyst, no blue coloration of the dispersion can be observed anymore (**Figure S2**), as the electrons are transferred to the formed metallic Pt particles where they are used for the hydrogen evolution and not stored in the material. All samples exhibit the same amount of co-catalyst, nevertheless a clear difference in the activity is observed. As the Pt particles prevent the storage of the electrons in surface defect states, the difference in the activity can be explained by the heat treatment and the amount of bulk defects. The heat-treated aerogels show a decreased charge carrier recombination and therefore higher activity compared to the semi-crystalline aerogel. This can be explained by the decreased number of surface and bulk defects due to the calcination process as well as the photocatalytic activity of exposed facets of the crystalline phase.[52] The photocatalytic activity is also improved by the sintered and chemically linked TiO2 nanoparticles, due to the wide distribution and therefore better separation of charge carriers, up to 340 µmol h^{-1} for the aerogel calcined at 500 °C (**Table 3**).[17]

Table 3. *Hydrogen evolution rates of the prepared TiO_2 aerogel samples.*

	Hydrogen evolution rate (with 0.1 wt.-% Pt) / µmol h^{-1}
as-synthesized	25.5
300 °C	176.5
400 °C	279.2
500 °C	331.8

The TiO_2 aerogels were all regained after the photocatalytic hydrogen experiments by washing and supercritical drying. XRD pattern after the photocatalytic hydrogen production experiments are shown in **Figure S3**. The XRD pattern of the heat treated aerogels show no changes, the small amounts of Pt added are not visible. Interestingly, the as-synthesiszed aerogel sample exhibits more pronounced reflections than before the experiments, but offers still a semi-crystalline character. Rietveld refinement indicated an increase of crystallinity of the as-synthesized TiO_2 aerogel after UV irradiation/photocatalytic hydrogen experiment from approx. 10 wt.-% to 40 wt.-% crystalline content. Zywitzki *et al.* already showed that amorphous TiO_2 can be prepared by an UV-light mediated synthesis using

$Ti(OEt)_4$ as titanium alkoxide precursor. The increase of crystallinity of the as-synthesized aerogel after UV-light exposure could be related to the UV irradiation with the Xe lamp used in the experiment. This will be further investigated in future studies.[47] Commercial anatase nanoparticles were measured in comparison to the as-synthesized TiO_2 aerogel to show the benefit of the aerogel prepared in the present work (**Figure S4**). The as-synthesized aerogel exhibits a better electron storage ability shown by the intense coloration compared to commercial anatase nanoparticles. The coloration of the commercial anatase nanoparticles is comparable to the coloration of the calcined aerogels. The BET surface area and XRD of the commercial anatase was also measured for comparison. The determined BET surface area is 311 $m^2 g^{-1}$. The XRD pattern is comparable to the 300 °C calcined aerogel sample with a comparable crystallite size (**Figure S5)**.

We showed that the material properties of the aerogels have a direct influence on the electron storage capability. To verify the differences in the amount of stored electrons in the aerogel samples, quantification of the stored electrons was done *via* the reduction reaction of Pt^{4+} to Pt^0 in the dark with high resolution detection of the evolved hydrogen evolution peak with a mass spectrometer every 13 seconds. Pt is one of the best candidates for this since the large work function of Pt (low Fermi level) forces the electrons to be transferred to Pt (trapping of electrons) as a Schottky contact between Pt and TiO_2 is formed.[53] Furthermore, Pt shows the lowest activation energy for H_2 evolution. Therefore Pt was chosen for the experiments in the dark.[54] **Figure 6** shows the hydrogen evolution peak after addition of 0.1 wt.-% Pt to the dispersed aerogel samples irradiated for 100 minutes. Additionally, the quantification was done for the commercial anatase nanoparticles for comparison. For this investigation, we make the viable assumption that all Pt^{4+} is reduced to Pt^0 and that the remaining stored electrons are used only for the hydrogen evolution reaction, no other reaction partners are present. Thus, the amount of stored electrons can be quantified. Moreover, no oxidation reaction is expected here, since it occurred already during the charging process (oxidation of methanol while storing the photogenerated electrons).

As the amount of added Pt solution is for all samples the same, the amount of stored electrons needed for the reduction of Pt^{4+} to Pt^0 is for all samples 2 µmol. The amount of evolved hydrogen differs, depending on the amount of stored electrons.

As expected, the dark hydrogen evolution of the as-synthesized aerogel in Figure 6 is the highest in comparison to the calcined aerogels and to the commercial anatase nanoparticles, and decreases with the calcination temperature. This fits to the intensity of blue coloration – the amount of Ti^{3+} – in the photographs in Figure 5, which decreases with increasing calcination temperature.

By integration of the hydrogen signal, the amount of electrons can be quantified. Two electrons are needed to evolve one mole of hydrogen. **Table 4** shows the result of the quantification experiments. The sum of the electrons used for the reduction of Pt^{4+} to Pt^0 and the hydrogen evolution equals the amount of stored electrons in the sample. The amount of stored electrons is in the range of 22.0 µmol for the as-synthesized aerogel and get lower from 11.6 µmol down to 4.8 µmol for the calcined aerogels. The commercial anatase nanoparticles store 13.0 µmol of electrons, which in the same range as for the 300 °C calcined aerogel. The difference in the surface area – 311 $m^2\ g^{-1}$ compared to 184 $m^2\ g^{-1}$ for the aerogel – does not have such a high influence on the electron storage ability than for the aerogel samples. Here, the different preparation conditions of the commerical anatase sample has to be taken into account, when comparing the commercial anatase nanoparticles with the aerogel samples. It seems that the crystallinity has a stronger influence on the electron storage ability for the commericial anatase than for the aerogel, where the surface area has the prominent effect on the electron storage ability. The dependency of the electron storage ability on the crystallinity was shown before for WO_3 electrodes.[33] Compared to the commercial anatase nanoparticles, the as-synthesized aerogel stores 1.7 times more electrons. As expected, the aerogel calcined at 500 °C stores the smallest amount of electrons with 4.8 µmol – 0.22 times of the as-synthesized aerogel – but shows the highest hydrogen evolution activity in the hydrogen evolution experiments with 4 times that of the as-synthesized aerogel without a co-catalyst.

The percentage of Ti^{3+} states – presumably the amount of stored electrons – formed in the 100 mg of TiO_2 aerogels and commercial anatase nanoparticles was also calculated (Table 4) and ranges from 0.4 % for the calcined aerogel at 500 °C to 1.8 % for the as-synthesized aerogel. The percentage of Ti^{3+} formed in the commercial anatase nanoparticles is 1.0 %.

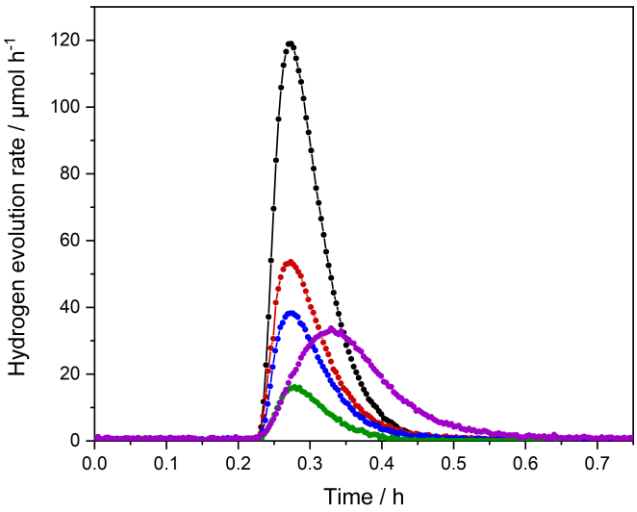

Figure 6. *Hydrogen evolution rates in the dark for the quantification of stored electrons in the as-synthesized (black), 300 °C (red), 400 °C (blue), and 500 °C (green) TiO_2 aerogel and in commercial anatase (purple) for comparison. The samples were irradiated for 100 min and it was waited that H_2 evolution was 0 µmol h^{-1} (this time was set to 0 h here), for a stable baseline for curve integration, then Pt solution was added after 0.2 h to reach 0.1 wt.-% and the hydrogen evolution was measured until no evolution was detected anymore.*

Table 4. *Amount of stored electrons, quantified by the reduction of Pt^{4+} to Pt^0 in the dark and measurement of evolved H_2 and percentage of Ti^{3+} states after charging for 100 min.*

	Amount of electrons by Pt^{4+} reduction (0.1 wt.- %) / µmol	Amount of electrons from H_2 evolution /µmol	Sum of amount of electrons from Pt^{4+} reduction and H_2 evolution / µmol	Percentage of Ti^{3+} states after charging / %
as-synthesized	2	20.0	22.0	1.8
300 °C	2	9.6	11.6	0.9
400 °C	2	7.1	9.1	0.7
500 °C	2	2.8	4.8	0.4
commercial anatase	2	11.0	13.0	1.0

Additionally to the quantification of the electrons, the absorbance of the aerogel dispersions was measured in the range between 350 nm to 800 nm before and after irradiation of the experiment shown in Figure 5. To detect the time-dependent fading in the absorbance of the dispersions, the absorbance was determined directly after the irradiation for 100 min, 30 min after irradiation stop, and 110 min after irradiation (**Figure S6**). For this test, dispersions of 100 mg of the TiO_2 aerogel in 150 mL of a 2.5 mol L^{-1} aqueous methanol solution were irradiated. The increase in absorption of the dispersions after the

irradiation for 100 min (charging) was detected at a wavelength of 600 nm and compared to the absorbance of the dispersion before irradiation (**Figure7**). The absorbance increase directly after irradiation for 100 min is most prominent in the as-synthesized aerogel and the aerogel calcined at 300 °C, being lower for higher calcination temperatures of the aerogel. This is in good agreement to the photographs taken and shown in Figure 5. A decay in absorbance increase after irradiation is most prominent for the sample calcined at 300 °C, and also detectable in the as-synthesized aerogel. For higher calcined samples, hardly any decay of the absorption increase is detectable in the investigated time range. The decay in the absorbance is attributable with a decreasing amount of stored electrons in the aerogel sample, which can be due to charge carrier recombination or either reduction reaction. Electron storage is preferred in aerogel samples with lower heat treatment, which goes directly in line with reduced rates for photocatalytic hydrogen evolution, in accordance with the photocatalysis results.

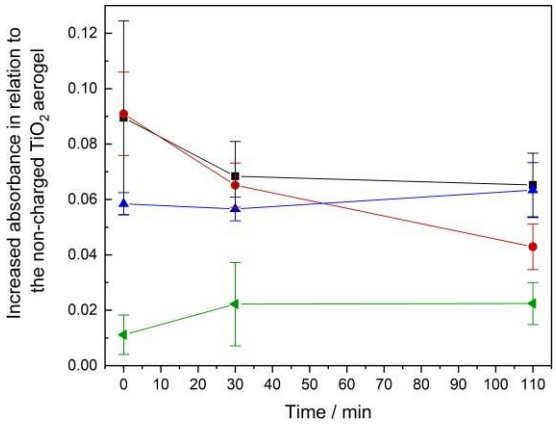

Figure 7. *Absorption changes measured after charging of as-synthesized (black) and calcined TiO_2 aerogels, 300 °C (red), 400 °C (blue), 500 °C (green) (top). The increase in absorbance at 600 nm after 100 min irradiation (charging, = 0 min) is given, followed by two additional measurements (30 min or 110 min after irradiation, respectively) without irradiation indicating color fading (bottom).*

Since the results lead to the conclusion that the as-synthesized aerogel seems to offer the best electron storage ability, further experiments were performed with this sample.

The influence of electron storage ability on the methanol concentration was additionally tested. Dispersions of 100 mg of the aerogel in 150 mL aqueous solution with different methanol concentrations ranging from 0.02 mol L^{-1} up to 19.7 mol L^{-1} were irradiated for 100 min while simultaneously hydrogen evolution was detected. Additionally, photographs of the dispersions were taken directly after the irradiation (**Figure 8**), enlarge versions of

the photograph are given in the *Supporting Information* (**Figure S7**). All dispersions show the typical blue coloration as indication of the storage of electrons and formation of Ti^{3+} states. Only a very slight coloration and presumably small amount of stored electrons are visible for the lowest methanol concentration of 0.02 mol L^{-1} after irradiation for 100 min. This goes in line with a negligible amount of evolved hydrogen. For all other methanol concentrations higher than 0.02 mol L^{-1}, a comparable hydrogen evolution rate between 0.8 and 1.1 µmol h^{-1} is detected. The higher the methanol concentration, the darker is the coloration of the dispersion after the same time of irradiation. Thus, the amount of stored electrons can be adjusted by the used methanol concentration. The higher the concentration of the hole scavenger is, the higher the amount of stored electrons, with hardly any changes in hydrogen evolution rates. From these results, it can be assumed that in case of very small amount of hole scavenger, the recombination rate at the surface defects is increased as the holes cannot react with methanol before recombining with trapped electrons. The higher the concentration of the hole scavenger, the more methanol can adsorb on surface defects and the charge carrier recombination is strongly reduced, which is visible in an increased coloration of the dispersion – an increased number of stored electrons and therefore Ti^{3+} states in the sample. This further supports the results from the hydrogen evolution experiments. These results pave the way for future hydrogen-on-demand application, when charging and hydrogen evolution can be spatially and timely separated.

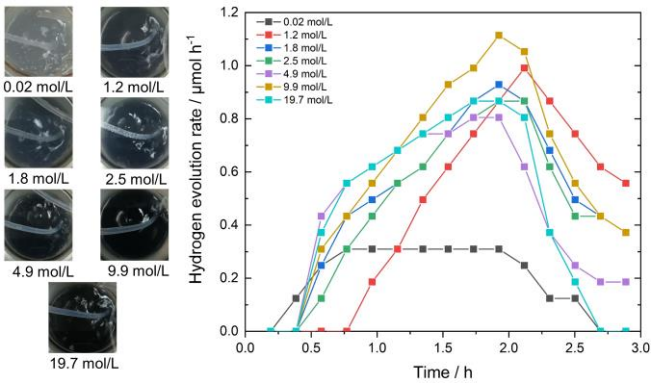

Figure 8. *Hydrogen evolution rates over time of the as-synthesized TiO_2 aerogel dispersed in aqueous methanol solutions with different methanol concentrations, plus photographs of the dispersions after an irradiation time of 100 min. Irradiation was stopped after 100 min.*

A material like the here presented as-synthesized TiO_2 aerogel with high electron storage

ability and high amount of surface defects offers the possibility to apply it for other reactions, for example in dark reduction reactions of very stable molecules. One of the currently most investigated reactions of this type is for example the nitrogen reduction reaction.[55,56] Surface oxygen vacancies can be beneficial for the N_2 adsorption and conversion, which makes the as-synthesized TiO_2 aerogel an interesting material for this research area.[57] Furthermore, Bahnemann *et al.* showed in 2011 that photoexcited electrons stored in TiO_2 colloids can reduce N_2.[24] Therefore, a similar experiment with the as-synthesized TiO_2 aerogel was performed. 100 mg of the as- synthesized aerogel sample was dispersed in 150 mL of an aqueous 2.5 mol L^{-1} methanol solution and irradiated for 100 min under argon to store electrons in the sample. Subsequently, the lamp was turned off and the gas was switched to nitrogen, flushing through the dispersion for 7 hours. Afterwards, a salicylate test was performed to determine the amount of produced ammonia. **Figure S8** shows the absorbance spectra of this salicylate test. An absorbance peak is visible after the reaction time of 7 hours (no signal without N_2), which related to an obtained ammonia yield of 5 µg L^{-1}. This initial positive test for dark nitrogen reduction reaction with stored photogenerated electrons on an as-synthesized TiO_2 aerogel sample gives rise to future research work on such aerogels for photocatalytic ammonia generation, in which the mechanism for this dark reaction will be investigated, too. Nevertheless, it opens up possibilities to optimize reaction conditions for the charging process and the dark reduction reaction separately in the future.

Conclusion

Mesoporous TiO_2 aerogels with large surface areas were prepared *via* acid-catalyzed sol-gel synthesis and supercritical drying. As-synthesized and calcined TiO_2 aerogels at 300, 400 and 500 °C exhibit surface area of 600, 184, 118 and 92 m^2 g^{-1}, respectively. Interestingly, even without calcination, the as-synthesized aerogel is partly crystalline with anatase crystallites.

TiO_2 aerogels are able to store photogenerated electrons in surface trap states upon illumination in water- methanol dispersions. The capacity to store photogenerated electrons increases with lower calcination temperature. Furthermore, the extent of

electron storage also depends on the methanol scavenger concentration. The amount of stored electrons for a constant methanol concentration was quantified by Pt^{4+} reduction and showed a maximum amount of stored electrons of 22 µmol for the as-synthesized TiO_2 aerogel. The as-synthesized aerogel stores 1.7 times more electrons than commercial anatase nanoparticles.

Increasing the calcination temperature to 500 °C results in decreased surface area, however in strongly increased hydrogen evolution rates in photocatalytic experiments.

Finally, nitrogen reduction to ammonia in the dark was performed with photogenerated stored electrons in TiO_2 aerogels as a first proof of concept, separating the charge carrier photogeneration from the nitrogen reduction reaction. This result paves the way for future application of such tailored and cheap TiO_2 aerogels in solar fuel-on-demand processes.

Acknowledgements

We thank Judith Zander (University of Bayreuth) for support in the NRR experiment, Lion Schumacher (University of Bayreuth) for XRD measurement, and Jonas Jungmann (University of Bayreuth) for physisorption measurement of the commercial anatase nanoparticles, Markus Heyer (DLR) for support in supercritical drying, Dr. Peter Mechnich (DLR), and Alexander Francke (DLR) for support in X-ray quantitative phase analysis.

Conflict of interest

The authors declare no conflict of interest.

Associated Content

Supporting Information

The Supporting Information is available: Tauc plots, supporting XRD patterns, photographs of charged aerogels, Absorbance measurements of the four TiO_2 aerogels dispersions, NRR experiment

Author Information

Corresponding Author:

Prof. Dr. Roland Marschall (ORCID: 0000
0002-1057-0459) Department of Chemistry,
University of Bayreuth Universitätsstraße

30, Bayreuth 95447, Germany
E-mail: roland.marschall@uni-bayreuth.de

Authors

Alexandra Rose
Dr. Pascal Voepel (ORCID:0000-0001-8233-7261)
Prof. Dr. Barbara Milow (ORCID: 0000-0002-6350-7728)
German Aerospace Center, Institute of Materials Research, Aerogels and Aerogel composites Linder Höhe, Köln 51147, Germany

Anja Hofmann
Department of Chemistry,
University of Bayreuth
Universitätsstraße 30, Bayreuth
95447, Germany

References

(1) Hüsing, N.; Schubert, U. Aerogels - Airy Materials: Chemistry, Structure, and Properties. *Angewandte Chemie - International Edition*. Wiley-VCH Verlag 1998, pp 22–45. https://doi.org/10.1002/(sici)1521- 3773(19980202)37:1/2<22::aid-anie22>3.0.co;2-i.

(2) Alwin, S.; Sahaya Shajan, X. Aerogels: Promising Nanostructured Materials for Energy Conversion and Storage Applications. *Materials for Renewable and Sustainable Energy*. Springer Science and Business Media Deutschland GmbH July 2020, p 3. https://doi.org/10.1007/s40243-020-00168-4.

(3) Song, K. C.; Pratsinis, S. E. Control of Phase and Pore Structure of Titania Powders Using HCl and NH 4 OH Catalysts. *J. Am. Ceram. Soc.* **2001**, *84* (1), 92–98. https://doi.org/10.1111/j.1151-2916.2001.tb00613.x.

(4) Choi, H.; Carboni, M.; Kim, Y. K.; Jung, C. H.; Moon, S. Y.; Koebel, M. M.; Park, J. Y. Synthesis of High Surface Area TiO2 Aerogel Support with Pt Nanoparticle Catalyst and CO Oxidation Study. *Catal. Letters* **2018**, *148* (5), 1504–1513. https://doi.org/10.1007/s10562-018-2355-y.

(5) Schäfer, H.; Milow, B.; Ratke, L. Synthesis of Inorganic Aerogels via Rapid Gelation Using Chloride Precursors. *RSC Adv.* **2013**, *3* (35), 15263–15272. https://doi.org/10.1039/c3ra41688g.

(6) Sadrieyeh, S.; Malekfar, R. The Effects of Hydrolysis Level on Structural Properties of Titania Aerogels. *J. Non. Cryst. Solids* **2017**, *457*, 175–179. https://doi.org/10.1016/j.jnoncrysol.2016.11.031.

(7) Anderson, M. L.; Stroud, R. M.; Morris, C. A.; Merzbacher, C. I.; Rolison, D. R. Tailoring

Advanced Nanoscale Materials through Synthesis of Composite Aerogel Architectures. *Advanced Engineering Materials*. Wiley-VCH Verlag 2000, pp 481–488. https://doi.org/10.1002/1527-2648(200008)2:8<481::AID-ADEM481>3.0.CO;2-O.

(8) Luna, A. L.; Matter, F.; Schreck, M.; Wohlwend, J.; Tervoort, E.; Colbeau-Justin, C.; Niederberger, M. Monolithic Metal-Containing TiO2 Aerogels Assembled from Crystalline Pre-Formed Nanoparticles as Efficient Photocatalysts for H2 Generation. *Appl. Catal. B Environ.* **2020**, *267*, 118660. https://doi.org/10.1016/j.apcatb.2020.118660.

(9) Parale, V. G.; Kim, T.; Phadtare, V. D.; Yadav, H. M.; Park, H. H. Enhanced Photocatalytic Activity of a Mesoporous TiO 2 Aerogel Decorated onto Three-Dimensional Carbon Foam. *J. Mol. Liq.* **2019**, *277*, 424–433. https://doi.org/10.1016/j.molliq.2018.12.080.

(10) Kim, T.; Parale, V.; Jung, H.-N.-R.; Kim, Y.; Driss, Z.; Driss, D.; Bouabidi, A.; Euchy, S.; Park, H.-H. Facile Synthesis of SnO2 Aerogel/Reduced Graphene Oxide Nanocomposites via in Situ Annealing for the Photocatalytic Degradation of Methyl Orange. *Nanomaterials* **2019**, *9* (3), 358. https://doi.org/10.3390/nano9030358.

(11) Parale, V. G.; Kim, T.; Lee, K. Y.; Phadtare, V. D.; Dhavale, R. P.; Jung, H. N. R.; Park, H. H. Hydrophobic TiO2–SiO2 Composite Aerogels Synthesized via in Situ Epoxy-Ring Opening Polymerization and Sol-Gel Process for Enhanced Degradation Activity. *Ceram. Int.* **2020**, *46* (4), 4939–4946. https://doi.org/10.1016/j.ceramint.2019.10.231.

(12) Bernardes, J. C.; Pinheiro, G. K.; Muller, D.; Latocheski, E.; Domingos, J. B.; Rambo, C. R. Novel Modified Nonalkoxide Sol–gel Synthesis of Multiphase High Surface Area TiO2 Aerogels for Photocatalysis. *J. Sol-Gel Sci. Technol.* **2020**, *94* (2), 425–434. https://doi.org/10.1007/s10971-020-05286-z.

(13) DeSario, P. A.; Pietron, J. J.; Taffa, D. H.; Compton, R.; Schünemann, S.; Marschall, R.; Brintlinger, T. H.; Stroud, R. M.; Wark, M.; Owrutsky, J. C.; Rolison, D. R. Correlating Changes in Electron Lifetime and Mobility on Photocatalytic Activity at Network-Modified TiO2 Aerogels. *J. Phys. Chem. C* **2015**, *119* (31), 17529–17538. https://doi.org/10.1021/acs.jpcc.5b04013.

(14) Panayotov, D. A.; Desario, P. A.; Pietron, J. J.; Brintlinger, T. H.; Szymczak, L. C.; Rolison, D. R.; Morris, J. R. Ultraviolet and Visible Photochemistry of Methanol at 3D Mesoporous Networks: TiO2 and Au-TiO2. *J. Phys. Chem. C* **2013**, *117* (29), 15035–15049. https://doi.org/10.1021/jp312583w.

(15) Parayil, S. K.; Psota, R. J.; Koodali, R. T. Modulating the Textural Properties and Photocatalytic Hydrogen Production Activity of TiO2 by High Temperature Supercritical Drying. *Int. J. Hydrogen Energy* **2013**, *38* (25), 10215–10225.

https://doi.org/10.1016/j.ijhydene.2013.06.015.

(16) Kwon, J.; Choi, K.; Schreck, M.; Liu, T.; Tervoort, E.; Niederberger, M. Gas-Phase Nitrogen Doping of Monolithic TiO2nanoparticle-Based Aerogels for Efficient Visible Light-Driven Photocatalytic H2production. *ACS Appl. Mater. Interfaces* **2021**, *13* (45), 53691–53701. https://doi.org/10.1021/acsami.1c12579.

(17) Lin, C. C.; Wei, T. Y.; Lee, K. T.; Lu, S. Y. Titania and Pt/titania Aerogels as Superior Mesoporous Structures for Photocatalytic Water Splitting. *J. Mater. Chem.* **2011**, *21* (34), 12668–12674. https://doi.org/10.1039/c1jm11992c.

(18) Puskelova, J.; Baia, L.; Vulpoi, A.; Baia, M.; Antoniadou, M.; Dracopoulos, V.; Stathatos, E.; Gabor, K.; Pap, Z.; Danciu, V.; Lianos, P. Photocatalytic Hydrogen Production Using TiO2-Pt Aerogels. *Chem. Eng. J.* **2014**, *242*, 96–101. https://doi.org/10.1016/j.cej.2013.12.018.

(19) Iorio, Y. Di; Aguirre, M. E.; Brusa, M. A.; Grela, M. A. Surface Chemistry Determines Electron Storage Capabilities in Alcoholic Sols of Titanium Dioxide Nanoparticles. A Combined FTIR and Room Temperature EPR Investigation. *J. Phys. Chem. C* **2012**, *116* (17), 9646–9652. https://doi.org/10.1021/jp301659t.

(20) Sachs, M.; Pastor, E.; Kafizas, A.; Durrant, J. R. Evaluation of Surface State Mediated Charge Recombination in Anatase and Rutile TiO2. *J. Phys. Chem. Lett.* **2016**, *7* (19), 3742–3746. https://doi.org/10.1021/acs.jpclett.6b01501.

(21) Bahnemann, D.; Henglein, A.; Lilie, J.; Spanhel, L. Flash Photolysis Observation of the Absorption Spectra of Trapped Positive Holes and Electrons in Colloidal Titanium Dioxide. *J. Phys. Chem.* **1984**, *88* (4), 709–711. https://doi.org/10.1021/j150648a018.

(22) Mohamed, H. H.; Dillert, R.; Bahnemann, D. W. Growth and Reactivity of Silver Nanoparticles on the Surface of TiO 2: A Stopped-Flow Study. *J. Phys. Chem. C* **2011**, *115* (24), 12163–12172. https://doi.org/10.1021/jp2031576.

(23) Mohamed, H. H.; Dillert, R.; Bahnemann, D. W. Kinetic and Mechanistic Investigations of the Light Induced Formation of Gold Nanoparticles on the Surface of TiO2. *Chem. - A Eur. J.* **2012**, *18* (14), 4314–4321. https://doi.org/10.1002/chem.201102799.

(24) Mohamed, H. H.; Dillert, R.; Bahnemann, D. W. Reaction Dynamics of the Transfer of Stored Electrons on TiO2 Nanoparticles: A Stopped Flow Study. *J. Photochem. Photobiol. A Chem.* **2011**, *217* (1), 271–274. https://doi.org/10.1016/j.jphotochem.2010.09.024.

(25) Mohamed, H. H.; Dillert, R.; Bahnemann, D. W. TiO 2 Nanoparticles as Electron Pools: Single- and Multi-Step Electron Transfer Processes. *J. Photochem. Photobiol. A Chem.*

2012, *245*, 9–17. https://doi.org/10.1016/j.jphotochem.2012.06.022.

(26) Mohamed, H. H.; Mendive, C. B.; Dillert, R.; Bahnemann, D. W. Kinetic and Mechanistic Investigations of Multielectron Transfer Reactions Induced by Stored Electrons in TiO2 Nanoparticles: A Stopped Flow Study. *J. Phys. Chem. A* **2011**, *115* (11), 2139–2147. https://doi.org/10.1021/jp108958w.

(27) Sakar, M.; Nguyen, C. C.; Vu, M. H.; Do, T. O. Materials and Mechanisms of Photo-Assisted Chemical Reactions under Light and Dark Conditions: Can Day–Night Photocatalysis Be Achieved? *ChemSusChem* **2018**, *11* (5), 809–820. https://doi.org/10.1002/cssc.201702238.

(28) Ng, C.; Ng, Y. H.; Iwase, A.; Amal, R. Visible Light-Induced Charge Storage, on-Demand Release and Self- Photorechargeability of WO3 Film. *Phys. Chem. Chem. Phys.* **2011**, *13* (29), 13421–13426. https://doi.org/10.1039/c1cp20412b.

(29) Ng, C.; Iwase, A.; Ng, Y. H.; Amal, R. Understanding Self-Photorechargeability of WO3 for H2 Generation without Light Illumination. *ChemSusChem* **2013**, *6* (2), 291–298. https://doi.org/10.1002/cssc.201200702.

(30) Schulz, M.; Hagmeyer, N.; Wehmeyer, F.; Lowe, G.; Rosenkranz, M.; Seidler, B.; Popov, A.; Streb, C.; Vos, J. G.; Dietzek, B. Photoinduced Charge Accumulation and Prolonged Multielectron Storage for the Separation of Light and Dark Reaction. *J. Am. Chem. Soc.* **2020**, *142* (37), 15722–15728. https://doi.org/10.1021/jacs.0c03779.

(31) Lau, V. W.; Lotsch, B. V. A Tour-Guide through Carbon Nitride-Land: Structure- and Dimensionality-Dependent Properties for Photo(Electro)Chemical Energy Conversion and Storage. *Adv. Energy Mater.* **2021**, 2101078. https://doi.org/10.1002/aenm.202101078.

(32) Kröger, J.; Jiménez-Solano, A.; Savasci, G.; Rovó, P.; Moudrakovski, I.; Küster, K.; Schlomberg, H.; Vignolo- González, H. A.; Duppel, V.; Grunenberg, L.; Dayan, C. B.; Sitti, M.; Podjaski, F.; Ochsenfeld, C.; Lotsch, B.V. Interfacial Engineering for Improved Photocatalysis in a Charge Storing 2D Carbon Nitride: Melamine Functionalized Poly(heptazine Imide). *Adv. Energy Mater.* **2021**, *11* (6). https://doi.org/10.1002/aenm.202003016.

(33) Ng, C.; Ng, Y. H.; Iwase, A.; Amal, R. Influence of Annealing Temperature of WO3 in Photoelectrochemical Conversion and Energy Storage for Water Splitting. *ACS Appl. Mater. Interfaces* **2013**, *5* (11), 5269–5275. https://doi.org/10.1021/am401112q.

(34) Takai, A.; Kamat, P. V. Capture, Store, and Discharge. Shuttling Photogenerated Electrons across TiO 2 ÀSilver Interface. https://doi.org/10.1021/nn202294b.

(35) Zhou, L.; Boyd, C. E. Comparison of Nessler, Phenate, Salicylate and Ion Selective Electrode Procedures for Determination of Total Ammonia Nitrogen in Aquaculture. *Aquaculture* **2016**, *450*, 187–193. https://doi.org/10.1016/j.aquaculture.2015.07.022.

(36) Bernardes, J. C.; Müller, D.; Pinheiro, G. K.; Rambo, C. R. Enhancing the Optical Transparency of TiO2 Aerogels with High Surface Area through Water-Based Synthesis. *Opt. Mater. (Amst).* **2020**, *109*, 110359. https://doi.org/10.1016/j.optmat.2020.110359.

(37) Alwin, S.; Ramasubbu, V.; Sahaya Shajan, X. TiO2 Aerogel–metal Organic Framework Nanocomposite: A New Class of Photoanode Material for Dye-Sensitized Solar Cell Applications. *Bull. Mater. Sci.* **2018**, *41* (1), 27. https://doi.org/10.1007/s12034-017-1532-8.

(38) Quintero, Y.; Mosquera, E.; Diosa, J.; García, A. Ultrasonic-Assisted Sol–gel Synthesis of TiO2 Nanostructures: Influence of Synthesis Parameters on Morphology, Crystallinity, and Photocatalytic Performance. *J. Sol-Gel Sci. Technol.* **2020**, *94* (2), 477–485. https://doi.org/10.1007/s10971-020-05263-6.

(39) Lermontov, S. A.; Straumal, E. A.; Mazilkin, A. A.; Baranchikov, A. E.; Straumal, B. B.; Ivanov, V. K. An Approach for Highly Transparent Titania Aerogels Preparation. *Mater. Lett.* **2018**, *215*, 19–22. https://doi.org/10.1016/j.matlet.2017.12.031.

(40) Moussaoui, R.; Elghniji, K.; ben Mosbah, M.; Elaloui, E.; Moussaoui, Y. Sol–gel Synthesis of Highly TiO2 Aerogel Photocatalyst via High Temperature Supercritical Drying. *J. Saudi Chem. Soc.* **2017**, *21* (6), 751–760. https://doi.org/10.1016/j.jscs.2017.04.001.

(41) Kandiel, T. A.; Dillert, R.; Robben, L.; Bahnemann, D. W. Photonic Efficiency and Mechanism of Photocatalytic Molecular Hydrogen Production over Platinized Titanium Dioxide from Aqueous Methanol Solutions. *Catal. Today* **2011**, *161* (1), 196–201. https://doi.org/10.1016/j.cattod.2010.08.012.

(42) Thommes, M.; Kaneko, K.; Neimark, A. V; Olivier, J. P.; Rodriguez-Reinoso, F.; Rouquerol, J.; Sing, K. S. W. IUPAC Technical Report Physisorption of Gases, with Special Reference to the Evaluation of Surface Area and Pore Size Distribution (IUPAC Technical Report). **2015**. https://doi.org/10.1515/pac-2014-1117.S

(43) Schlumberger, C.; Thommes, M. Characterization of Hierarchically Ordered Porous Materials by Physisorption and Mercury Porosimetry—A Tutorial Review. *Adv. Mater. Interfaces* **2021**, *8* (4), 2002181. https://doi.org/10.1002/admi.202002181.

(44) Bardestani, R.; Patience, G. S.; Kaliaguine, S. Experimental Methods in Chemical Engineering: Specific Surface Area and Pore Size Distribution measurements—BET, BJH,

and DFT. *Canadian Journal of Chemical Engineering*. Wiley-Liss Inc. November 2019, pp 2781–2791. https://doi.org/10.1002/cjce.23632.

(45) Voepel, P.; Weiss, M.; Smarsly, B. M.; Marschall, R. Photocatalytic Activity of Multiphase TiO2(B)/anatase Nanoparticle Heterojunctions Prepared from Ionic Liquids. *J. Photochem. Photobiol. A Chem.* **2018**, *366*, 34–40. https://doi.org/10.1016/j.jphotochem.2018.03.019.

(46) Dette, C.; Pérez-Osorio, M. A.; Kley, C. S.; Punke, P.; Patrick, C. E.; Jacobson, P.; Giustino, F.; Jung, S. J.; Kern, K. TiO2 Anatase with a Bandgap in the Visible Region. *Nano Lett.* **2014**, *14* (11), 6533–6538. https://doi.org/10.1021/nl503131s.

(47) Zywitzki, D.; Jing, H.; Tüysüz, H.; Chan, C. K. High Surface Area, Amorphous Titania with Reactive Ti3+ through a Photo-Assisted Synthesis Method for Photocatalytic H2 Generation. *J. Mater. Chem. A* **2017**, *5* (22), 10957–10967. https://doi.org/10.1039/c7ta01614j.

(48) Kong, M.; Li, Y.; Chen, X.; Tian, T.; Fang, P.; Zheng, F.; Zhao, X. Tuning the Relative Concentration Ratio of Bulk Defects to Surface Defects in TiO2 Nanocrystals Leads to High Photocatalytic Efficiency. *J. Am. Chem. Soc.* **2011**, *133* (41), 16414–16417. https://doi.org/10.1021/ja207826q.

(49) Kiwi, J.; Grätzel, M. Optimization of Conditions for Photochemical Water Cleavage. Aqueous Pt/TiO2 (Anatase) Dispersions under Ultraviolet Light. *J. Phys. Chem.* **1984**, *88* (7), 1302–1307. https://doi.org/10.1021/j150651a012.

(50) Furube, A.; Asahi, T.; Masuhara, H.; Yamashita, H.; Anpo, M. Direct Observation of a Picosecond Charge Separation Process in Photoexcited Platinum-Loaded TiO2 Particles by Femtosecond Diffuse Reflectance Spectroscopy. *Chem. Phys. Lett.* **2001**, *336* (5–6), 424–430. https://doi.org/10.1016/S0009-2614(01)00128-2.

(51) Ikeda, S.; Sugiyama, N.; Murakami, S.; Kominami, H.; Kera, Y.; Noguchi, H.; Uosaki, K.; Torimoto, T.; Ohtani, B. Quantitative Analysis of Defective Sites in titanium(IV) Oxide Photocatalyst Powders. *Phys. Chem. Chem. Phys.* **2003**, *5* (4), 778–783. https://doi.org/10.1039/b206594k.

(52) Yan, J.; Wu, G.; Guan, N.; Li, L.; Li, Z.; Cao, X. Understanding the Effect of Surface/bulk Defects on the Photocatalytic Activity of TiO2: Anatase versus Rutile. *Phys. Chem. Chem. Phys.* **2013**, *15* (26), 10978. https://doi.org/10.1039/c3cp50927c.

(53) Yang, J.; Wang, D.; Han, H.; Li, C. Roles of Cocatalysts in Photocatalysis and Photoelectrocatalysis. *Acc. Chem. Res.* **2013**, *46* (8), 1900–1909. https://doi.org/10.1021/ar300227e.

(54) Trasatti, S. Work Function, Electronegativity, and Electrochemical Behaviour of Metals. III. Electrolytic Hydrogen Evolution in Acid Solutions. *J. Electroanal. Chem.* **1972**, *39* (1), 163–184. https://doi.org/10.1016/S0022-0728(72)80485-6.

(55) Ziegenbalg, D.; Zander, J.; Marschall, R. Photocatalytic Nitrogen Reduction: Challenging Materials with Reaction Engineering. *ChemPhotoChem* **2021**, *5* (9), 792–807. https://doi.org/10.1002/cptc.202100084.

(56) Cheng, M.; Xiao, C.; Xie, Y. Photocatalytic Nitrogen Fixation: The Role of Defects in Photocatalysts. *Journal of Materials Chemistry A*. Royal Society of Chemistry August 2019, pp 19616–19633. https://doi.org/10.1039/c9ta06435d.

(57) Li, C.; Wang, T.; Zhao, Z.-J.; Yang, W.; Li, J.-F.; Li, A.; Yang, Z.; Ozin, G. A.; Gong, J. Promoted Fixation of Molecular Nitrogen with Surface Oxygen Vacancies on Plasmon-Enhanced TiO 2 Photoelectrodes . *Angew. Chemie* **2018**, *130* (19), 5376–5380. https://doi.org/10.1002/ange.201713229.

8.2 Supporting Information

Supporting Information

Photocatalytic activity and electron storage ability of TiO_2 aerogels with adjustable surface area

Alexandra Rose[a§], Anja Hofmann[b§], Pascal Voepel[a], Barbara Milow[a], Roland Marschall[b]

[a] A. Rose, Dr. P. Voepel, Prof. B. Milow
German Aerospace Center
Institute of Materials Research
Aerogels and Aerogel composites
Linder Höhe, Köln 51147, Germany

[b] A. Hofmann, Prof. R. Marschall
Department of Chemistry
University of Bayreuth
Universitätsstraße 30, Bayreuth 95447, Germany
E-mail: roland.marschall@uni-bayreuth.de , ORCID: 0000-0002-1057-0459

§: These authors contributed equally to the manuscript.

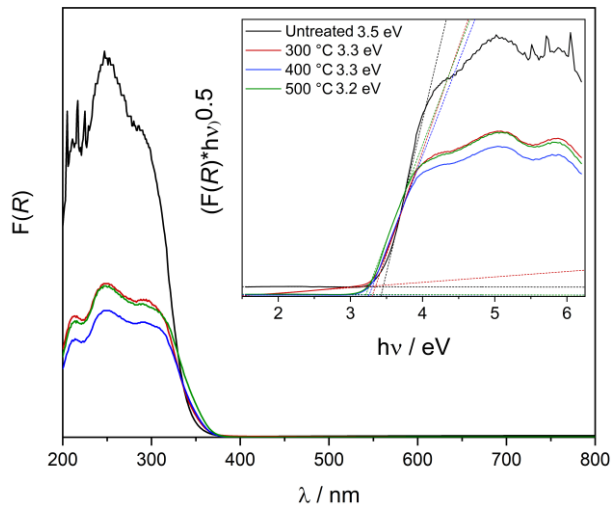

Figure S1. *Kubelka-Munk UV-vis spectra and Tauc plots (inset) of the untreated aerogel (black), the 300 °C (red), the 400 °C (blue), and the 500 °C (green) calcined aerogels.*

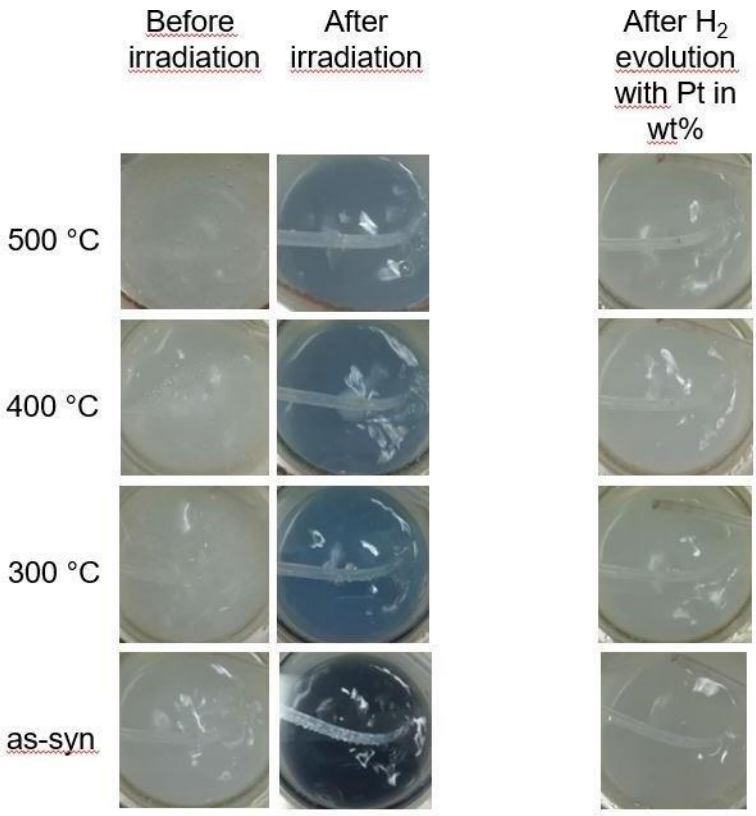

***Figure S2**: Enlarged photographs from Figure 5, showing the coloration of the different photocharged aerogel dispersions.*

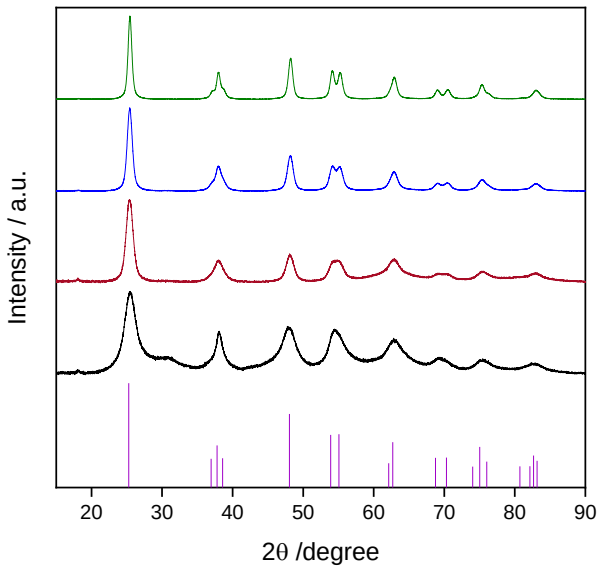

***Figure S3.** XRD patterns of the untreated TiO_2 aerogel (black) and aerogels calcined at 300 °C (red), 400 °C (blue) and 500 °C (green) after photocatalytic hydrogen production reaction. Reference pattern of anatase TiO_2 (PDF-21-1272) is shown for comparison. Normalized data to the range 0 to 100 related to the highest signal.*

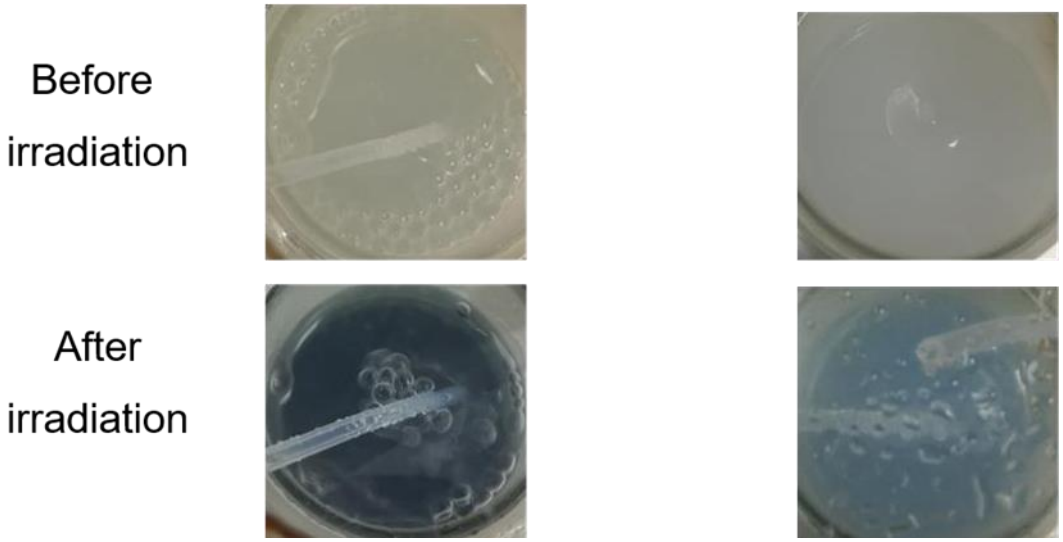

***Figure S4**: Comparison of the electron storage ability of as-syn TiO_2 aerogel and commercial anatase nanoparticles. Lamp was turned on after 30 minutes and off after 90 minutes irradiation. For this comparison 50 mg of the corresponding sample was used for the measurement, a 300 W Xe lamp and a 10% methanol solution.*

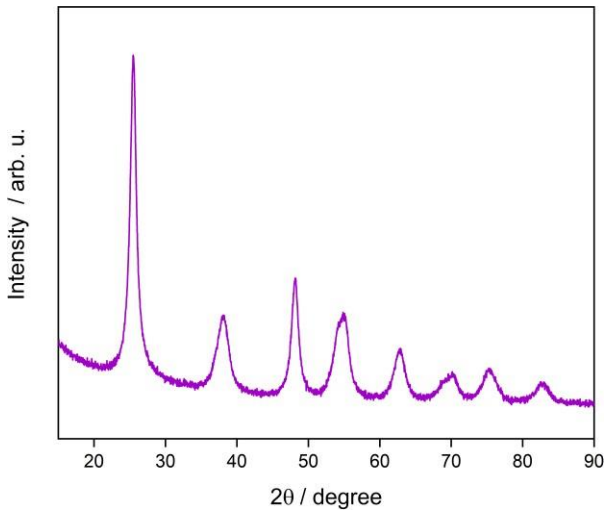

***Figure S5**: XRD pattern of commercial anatase powder.*

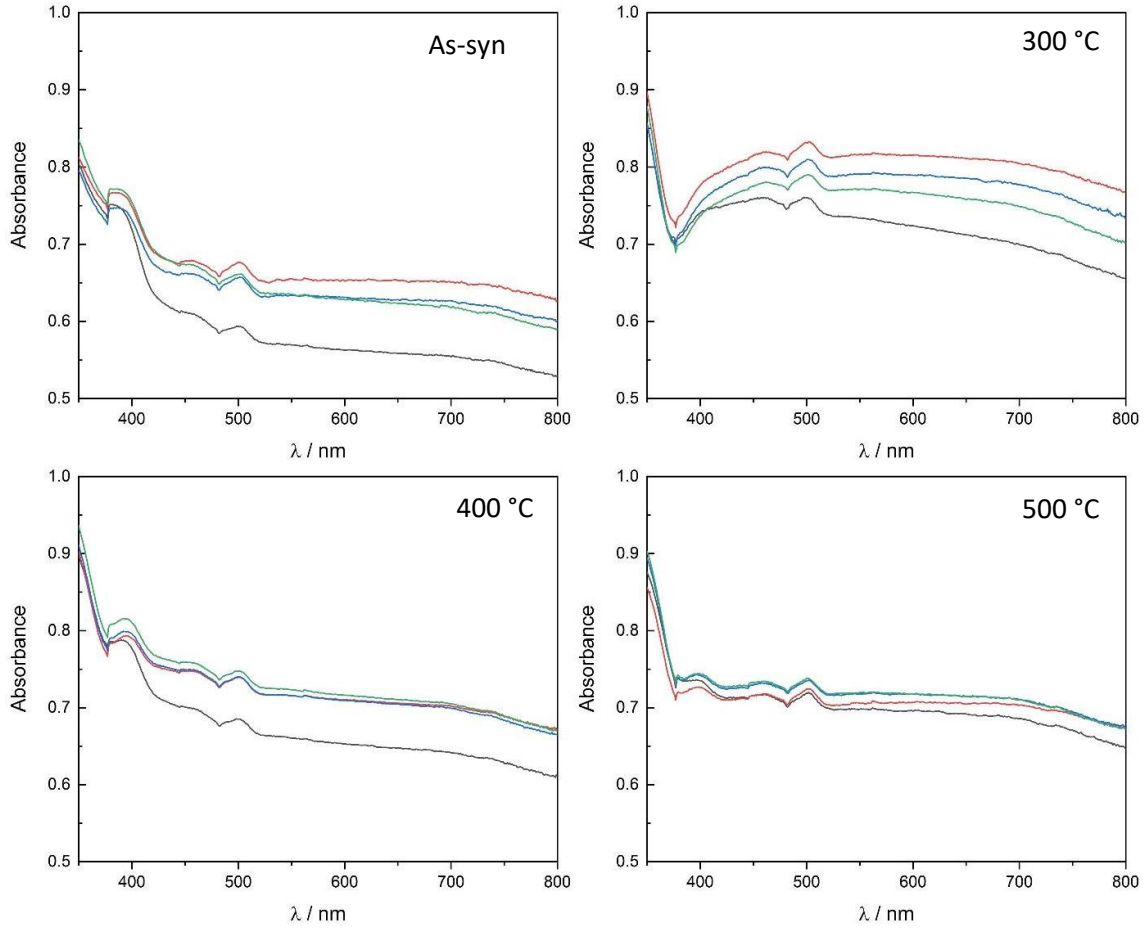

Figure S6. *Absorbance measurements of the four TiO_2 aerogels dispersions, before irradiation (gray), directly after 100 min of irradiation (green), 30 min after irradiation (blue) and 1 h 50 min after irradiation (red).*

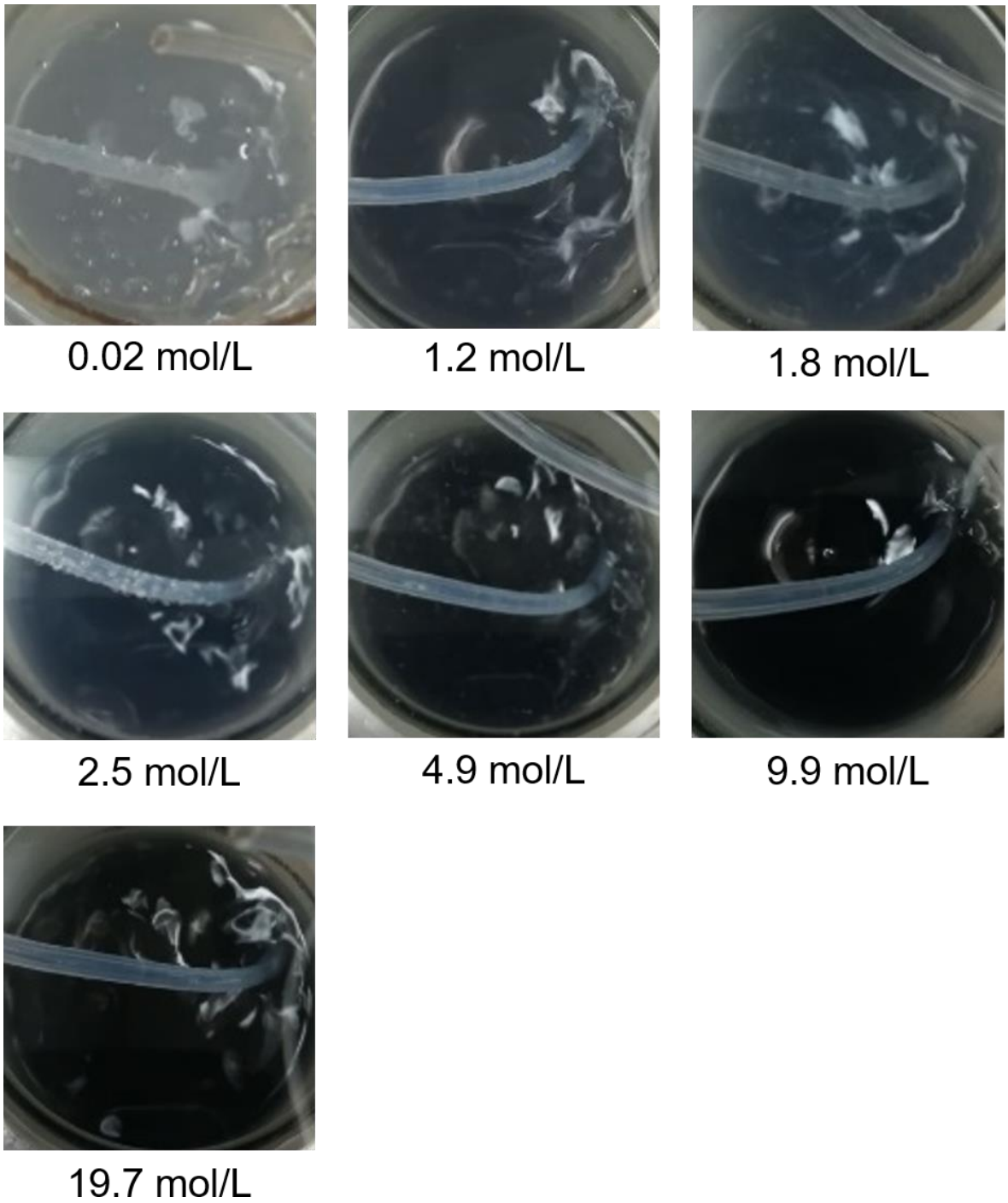

***Figure S7**: Enlarged photographs of photocharged TiO_2 aerogel dispersion with different MeOH concentration in water.*

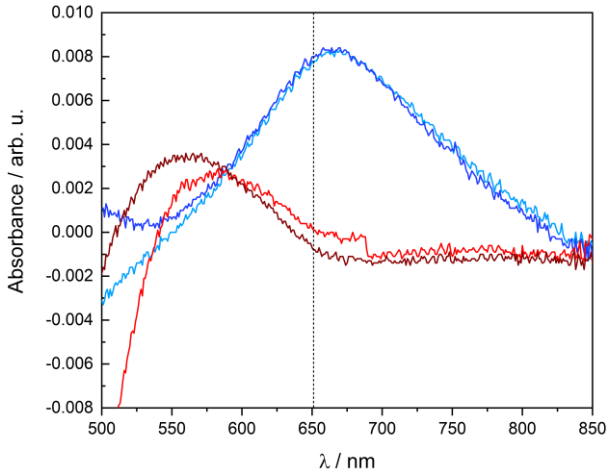

Figure S8. *Absorbance spectra of the salicylate test of the solution after dark nitrogen reduction reaction with photocharged as-synthesized TiO_2 aerogel sample for quantitative determination of the obtained NH_3 concentration. The test was performed twice to verify the result (light and dark blue). The dashed line is the absorbance maximum, which was used for the calibration. Two additional control experiments are given showing no ammonia generation: in red is an identical measurement in argon gas, and in brown is the baseline before photocharging (nitrogen gas, dark, no photocharging yet). The maximum at 550 nm is not related to ammonia, but from the nitroprusside during the salicylate testing.*

9 List of Publications

Peer-reviewed publications

- **A. Hofmann**, M. Weiss, J. Timm, R. Marschall, "Perovskite-type oxynitride nanofibers performing photocatalytic oxygen and hydrogen generation" *Adv. Mater. Interfaces* **2021**, *8*, 2100813, https://doi.org/10.1002/admi.202100813

- **A. Hofmann**, M. Weiss, R. Marschall, "Fast low temperature synthesis of layered perovskite heterojunctions for overall water splitting" *J. Phys. Energy* **2021**, *3*, 014002, https://doi.org/10.1088/2515-7655/abc07a

- C. Suchomski, D. J. Weber, P. Dolcet, **A. Hofmann**, P. Voepel, J. Yue, M. Einert, M. Möller, S. Werner, S. Gross, I. Djerdj, T. Brezesinski, B. M. Smarsly, „Sustainable and surfactant-free high-throughput synthesis of highly dispersible zirconia nanocrystals" *J. Mater. Chem. A* **2017**, *5*, 16296, https://doi.org/10.1039/C7TA02316B

- P. Voepel, C. Suchomski, **A. Hofmann**, S. Gross, P. Dolcet, B. M. Smarsly, "In-depth mesocrystal formation analysis of microwave-assisted synthesis of $LiMnPO_4$ nanostructures in organic solution", *CrystEngComm* **2016**, *18*, 316, https://doi.org/10.1039/C5CE01946J

Publications without review process

- A. Rose, **A. Hofmann**, P. Voepel, B. Milow, R. Marschall, "Photocatalytic activity and electron storage capability of TiO_2 aerogels with adjustable surface area" *ChemRxiv*, DOI: 10.26434/chemrxiv-2021-vxkpq-v2, 2022.

10 Contributions to Conferences

Contributions relating to this thesis

- "Perovskite-type Oxynitride Nanofibers Performing Photocatalytic Oxygen and Hydrogen Generation", **Anja Hofmann**, Morten Weiss, Jana Timm, Frank E. Osterloh, Roland Marschall (oral) **and** "Photocatalytic activity and electron storage capability of TiO_2 aerogels with adjustable surface area", Alexandra Rose, **Anja Hofmann**, Pascal Voepel, Barbara Milow, Roland Marschall (poster), *23rd International Conference on Photochemical Conversion and Storage of Solar Energy (IPS-23)*, Lausanne, Switzerland, 02nd to 05th August 2022, **oral and poster** contribution.

- "Perovskite-type Oxynitride Nanofibers Performing Photocatalytic Oxygen and Hydrogen Generation", **Anja Hofmann**, Morten Weiss, Jana Timm, Roland Marschall*, European Materials Research Society (E-MRS) 2022 Spring Meeting Virtual Conference*, online, 30th May to 03rd June 2022, **oral** contribution.

- "Fast low temperature synthesis of layered perovskite heterojunctions for overall water splitting", **Anja Hofmann**, Morten Weiss, Roland Marschall **and** "Perovskite-type Oxynitride Nanofibers Performing Photocatalytic Oxygen and Hydrogen Generation", **Anja Hofmann**, Morten Weiss, Jana Timm, Roland Marschall, *4th International Solar Fuels Conference (ISF-4)*, online, 26th to 29th July 2021, **2 poster** contributions.

- "Conversion of electrospun layered perovskite nanofibers to perovskite oxynitrides for visible light absorption", **Anja Hofmann**, Roland Marschall, *Inaugural CataLight Young Scientist Symposium on Light-Driven Catalysis*, online, 10th to 26th November 2020, **oral** contribution.

- "Ammonium nitrate-assisted synthesis of $Ba_5Ta_4O_{15}$ and its heterojunctions for photocatalytic overall water splitting", **Anja Hofmann**, Roland Marschall, *Virtual Conference on Inorganic Chemistry by GDCh divisions of Inorganic Chemistry and*

Solid-State Chemistry & Materials Research , online, 29th to 30th September 2020, **poster** contribution.

- "Tailoring layered oxide nanofibers for enhanced photocatalytic water splitting performance", André Bloesser, **Anja Hofmann**, Roland Marschall, *7th International Conference on Semiconductor Photochemistry (SP-7)*, Milano, Italy, 11th to 14th September 2019, **poster** contribution.

Additional contributions

- "Three dimensional characterization of electrospun nanofibers by X-ray nano-CT", **A. Hofmann**, J. Martins de Souza e Silva, M. Sieland, G. Beck, N. C. Hildebrandt, S. Werner, R. Marschall, B. M. Smarsly, R. B. Wehrspohn, A. W. Maijenburg, *19th Conference on Inorganic Chemistry by GDCh divisions of Inorganic Chemistry and Solid-State Chemistry & Materials Research*, Regensburg, Germany, 24th to 27th September 2018, **poster** contribution

- "Three dimensional characterization of electrospun nanofibers by X-ray nano-CT", **A. Hofmann**, J. Martins de Souza e Silva, M. Sieland, G. Beck, N. C. Hildebrandt, S. Werner, R. Marschall, B. M. Smarsly, R. B. Wehrspohn, A. W. Maijenburg, *ELectrospinning for ENergy conference (ELEN-2018)*, Montpellier, France, 13th to 15th June 2018, **oral** contribution

11 Research visits

- Six-week stay at the research group of Prof. Frank. E. Osterloh, Department of Chemistry, University of California, Davis, United States, 01st November to 15th December 2021.

12 Danksagung

Zunächst möchte ich Herrn Prof. Roland Marschall dafür danken, mir die Möglichkeit gegeben zu haben meine Doktorarbeit zu einem sehr vielseitigen und interessanten Thema in seiner Arbeitsgruppe anfertigen zu können. Sein entgegen gebrachtes Vertrauen, das Fördern und Fordern, als auch die vielen wissenschaftlichen Gespräche haben diese Arbeit und meine persönliche Entwicklung in dieser Zeit erst möglich gemacht.

Besonderer Dank gilt Ihm und Herrn Prof. Frank E. Osterloh für die Ermöglichung des 1,5-monatigen Forschungsaufenthaltes in den USA an der UC Davis im Rahmen dieser Doktorarbeit. Herrn Prof. Frank E. Osterloh danke ich für die Betreuung in dieser Zeit und die Möglichkeit einen Einblick in die interessante Messmethodik der Oberflächenphotospannungsspektroskopie zu bekommen. Dem Bavaria California Technology Center (BaCaTeC) danke ich für die Finanzierung des Aufenthalts.

Herrn Prof. Greiner gilt der Dank für die Übernahme des Zweitgutachtens für die vorliegende Arbeit. Weiterhin möchte ich mich für die Möglichkeit der Benutzung der Elektrospinn-Anlagen in Seinen Laboren zu Beginn meiner Promotion bedanken. Dr. Mina Heidari und Dr. Xiaojian Liao danke ich für die Einweisung.

Weiterer Dank geht an alle ehemaligen und jetzigen AG-Mitglieder und Arbeitskollegen, sowie an die Studenten für die tolle Zusammenarbeit und Hilfsbereitschaft. Ohne sie alle wäre diese Arbeit nicht möglich gewesen. Spezieller Dank soll hier an Dr. Jana Timm, Judith Zander, Dr. Morten Weiß, Jonas Jungmann, Mirco Ade, André Blößer und Christopher Simon gehen, sowie an Agnes Specht, Henrike von Wedel, Andreas Jehle und Lion Schumacher. Jana Timm und Jonas Jungmann danke ich für die durchgeführten Physisorptionsmessungen. Jana Timm gilt weiterhin ein großer Dank für die vielen hilfreichen wissenschaftlichen Diskussionen, Hilfestellungen und Ratschläge und die Durchführung von Elementaranalyse-Messungen. Bei Jonas Jungmann möchte ich mich außerdem für seine allgemeine Hilfe bei Bestellungen und im Laborbetrieb bedanken. Judith Zander und Morten Weiß danke ich für die vielen langen Tage, die Sie häufig mit mir in der Uni für Messungen verbracht haben und für ihre Unterstützung. Morten Weiß gilt spezieller Dank für die Durchführung und Auswertung von XPS-Messungen als auch für die

Rietveld-Verfeinerungen und für die Hilfestellungen bei speziellen Messprogrammen für photokatalytische Messungen. Christopher Simon danke ich für die TEM-Aufnahmen.

Weiterhin möchte ich mich bei Frau Martina Heider für ihre Hilfe am REM und EDX bedanken. Lena Geiling gilt mein Dank für die Durchführung von TG-MS-Messungen.

Ich möchte auch allen Arbeitsgruppenmitgliedern der AG Osterloh an der UC Davis in den USA meinen Dank für ihre nette Aufnahme in ihre Arbeitsgruppe im Zeitraum meines Aufenthaltes und für ihre Unterstützung im Labor aussprechen. Es war eine besondere Zeit, die einen erheblichen Beitrag für meine persönliche und berufliche Weiterentwicklung geleistet hat. Besonderer Dank gilt hier Anna Kundmann für Ihre Einweisung in die Messtechnik und Datenauswertung.

Der Familie Aue danke ich für die Unterkunft und die nette Aufnahme in Ihre Familie für die Zeit meines Aufenthalts an der UC Davis.

Ein ganz großes Dankeschön geht an alle Korrekturleser dieser Arbeit.

Zu guter Letzt möchte ich mich besonders bei meiner Mutter bedanken, für ihren Rückhalt und ihre bedingungslose Unterstützung dabei meinen eigenen Weg zu gehen und mich in jeder Lebenslage zu unterstützen.

13 (Eidesstattliche) Versicherung und Erklärungen

(§ 9 Satz 2 Nr. 3 PromO BayNAT)

Hiermit versichere ich eidesstattlich, dass ich die Arbeit selbstständig verfasst und keine anderen als die von mir angegebenen Quellen und Hilfsmittel benutzt habe (vgl. Art. 64 Abs. 1Satz 6 BayHSchG).

(§ 9 Satz 2 Nr. 3 PromO BayNAT)

Hiermit erkläre ich, dass ich die Dissertation nicht bereits zur Erlangung eines akademischen Grades eingereicht habe und dass ich nicht bereits diese oder eine gleichartige Doktorprüfung endgültig nicht bestanden habe.

(§ 9 Satz 2 Nr. 4 PromO BayNAT)

Hiermit erkläre ich, dass ich Hilfe von gewerblichen Promotionsberatern bzw. -vermittlern oder ähnlichen Dienstleistern weder bisher in Anspruch genommen habe noch künftig in Anspruch nehmen werde.

(§ 9 Satz 2 Nr. 7 PromO BayNAT)

Hiermit erkläre ich mein Einverständnis, dass die elektronische Fassung der Dissertation unter Wahrung meiner Urheberrechte und des Datenschutzes einer gesonderten Überprüfung unterzogen werden kann.

(§ 9 Satz 2 Nr. 8 PromO BayNAT)

Hiermit erkläre ich mein Einverständnis, dass bei Verdacht wissenschaftlichen Fehlverhaltens Ermittlungen durch universitätsinterne Organe der wissenschaftlichen Selbstkontrolle stattfinden können.

Ort, Datum	Anja Hofmann